June 29, 2006

Seismic Evaluation of Hydrocarbon Saturation in Deep-Water Reservoirs

Grant/Cooperative Agreement DE-FC26-02NT15342.

FINAL REPORT

Report Period Start Date: September 1, 2002
Report period End Date: April 30, 2006

Primary Author: Dr. Michael Batzle

Prime Contractor: Colorado school of Mines
Department of Geophysics
1500 Illinois St.
Golden, Colorado 80401

Subcontractors: University of Houston
Texas A&M University

Industrial Collaborators: Paradigm, Veritas

Principal Investigators:

M. Batzle - Colorado School of Mines
D-h Han - University of Houston (formerly: Houston Advanced Research Center)
R. Gibson - Texas A&M University
Huw James - Paradigm Geophysical

Disclaimer:

Abstract:

During this last period of the "Seismic Evaluation of Hydrocarbon Saturation in Deep-Water Reservoirs" project (Grant/Cooperative Agreement DE-FC26-02NT15342), we finalized integration of rock physics, well log analysis, seismic processing, and forward modeling techniques. Most of the last quarter was spent combining the results from the principal investigators and come to some final conclusions about the project. Also much of the effort was directed towards technology transfer through the Direct Hydrocarbon Indicators mini-symposium at UH and through publications.

As a result we have:

- Tested a new method to directly invert reservoir properties, water saturation, Sw, and porosity from seismic AVO attributes
- Constrained the seismic response based on fluid and rock property correlations
- Reprocessed seismic data from Ursa field
- Compared thin layer property distributions and averaging on AVO response
- Related pressures and sorting effects on porosity and their influence on DHI's.
- Examined and compared gas saturation effects for deep and shallow reservoirs
- Performed forward modeling using geobodies from deepwater outcrops
- Documented velocities for deepwater sediments
- Continued incorporating outcrop descriptive models in seismic forward models
- Held an open DHI symposium to present the final results of the project
- Relations between Sw, porosity, and AVO attributes
- Models of Complex, Layered Reservoirs
- Technology transfer

Several factors can contribute to limit our ability to extract accurate hydrocarbon saturations in deep water environments. Rock and fluid properties are one factor, since, for example, hydrocarbon properties will be considerably different with great depths (high pressure) when compared to shallow properties. Significant over pressure, on the other hand will make the rocks behave as if they were shallower. In addition to the physical properties, the scale and tuning will alter our hydrocarbon indicators. Gas saturated reservoirs change reflection amplitudes significantly. The goal for the final project period was to systematically combine and document these various effects for use in deep water exploration and transfer this knowledge as clearly and effectively as possible.

Contents:

Figures:

Executive Summary:

This was a joint project involving research at The University of Houston, Texas A&M University, the Colorado School of Mines, and Paradigm Geophysical Corporation we are combining rock measurements, observed property trends, forward modeling, and interpretation of 2-D seismic data to further develop our ability to predict hydrocarbon saturation.

To complete this research, our effort was to summarize and link the results ascertained from subsequent quarters. Also there was a major focus on technology transfer. We made significant steps towards our goal of ascertainment of the type and level of saturation of hydrocarbons in situ from seismic data. A new inversion method was tested to directly invert reservoir properties, water saturation, Sw, and porosity from seismic AVO attributes. The new inversion scheme is based on restricting the solutions based on rock physics relations. Testing of the technique on the King Kong, Lisa Anne data set shows that densities and saturations are better constrained and economic versus uneconomic gas accumulations can be resolved.

A suite of sand samples from the Gulf of Mexico was used evaluate the range of sand properties we can anticipate for deep water reservoirs. The gain factor, G, controlling the velocity response to fluids is restricted over a narrow range. We have also documented the significant pressure and sorting effects on porosity. Deep water sands have unique characteristics that are not well represented by artificial sand packs.

We have also analyzed the AVO response of deep and shallow gas sands. We have reprocessed seismic data from Ursa field and calculate composite reflection coefficient. Statistical models were generated using different autocorrelation functions expressed in the vertical wave number domain. Realizations from both generic distributions and those generated measured from shallow analogs show that the the near-offset reflectivities are far more sensitive to the exact nature of the distributions.

In addition, we have been able to effectively apply geologic outcrop models as constraints during the modeling process. Turbidite sequences have a variety of morphologies. Thick composite sand channels are often encased by thinner, but continuous sand sheets. Channel flanking sequences can be stacks of thin layers of alternating sands and shales. Such heterogeneous lithologies can form complex saturation and rock property profiles. Thes observed sequences can now be used to refine the distributions used in our forward modeling.The final quarter was aimed at technology transfer and integrating our various findings, tying up loose ends, testing the techniques on remaining data sets, and summarizing all that had been learned. We will provide this suite of information and show how it can be practically applied to improving DHI's technology in deepwater settings. We held a final industry DHI mini-symposium last spring in Houston to help disseminate the results and get direct industry feed-back.

Major Accomplishments:

- Use of outcrop analogues to predict lithology influence on the seismic signature
- Differentiating “fizz-gas” from commercial gas reservoirs: Rock physics base
- Seismic Dispersion and Attenuation: Observations and Mechanisms
- Improved Models and Processing Schemes for Frequency Dependent AVO for Stratified Reservoirs
- An integrated case study for detecting low saturation gas
- Constraining C for fluid properties inversion.
- Seismic interpretation of water saturation based on reflectivity transforms
- Petrophysics Meets Seismic: An integrated approach to seismic amplitude evaluation in the deepwater EGOM
- Elastic Models for Heavy Oil Sands
- Interpreting DHI’s in Eocene reservoirs - Deep Water Brazil
- Integration of uncertain subsurface information into multiple reservoir simulation models
- Integrating Neural Networks and fuzzy logic for improved reservoir property prediction and prospect ranking
- Dual Porosity Biot-Barenblatt Model: Reflection and Transmission Coefficients
- Practical Application of Rock Physics in Exploration and Production

Results and Discussion

Introduction

One of the major challenges of this study was to separate the various fluid effects from rock effects on seismic signature for in situ conditions. All of the different components that impact seismic signature can be seen in Figure 1. One of the common threads that can hold the key to understanding all of the components is the geology. One of the major problem that has been encountered in Direct Hydrocarbon Indicator (DHI) analysis is differentiating "fizz-gas" from commercial gas reservoirs. Identifying Fizz gas is still an ill defined concept and many times a reservoir with no commercial gas accumulation that results in "dry hole" is interpreted to be a result of fizz gas. In many cases the Geophysicist finds a DHI in seismic but the Petrophysicist says there is no gas from log. Rock Physics indicates there is no way to tell fizz or reservoir gas saturation simply from velocity data. Within the industry, it is often politically incorrect and economically unjustified to study false DHI's therefore the Fizz gas phenomenon remains ambiguous. During this project we have tried to provide some answers to key questions associated with interpretation of hydrocarbon saturation especially gas saturation. Methods such as inversion of saturation and porosity from seismic AVO,

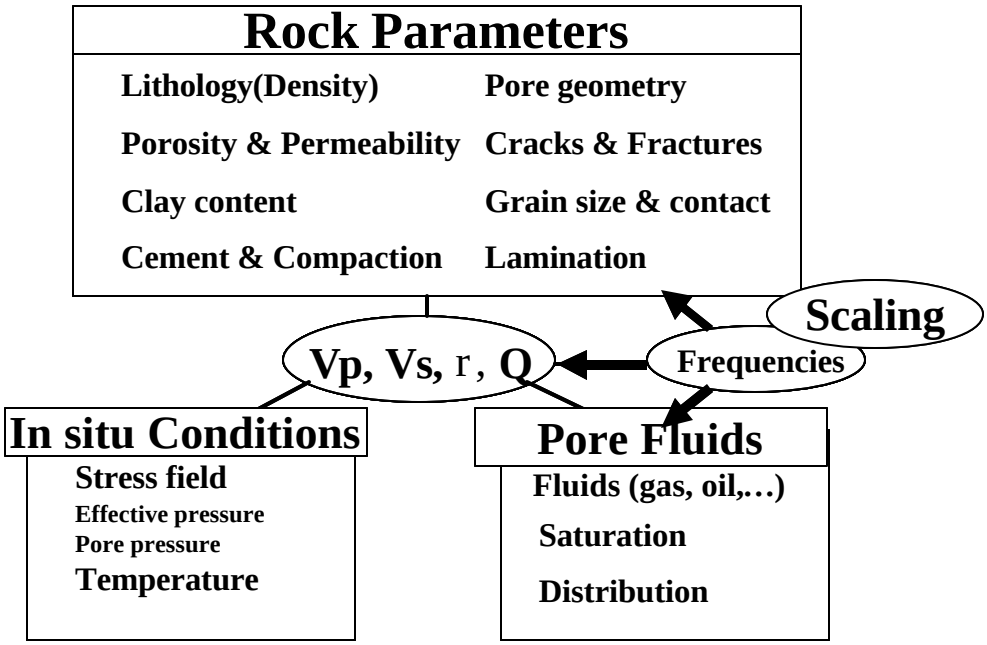

Figure 1. Relationship of various rock and fluid properties important for Direct Hydrocarbon Indicators.

Test Sites

Our various test sites were chosen based on the availability of samples, well logs, and seismic data. The locations of our Gulf of Mexico sites are shown in Figure 1. The general condition of each area and types of data available are listed in Table 1. Although the Troika data through was deemed of very poor quality, this is the only other field for which we have core samples. The Troika samples were measured ultrasonically and have been used as analogs to our other areas.

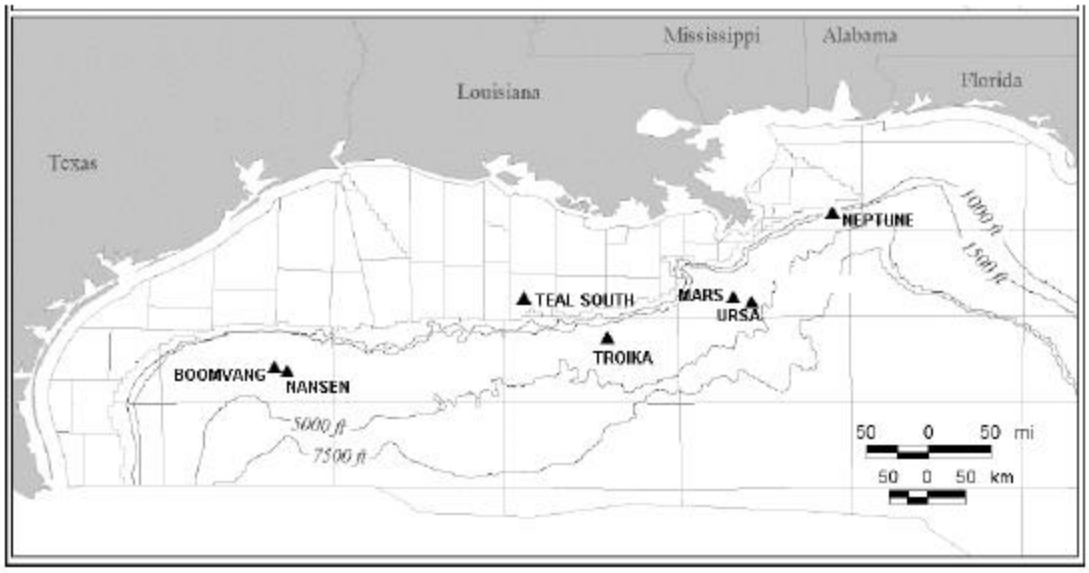

Figure 2. Test site locations, Gulf of Mexico. Modified from Baud et al., 2002.

Table 1

Field	*Attribute*	*Status*
Neptune	*High quality seismic data*	*Veritas 2-D line, Logs obtained*
Nansen	*Core samples & logs available*	*Samples measured, Logs obtained*
Ursa	*Multiple real and false HCI*	*TGS 2-D lines, Logs obtained*
Mars	*Complex stacked turbidites*	*Logs obtained*
Troika	*Some data already published*	*Some samples measured*
Mars	*Published data, salt confined*	*Veritas 2-D lines, Logs obtained*
Boomvang	*Near Nansen (Kerr-McGee)*	*Samples & logs obtained*
Viking Gr.	*Prestack seismic and logs available*	*Data at CSM and TAMU*
Teal South	*Shelf, only one well, data available*	*Post-stack data at TAMU*

Inversion of Sw and porosity from seismic AVO

A new inversion method was tested to directly invert reservoir properties, water saturation, Sw, and porosity from seismic AVO attributes. This method is different from the conventional methods where reservoir properties are usually derived from the impedances inverted from seismic amplitudes. The workflow first establishes the relationships between the seismic AVO attributes to Sw and porosity using the rock physics relationships; then inverts these properties directly. The new method is different from conventional AVO classification because it provides quantified reservoir properties, not just the fluid type. This new method is applied to seismic data from the Gulf of Mexico. Water saturation and porosity are inverted at the target horizons for small 3D cubes around two wells. Rock physics relations are derived from the first well and used for inversion. The inverted Sw correctly predicts the gas saturation at the second well. Reservoir properties are inverted in two steps conventionally: first impedances are inverted from seismic data, and then impedances are converted into reservoir properties using relationships derived at the wells (see for example, Dubucq et al., 2001; Vernik, et al, 2002). This method is commonly used because the inversion of the impedances and their conversion (using regression methods) to reservoir properties, such as water saturation and porosity, are relatively stable processes. But the drawback is that the link between the seismic data and reservoir properties are weak – the amplitude changes caused by the reservoir properties are usually not maintained. The new method addresses the weak link between rock physics and seismic impedance by directly linking seismic data and reservoir properties and inverting these properties from the seismic data. Figure 3 shows a comparison of the new method and conventional impedance inversion. In this presentation, the workflow, Figure 3, is described, then the new method is tested using field data.

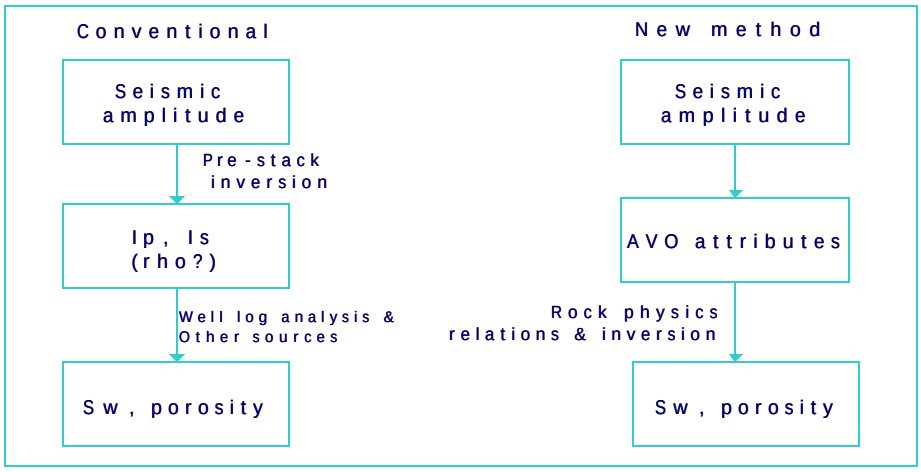

Figure 3. Workflow: conventional and new methods for Sw and porosity inversion.

Impact of pressure on velocity and modulus

Fluid saturation effect results in an increase of P-wave velocity and decrease of shear velocity. But more clearly, we see an increasing bulk modulus but maintain a constant for rigidity (shear modulus). The pore pressure effect results in a decreasing bulk modulus and increasing pore pressure. For dry rock the Vp/Vs ratio decreases with decreasing pressure. This means that bulk modulus drops faster than shear modulus with decreasing pressure for consolidated dry rocks. The fluid saturated Vp/Vs ratio is higher than dry bulk modulus due to increasing bulk modulus as well as P-velocity and decreasing S-velocity due to increasing density. Also, the fluid saturated Vp/Vs ratio increases with decreasing pressure due to faster drop of shear modulus than bulk modulus with decreasing pressure. An example of these measurements can be seen in Figure 4.

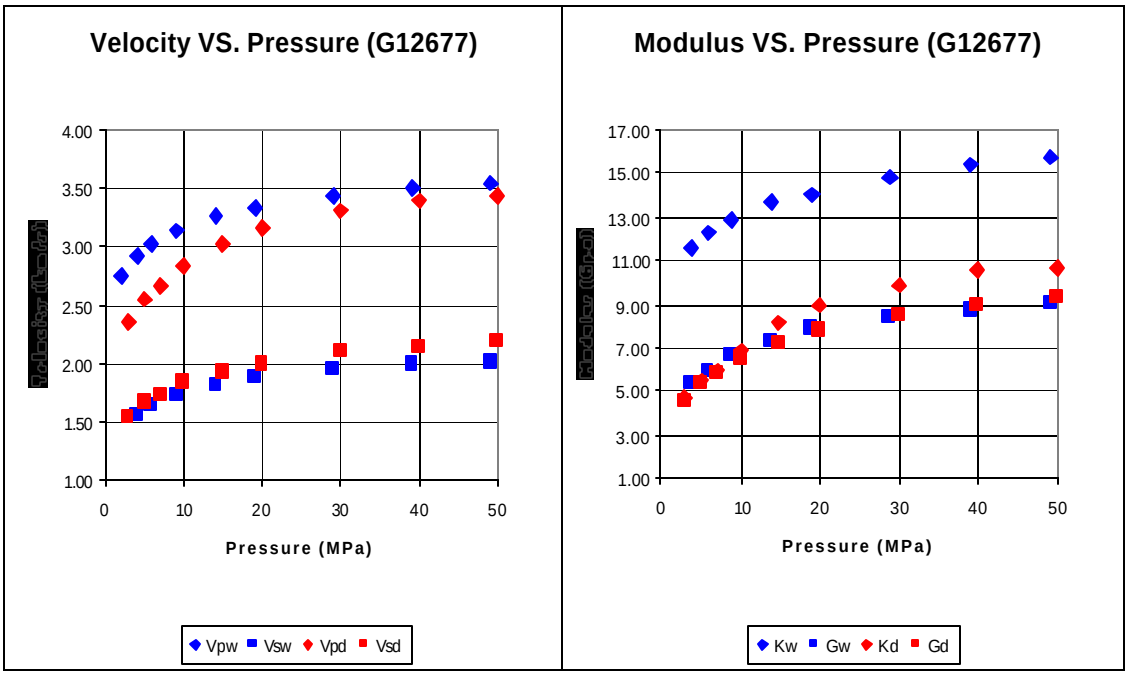

Figure 4. Velocity versus pressure and modulus versus pressure.

Water saturation estimation with Support Vector Machine

Low saturation gas and commercial gas have close amplitude responses at shallow water reservoir (less than 2000 m) because a small amount of gas can dramatically reduce the bulk modulus of the gas-water mixture. Increasing the depth of reservoir, the bulk modulus of gas increase gradually. Gas saturation can be significant to affect bulk modulus of gas-water mixture. This improves the chances to discriminate low saturation gas from commercial gas with seismic data. we trained a Support Vector Machine (SVM) with a saturation log data from Gulf of Mexico, then apply it to regress the water

saturation from seismic data. Validations of SVM regression on the gas andlow saturation gas show it is possible to separate commercial gas and low saturation gas at deep water reservoirs. Low saturation gas or "fizz" refers that the percentage of gas in the pore volume is small (less than 25%). The discrimination between low saturation gas and economical gas attracts much attention because wells are classified as "dry holes" even when small amounts of hydrocarbons exist in the reservoir. Discrimination between fizz and economical gas will reduce exploration cost and improve efficiency.

At low-pressure condition (shallow depth < 2000 m), gas modulus is much less than 0.1 GPa. The presence of a small amount of gas can dramatically reduce the P-wave velocity of the reservoir, so "fizz" and economic gas saturations have nearly the same seismic responses. This well known physical phenomena can be modeled by Gassmann's equation (Domennico, 1976). Under higher pressure condition (depth greater than 2000 m), modulus of gas-water mixture shows progressive decrease with increasing gas saturation (Han and Batzle, 2002). This improves the chances to discriminate low saturation gas from commercial gas with seismic data.

Our objective of this study is to estimate the water saturation from seismic volume at deep-water reservoir. We first train a Support Vector Machine (SVM) to learn the water saturation log from seismic trace nearest to the wellbore. With this SVM, we estimate water saturation with all the traces in the seismic volumes from the commercial gas reservoir and low saturation gas reservoir.
An SVM is an algorithm using selected subset of data (known as support vectors) in function estimation. We explain this algorithm in detail in the following section.

SVM regression

Support Vector Machines were introduced to the computer learning community in the mid 1990s (Vapnik, 1995) and are just beginning to applied in geophysical field (Kuzma, 2004; Li and Castagna, 2003; Zhao et al., 2005). They are most commonly used to solve very large classification problems such as handwritten digit recognition and document sorting. However, SVMs can also be used for regression (Smola and Scolkopf, 2004). This part introduces SVM regression based on Smola and Scolkopf's tutorial.

Suppose we are given training data $\{(x_1, y_1), \ldots, (x_l, y_l)\}$, $x_i \in R^d$ is "d" dimension vector, $y_i \in R$. In ε–insensitive Support Vector regression, our goal is to find a function $f(x)$ that has at most ε deviation from the actually obtained targets y_i for all the training data, and at the same time is as flat as possible. In other words, we do not care about errors as long as they are less thanε, but will not accept any deviation larger than this. Suppose our target function has a linear form

$$f(x) = \langle w, x \rangle + b \quad \text{with} w \in R^d, b \in R \qquad (1)$$

where $\langle \cdot, \cdot \rangle$ denotes the dot product in R^d. Flatness in the case of (1) means that one seeks a small w. One way to ensure this is to minimize the norm, i.e. $\| w \|^2 = \langle w, w \rangle$. We can write this problem as a convex optimization problem:

$$\text{minimize} \quad \frac{1}{2}\|w\|^2$$

$$\text{subject to} \quad \begin{cases} y_i - \langle w, x_i \rangle - b \le e \\ \langle w, x_i \rangle + b - y_i \le e \end{cases} \qquad (2)$$

The assumption in (2) was that such a function f actually exists that approximates all pairs (x_i, y_i) with e precision. If we want to allow for some errors, we may introduce variables ξ_i, ξ_i^* to arrive at formulation (3):

$$\text{minimize} \quad \frac{1}{2}\|w\|^2 + C\sum_{i=1}^{l}(x_i + x_i^*)$$

$$\text{subject to} \quad \begin{cases} y_i - \langle w, x_i \rangle - b \le e + x_i \\ \langle w, x_i \rangle + b - y_i \le e + x_i^* \\ x_i, x_i^* \ge 0 \end{cases} \qquad (3)$$

The constant C > 0 determines the trade-off between the flatness of f and the amount up to which deviations larger than e are tolerated. This corresponds to dealing with a so called e-insensitive loss function $|\xi|_\varepsilon$ described by

$$|x|_e = \begin{cases} 0 & \text{if } |\xi| = \varepsilon \\ |x| - e & \text{otherwise.} \end{cases} \qquad (4)$$

Figure 5 depicts the situation graphically. Only the points outside the shaded region contribute to the cost insofar, as the deviations are penalized in a linear fashion.

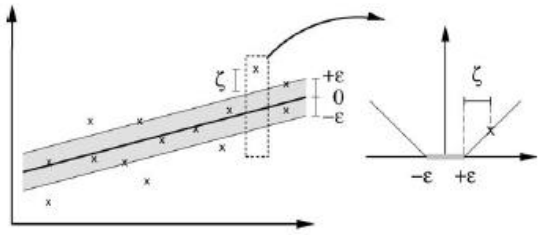

Figure 5. The soft margin loss setting for a linear SVM (from Smola and Scolkopf, 2004)

From the objective function and the corresponding constraints (3), we may construct a Lagrange function by introducing a dual set of variables:

$$\begin{aligned} L = {} & \frac{1}{2}\|w\|^2 + C\sum_{i=1}^{l}(x_i + x_i^*) - \sum_{i=1}^{l}(h_i x_i + h_i x_i^*) \\ & - \sum_{i=1}^{l} a_i (e + x_i - y_i + \langle w, x_i \rangle + b) \\ & - \sum_{i=1}^{l} a_i^* (e + x_i^* + y_i - \langle w, x_i \rangle - b) \end{aligned} \qquad (5)$$

Here L is the Lagrangian and h_i, h_i^*, a_i, a_i^* are Lagrange multipliers. Hence the dual variables in (5) have to satisfy positivity constraints, i.e.

$$a_i^{(*)}, h_i^{(*)} \ge 0 \qquad (6)$$

Note that by $a_i^{(*)}$, we refer to a_i and a_i^*.

The Lagrange function (5) has a saddle point with respect to the primal and dual variables at the solution. At the saddle point condition, the partial derivatives of L with respect to the primal variables (w, b, x_i, x_i^*) have to vanish for optimality.

$$\frac{\partial L}{\partial w} = w - \sum_{i=1}^{l} (\alpha_i - \alpha_i^*) x_i = 0 \qquad (7)$$

$$\frac{\partial L}{\partial b} = \sum_{i=1}^{l} (\alpha_i - \alpha_i^*) = 0 \qquad (8)$$

$$\frac{\partial L}{\partial x_i^{(*)}} = C - \alpha_i^{(*)} - \eta_i^{(*)} = 0 \qquad (9)$$

Substituting (7), (8), and (9) into (5) yields the dual optimization problem.

$$\text{maximize} \begin{cases} -\frac{1}{2} \sum_{i,j=1}^{l} (\alpha_i - \alpha_i^*)(\alpha_j - \alpha_j^*) \langle x_i, x_j \rangle \\ -\varepsilon \sum_{i=1}^{l} (\alpha_i + \alpha_i^*) + \sum_{i=1}^{l} y_i (\alpha_i - \alpha_i^*) \end{cases} \qquad (10)$$

$$\text{subject to } \sum_{i=1}^{l} (\alpha_i - \alpha_i^*) = 0 \text{ and } \qquad \alpha_i, \alpha_i^* \in [0, C]$$

In deriving (10) we already eliminated the dual variables η_i, η_i^* through condition (9) which can be reformulated as $\eta_i^{(*)} = C - \alpha_i^{(*)}$. Equation (8) can be rewritten as follows

$$w = \sum_{i=1}^{l} (\alpha_i - \alpha_i^*) x_i, \text{ thus}$$

$$f(x) = \sum_{i=1}^{l} (\alpha_i - \alpha_i^*) \langle x_i, x \rangle + b \qquad (11)$$

Equation (11) shows that w can be completely described as a linear combination of the training pattern x_i.

The term b can be computed by the Karush-Kuhn-Tucker (KKT) conditions. These conditions state that at the point of the solution the product between dual variables and constraints has to vanish.

$$\begin{aligned} \alpha_i (\varepsilon + x_i - y_i + \langle w, x_i \rangle + b) &= 0 \\ \alpha_i^* (\varepsilon + x_i^* + y_i - \langle w, x_i \rangle - b) &= 0 \end{aligned} \qquad (12)$$

and

$$\begin{aligned} (C - \alpha_i) x_i &= 0 \\ (C - \alpha_i^*) x_i^* &= 0 \end{aligned} \qquad (13)$$

Equation (12) and (13) allow us to make several useful conclusions. Firstly only samples (x_i, y_i) with corresponding $\alpha_i^{(*)} = C$ lie outside the ε-insensitive tube. Secondly $\alpha_i \alpha_i^* = 0$, i.e. there can never be a set of dual variables α_i, α_i^* which are both simultaneously nonzero. This allows us to conclude that

$$\varepsilon - y_i + \langle w, x_i \rangle + b \geq 0 \text{ and } \quad x = 0 \text{ if } \alpha_i < C \qquad (14)$$

$$e - y_i + \langle w, x_i \rangle + b \leq 0 \quad \text{if } a_i > 0 \qquad (15)$$

In conjunction with an analogous analysis on a_i^* we have

$$\max \{-e + y_i - \langle w, x_i \rangle \mid a_i < C \text{ or } a_i^* > 0\} \leq b \leq \qquad (16)$$

$$\min \{-e + y_i - \langle w, x_i \rangle \mid a_i > 0 \text{ or } a_i^* < C\} \qquad (17)$$

If some $a_i^{(*)} \in (0, C)$ the inequalities become equalities. Then the b term can be calculated by choosing any i.

Calculation of water saturation log

We applied the following steps in calculation of water saturation log:
1. Calculate shale percentage with Gamma ray log;
2. Convert shale percentage to different lithology;
3. Determine input parameters (water and gas density, water resistivity) according to depth, temperature, and resistivity of water saturated sand zone;
4. Solve saturation and porosity for different lithology.

Shale percentage (Vsh) can be calculated from Gamma ray log according to equation (18):

$$Vsh = \frac{GR - GR_{sand}}{GR_{shale} - GR_{sand}} \qquad (18)$$

Here GR is the reading from Gamma ray log; GR_{sand} is the Gamma ray reading from sand zone; and GR_{shale} is the Gamma ray reading from shale zone. In our following examples, when shale percentage is 50% and above, we consider this interval as shale; and when the shale percentage is below 50%, we consider this interval as sand.

We also need calculate porosity and water saturation of reservoir For porous sand reservoir water saturation (S_w) can be calculated by the Archie's law (…..):

$$S_w = \sqrt{\frac{0.81 / f^2 \times R_w}{R_t}} \qquad (19)$$

where Rw is resistivity of formation brine. The formation resistivity (R_t) of sand zones can be read directly from the resistivity log. Bulk density is usually calculated from grain density and fluid density:

$$r = (1 - f) r_{ma} + r_f f \qquad (20)$$

Where ρ_{ma} is the grain density and ρ_f is the fluid density. Fluid density can be expressed by gas density and water density (Here the fluid in our reservoir consists only gas and water):

$$r_f = S_w r_w + (1 - S_w) r_g \qquad (21)$$

Where ρ_w is the water density and ρ_g is the gas density. With equation (19), (20), and (21), porosity can be expressed as:

$$f = \frac{r_{ma} - r + (r_w - r_g) \times 0.9\sqrt{R_w / R_t}}{r_{ma} - r_g} \qquad (22)$$

With porosity derived by equation (22), we substitute it into equation (19) and get the water saturation for sand interval. For shale interval, we set water saturation as 100%.

Field examples

The dataset used in this paper is the 3D seismic data from the Green Canyon in Gulf of Mexico. From the post-stack seismic profile, two amplitude anomalies are identified. Around the first amplitude anomaly – King Kong field, Block 473 No. 1 well (later referred as King Kong well) was drilled and discovered commercial gas. Around the second amplitude anomaly which is 6 km away from the first anomaly, Block 474 No. 1 well (later referred as Lisa Anne well) was drilled was drilled and encountered a low-saturation gas. Cross sections of amplitude anomalies and well log information can be found in O'Brien (2004).

The top reservoir of King Kong is at the depth of 3300 m. According geopressure gradient and geothermal gradient, the overburden pressure is around 34 MPa and the temperature is around 70 ? . Then gas density is calculated as 0.25 g/cc with FLAG program (FLAG program is rock property calculation program developed by DHI consortium). Considering the reservoir depth, we use 1.02 g/cc as water density. Grain density of 2.65 g/cc for quartz is used in the calculation.

We choose the window 200 ms above and 200 ms below the top horizon as the target interval. The sample rate of original seismic data is 4 ms. The trace nearest the wellbore is decimated into 1 ms to match the sample rate of saturation log. We use the trace nearest King Kong well as the training seismic data.

Figure 6 shows the calculated water saturation curve (green) and the saturation curve regressed from nearest seismic trace of King Kong well (blue). An ε value of 0.00001 is used in SVM regression. We tested different ε values of 0.1, 0.05, 0.01, 0.005, 0.001, and 0.00001. Smaller ε value matches the regression closer to the input water saturation log. Although the saturation curve regressed from seismic data (blue) has perturbations at non-reservoir time locations, it matches the input water saturation curve (green) very well at the reservoir level (3950 ms to 4010 ms).

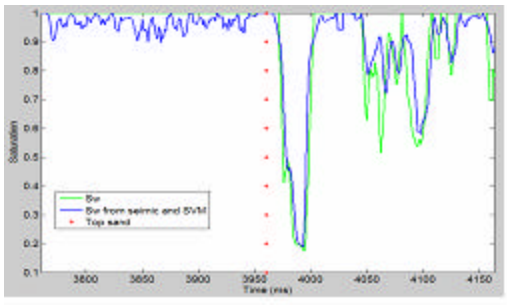

Figure 6. The saturation logs (original and regressed from seismic trace with SVM).

With the SVM trained from the trace nearest King Kong well, we use individual traces from seismic volume of King Kong and Lisa Anne to estimate the water saturation.

Figure 7 shows the cross sections of estimated water saturation from King Kong (left) and Lisa Anne (right). The continuous brown color in cross section of King Kong shows continuous low water saturation at reservoir level (from top horizon to 30 ms section below). This indicates gas saturation at King Kong reservoir is above 70%. On the cross section of estimated water saturation from Lisa Anne, there is no well-developed low water saturation zone. This suggests if Lisa Anne prospect has gas, the gas saturation must be low.

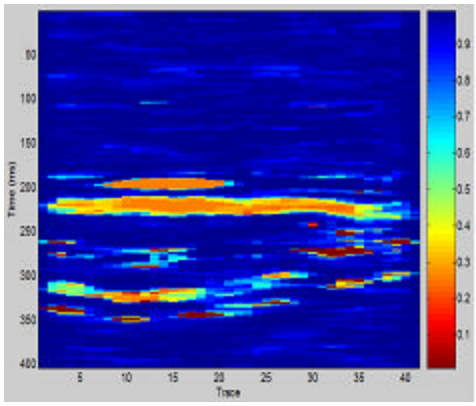

Figure 7. The cross sections of estimated water saturation from King Kong (left) and Lisa Anne (right).

Figure 8 shows the maps of estimated water saturation from King Kong (left) and Lisa Anne (right). These two maps are based on the top horizons of each reservoir. The water saturation map of King Kong has a continuous zone with water saturation below 30%. The water saturation map of Lisa Anne shows the reservoir has water saturation higher than 40%.

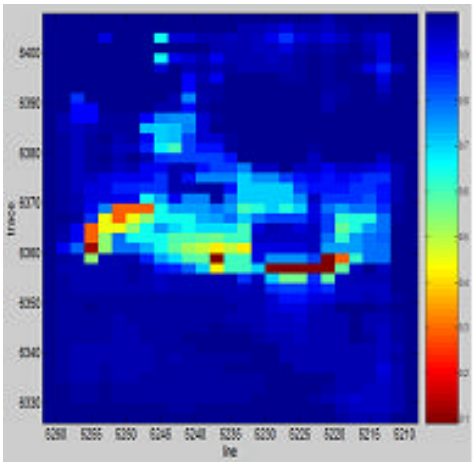

Figure 8. The cross sections of estimated water saturation from King Kong (left) and Lisa Anne (right).

With a water saturation log calculated from density and resistivity logs of a gas well, we trained an ε-insensitive Support Vector Machine to regress the water saturation from seismic data. SVM regression offers a way to estimate the water saturation away from wellbore. The lateral variation of water saturation helps greatly to evaluate the reservoir quality. Validations of SVM regression on the gas reservoir and a prospect of low saturation gas show it is possible to separate commercial gas and low saturation gas.

Velocities of deepwater reservoir sands

Deepwater reservoirs, those in water depths ranging from 1000 m to more than 3000 m, often consist of young turbidite sediments associated with early hydrocarbon charge, overpressure build up, and seal with retarded diagenesis. Deepwater sands maintain shallow properties even at great depths (e.g., 18 000 ft) but these weakly cemented sands—with a history of progressive compaction and cementation—differ from surface sediments. Current understanding of the properties of deepwater sands, mainly based on log and seismic data, has proved insufficient and risky. In 1998, the GDC team showed a statistical distribution of velocity and density of deepwater sands as a function of depth relative to seafloor depth. These data revealed a general compaction (depth) effect on sand properties. However, significant scattering in the data suggests many parameters need to be further examined. Spencer and Thompson (1994) showed that the acoustic properties of loose sands are controlled by grain contacts. Han (1994) demonstrated that the shear-wave velocities are particularly sensitive to weak cementation. Han (1986), Marion et al. (1992), and Yin (1992) have systematically investigated porosity/velocity of various mixtures of loose sands and clays. The results have revealed a gradual effect of clay content on porosity and velocity which has been used to simulate properties of shaly sands and sandy shales. Zimmer et al. (2002) studied velocities of packed sands and glass beads with different sorting combinations. The data showed a significant effect of pressure on velocities and a sorting effect on porosity. However, sediment compaction is not an elastic process. Both pressure and time of duration on sediments affect compaction and laboratory compaction, done in days, may not simulate natural compaction which occurs over millions of years. Thus, the general applicability to deepwater sands of results based on such data is questionable. In contrast, the results in this study are based on measurements of a suite of sand samples from the Gulf of Mexico. Although the samples are limited, we feel the results are significant and might suggest a DHI.

Texture of deepwater sands

The core samples come from two wells in water depths of 4000 ft and two reservoir formations at depths of 12 000 ft (shallow) and 17 700 ft (deep). Both reservoir sands were overpressured with differential pressure (overburden pressure minus pore pressure) around 2000 psi (13.8 MPa) for the shallow sands and 4000 psi (27.6 MPa) for the deep sands. Figure 9 shows that the porosity, bulk, and grain density of samples are differentiated into three distinct groups by porosity. These include a group of eight shallow samples with very high porosity (VHP) of 30-35% and a group of 17 deep samples with high porosity (HP) of 24-30%. The third group, low-porosity samples (<20%), are silt and shale, which is not the focus for this study. Deep samples with low

porosity might have been subjected to more compaction and cementation than shallow samples. For the samples from the same formation, range of porosity is related to sample sorting—high-porosity samples may have had better initial sorting than low-porosity samples from similar depth.

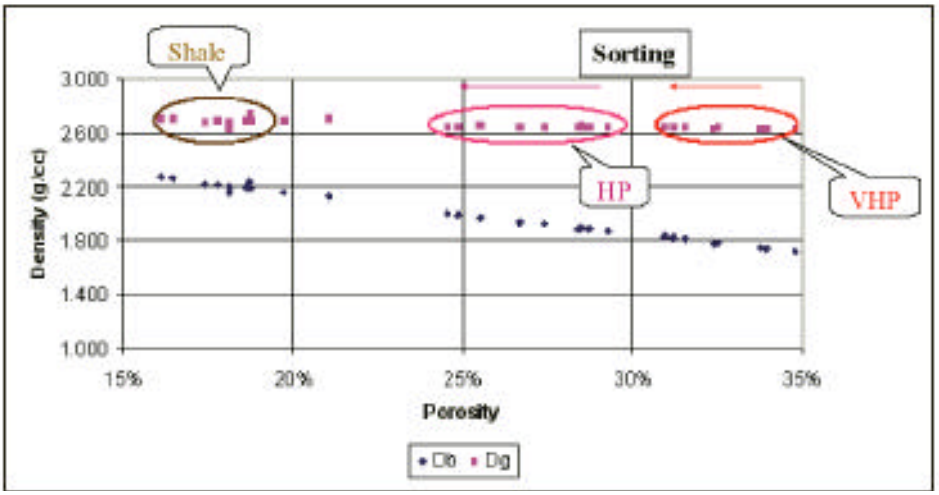

Figure 9. Dry-bulk and grain density as a function of porosity for the shallow (12000 ft) and deep (17700 ft) sands

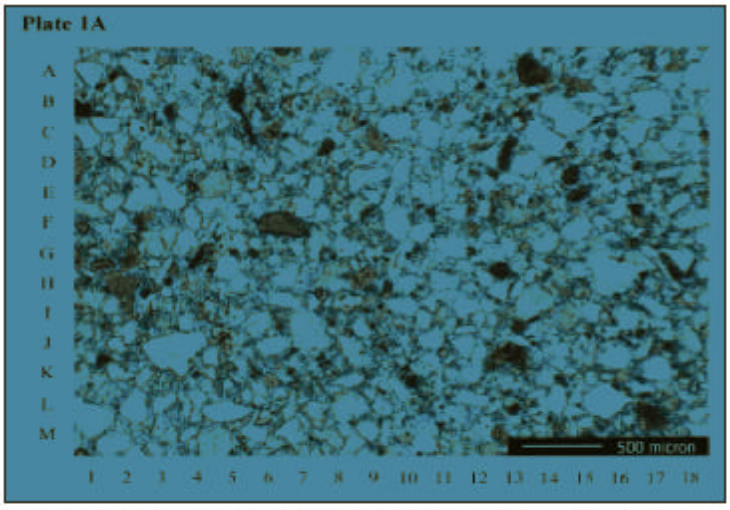

Figure 10. thin section for a deepwater clean unconsolidated fine sand sample.

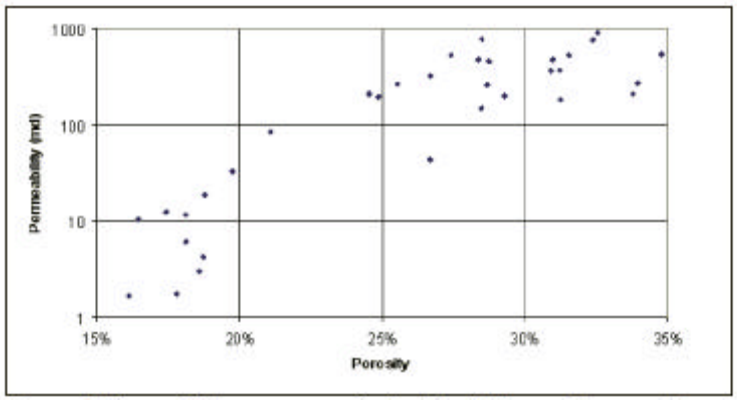

Figure 11. permeability versus porosity for the shallow and deep sands and shales.

All samples are relatively clean, fine grain sands with no cementation (Figure 2). Grain density is about 2.65 g/cc, typical for clean sands. Dry bulk density decreases linearly with porosity. Measured gas permeability typically ranged from 100 to 1000 md (Figure 3). Although the samples are unconsolidated, the measured data suggest that they have maintained in-situ grain packing and structures with negligible damage during coring and

pressure release processes. Porosity measured at room pressure is higher than that at in-situ differential pressure con- ditions. Our data show that after conditioning prepressure to that in situ, the effect of pressure cycling is limited, especially on velocities. We also measured total porosity reduction with in-situ differential pressure (Figure 12). In this case, porosity reduction ranged from 1 to 2% porosity unit for the in-situ differential pressure (2000 psi and 4000 psi for the shallow and the deep sands, respectively). The porosity reduction shows no relation to the porosity and is less dependent on the in-situ differential pressure. This may reveal that porosity relaxation due to the in-situ pressure relaxation is a unique measure of the degree of compaction and cementation of the rock frame. The measured porosity reduction in deepwater sands with in-situ packing and structure is significantly less than 3-4% porosity unit, which has been observed on laboratory-acked samples. These data reveal that the porosity reduction may be an indicator for the integrity and damage of core samples. The total porosity reduction (3-4%) measured on shaly and shale samples is much higher than on sand samples although porosity of shale samples at room pressure is significantly lower.

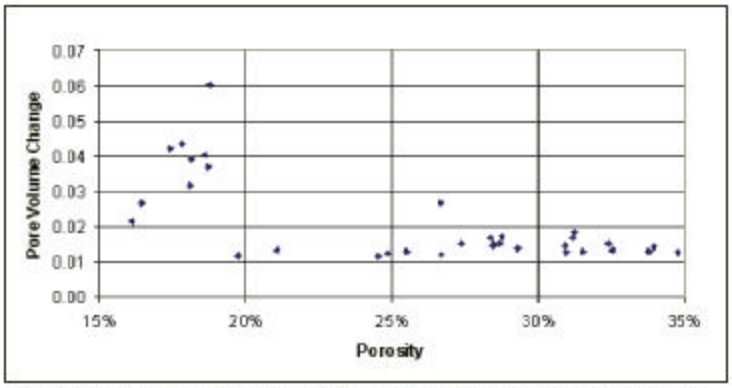

Figure 12. Total pore volume reduction is around 1.5% porosity unit for deepwater sands with no relation to porosity. There is much high porosity reduction for shale y sands and shales.

Velocity measurements

Figure 13 shows that, for dry and brine-saturated sands, both VP and VS tend to increase with increasing pressure.

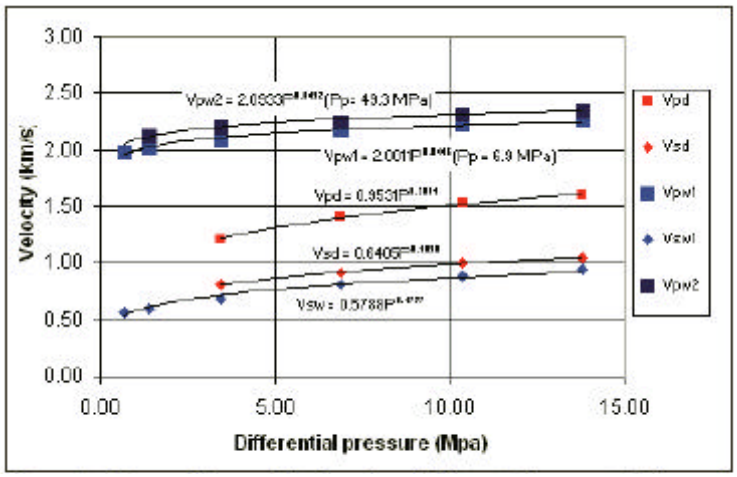

Figure 13. Measured dry and brine saturated P and S wave velocities on a typical deepwater sand sample (for about 12, 000 ft) as function of differential pressure.

The velocity increment is high at low pressure and low at high pressure. The effect of pressure on velocities can be modeled by a power law

$$V_P = a * P^{1/b} \qquad (23)$$

where a is velocity at unit pressure. In the grain contact model (Mindlin, 1949), b equals 6. For loose-sand samples, grain contact is not perfect and tends to be better with increasing pressure compaction. We have observed that the b value of deepwater sand samples is in general around 6 or less, and can be as small as 4.5. The lower b value is similar to that of laboratory-packed sand samples. The higher b value suggests better grain contact and less pressure dependence on velocity. Dry S-wave velocity shows a slightly greater b value. Brine saturation stiffens the sand frame and increases bulk density, which causes an increase of P-wave velocity and a decrease of S-wave velocity. It also causes less pressure dependence on velocity. The b value for brine-saturated P-wave velocity increases to more than 15, which suggests significant reduction of the pressure dependence of P-wave velocity. However, the pressure dependence of S-wave velocity is only slightly affected. Figure 6 shows dry P- and S-wave velocity as a function of porosity. These data also include repackaged loose sands (LS) samples from damaged (collapsed) core samples, and

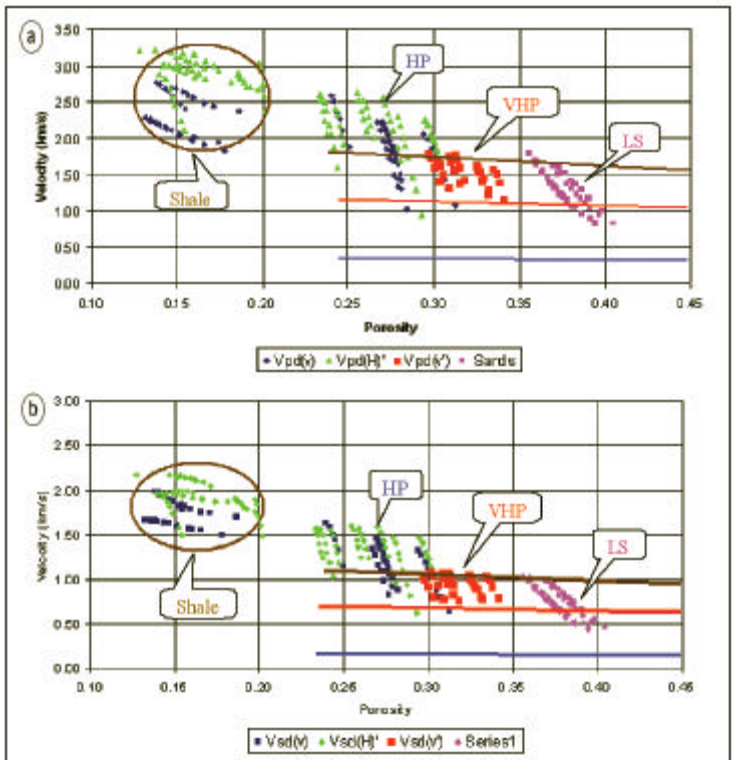

Figure 14. (a) measured dry Vp versus porosity . (b) Measured dry Vs versus porosity.

data lines covered porosity from 24 to 40% and differential pressures of 0.05, 3.45, and 0 MPa for loose sand and glass bead samples (LGS) (Zimmer et al., 2002). P- and S-wave velocities of shallow sands are significantly lower than those of deep sands, although the upper limit of pressure is 13.8 MPa for the shallow sands and 27.6 MPa for the deep sands. Both the *VP* and *VS* of the VHP sands data show remarkable consistency with data of the LS sands and the LGS lines. But porosity compaction of the naturally compacted VHP sands is much smaller than repackaged samples. The VHP samples also show that velocities at differential pressure of 13.8 MPa are consistent with the velocity trend of the LGS samples at differential pressure of 20 MPa. And the velocities of the VHP samples at differential pressure of 3.45 MPa are higher than that of LS and LGS sands. These results suggest that the VHP sands are in an early compaction stage, and the velocities show a transition behavior from the repacked loose sands (the LS and the LGS sands). However, the HP sands—with more compaction (low porosity) at deeper depths—show a significantly high-velocity trend (take off the pressure effect). S-wave velocities of the VHP sands show less relevance to porosity and are around 1.0 km/s, significantly less than for the deep sands. Significant separation in shear velocity of the VHP (shallow) from HP (deep) sands suggests that effects of compaction and cementation are mainly to stiffen sand rigidity for deep sands (Figure 7).

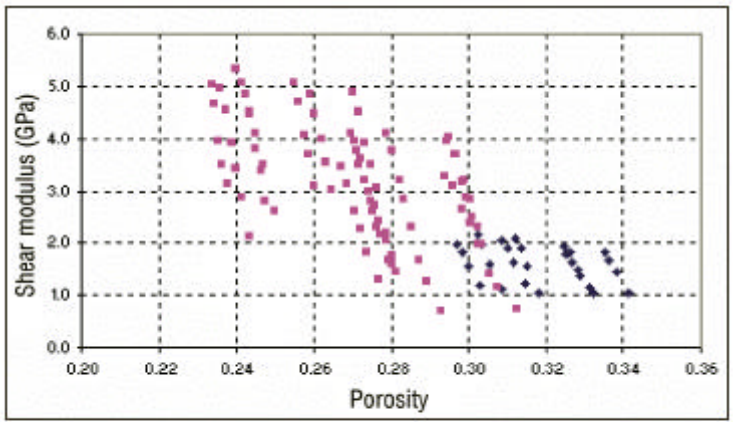

Figure 15. The HP (deep) sands have much higher shear modulus than those of the VHP (shallow) sands.

We concluded from these data that velocities of the VHP sands are less pressure-dependent than the HP (deep) sands.That may not represent in-situ condition and might possibly be induced by core damage on the VHP sands during coring. With high pressure in situ, the rock frame is stronger due to additional cementation. When pressure is released during coring, weak cement can be cracked due to extensional residual stress caused by relaxation of grain deformation. These induced cracks can cause the high-pressure effect on velocities. But this is not the case for loose sand samples.

Effect of fluid saturation on velocities.

We measured velocities on brine-saturated samples to examine the effect of fluid saturation. We first examined the fluid-saturation effect on the shear modulus. Figure 16 shows measured and calculated modulus of VHP sand samples at a differential pressure of 2000 psi.

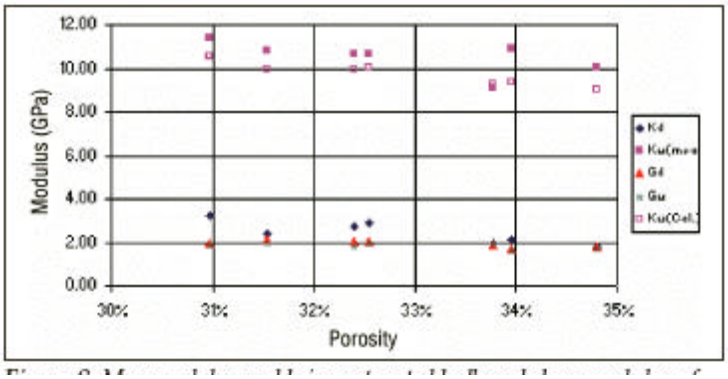

Figure 16. Measured dry and brine saturated bulk and shear modulus of BHP sand samples in comparison to modulus calculated with Gassmanns's equation.

These data suggest that shear modulus remains constant, as predicted by Gassmann's equation, with water saturation for the sand samples. The data also show that the shear

modulus is equal or slightly less than the dry bulk modulus. We compared the brine-saturated bulk modulus based on measured dry velocities calculated with Gassmann's equation to the bulk modulus based on measured brine-saturated velocities. The calculated modulus is few percent lower. Data measured on the deep (HP) sands showed a similar trend. We conclude that velocity dispersion is minimal for those porous sands. The fluid-saturation effect is mainly on the bulk modulus as shown in the simplified Gassmann's equation (Han and Batzle, 2004)

$$K_s = K_d + G(\phi) * K_f \qquad (24)$$

Here G (f) is the gain function, which is a dry rock frame property. Figure 9 shows dry and brine-saturated bulk modulus at high pressure. Data show that dry bulk modulus increases significantly with decreasing porosity: 2.0 GPa at porosity of 35% to 7.0 GPa at porosity of 24%. The brine saturation causes a significant increase of bulk modulus. However, the increment of ?K tends to be a constant and not sensitive to porosity. Consequently, we can use the increment in bulk modulus ?Kd to calculate the gain function.

$$G(\phi) = \Delta K_d / K_f \qquad (25)$$

Figure 17 shows the gain function for the shallow (VHP) and deep (HP) sand. The gain function for deepwater unconsolidated sands is distributed in a narrow range with the upper bound derived from the Reuss bound and the lower bound constant around 2.5. The gain function decreases with increasing pressure and seems more sensitive to pressure for the HP sands (core damage effect?) than the VHP sands. The lower bound of the gain function seems consistent with

$$G = D^2 * \phi * (2 - D * \phi)^2; \quad D = 2.1 \qquad (26)$$

higher than those of consolidated reservoir sandstones (Han and Batzle, 2003). Figure 18 shows that brine-saturated velocity is less dependent on porosity. We have developed an empirical model based on Reuss bound to model velocities. The Reuss bound of P-wave modulus is

$$M_{Reuss} = \frac{M_0}{1 + \left(M_0 / K_f - 1\right) * \varphi} \qquad (27)$$

We can derive P-wave velocity as

$$V_P = (M/\rho)^{0.5} = \left(\left(\frac{M_0}{1 + n * \varphi}\right) / \rho\right)^{0.5} \qquad (28)$$

where M0 is P-wave mineral modulus, and assumed equal to 83 GPa. The coefficient n is used to simulate different pressure effect on velocities. For S-wave velocity, a similar model can be used by replacing M0 with grain shear modulus µ0 (assume µ0 is equal to 33 Gpa). This formulation is purely empirical and may be used to describe velocity-

pressure-porosity relations. The n value can be calibrated locally. Zimmer et al. (2002) used the modified Reuss model (Dvorkin and Nur, 1996) to simulate the sorting effect on dry velocity-porosity relation for packaged sand samples. We found that their method is not proper for our data because geologic compaction affects the dry velocity-porosity relation of deepwater sands. The laboratory-packed (LS and LGS) sand samples show a sorting effect to reduce porosity, and almost no effect on dry velocities, but a large brine-saturation effect on P-wave velocity of poorly sorted, low-porosity sands. In comparison with laboratory-packed samples, deepwater sands show limited sorting effect and more geologic compaction effect: dry velocities of deepwater sands are significantly higher than those of the LS and LGS sands, and increase with decreasing porosity. The brine saturation effect on bulk modulus remains a constant (constant gain function). Consequently, water-saturated velocities more or less follow the Reuss trend and are less dependent on porosity.

P-wave and S-wave relationship

Dry P- and S-wave (shear) modulus are related to *VP/VS* ratio as follows:

$$\frac{M}{\mu} = \frac{V_p^2}{V_s^2} \tag{29}$$

Figure 19 plots dry shear and P-wave modulus with regression relationship as

$$\mu = -0.0035 * M^2 + 0.4399 * M - 0.1583 \tag{30}$$

The relation can be used to derive dry shear modulus from the dry P-wave modulus. At high-pressure, the shear modulus tends to be linearly proportional to P-wave modulus (the red line in Figure 19) with a ratio of 0.42. This ratio is equivalent to k/μ ratio of 1.05. This value tends to increase with decreasing differential pressure. This tight relationship between dry bulk and shear modulus provides an internal constraint on fluid-saturation effects on velocity. Figure 20 shows measured *VP/VS* ratio versus porosity for dry and brine-saturated samples. The data reveal that dry *VP/VS* ratio is around 1.6 and did not show significant relation with porosity except slightly increasing with decreasing porosity for samples from the same formation. Under brine-saturated conditions, *VP/VS* ratio (~2.1) for the deep HP sands is significantly less than for (~2.5) shallow VHP sands. This is due to less compaction and no cementation for the shallow VHP sands with low shear modulus and high porosity. The data also show that the HP water saturated sands have *VP/VS* ratio that is similar to nearby shale samples.

Hydrocarbon indicators in deepwater sands

Many hydrocarbon indicators have been proposed (Russell et al., 2003). We propose a DHI with clear physical meaning. In order to identify the fluid from seismic, the key is the sensitivity of fluid effect on P-wave modulus given as:

$$M_s = M_d + G * K_f \tag{31}$$

For deepwater, turbidite, unconsolidated sand reservoirs, we can apply the above results to obtain a new hydrocarbon indicator. Assuming, we can determine the porosity of sand frame, bulk modulus of pore fluid (brine) and grain (mineral) modulus, from P-wave

modulus of brine saturated sands, we can calculate dry rock frame properties based on Gassmann's equation—actually the modified Gassmann's equation with

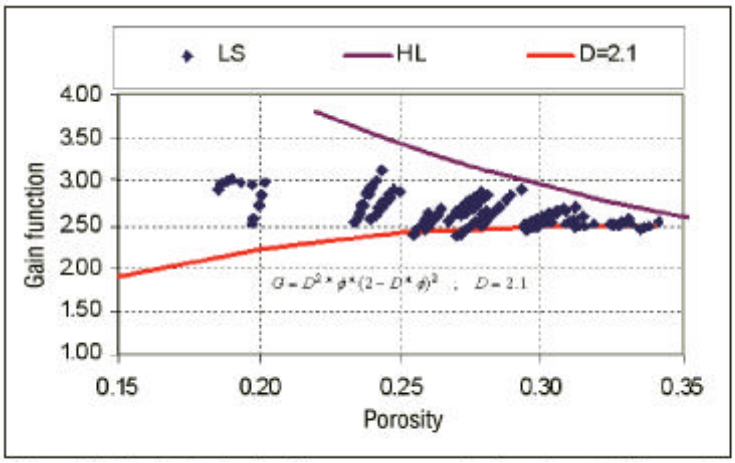

Figure 17. Derived gain function porosity. Low bound of the gain function for deepwater sands is around 2.5.

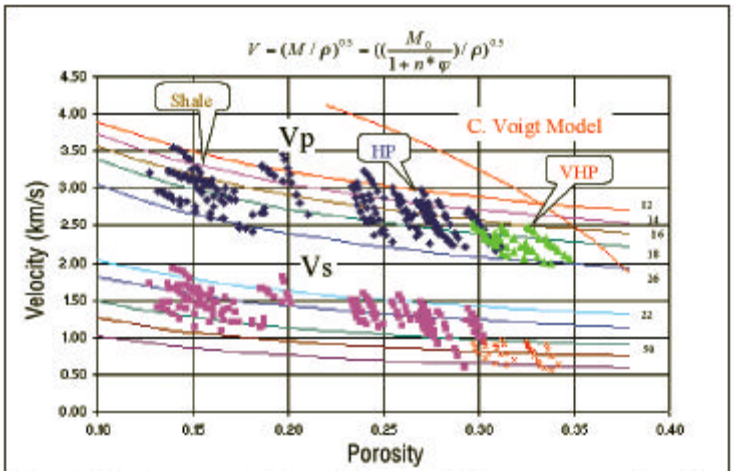

Figure 18. Water saturated P- and S- wave velocity versus porosity with modeled velocity/porosity trend.

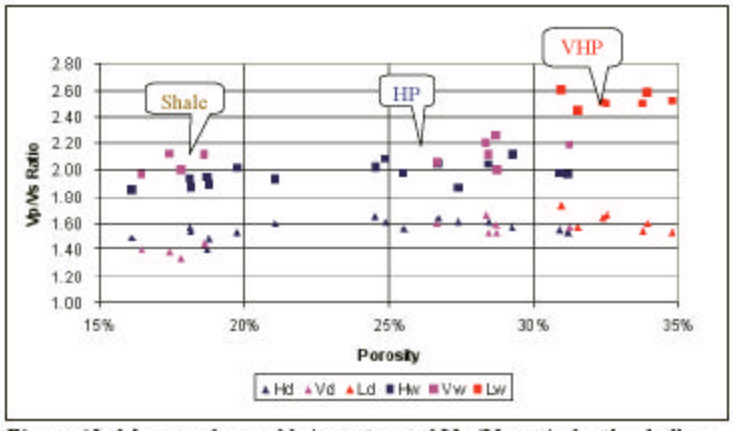

Figure 19. measure dry and brine saturated Vp/Vs ratio for the shallow VHP and deep HP sands.

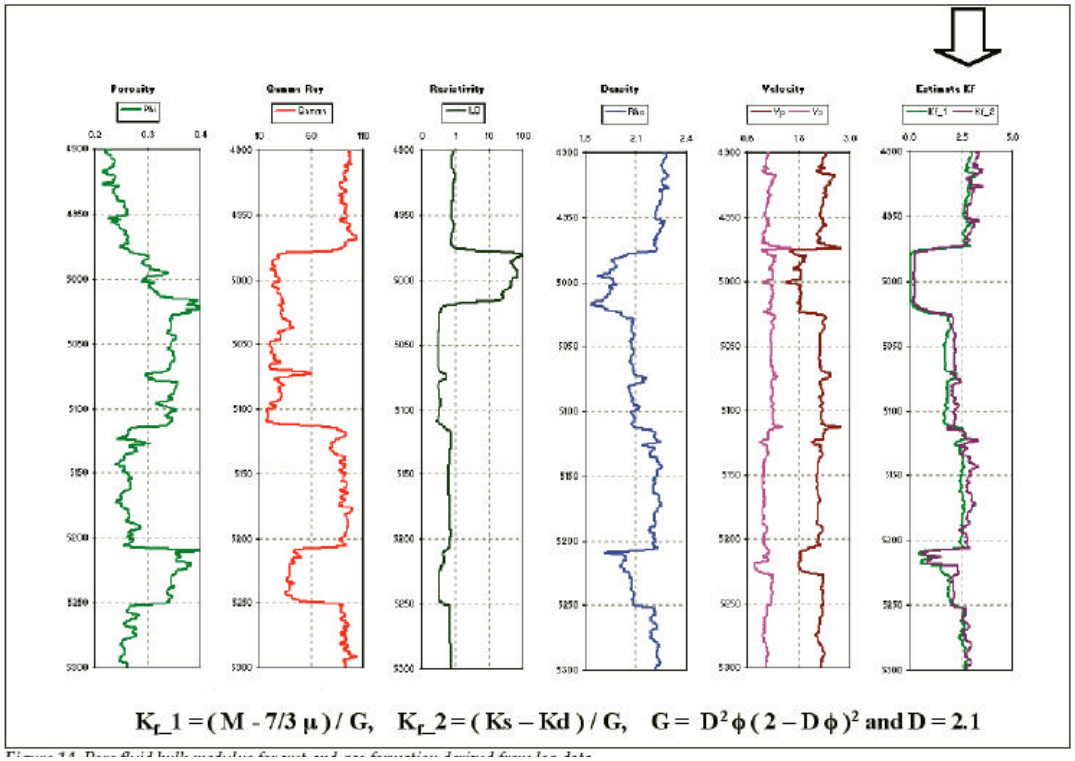

Figure 20. Pore fluid bulk modulus for wet and gas formation derived from log data.

P-wave modulus (Han and Batzle, 2004). The brine-saturation effect (?K, or call fluid factor) should be consistent with brine modulus and the gain function. The dry rock frame properties should be consistent with the measured data trend. By applying the gain function, we can directly calculate brine modulus, which should be consistent with the true in-situ value. With properties of dry rock frame we could also estimate hydrocarbon-saturation effect, or estimate fluid modulus based on P-wave modulus of reservoir sands and the gain function. Figure 21 shows estimated fluid modulus for a log data. Results show that we can directly estimate realistic brine modulus from wet zones and pore fluid

modulus from gas zones. In the shale zone, brine modulus is overestimated due to applying the gain function for sands. An abnormally high brine modulus is a good lithology (shale) indicator. We also compared different hydrocarbon indicators for deepwater environment (Figure 15). We have calculated 15 hydrocarbon attributes for gas (90% gas, 10% brine), fizz gas (90% brine, 10% gas), and brine sands. In comparison with brine-saturated sands (background), five attributes (?K, ?*?, ?*?K, ?*Kf and Kf) show higher but similar sensitivity to differentiate gas from fizz gas and wet sands. And the sensitivity of all attributes is basically determined by the fluid modulus (Kf). Clearly, in order to obtain accurate, meaningful interpretation of seismic attributes or forward modeling, we have to better understand measurements and models for hydrocarbon fluid properties. We have not yet been able to extract fluid modulus from seismic data. However, with improved seismic data and constraints from rock and fluid parameters, we expect to map pore fluid modulus based on seismic data in the near future. Here, we discuss only elastic seismic attributes related to hydrocarbon fluids. Seismic wave dispersion and attenuation are also associated with hydrocarbon fluid saturation but via a very different mechanism. Greater wave dispersion and attenuation are especially associated with fizz gas saturation, which can used as additional hydrocarbon indicators. We will discuss them in a future paper.

Deepwater reservoir sands with unique sedimentary processes show progressive effect of compaction and cementation on porosity and frame velocities, which also incorporates the grain texture and fluid migration. 1) Compaction is a major driving force. Poor sorting will provide room for low initial packing porosity and more potential for continued compaction. 2) For deepwater sands, overpressure and early charge of hydrocarbon often block pore fluid flow and minimize the cementation effect. 3) With increasing depth and age, porosity reduces and dry velocities increase. The effect of fluid saturation on the modulus of deepwater sands can be estimated by a constant fluid factor: the constant gain function (2.5) times the fluid modulus. 4) Velocity dispersion in deepwater sands is relatively small. 5) Compaction and weak cementation increases shear rigidity more than bulk modulus. 6) P- and S-wave velocities of water-saturated sands follow the Reuss trend, and show less dependence on porosity. 7) The effect of pressure on the velocity of VHP sands is relatively small. With weak cementation, the effect of pressure on velocity increases, which may be caused by core damage. 8) The dry shear modulus at high pressure is proportional to P-wave modulus. The sensitivity of elastic seismic attributes to hydrocarbon saturation is basically controlled by the pore fluid modulus. The greater the difference of pore fluid modulus leads to a greater differential in seismic attributes, and greater potential to differentiate pore fluids seismically. However, it is also constrained by the degree of compaction and cementation of sand frame. More compaction and cementation equals less potential to differentiate different pore fluids. Therefore, we can conclude that detecting a shallow gas reservoir is relatively easier, but differentiating a gas from fizz reservoir is harder. For deepwater loose sand reservoirs with high pore pressure, we may be able to detect a gas reservoir and differentiate gas from fizz gas reservoirs. Potentially, we can map pore fluid modulus directly from seismic data. However, with increasing depth and age, as well as compaction and cementation, the elastic seismic attributes of sand formation tend to be less sensitive to saturations of different fluids. We will have less ability to detect gas reservoirs and more difficulty in differentiating gas and fizz gas reservoirs.

Relations between Sw, porosity, and AVO attributes

The relationship between the seismic AVO attributes and reservoir properties (Sw and porosity) can be established through P and S wave velocities and density. To start with, (Sw, porosity) are related to (Vp, Vs, rho) using Gassmann and other relations (Han and Batzle, 2004; Mavko, et al., 1998). Figure 3 shows the relationships between the rock physical properties (Vp, Vs and density) and water saturation at 25% porosity. Note that a large drop in Vp (in black) can be observed when water saturation drops by a small amount from 100%. But the drop is slower in deep-water environments where the Vp of low gas saturated sand can be slower than the fully gas saturated sands (Han and Batzle TLE, 2002). It is important to build these relations for any study region to ensure the success of the prediction. Figure 4 shows the general relationships between (Vp, Vs, density) and porosity with 90% water saturation. For the next step, the connections between seismic AVO attributes and reservoir properties are built using the Zoeppritz equations or Aki and Richards approximations (Aki and Richards, 1980). Here the Aki and Richards approximation is used. Figure 5 shows the responses of seismic AVO attributes (intercept and gradient) to water saturation and porosity. It is possible to add the effect of the volume of shale using the Xu and White model (Xu and White, 1995) for shaly sands in the future, but currently this effect is ignored because our measured sands are relatively clean.

Models of Complex, Layered Reservoirs

A major goal of our research efforts has been to better characterize the properties of seismic waves reflected from stratified reservoirs models. While conventional processing of seismic data using amplitude variation with offset (AVO) analysis is founded on a model that assumes a seismic reflection originates from a single interface between two homogeneous materials, most reflections will in fact be generated by the interaction of an incident wave with a the rock within a vertical section of rock such as the complete reservoir layer. Therefore we have sought to understand the limitations of the conventional models for investigating the dependence of seismic reflection amplitudes on the angle of incidence of the wave striking the reservoir. This better, more quantitative understanding of the influence of the spatial structure of the reservoir layer, which is turn related to the geological processes that formed the rock layer and, potentially, to its suitability as a hydrocarbon reservoir. Our developments consider stochastic models generated using specified probability distributions to generate seismic velocity profiles and specific models of turbidite reservoirs that are based on field data. The former provide clear insights into the basic physical phenomena affecting seismic amplitudes, while the latter show how the results are relevant to practical applications. Below we summarize both sets of developments.

Stochastic models – influence of reservoir structure on reflections

We define the composite reflection coefficient as the complex-valued amplitude of the total P-wave signal reflected by a plane-layered formation that is somewhat smaller than the incident seismic wavelength. In other words, when a P-wave strikes a reservoir layer, for example, that includes vertical stratification, the wave will reflect from both the to

and bottom of the reservoir as a P-wave. However, inside the reservoir layer, it will also convert back and forth from a P-wave to an S-wave, and it will also reflect multiple times within the layer. The composite reflection coefficient is a measure of all of this energy that propagates back up to the receiver as a P-wave in the layer overlying the reservoir. Because the model we apply assumes that this reservoir is composed of horizontal layers, it is possible to solve a simple system of four equations for this amplitude using classical propagator matrix methods in a fast and efficient manner (Aki & Richards, 2002).

To investigate how the spatial structure of velocity variations within a reservoir can influence the magnitude of waves reflected from it, we tested several sets of models with different types of velocity distributions. In each, the magnitude of velocity variation every 0.15 m was selected at random. With no further calculations, there is no correlation of velocity from layer to layer. However, in geological settings like turbidite sequences, velocity will be correlated over distances related to the thickness of sands deposited in a turbidite flow, for example. Such structure can be introduced by applying a von Karman correlation function in the wavenumber domain (Sato and Fehler, 1997),

$$f(k,a,n) = \frac{2a(a^2m^2+1)^{-k-1/2}\sqrt{p}\,n^2\Gamma(k+1/2)}{\Gamma(k)} \tag{32}$$

where k is wavenumber and a is correlation length. Results presented here apply n=1/5, where n is a parameter that controls the "roughness" of the model. Using techniques summarized by Sato and Fehler (1997), the uncorrelated velocity profile can be adjusted to have the correlation defined by equation 1, which will be much more realistic. We also generate models using a Gaussian spatial correlation function, though it is not likely to be provide as realistic a model of typical formations, given that it is very smooth:

$$f(k,a) = \frac{e^{-k^2/(2a^2)}}{\sqrt{2p}\,s} \tag{33}$$

Examples of models for both of these correlation functions are compared to a model generated with no spatial correlation in Figure 21. Both the exponential and Gaussian models used a=5 m, and all three realizations applied a Gaussian PDF to generate perturbations in the bulk modulus for layers 0.15 m thick. Shear modulus values were correlated with the bulk modulus so that the Vp/Vs ratio remained near 1.8 in all layers.

For each type of model, 50 realizations were generated using the same random number seed to force models to have the same general velocity fluctuations and to cause the exponential and Gaussian models to have comparable structure (e.g., Figure 21).

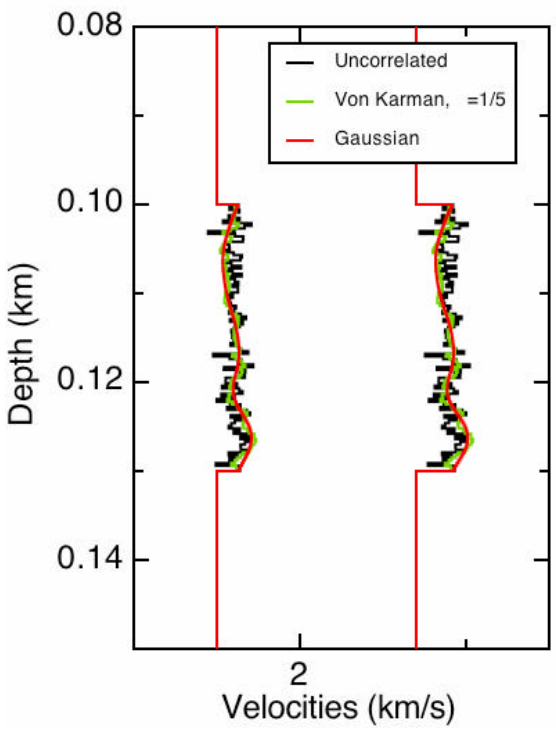

Figure 21. An example realization of each of the model types, one without spatial correlation, and two with the von Karman and Gaussian spatial correlations defined in the text.

The magnitude of the P-wave composite reflection coefficient was then computed for an incident plane P-wave with a frequency of 30 Hz. Statistical summaries provide a quantitative assessment of composite coefficient results for all model types (Figure 22). The spatially uncorrelated models have the least scatter in amplitudes, because the interference of reflections from the surfaces of each layer tends to cancel out. However, spatial correlation causes the model to have a few zones of higher or lower velocity, and the reflections from these tend to superpose in more complex ways, leading to more variability. This is especially true for the Gaussian models. We also show amplitudes for simplified, homogeneous reservoir layer models obtained from Backus averaging in this figure (Backus, 1962). It is interesting to note that the averaging procedure underpredicts the mean response, and it obviously fails to provide any prediction of the variability of the AVO parameters.

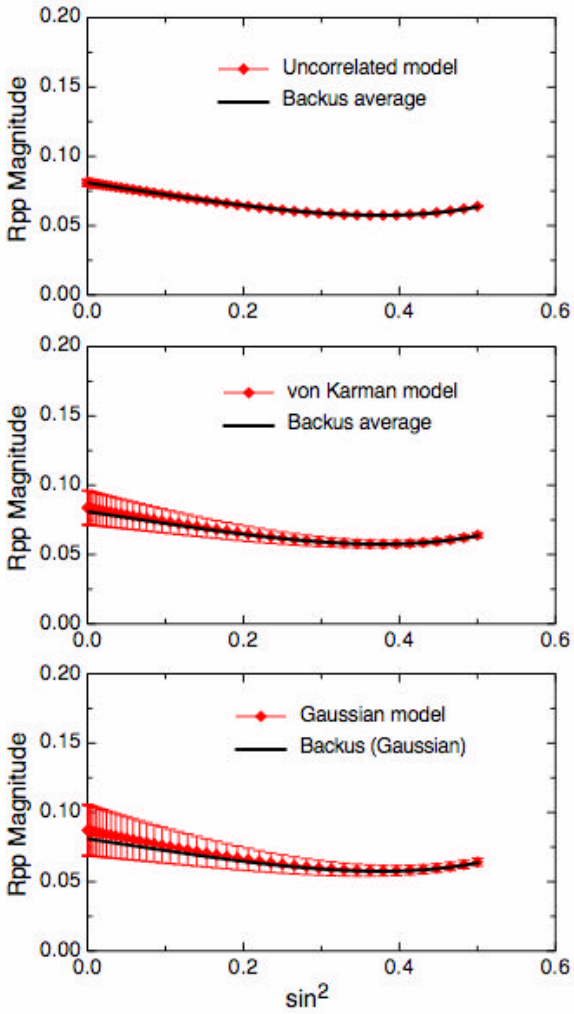

Figure 22. Statistics of the reflection coefficients for composite reflection coefficients generated using the three spatial correlation functions and for the Backus average versions of each model. In each case, 50 realizations were considered. Error bars corresponding to one standard deviation are displayed for the stochastic models, though not for Backus average results which have negligible scatter on the scale of these plots.

Typical AVO analysis is founded on the result suggesting that the seismic amplitude is approximately a linear function of the squared sine of the angle of incidence (Shuey, 1985). Fitting a line to the measurements produces an intercept and gradient that can help to distinguish hydrocarbon-bearing formations from non-productive sites. In Figure 18, we show such a display for parameters measured from the reflection coefficients shown in Figure 23. As would be expected from Figure 22, the Gaussian correlation function produces the largest scatter in reflection amplitudes. To test how internal reservoir structure might affect hydrocarbon detection, we took the same models and recomputed velocities by applying conventional Gassmann equation fluid substitution as follows. For each 5 m interval inside the 30 m layer, we assigned it to be hydrocarbon bearing with a probability P_{hyd}. If the formation were selected to be hydrocarbon rich, we performed recomputed the velocities and density assuming a gas saturation of 0.8,

otherwise the seismic properties were unchanged. For one set of models we set P_{hyd} to be 0.3, and in a second application, we chose P_{hyd} =0.6. Thus in the former case, the models on average containing about 10 m of hydrocarbon bearing internal layers, while the models in the latter case had 20 m of the total 30 m thickness that contained hydrocarbons. This model specification may be more realistic than many typical modeling procedures that assume that entire formation is uniformly saturated with hydrocarbons. The resulting AVO parameters are shown in Figure 24, which also includes the full brine saturated result for the von Karman spatial correlation function for reference. In this case, we see that the hydrocarbon AVO signals are different from the brine case, even when P_{hyd} =0.3. However, this difference is not too large, and seismic noise or processing errors could make it difficult to determine which cluster a particular measurements falls in.

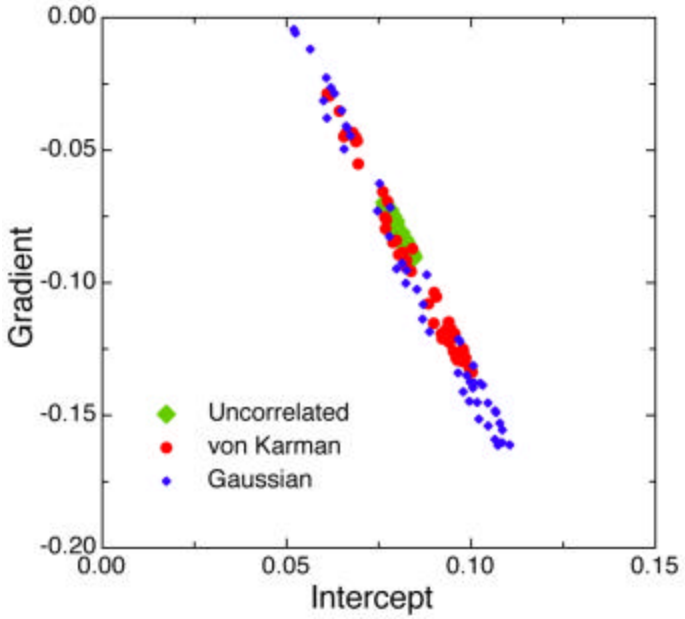

Figure 23. AVO parameters, the intercept and gradient, displayed for each of the three classes of models for which we computed composite reflection coefficients.

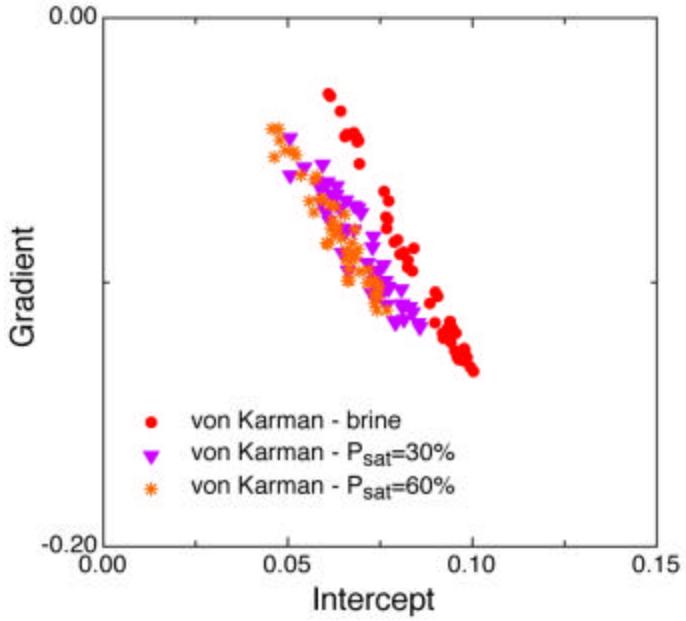

Figure 24. AVO parameters measured from computed composite reflection coefficients for models with and without hydrocarbons. The red points are the same as the red points in Figure 18 (the brine only case). See text for details of the hydrocarbon saturation modeling.

Seismic turbidite models

The results for the stochastic models provide basic physical insights into changes in seismic reflection amplitudes, but they may or may not be particularly realistic. Given the important of turbidite models for deep water sites, we also developed a simple work flow to create models for a specific field. This approach provides a method for generating stochastic models with velocity and thickness variations that are representative of observed turbidite sequences.

Briefly, the thicknesses of sands and shales are measured using formation microscanner logs, and cumulative distribution functions for the thickness of each lithology are created by tabulating these measurements. Similarly, velocity and density logs provide distributions for these two parameters as well. A specific stochastic turbidite model (STM) is then generated as follows. The model generation begins by specifying a desired total thickness for the turbidite sequence. We then randomly select a bed thickness and a density value from the relevant CDFs, alternating sand and shale until the total thickness is obtained. Examples below use a total thickness value of 30m. If the last layer generated results in a total thickness greater than 30 m, then the thickness of the last bed will be truncated so that the total remains 30 m.

As an example, we used publicly available logs from the Ocean Drilling Program to measure layer thickness, velocity and density from the Amazon Fan. Published studies provide guidelines for correctly identifying layers deposited by turbidites (Pirmez et al., 1997; Hiscott et al., 1992). These distributions are shown in Figure 25 and they show the characteristic differences in sand and shale properties. To apply the model to Gulf of Mexico studies, the distributions were shifted so that the mean velocities and densities

correctly reproduce those found in well logs. We used Vs=Vp/2.25, based on the average of well logs measurements, to estimate shear wave velocity in the models. A sample model is shown in Figure 26, which compares the STM result to a simpler binary model, a type of model that is often utilized in these studies (e.g., Stovas et al, 2004; Takahashi et al., 1999). Synthetic seismograms generated for this model show that results are frequency dependent, as expected given the structure in the models. Additional results also show that the binary models tend to underpredict the variability in seismic signals, which may be important for practical applications. In Figures 27 and 29, we show one set of seismograms and the AVO parameters measured from multiple realizations of the STM and turbidite models.

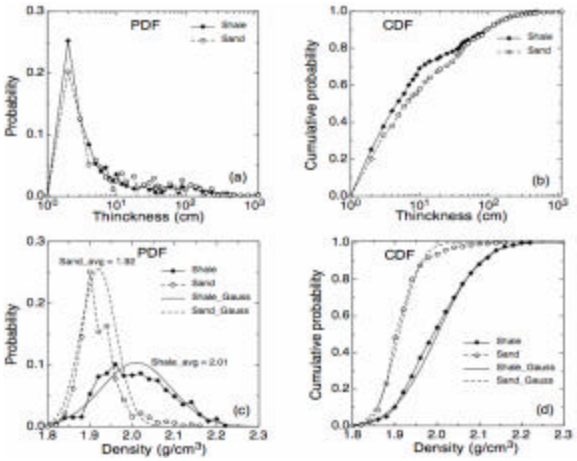

Figure 25. Probability (a) and cumulative density functions of bed thickness (b) for sand and shale beds, and probability (c) and cumulative density functions of density (d) for sand and shale beds.

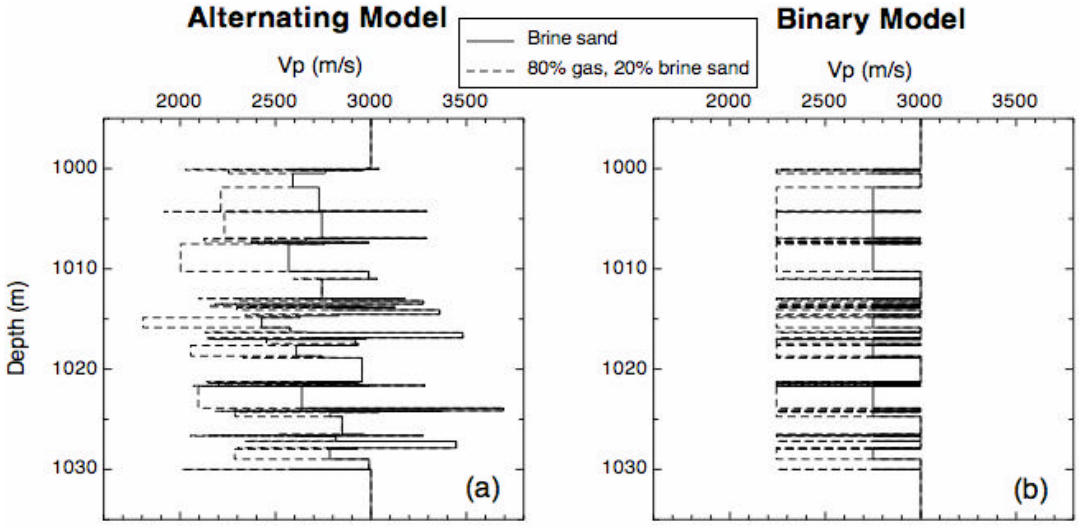

Figure 26. Example of a 30 m thick STM. (a) In the STM, sand and shale beds alternatively appear with a large heterogeneity of layer thicknesses and velocity. (b) In the binary model, the model has the same thickness distribution, but with identical sand and shale properties.

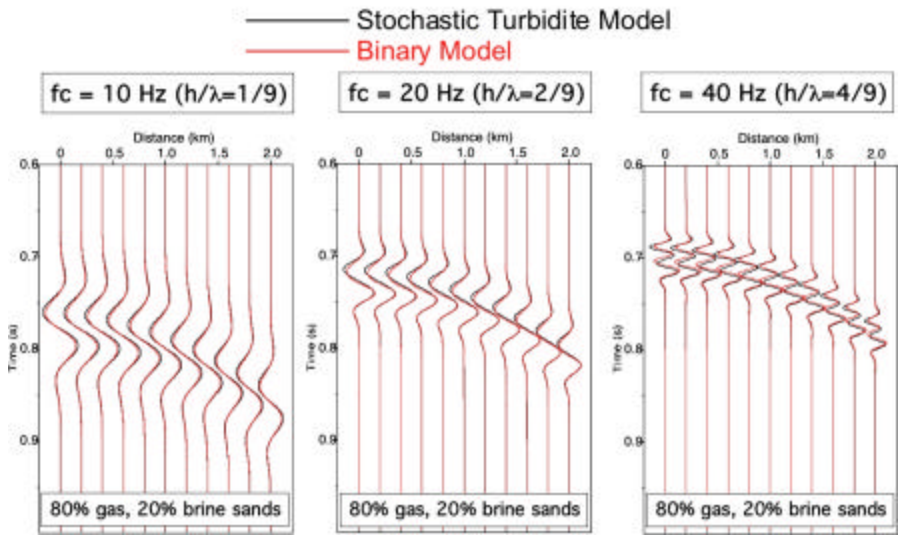

Figure 27. Synthetic seismograms for a representative turbidite model generated using our new approach and the more frequently applied binary model approach (see Figure 6). At higher frequencies, the differences in velocity structure become more important.

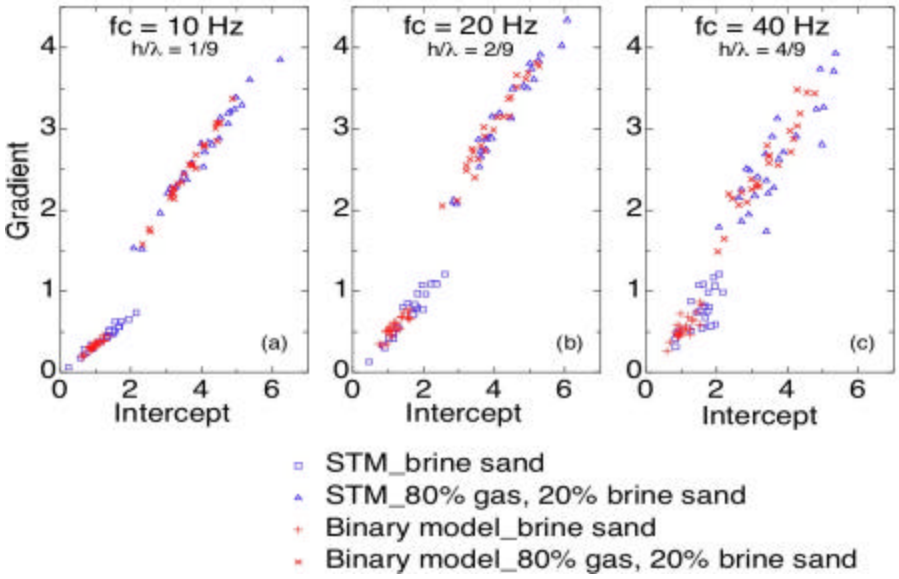

Figure 28. AVO parameters measured from multiple realizations of the STM and binary turbidite models. Turbidite models underpredict uncertainty in estimated AVO parameters, even at lower frequencies.

Improved Frequency-Dependent Processing for AVO

Results of the previous section show one source of frequency dependence in reflection amplitudes, the superposition of reflections from boundaries within a reservoir layer. Frequency dependence might also arise from attenuation related affects directly associated with hydrocarbons. In any case, accurate processing of data to detect these effects is essential. We have developed methods to improve the detection of such frequency-dependent anomalies in AVO measurements, with special emphasis on improved signal-to-noise ratio and avoiding the introduction of processing errors. Our

study of field data from the Teal South location led to the development of a workflow including a correction for NMO stretch that distorts higher frequencies in the data. This correction is a target based approach based on simple analytic expressions presented by Dunkin and Levin (1973). Spectral decomposition of the corrected data showed that there was negligible frequency dependence of AVO. A field data set from the Gulf of Mexico presented an additional difficulty because of its relatively low signal-to-noise ratio. This can be improved by "substacking" that data, that is, stacking four adjacent traces in a common reflection point (CRP) gather to suppress noise. We tested this approach on synthetic seismograms to verify its accuracy, and have also tested it on the field data. In addition to greatly improving AVO analysis with minimal distortion of frequency content, it also accelerates the spectral decomposition that is the most time-consuming part of the workflow after migration.

Figure 29 shows sample field data before and after the substack procedure. Figure 29a shows reflections from two target reservoirs. The NMO stretch is clearly visible at far offset traces, while its correction compacted the wavelet. Also, the alignment of events has been improved significantly resulting in more accurate AVO inversion results. After the spectral decomposition, we barely see any coherent events in high frequency data (Figure 30). After stretch correction, stronger amplitude at far offset from low frequency data has been reduced while very weak amplitude in high frequency data has been recovered. Notice that we only corrected processing artifacts based on the accurate equation that computes the stretch ratio. Though the changes are significant, this correction will not affect any change in frequency content by other factors such as tuning and attenuation. Also changes of amplitude are much smoother due to the substack scheme that increased S/N ratio. Crossplots of two frequency slices over 20 CMP gathers show us significant improvement in our final output (Figure 31). The biased strong low frequency anomaly has been corrected, while background trend only from high frequency data before stretch correction give us accurate attribute information after the stretch correction.

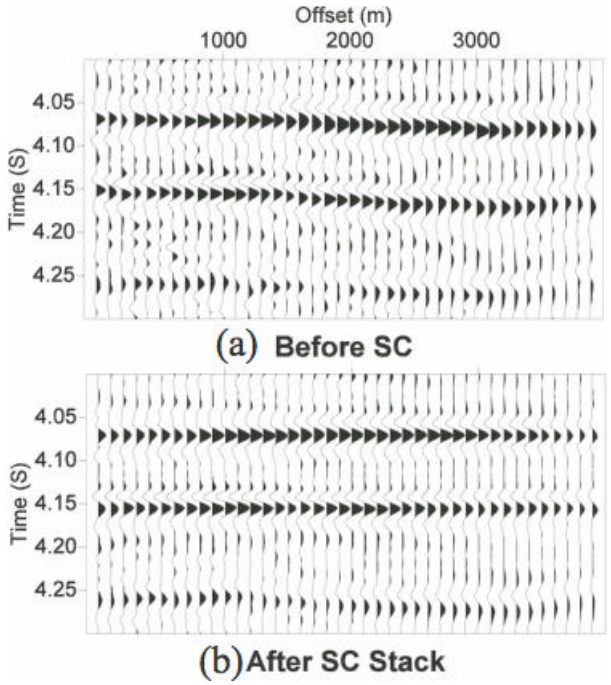

Figure 29. Two GOM deep-water CRP gathers (a) before stretch correction and (b) after stretch correction and substack. Note the increased S/N ratio in addition to improved event alignment. In (a), only every fourth trace is shown for simpler comparison to part (b).

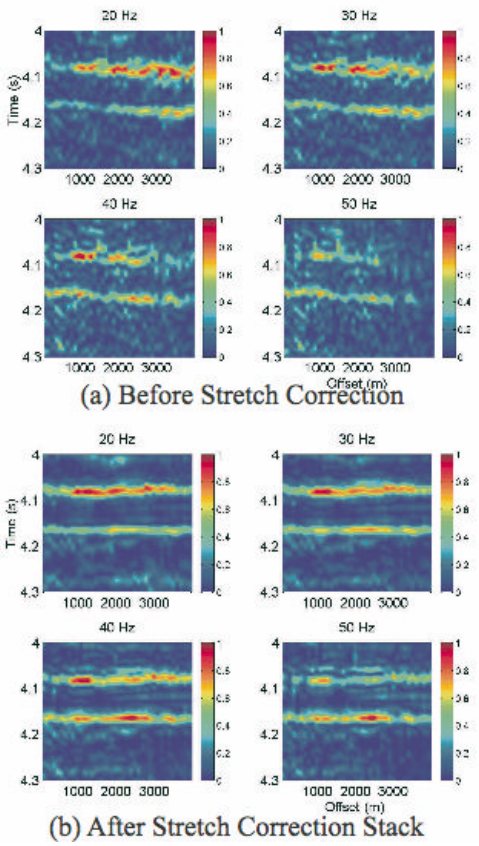

Figure 30. Spectral decomposed prestack gathers (a) before stretch correction and (b) after stretch correction. Each CRP gathers show four frequency slices: 20, 30, 40, 50 Hz. Notice the reduction of the far offset amplitude at 20 Hz and increase of overall amplitude at 50 Hz after stretch correction and stack.

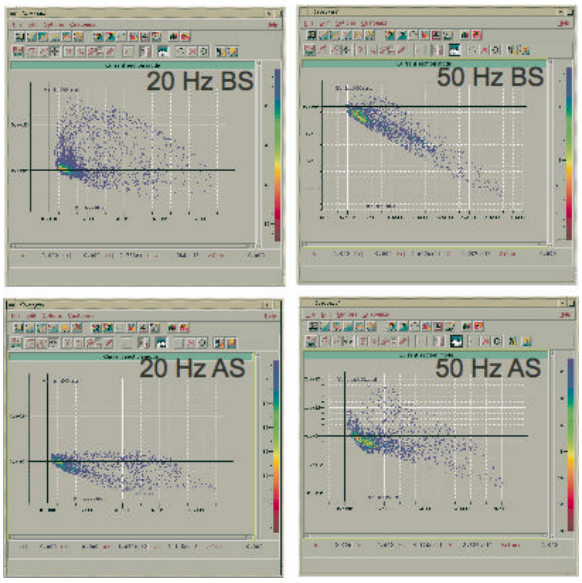

Figure 31. Crossplots of NI and gradient after stretch correction and stack at 20 and 50 Hz. At 20 Hz, false anomaly has been moved to the correction positions, while corrected anomalies show up at 50 Hz. BS: Before Stretch correction, AS: After stretch correction.

Outcrop observations

Well-studied deepwater outcrops are located in the Permian Brushy Canyon Formation in the Guadalupe Mountains National Park and Delaware Mountains of West Texas (Figure 3.1). Direct observations of the outcrop were performed during May 2004. The field observations, combined with previous work done in the Brushy Canyon formation by the CSM Slope and Basin Consortium, will aid in development of realistic seismic models. This will help to predict architectural elements and geobodies in deep marine settings and better identify the relationship between geologic facies to seismic response. One major difference between Brushy Canyon sediments and the Ursa field Gulf of Mexico (GOM) settings is that the Brushy Canyon is sand rich setting while the Ursa field is a mud rich setting. This chapter will give an overview of the Brushy Canyon geology and then discuss the architectural elements of the Brushy Canyon outcrops that will be used as analogs to the Ursa deepwater data sets.

Geologic framework of Brushy Canyon

During middle Permian time, West Texas was the site of an epicontinental sea, which had a restricted southern opening to the ocean (Borer and Gardner, 2000). The Permian Delaware basin contains many submarine channel fans that act as the main conduits of clastic sediment flow connecting the shelf to the basin floor. The basin is lined with a carbonate shelf. During lowstand cycles rivers flowed across the sub-arial exposed carbonate shelf carrying sediment into the basin and carving incised valleys which later focused and confined sediment deposition into the Delaware basin. The Brushy Canyon formation is exposed as an oblique striking transect that is continuously exposed along the western margin of the basin and holds 80 km of outcrops that include canyon, upper slope, to basin floor exposures (Batzle et al., 2000, Gardner et al., 2003). A map of the area can be seen in Figure 32.

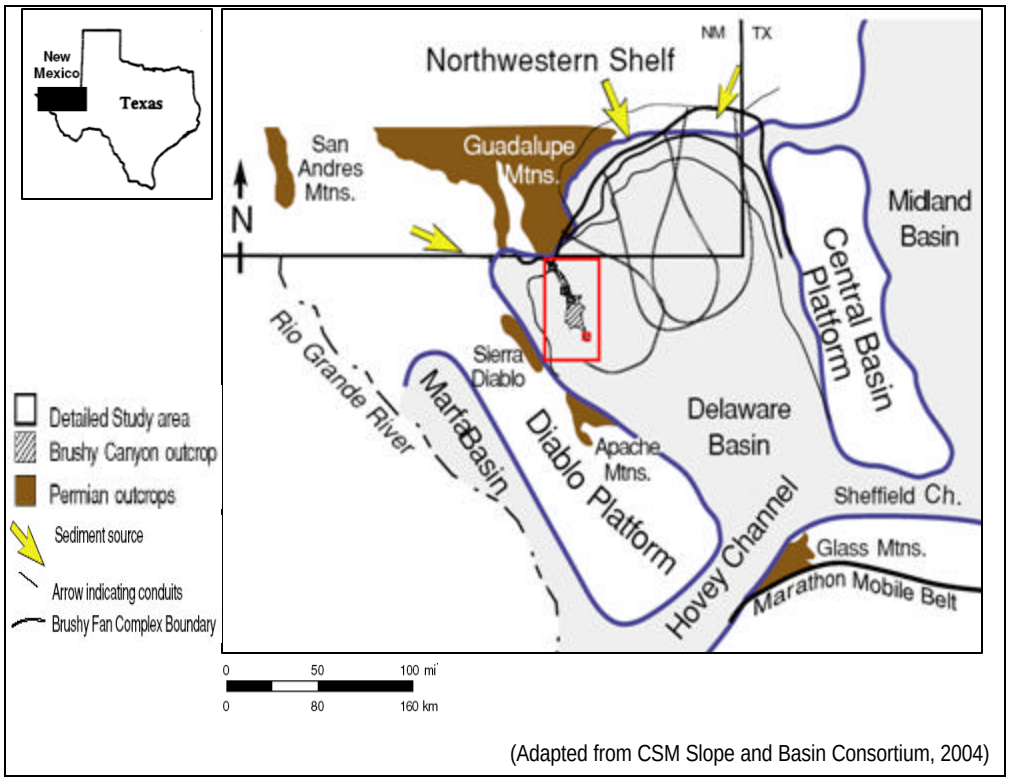

Figure 32. Map of the Delaware basin showing sediment source in yellow arrows, depositional basin floor fans, and the Brushy Canyon depositional area which is outlined in red (Adapted from Gardner and Borer, 2002).

Basinal cycles of destabilization, slope adjustment, and sediment gravity flows, followed by initiation and growth phases, shape deposition within the basin (Carr et al., 2000). The Brushy Canyon formation was deposited in a 3rd order lowstand systems tract indicating falling sea level at time of deposition. The gradient of the rimmed carbonate shelf (blue) controlled depositional patterns, incised valleys in the upper slope focused sediments into the basin (yellow arrows). Various phases of deposition of the Brushy Canyon formation occur as a function of the slope gradient and sediment supply (Figure 33).

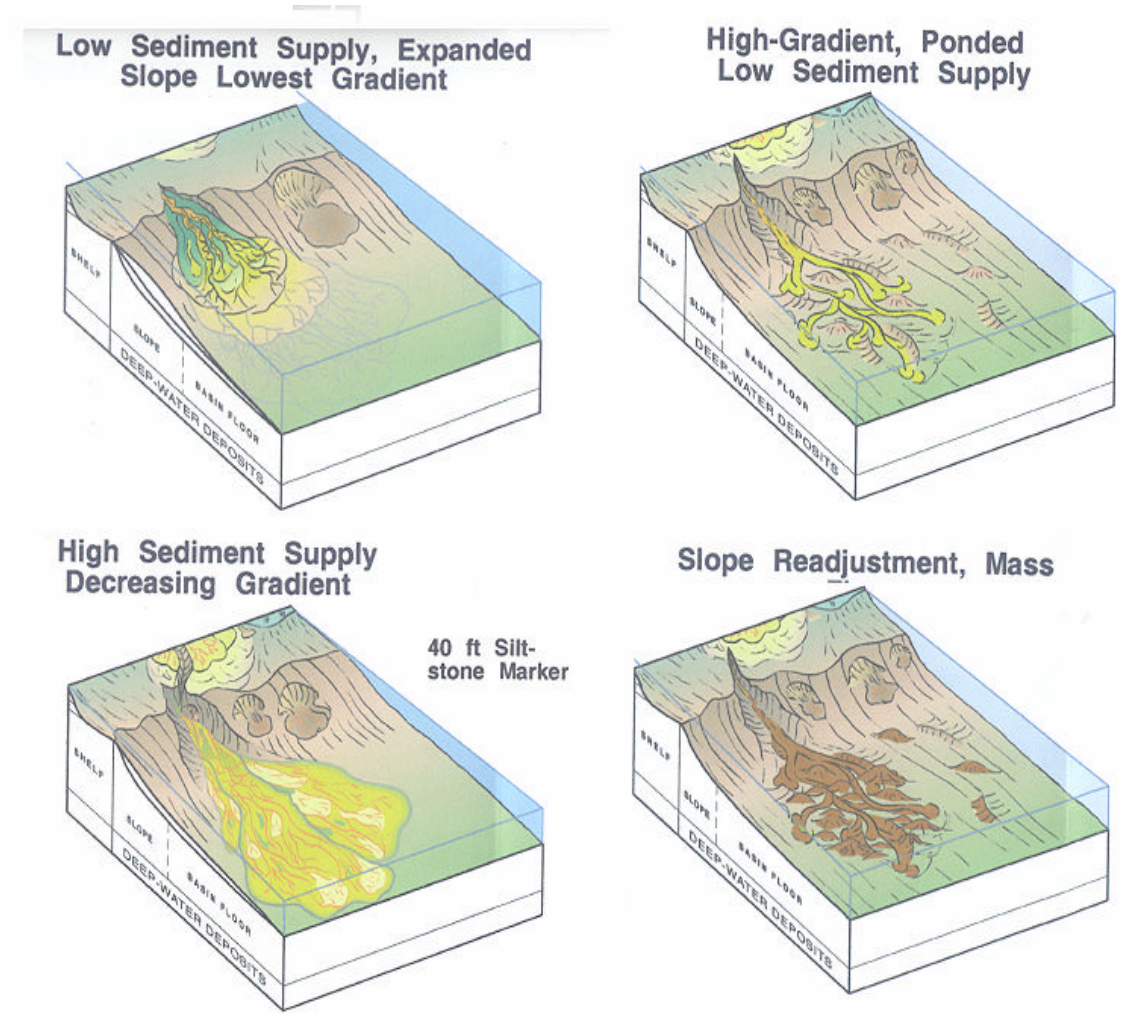

Figure 33. Phases of deposition in relation to the slope gradient (Borer, 2005).

The Brushy Canyon Outcrop is a sequence of seven submarine fans of a 3rd order composite sequence, approximately 2 my in age (Gardner et al., 2000). The Brushy Canyon fan complex includes the lower part of the Cherry Canyon Formation and is divided into upper, middle, and lower members as can be seen in Figure 34. The lower member contains many lowstand fan sediments and sequence boundaries.

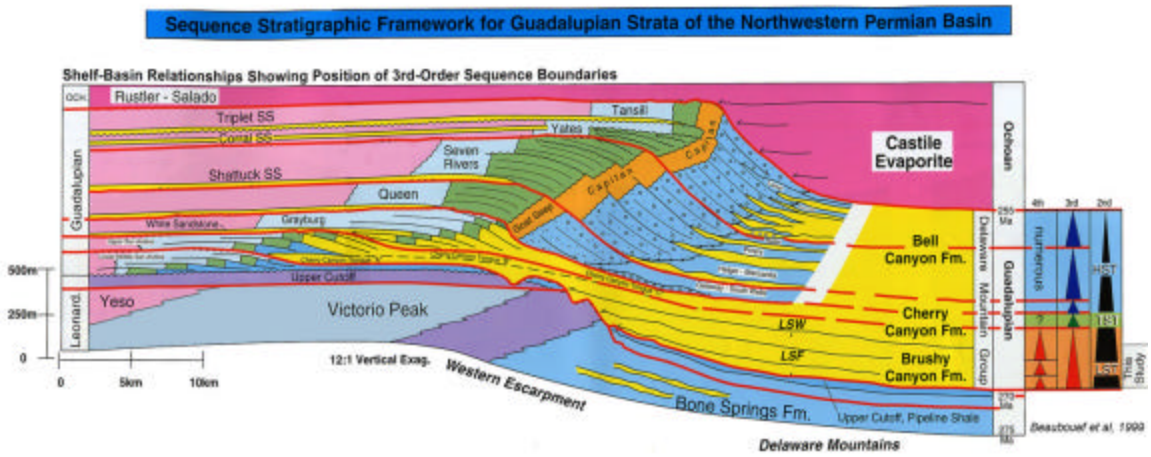

Figure 34. Sequence stratigraphic framework for Guadalupian strata of the Northwestern Permian Basin. HST, TST and LST describe high sea level systems tract, transgressive sea level and low sea level systems tracts respectively (Modified from Kendall, 2003).

Figure 35 shows the 3rd order (1-10 my cycle) sequence boundaries in the basin and the sequence stratigraphic framework for deposition in the basin. The northern, central, and southern exposures of the outcrop correspond to proximal, central and distal parts of the basin (Gardner et al., 2003). As one moves upward through the middle to upper Brushy an increase channel fill assemblages with drape surfaces is observed. In addition, siltstones and volcanic ashes mark periods of sediment starvation within the basin. These are good markers in well log and seismic data because they are highly correlatable and have highest impedance contrast (Gardner et al., 2003). All of these features are formed by cycles of sediment gravity flows into the basin. According to Gardner (2002), sediment gravity flow conditions at the time of deposition can be related to lithology, sediment structure and texture. In the Brushy Canyon Formation, cyclicity and facies patterns are representative of flow efficiency (the capability of gravity flow to transmit sediments basinward) over time. These observations have given insight into the relationship between deepwater facies, rock properties and formation of geobodies and helped to develop models that can be related to other deepwater depositional systems.

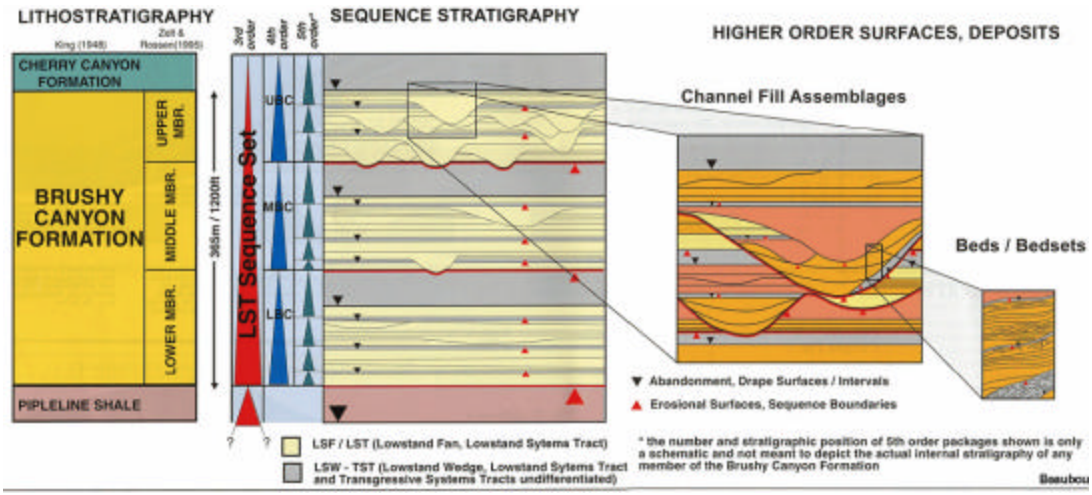

Figure 35. Hierarchy of bounding surfaces and schematic depiction of large scale progradational stacking patterns found in the lower Delaware mountain group of the Brushy Canyon formation (Adapted by Kendall, 2003, Beaubouef et al., 1999).

Brushy Canyon architectural elements

In the shelf, slope, to basin profile, architectural elements such as channels, sheet sands, levee overbank and siltstone deposits form as a product of cycles of erosion, bypass and channelization due to sediment gravity flows. Submarine channels form depressions that have been carved by erosion from sediment gravity flows and deepwater currents. The channels confine, focus, and direct gravity flows down a gradient into the basin and flows can be completely confined, partially confined or unconfined. (Gardner et al., 2003). Figure 36 shows a schematic view of one Brushy Canyon fan conduit and illustrates the cycles of deposition (Gardner et al, 2005).

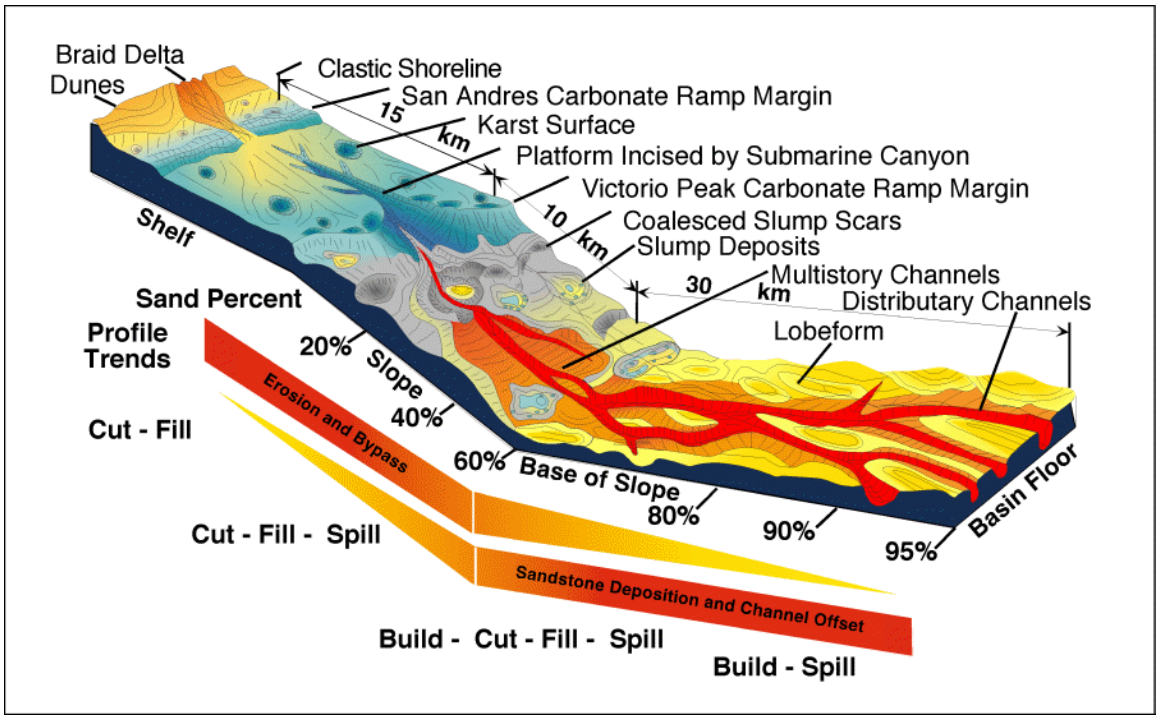

Figure 36. Schematic depiction of changing architectural styles and depositional patterns inferred along the slope and basin profile of one Brushy Canyon fan conduit (Gardner et al, 2005).

Channel Lobe Transistion Zones (CLTZ) mark changes from confined to unconfined flow in cycles of cut-fill and spill models as identified by Borer and Gardner (2000). A hierarchical structure of sedimentary bodies is formed by the CLTZ's, where smaller scale channels can form inside larger scale channel bodies. The build-cut–fill-spill concept (Gardner and Borer, 2000) provides a complete model of the arrangement of lobe and channel fill, which are comprised of channel, overbank, wedge and sheet bodies. The CLTZ is commonly linked to lower slope and proximal basin floor and commonly indicates the base of slope (Mutti and Normark, 1987). Examples of these features are shown in the schematic in Figure 37.

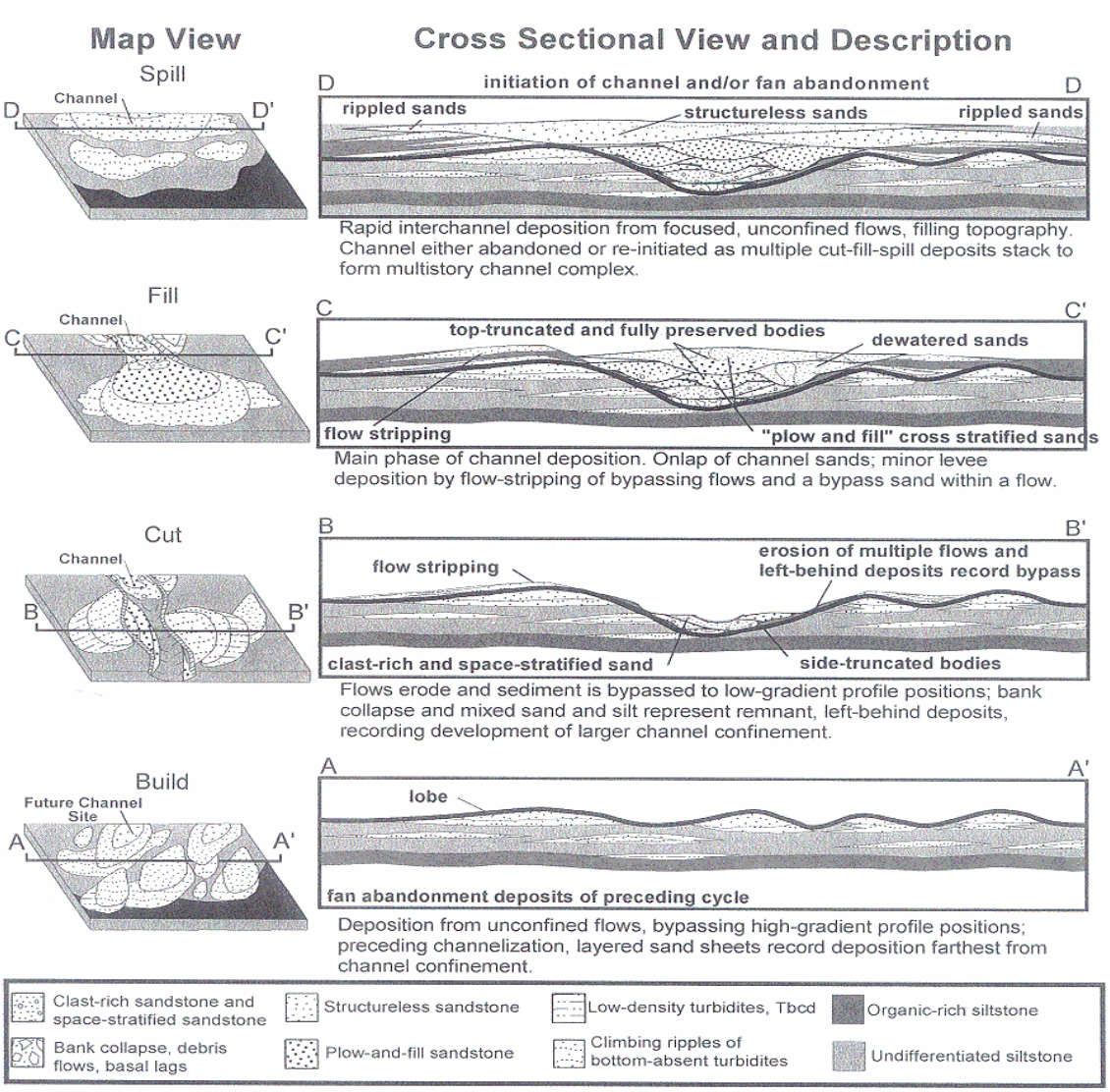

Figure 37. Spatial and temporal controls on channel overbank deposition in the Brushy Canyon Formation (Borer, 2005).

General observations of Brushy Canyon formation architecture include an increase in net-to-gross and decrease in channel body size downdip (Borer, 2000). Although channel complexes and fan conduits increase in size down-dip, they are encased in higher proportions of overbank deposits that contribute to channel offset down-dip. In addition, master bounding surfaces occur in proximal slope and canyon settings. (Borer and Gardner, 2000)

Four main architectural elements in the Lower Brushy Canyon formation in Colleen Canyon (Carr et al., 2000) include sheet sands, tabular siltstone, channel forms, and channel flanking wedges (Figure 38).

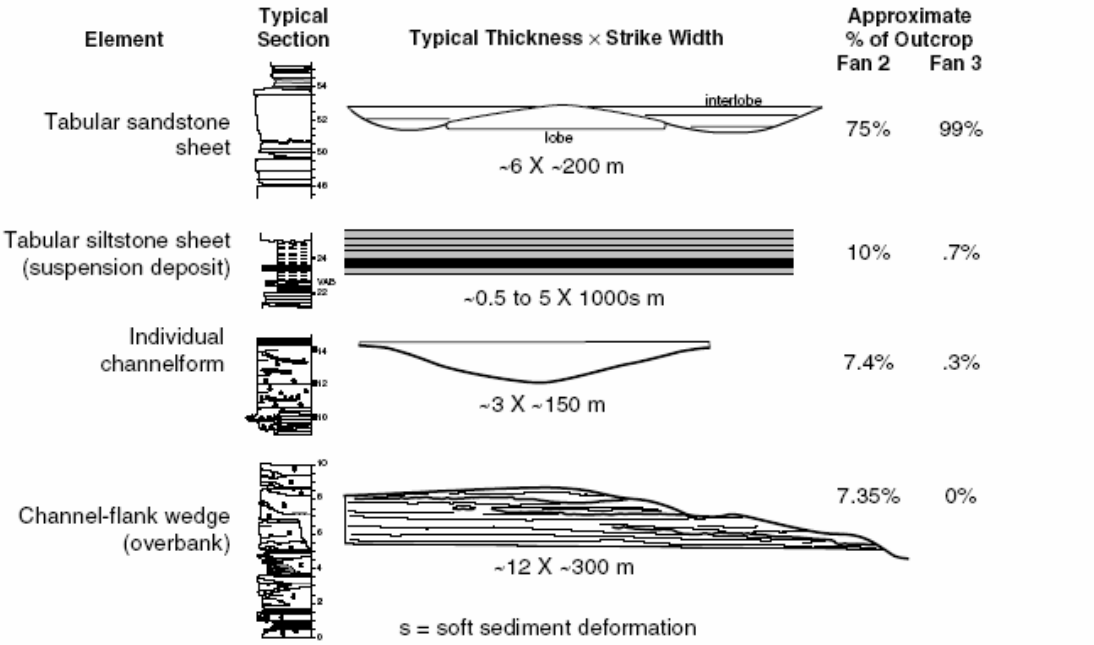

Figure 38. Schematic of geometry and facies of architectural elements found in the Brushy Canyon Formation at Colleen Canyon (Adapted from Carr, 2000).

Channel architecture can be quite complex in the Brushy Canyon deposits. Four scales of channel architecture are identified by Gardner (2003) in the Brushy Canyon system. These are (1) the single story channel and lobe; (2) the composite channel, overbank wedge, sandstone siltstone sheets; (3) the channel complex, including confined and laterally migrating types; and (4) the fan scale channel fairways and inter-fairways. A schematic of the four different scales of channel facies architecture can be seen in Figure 39.

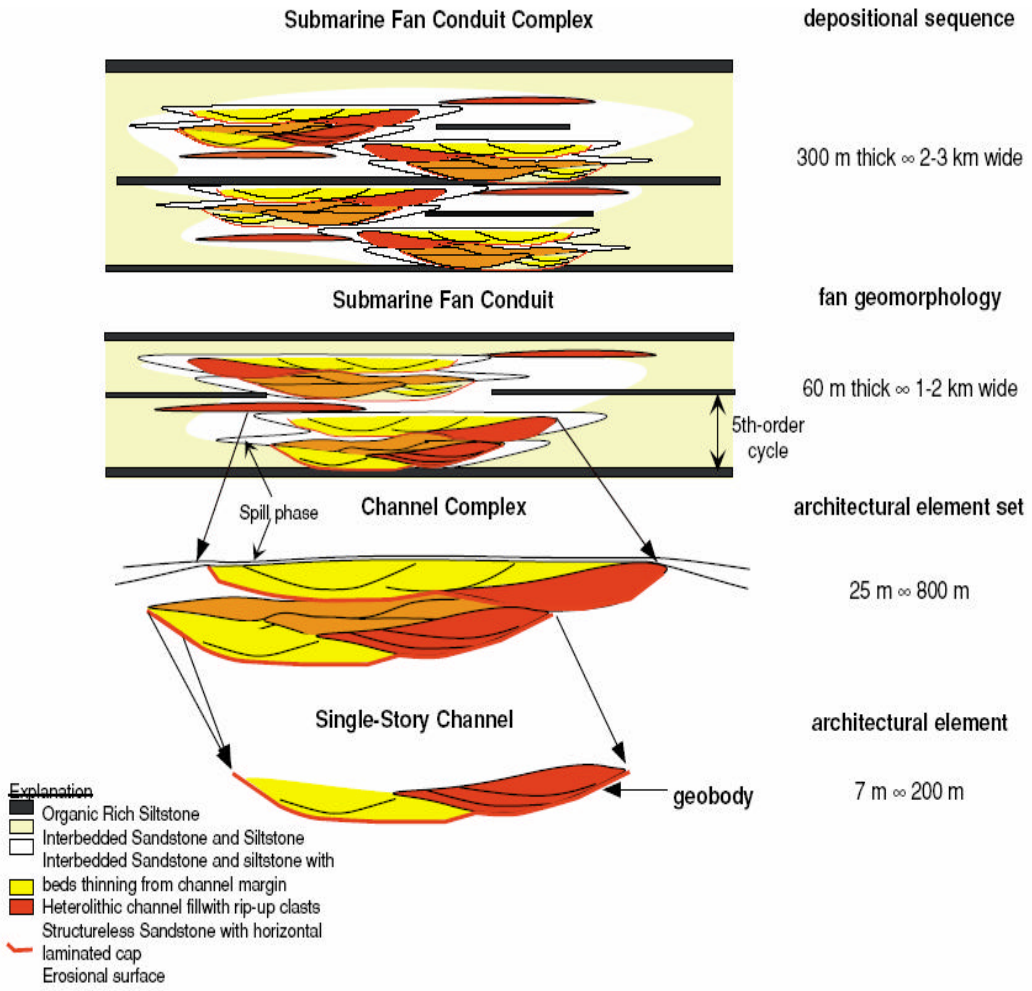

Figure 39. Schematic of the four scales of architectural facies of channel deposits (Gardner and Borer, 2000).

Figures 40-42 display the changes in channel architecture in the transition from shelf to basin along the depositional profile. Figure 40 shows middle slope channels, which are confined and non-amalgamated and seperated by siltstones which drape the channel base.

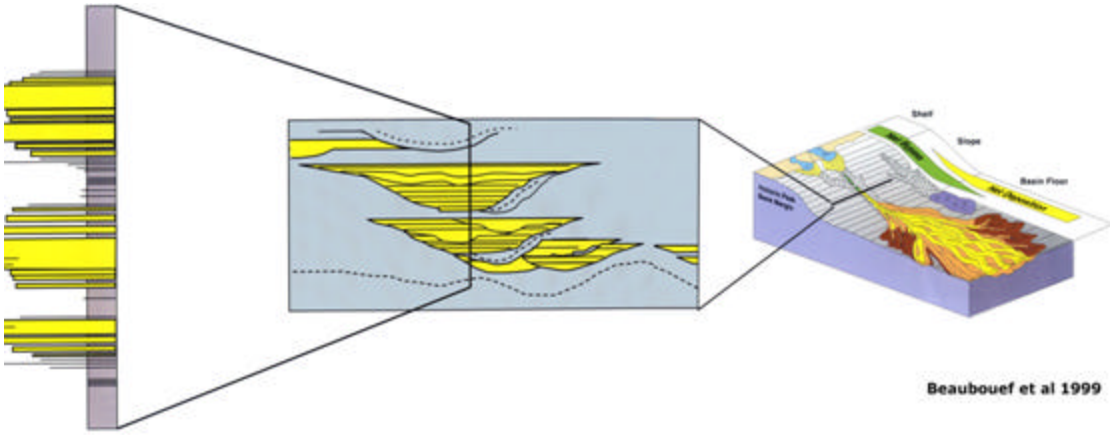

Figure 40. Middle slope channel (Adapted from Kendall, 2003, Beaubouef et al., 1999).

Figure 41 shows a toe of slope channel complex illustrating amalgamated channel bodies. In between these amalgamated channels are silts and higher net-to-gross sands line the channel bases.

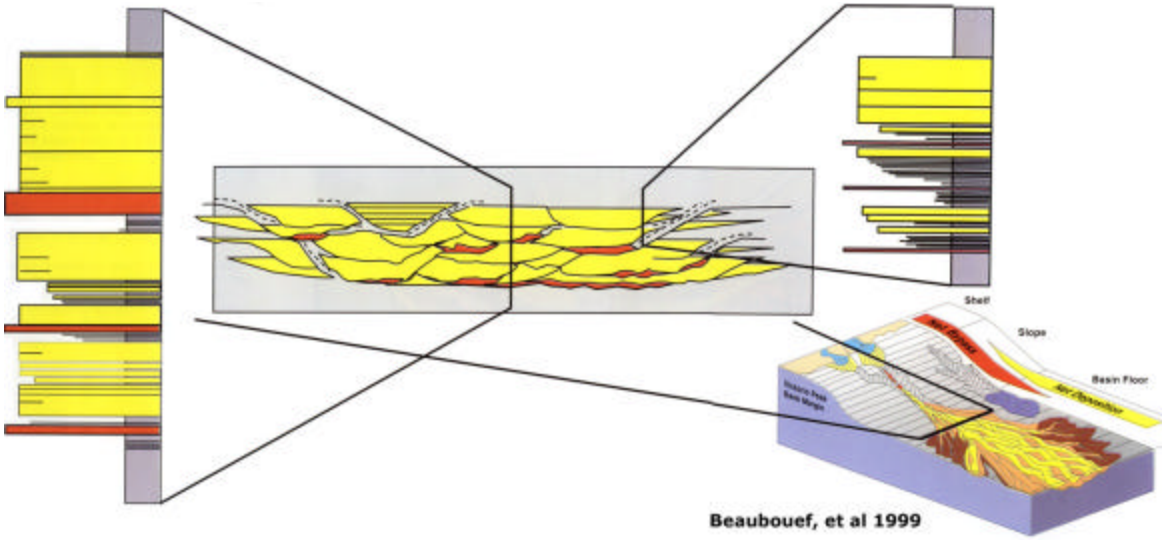

Figure 41. Toe of slope channel complexes (Adapted by Kendall, 2003, Beaubouef et al., 1999).

As sediment moves downslope amalgamated channel complexes occur (Figure 42) and are separated by interbedded sands and silts, which have a higher amount of silt deposits.

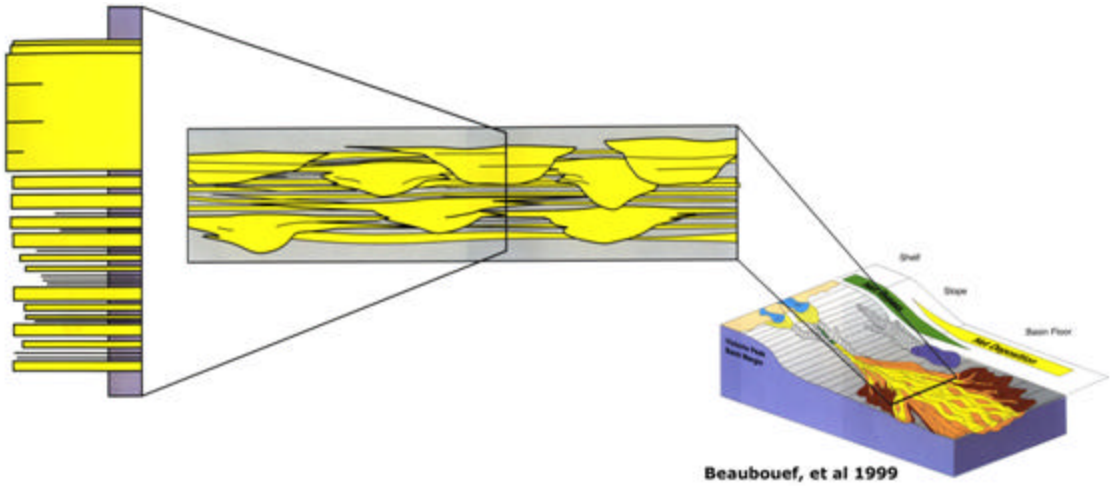

Figure 42. Proximal basin floor channel complexes (Adapted from Kendall, 2003, Beaubouef et al., 1999).

At the middle slope channel deposits become unconfined amalgamated and spread radially on the basin floor. This occurs due to energy loss and topography. These channel bodies are separated by interbedded sands and silts. The fourth architecture noted was levee overbank deposits. Levee overbank deposits are fine grained to thin bedded turbidite sediments that can be laterally extensive and are adjacent to main channels in a turbidite system (Mutti and Normark, 1991). Thin beds are commonly associated with levee overbank and are interpreted to include levee, interchannel and outer fan fringe deposits and are composed of fine grained sands or silt and graded beds (Shew et al., 1994). Expressions of these features in outcrop can be seen in the next section.

Outcrops to be used for modeling

The main architectural elements that will be used later in this work for modeling will be sheet sands, channel sands and levee/overbank deposits. Sheet sands are fan lobe deposits that are laterally continuous. Sheet sands are composed of multiple lobes and lack channel fills. Lobes are unconfined sandbodies associated with non-channelized deposition. They have tabular geometry and can be amalgamated (non-layered) or non-amalgamated (layered). Highly amalgamated sheets are high net/gross, stacked assemblages, of "top absent" Bouma sequences and can be difficult to separate. Non-amalgamated sheets are lower net/gross with complete Bouma sequences. Sheets range from thick to thin bedding and can be separated by thin siltstone interbeds. Sheet sands form in high-density sediment gravity flows. In seismic usually they are above tuning thickness, are highly correlatable and continuous between wells. In well logs they tend to be blocky to serrate and have flat top and base and therefore are easy to identify. Figures 43-44 show examples of amalgamated and non amalgamated sheet sands in outcrop. The observations from these sheet sands in outcrop will be used to model sheet sands in the Ursa field.

Figure 43. Amalgamated sandstone sheets from the Lower Brushy Canyon outcrops, height of outcrop is roughly 40 m (CSM Slope and Basin Consortium, 2005).

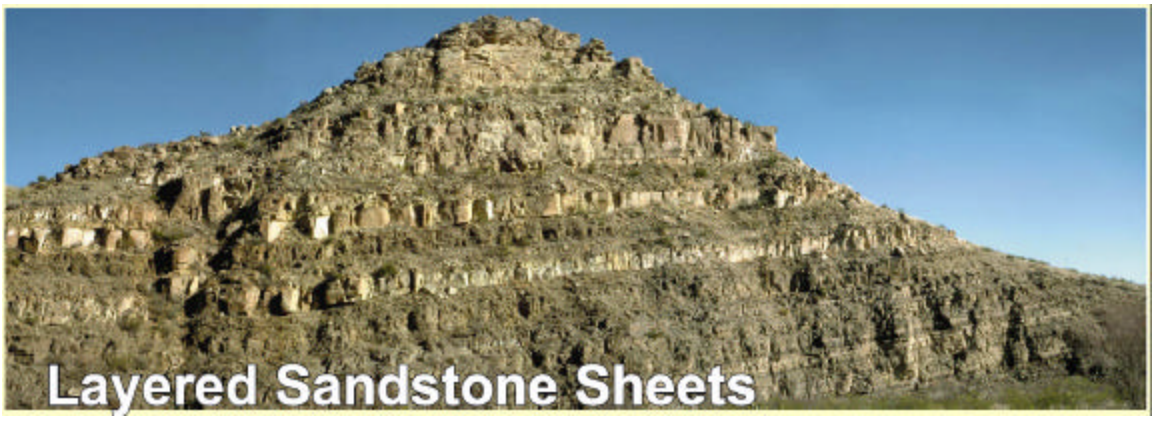

Figure 44. Layered sandstone sheets from the Lower Brushy Canyon outcrops. Note fine layering within sheets in lower right. Height of outcrop is roughly 27 m (CSM Slope and Basin Consortium, 2005).

Figures 45 and 46 show outcrop expressions of channel sands. Figure 45 shows a channel feature overly overlying a thick siltstone, which sits on top of sheet sands.

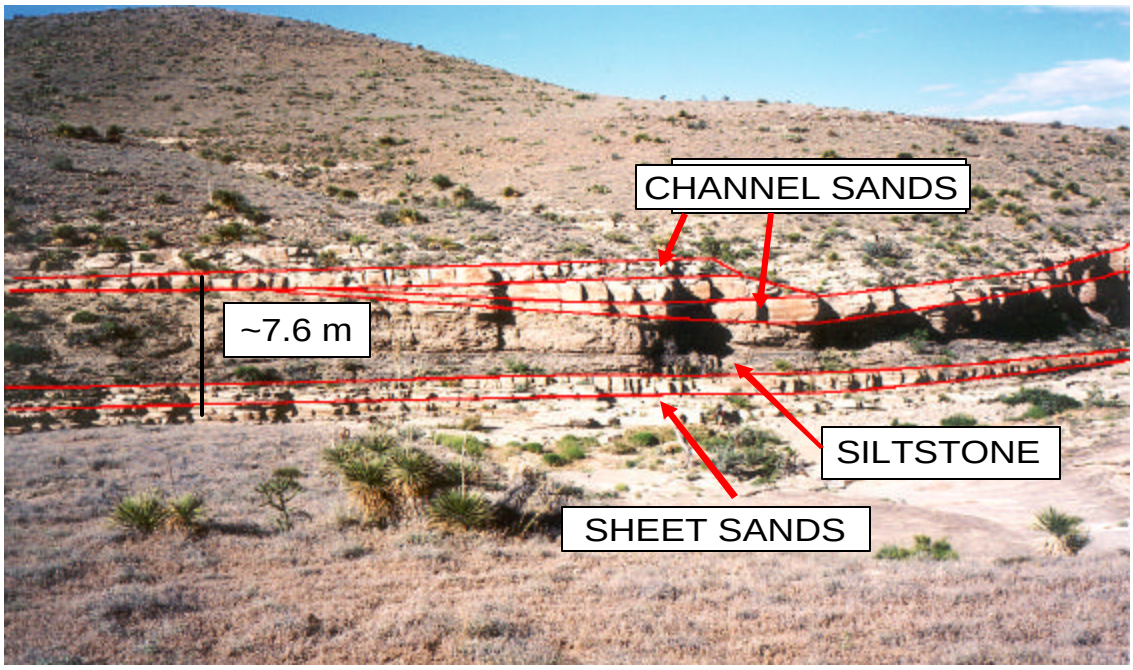

Figure 45. Amalgamated sandstone sheets overlying thick siltstone sheet from the Brushy Canyon outcrops.

Channel bodies form in hierarchies and stack to form multistory and multilateral channel complexes, and can vary from 30-150 m width. Single story channel bodies are generally 100-200 m wide and confined to one depression. Channels are cut and filled by sediments from multiple events to form geobodies. Composite channels are sand bodies that have been compounded and contain channel bars/fills that represent a common migration from a genetically related sand body (Gardner et. al, 2003). Channel complexes are composed of stacked channel features that migrate laterally across fairways or confine multiple channel belts to an erosional depression (Gardner et. al, 2003). Channel complexes can range from 600m-1.5 km wide and 20-50 km thick. Figure 46 shows a single story amalgamated channel with a siltstone drape, channel axis and channel margin. In seismic single story channels are usually below seismic resolution but channel complex features usually occur as small erosional depressions. They can be difficult to correlate between wells due to their sinuous nature. In well logs they tend to have blocky to serrated signatures depending on the ratio of sand to shale content. Channels can be more difficult to identify than sheet sands in deepwater subsurface data.

Channel wedge elements are comprised over levee/overbank deposits that flank, interfinger and thin away from channel margins. Wedge elements contain interbedded sands and siltstones (Carr et al., 2000). Figures 47, 48 and 49 show levee overbank deposits. These overbank deposits are show as wedge shaped bodies in seismic and are usually bathymetrically elevated with relation to the channel fill feature. In well logs they can be difficult to identify as reservoir rocks because of the high shale content they will be easily overlooked. Levee overbank areas have potential for reservoir quality because thin-bedded sands tend to be highly laterally extensive and can have high permeability porosity, and good trap potential (Weimer, 2003).

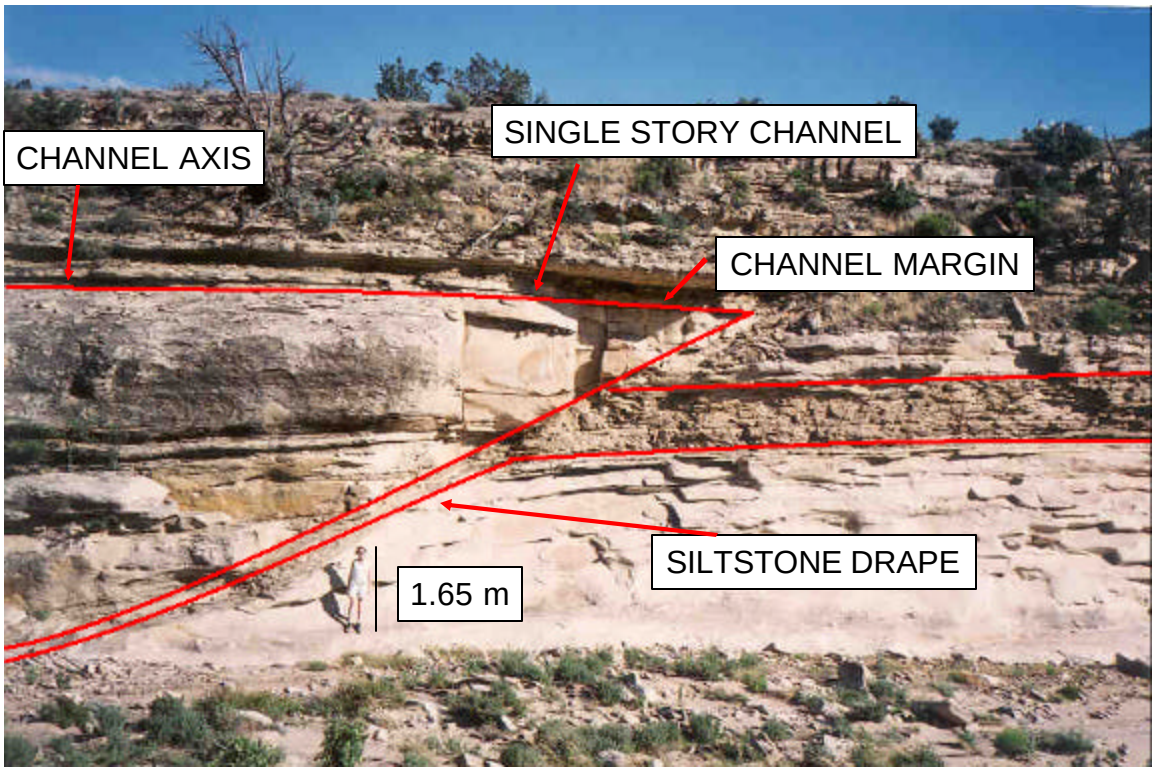

Figure 46. A single story channel form with siltstone drape.

Figure 47 and 48 show interbedded sands and shales of these levee overbank deposits for proximal and distal deposits respectively. Figure 49 shows a levee overbank wedge at a much larger scale. Key architectural elements such as sheet sands, channel bodies and levee over bank deposits will be the main features that will be implemented in the forward modeling.

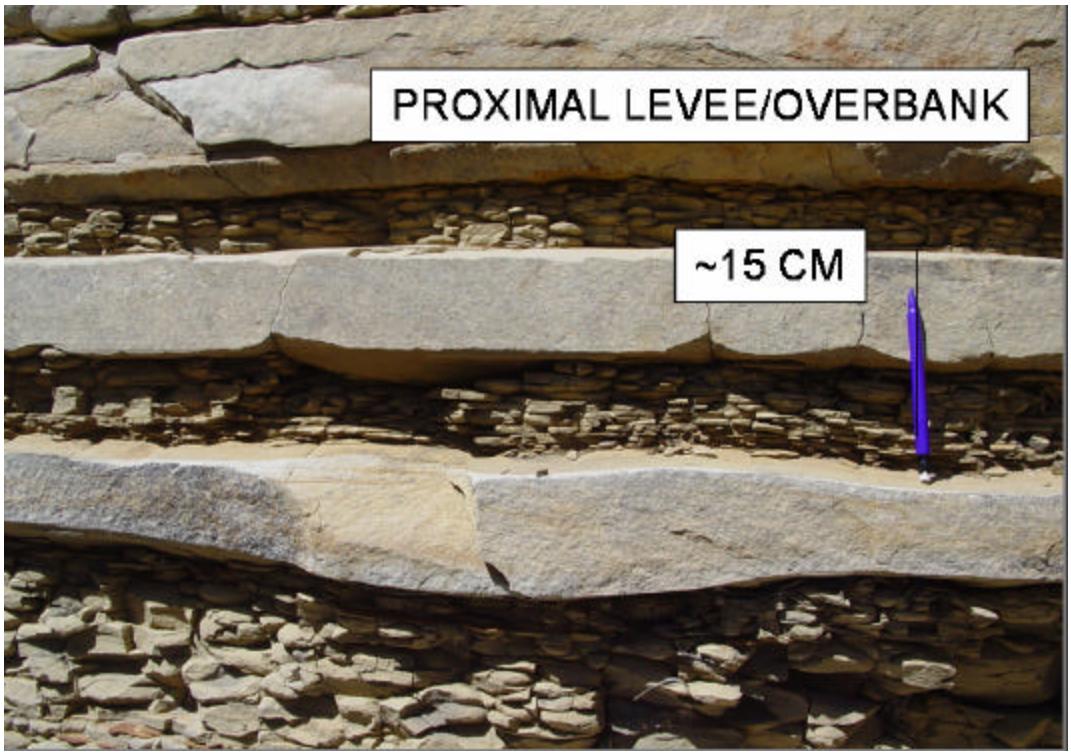

Figure 47. Proximal levee overbank deposit. From Lower brushy canyon deposits.

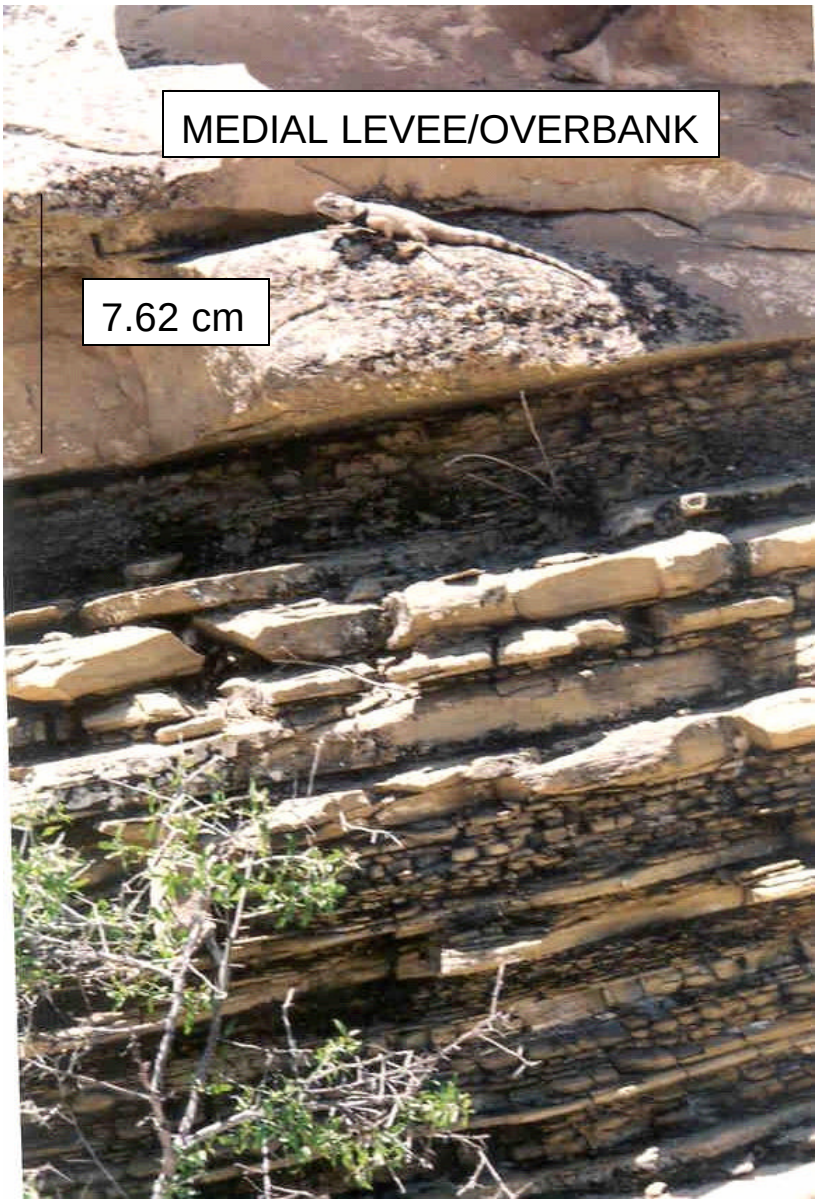

Figure 48. Small scale levee overbank facies comprised of interbedded sands and silts.

Figure 49. Large scale levee overbank facies (Courtesy of Slope and Basin Consortium, Gardner et.al., 2006).

Summary

The aforementioned architectural elements can be seen clearly in outcrop and related to positions along the depositional profile. In the Brushy Canyon formation it is clear that bed thickness is highly variable and dependent upon migration of the channel lobe systems through time (Gardner, et al., 2003). By utilizing the outcrop geometries as well as vertical and lateral changes in facies, the variability can be taken account and will aid in the development of realistic seismic models and help to generate more robust models that represent changes in the channel lobe systems. These observed architectural elements will need to be modified for application to small confined basins typical of the GOM. The sheet sand, channel sands and levee overbank deposits discussed in this chapter will be used to model Ursa deepwater seismic data in the Gulf of Mexico.

Ursa Data

The Ursa field is one of five prolific producing deepwater fields that are located in the Mars-Ursa intraslope basin, Mississippi Canyon, Gulf of Mexico (GOM). This basin is located approximately 210 km southeast of New Orleans, Louisiana and is in approximately 915-1200 m water depth (Meckel et al., 2002). A map of the basin can be seen in Figure 50. As of 2001, there were five major discoveries in the basin: Mars, Ursa, Crosby, King, and Princess.

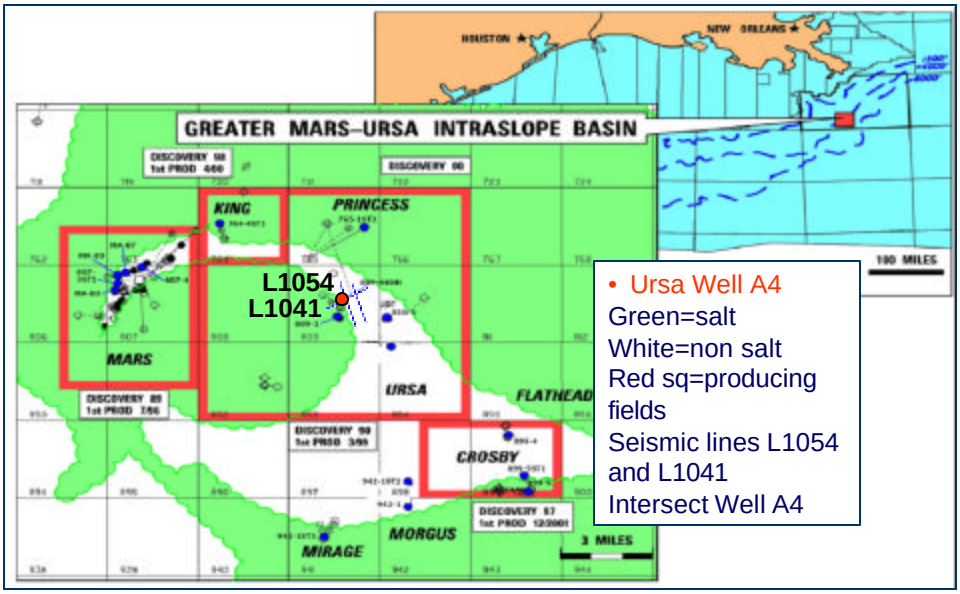

Figure 50. Map of the greater Mars-Ursa intraslope basin, Mississippi Canyon, deepwater GOM. Red circle shows Ursa well, blue lines show 2-D seismic. Producing field boundaries shown in red squares. Wells shown in blue circles. (Adapted from Meckel et al., 2002).

Between 1989 and 2001, these five major producing fields produced 314 Million Barrels of Oil (MMBO) and 375 Billion Cubic Feet of Gas (BCFG) resulting in 379 Million Barrels of oil equivalent (MMBOE) (Meckel et al., 2002). Each field consists of stacked turbidite reservoirs that have ponded in the salt bounded intraslope confined basins and are Miocene and Pliocene in age. Due to the success of these fields, they have been widely studied and, therefore, have a significant amount of information published about them. In this chapter, the Ursa geologic framework and rock and fluid properties will be discussed. In a later chapter, geobody models developed from the Brushy Canyon outcrops will be calibrated to Ursa subsurface data. Forward models will be built and compared to the Ursa data, which will enhance interpretation of features in seismic and well log data from the Ursa field. Published works will be used to confirm and enhance interpretation.

Gulf of Mexico data

The Mars-Ursa intraslope basin has a large amount of data. For this study three 2-D seismic lines (images) are available: line 1041, 1054, and 1046. The pre-stack seismic traces for line 1041 are also available. The map of the seismic lines and well log Ursa No 1 tie can be seen in figure 51 according to Hilterman (2001), the 2-D data were acquired by a 6000 m marine streamer with a receiver interval of 25 m and shot interval of 50 m. The reflections from deeper reservoirs have contamination from the salt masses on the far offset traces. Slumping in the first two seconds can affect transmitted amplitude and event timing of deeper reflections (Hilterman, 2001). These issues were addressed with processing that was performed by TGS. One well log (Ursa No. 1) was available for analysis and this log intersects seismic lines 1041 and 1054, as can be seen in Figure 52. The log was received in corrected form by Fred Hilterman, therefore it is assumed that

editing and normalization of log curves is sufficient. Logs were corrected for invasion and borehole washout. In his analysis, Hilterman points out that an exact synthetic match is not expected to occur because the seismic line does not exactly traverse the well (+/- 5m).

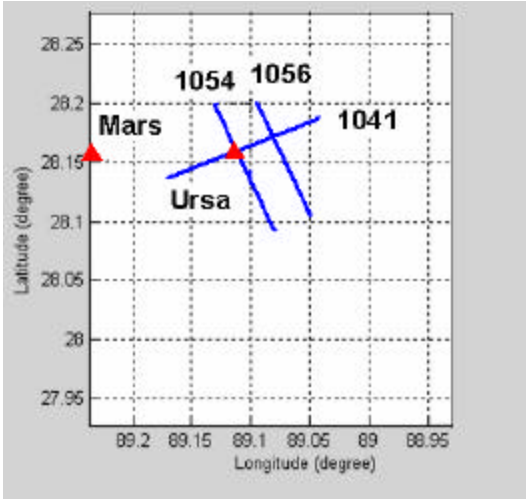

Figure 51. Map of seismic lines and the Ursa #1 well log. 2-D seismic lines in blue and red triangles are well logs. Line 1041 and 1054 intersect the Ursa well 9red triangle).

Also, amplitude reflections will not be truly reconstructed with 2-D migration over a 3-D structure, so the well log was stretched and squeezed to account for these problems (Hilterman, 2001). Hilterman's synthetic to well tie can be seen in Figure 52. In addition to the single well log that was corrected by Hilterman, there are also many well logs available in analog form from Minerals Management Services. Four wells from the basin were used to enhance rock properties analysis of Ursa reservoir intervals and calibrate the calculated shear log. In addition to this data there are many publications that offer insight into the geologic and geophysical properties of the Ursa basin, such as "Genetic Stratigraphy, Stratigraphic Architecture, and reservoir Stacking Patterns of Upper Miocene-Lower Pliocene greater Mars-Ursa Intraslope Basin Mississippi canyon Gulf of Mexico" (Meckel et al., 2002), which has been instrumental in the understanding of the Ursa basin. This paper, in addition to personal communication with Meckel, has helped to compensate for our lack of 3-D seismic data when trying to predict the influence of geology on the seismic signature and occurrence of Direct Hydrocarbon

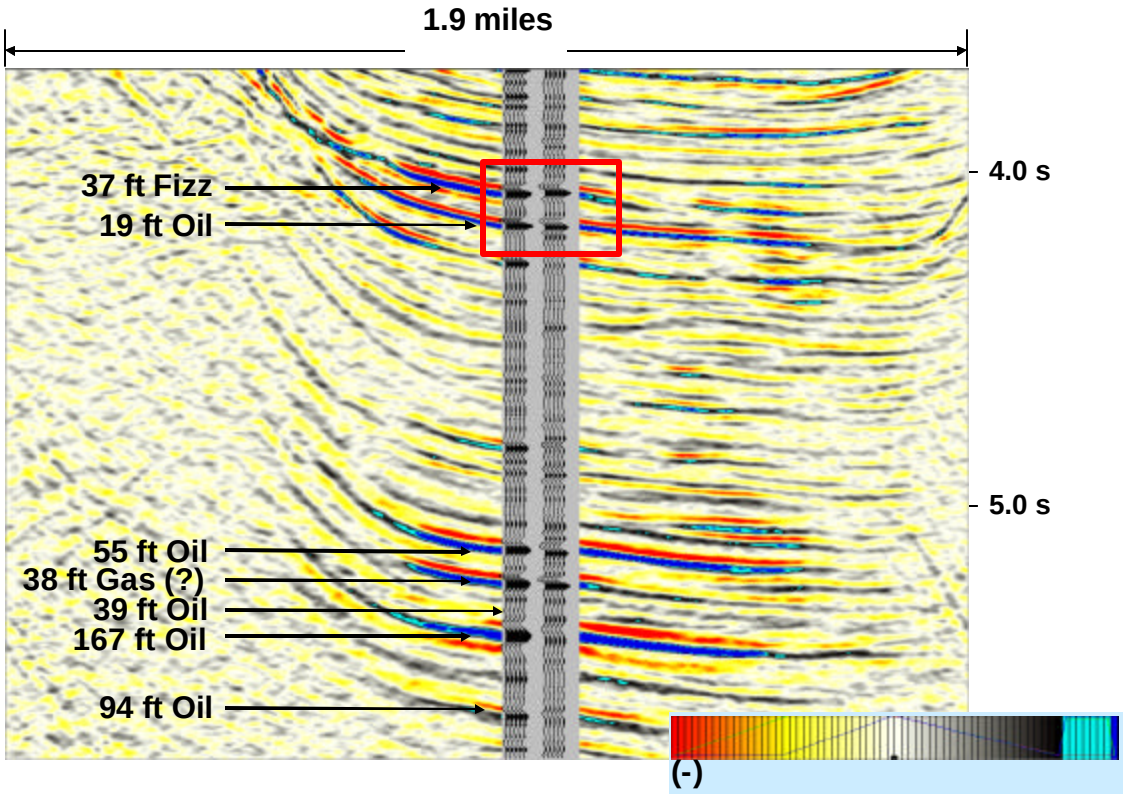

Figure 52. Fred Hilterman's close up of identified reservoirs intervals and synthetic well tie for line 1041. Here oil and gas saturated intervals are identified (Adapted from Hilterman, 2001).

Indicators (DHI's). Hilterman's studies of DHI's in the Ursa field and some of the interpretation from his book (Hilterman, 2001) are used as the basis for the following work. In addition, Prather et al. (1998) developed a classification for lithologic calibration and stratigraphic succession of seismic facies of intraslope basins deepwater Gulf of Mexico, and this was used as a basis to understand the geologic influence of deepwater geologic features on seismic facies in the Ursa basin. A complete understanding of the data and interpretations of the data were achieved by developing an understanding of the geologic setting in which Ursa field formed.

Geologic framework

The geologic framework of the Mars-Ursa Intraslope was adapted from the stratigraphic interpretation of Meckel et al. (2002). Figure 53 shows a useful schematic map of geologic deposition within the basin.

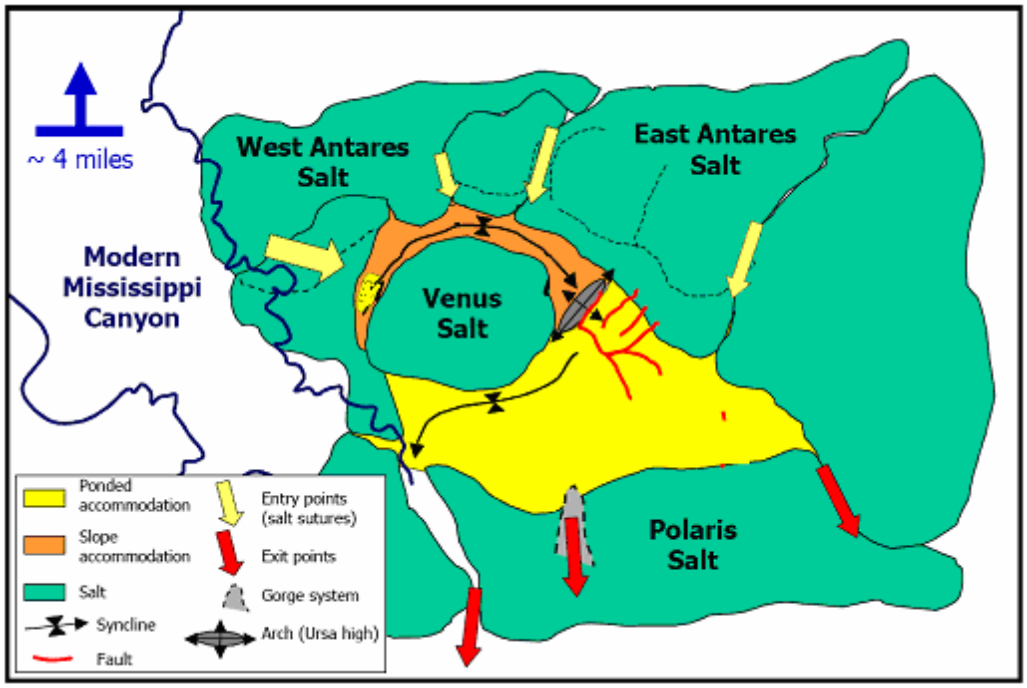

Figure 53. Schematic showing geologic profile of Ursa Basin (Adapted from Meckel et al., 2002).

The basin is composed of cyclic deposition of couplets of sheet sands and channelized or amalgamated systems bounded by condensed sections. The sheet sands and channel systems are separated by bypass erosion or avulsion surfaces. The sheet sand condensed section couplets form 4th order cycles, and according to Meckel et al. (2002) are the building blocks for seismic facies assemblages that are on the 3rd-order scale. These assemblages follow the fill-spill patterns characteristic of the mini basin setting.. Condensed sections form from pelagic sediments falling out of the water column and can be associated with abrupt changes in overpressure (Meckel et al., 2002).

According to Meckel (2002), the Ursa basin depositional environment is controlled by cycles of salt tectonics, subsidence, eustacy, and turbidite gravity flows. Four salt bodies dominate the basin (Figure 53). East and West Anteras salt, Venus, and Polaris Salt. Sediment is focused into the basin by entry points via sutures in the salt structures and inside the basin; sediment is deflected by topographic changes from salt presence. Gravity flows can fluctuate with eustacy, causing amounts of the sediment to change with the sea level. Once the sediment load is large enough, salt is activated and withdrawal

results in shifts followed by subsidence of the sediments. Basin entry points can have different facies associated with them as pointed out by Winker and Booth (2000).

Third-order stratigraphy is composed of two main seismic facies assemblages; ponded and bypass assemblages. According to Meckel (2002), Figure 54 shows a schematic of the depositional cycles of ponding and bypass facies.

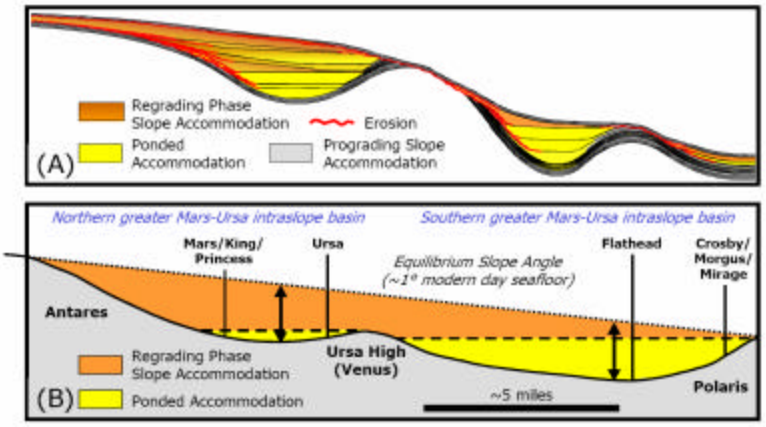

Figure 54. Confined basin setting schematic shows ponded accommodation and bypass as well as erosional features in the Mars-Ursa Intraslope Basin (Meckel et al., 2002).

Ponded facies have high amplitude, convergent, baselapping reflectors, localized chaotic reflectors and continuous sequence bounding reflectors. They form in confined settings where accommodation is greater than the rate of sediment supply, allowing sediments to accumulate in the mini-basin. Bypass facies have moderate to low amplitudes, thinning, non-onlapping seismic reflectors and extensive chaotic reflection, with minimal convergence at the basin margins (Meckel et al., 2002). The proximal to distal progradation in Gulf of Mexico sediments dominates both lateral trends and vertical trends as well.

Fourth-order stratigraphy is mainly composed of couplets of sheet sands and channelized or amalgamated systems. These couplets are bounded by condensed sections and divided by surfaces of bypass and erosion. Sheet sands are defined in Meckel's paper as areally extensive bodies with tabular or tapering (wedge shaped) seismic geometries. They are internally homogeneous in reservoir properties and highly correlatable between wells. In the Ursa basin, Green Bice, Terra Cotta, Lower Yellow, Magenta, Carmine, Sub-Voilet, Ultra Blue, Pink and Scarlet sands are names of interpreted sheet sands in the basin. They are large in lateral extent and usually occur as single seismic events. On well logs they are usually flat based and blocky to bell shaped and highly correlatable over long distances. By contrast, channels and amalgamated systems are defined by Meckel (2002) as areally limited sand bodies with shingled seismic geometries, internally heterogeneous reservoir properties, and low correlatability between wells. Meckle identifies Aqua Terra Cotta, Purple, Above Magenta sands as amalgamated channel systems and Upper Yellow, Violet, Light Blue, and Above Pink sands as non-amalgamated channels. These reservoirs are expressed as one or more seismic events and are difficult to correlate across the basin. A summary of these different seismic facies and

their log and seismic expressions can be seen in Table 2 below. Figure 55 shows the depositional history of some of the aforementioned significant reservoir intervals in the Mars-Ursa intraslope basin from Meckel (2002).

	Geologic	Well log	Seismic
Sheet Sand	Good lateral continuity, tabular geometry, fairly heterogeneous	Single to multiple units Blocky and bell shaped with flat bottoms Highly correlatability	Wedge shape and usually expressed as a single seismic event
Non Amalgamated channel	Thick to thin bedded, internally homogeneous	Blocky and bell shaped Poor correlatability	Shingled Seismic Sub parallel
Amalgamated Channel	Limited sand bodies	Blocky and rounded or serrate and change over distance	Shingled seismic geometry Sub parallel
Slope and Debris Flow/Mudstone	Soft sediment deformed , planar laminated silty claystone	High gamma Poor correlatability	Chaotic discontinuous
Thin Bed levees	Thinly bedded sands and silts <4" beds	Thinly bedded /laminated sands and silts fining uppward Poor correlatability	"gull wing" to sub parallel
Condensed Section	Composed of mud and organics represent long time intervals maximum water depths separate sheet sands below from channelized surfaces	High gamma values Highly correlatability	Occur at base of sheet sands; acoustically "hard" seismic events Continuous and high amplitude

Table 2 Summary of well log and seismic expression of deepwater facies in the Mars-Ursa intraslope basin.

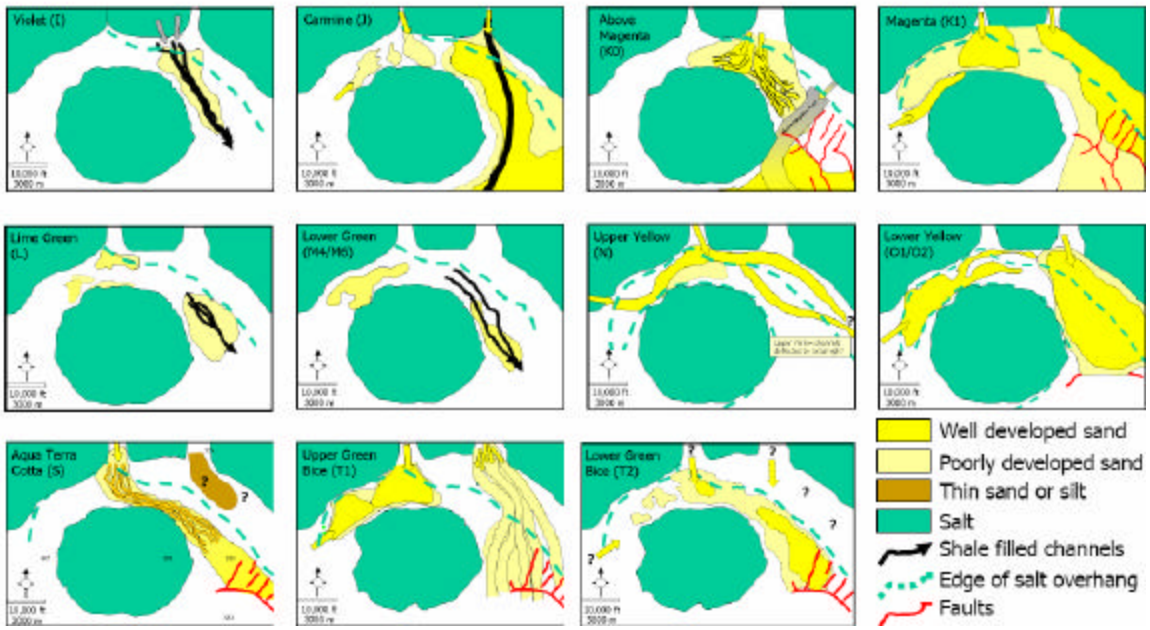

Figure 55. Schematic of depositional history of Mars-Ursa intraslope basin showing some of the major reservoirs (Adapted from Meckel et al., 2002).

The well log and seismic expressions of some of the significant reservoirs in the Mars-Ursa intraslope basin can be seen in the well logs (Figure 56) and seismic 2-D profile (Figure 57) below. Meckel's (2002) interpretation of logs from Mars, Princess, and Ursa A4 were extended to the Ursa 1 well and integrated with Hilterman's (2001) interpretation of fluid presence. In this well the green is oil and the red is gas. Yellow intervals represent sandy intervals with low gamma readings while high resistivity. Interpreted sheet sands such as Lower Yellow, show high corelability between wells and channels such as Above Magenta show low corelability between wells.

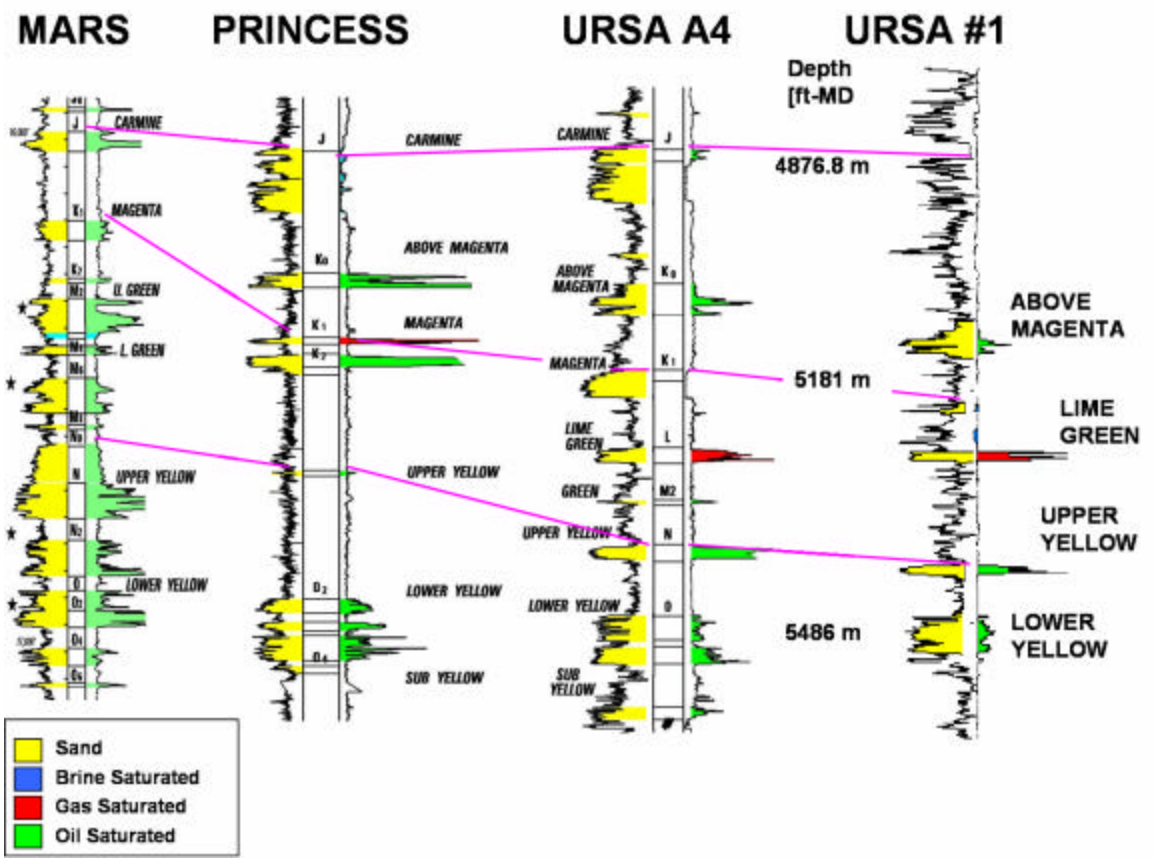

Figure 56. Well log correlation of significant reservoir intervals connected across the Mars-Ursa intraslope basin. The right log in each well shows resistivity, the left log shows gamma. High gamma intervals represent the shale baseline, deviations from the baseline are sands. Low resistivity values indicate water saturated shale. High resistivies (deflection to right) indicate hydrocarbon presence, where red is gas, green oil saturated reservoir.

The main reservoir intervals that were chosen for modeling are interval A Upper reservoir interval, Interval C Above Magenta reservoir interval and interval H the Lower Yellow interval. These were interpreted as levee overbank, amalgamated channel sand and sheet sands respectively. The main reason these three intervals were chosen is because they are representative of the three main architectural elements that can form reservoirs in deepwater settings.

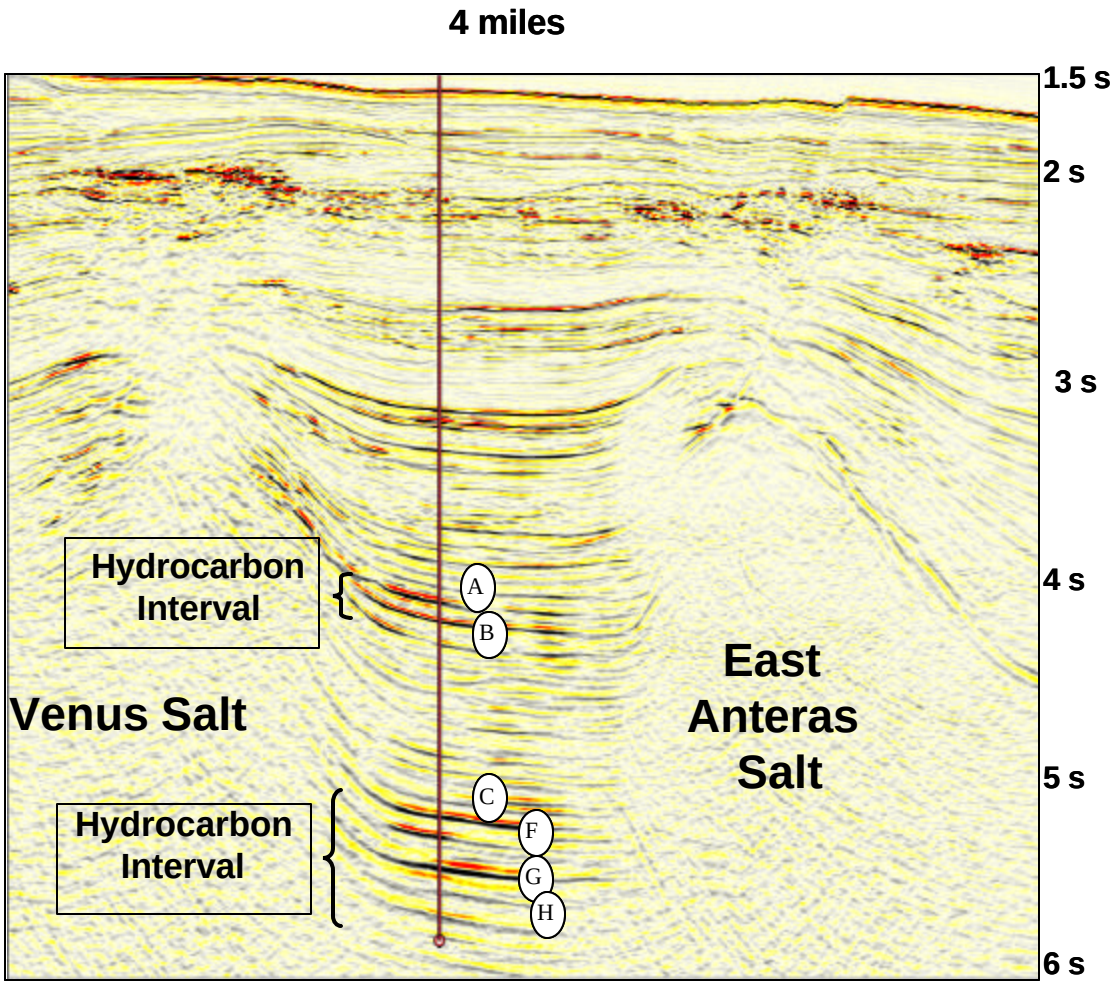

Figure 57. Ursa seismic line 1041 shows major hydrocarbon intervals indicated by bright spots and the log intersection for Ursa 1 well. A and B correspond with Upper and Lower reservoirs intervals. C,F,G and H correspond with Above Magenta, Lime Green, and Upper and Lower Yellow reservoirs respectively (Hilterman, 2001).

Shear wave prediction

There was no shear wave in the original well log data set. In order to calculate synthetic AVO parameters and perform fluid substitutions a shear log is needed. An estimated shear wave was received from Han (2006), which was calculated using Gassmann's equation and Han's empirical relationship that relates compressional velocity and shear velocity. A plot of the Ursa compressional wave data is made with the calculated shear velocity and can be seen in Figure 58.

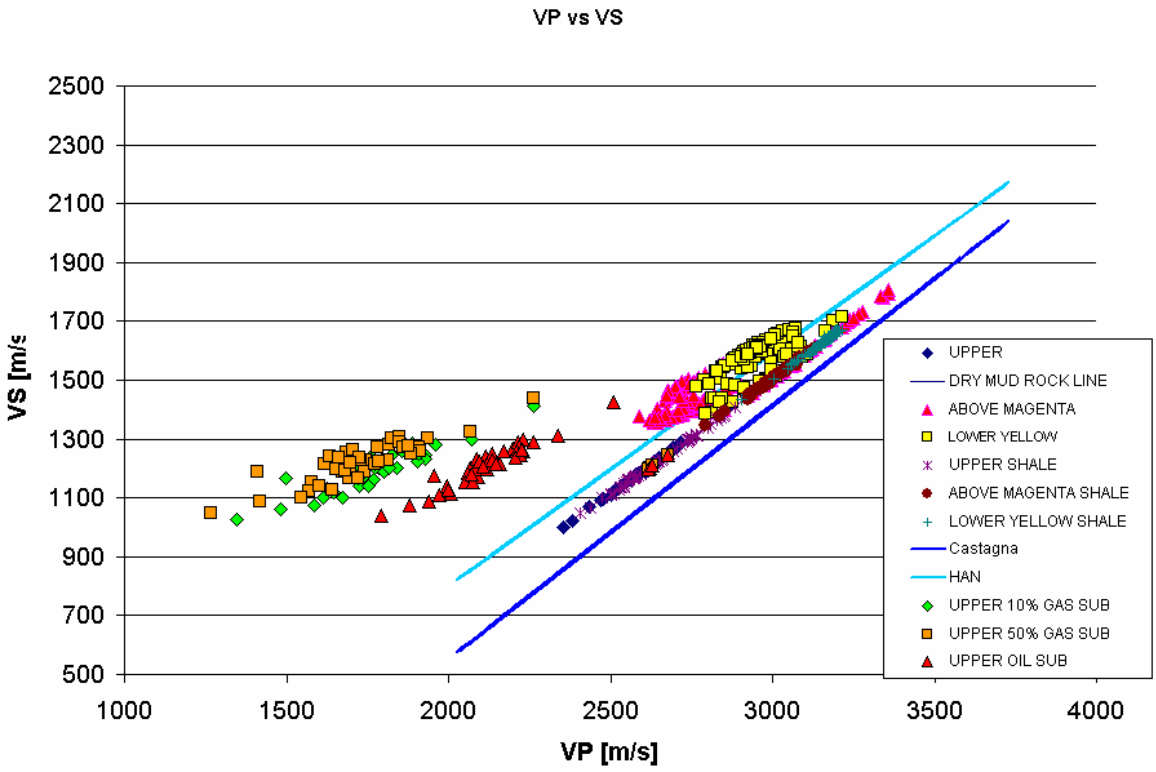

Figure 58. The empirical relationships of Han and Castagna plotted with the Ursa data for three reservoir and three shale (caprock) intervals as well as fluid substituted interval in the Upper reservoir.

In this figure the mudrock (caprock) and reservoir intervals are plotted for three reservoir intervals Upper, Above Magenta and Lower Yellow. Ursa reservoir caprock intervals are between the two blue lines that represent empirical relationships between compressional and shear velocity. The Upper reservoir interval, which is a thin bedded interval, also occupies the shale baseline. The oil and brine saturated reservoir intervals deviate from this baseline. The empirical relationships are derived by Han and Castagna (Equations 4.1 and 4.2) (Mavko et al., 1998). They are both empirical relationships that have been derived from controlled laboratory data for mudrock and sands respectively.

Castagna Mudrock $V_s = 0.8621V_p - 1.1724.$ (34)

Han GOM Sand $V_s = 0.7936V_p - 0.7868.$ (35)

In addition to comparing calculated data to empirical measurements the Vp/Vs ratio was analyzed. Some of the ratios seemed too high being on the order of 2.1-2.3. These values were compared with published deepwater sand Vp/Vs ratios (Han and Batzle, 2006) which had high values of 2.1, and therefore the values were deemed acceptable.

Pressure trend

The Ursa field has a change in pressure gradient at depth that has a significant impact on velocity and density with depth. At approximately 4050 m, there is a change from normal pressure to overpressure. Meckel's paper lists pressure for various reservoir intervals and this pressure change was plotted with respect to depth and can be seen in Figure 59. In addition to Ursa pressures, there is also a plot of the lithostatic and hydrostatic pressure and overpressure. The lithostatic and hydrostatic pressure gradient with respect to depth, are the same in water and are assumed to be .00113 MPa/m (.5 psi/ft) because there is only water and no lithologic pressure effects. (Once below the earth's surface, the pore pressure gradient is controlled by hydrostatic pressure, which is assumed to be .00113 MPa/m and lithostatic pressure gradient, which increases to .0226 MPA/m (1 psi/ft).) The overpressure gradient is .0181 MPA/m (.8 psi/ft). As can be seen in figure 59, the Ursa points are all overpressured and an increase to high overpressure occurs at around 5400-5600 m in well number one. There are normal pressure reservoirs that occur at shallow points in the well but no actual measurements of those pressures ere obtained and are therefore not plotted. To analyze the impact of pressure on rock properties, plots of background trends with depth were plotted for compressional and shear velocity, as well as density. These plots can be seen in Figure 60, 61, and 62 respectively.

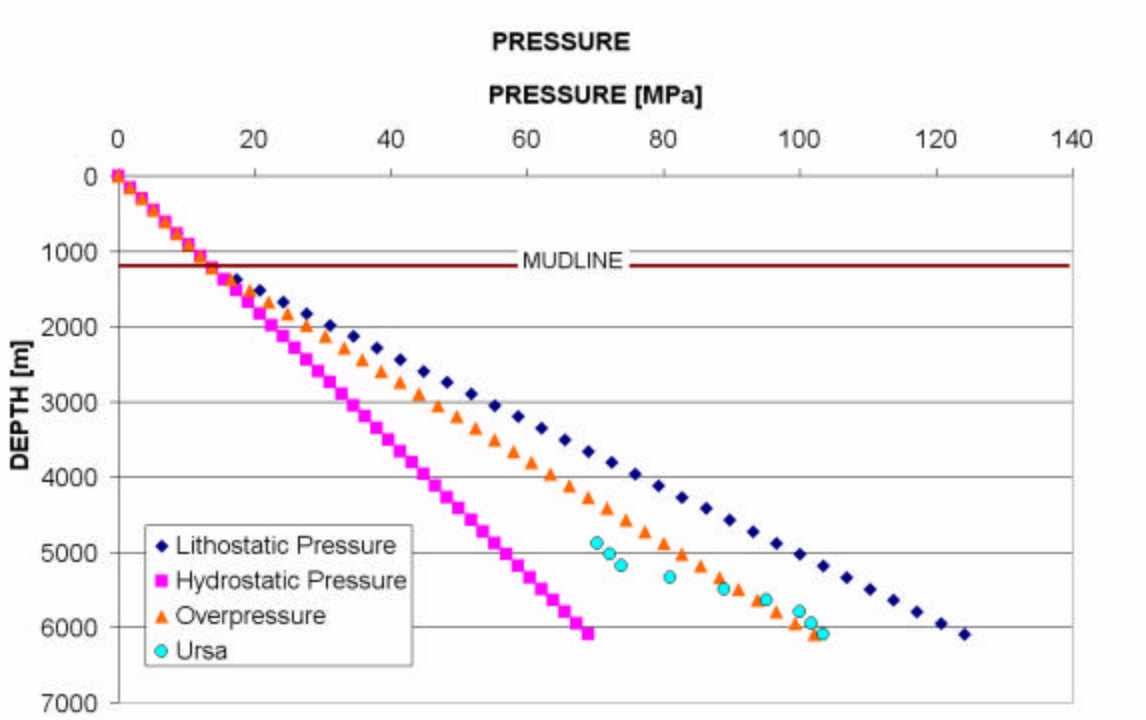

Figure 59. Ursa pressure gradient in relation to standard lithostatic, hydrostatic and overpressure gradient.

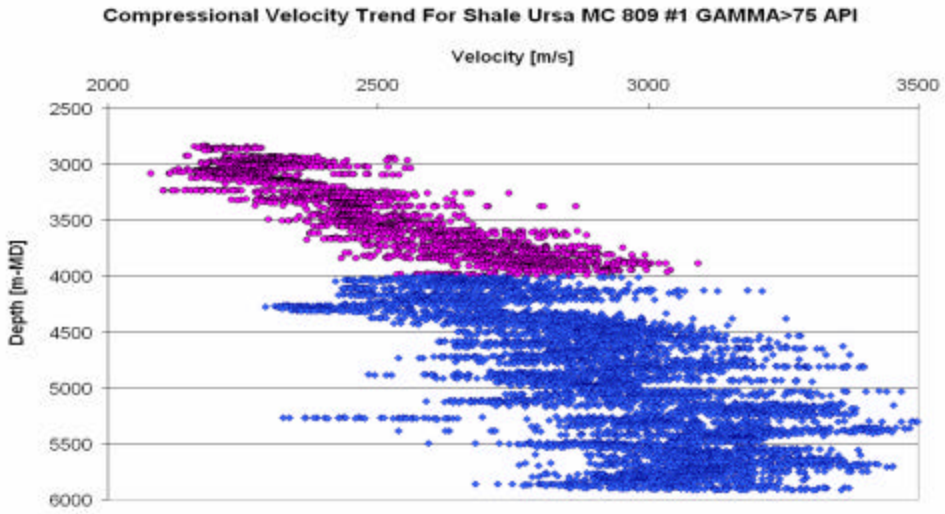

Figure 60. The compressional velocity trend of background for gamma >85 API in Ursa well #1 MC809. Two major trends are identified.

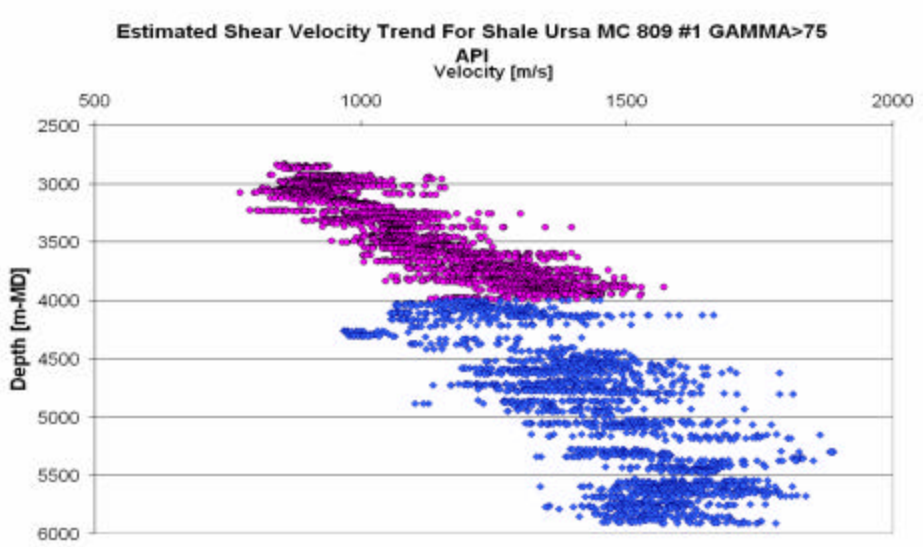

Figure 61. Shear velocity trend for the background for gamma > 85 API for Ursa well 31 MC 809. Two trends are identified.

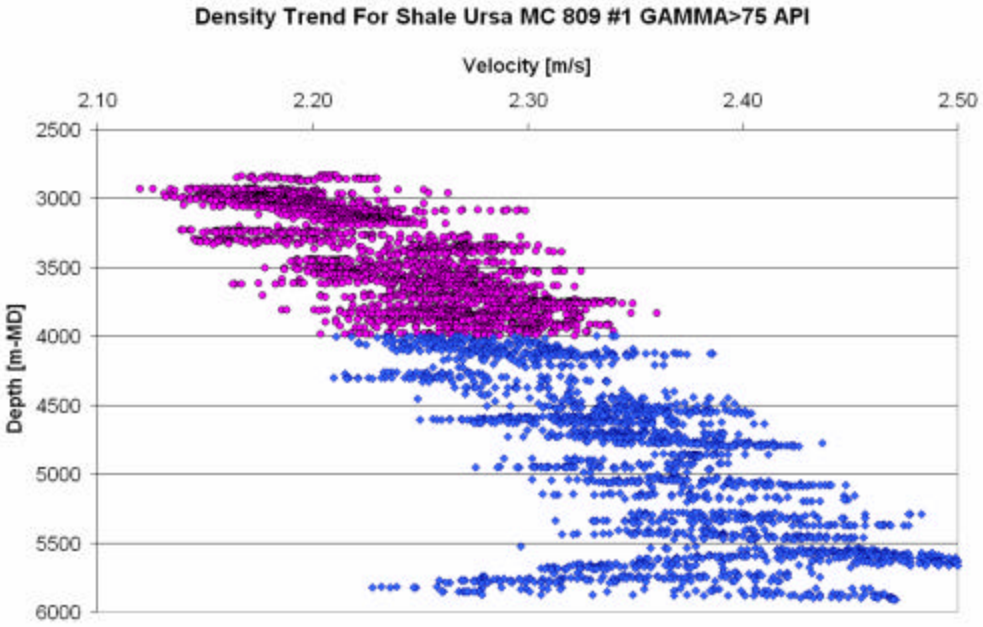

Figure 62. Density trend for the Ursa well log #1 for gamma > 85 API for Ursa well #1 MC 809, two trends are identified.

In these figures, there is a distinct deviation from the shallower, more linear trends in velocity and density at around 4300 m depth, and also at 5600 m depth. The 4300 m deviation also corresponds to the change between seismic facies, which could be the transition from the 3rd order bypass seismic facies to ponded seismic facies and change from normal to overpressure. The deeper deviation corresponds to pressure changes

plotted in Figure 62 at around 5400-5600 m depth. This could be associated with the change from overpressure to highly overpressured areas. Also, small perturbations may be associated with pressure cells. These changes must be considered when constructing geologic models. By calibrating the models pressure trends and background trends in the subsurface, we can account for changes that may significantly impact seismic signature.
Rock and fluid properties.

To calibrate reservoir models, rock properties analysis was performed on various 4th-order seismic facies that were interpreted in Meckel's (2001) paper. Histograms and Cumulative Density Functions (CDF) were constructed and used to predict the frequency of occurrence of rock properties, and describe the probability that a rock property may take on a value less than or equal to that value. These diagrams were used to determine mean velocity and density for different reservoir intervals representing architectural elements such as sheet sands, amalgamated and non amalgamated channels, channel overbank deposits and reservoir cap rock at varying depths, which include pressure changes. Figure 63 shows one example of a reservoir interval that was used

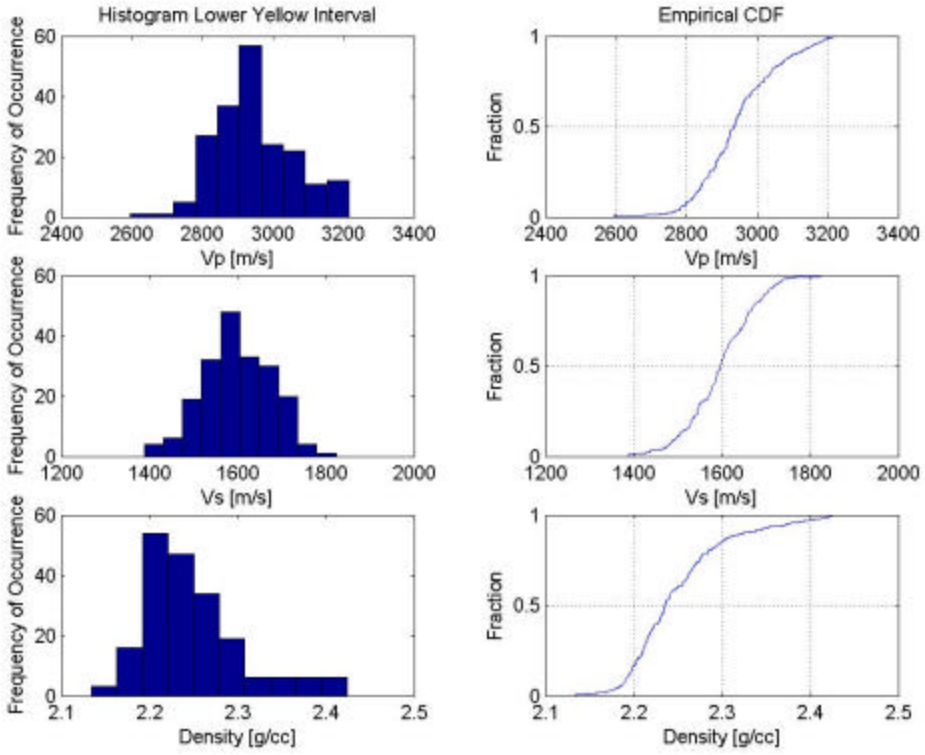

Figure 63. Shows histogram and cumulative frequency distribution (CDF) of Vp, Vs and density for the Lower Yellow sheet sand reservoir interval.

The mean and mode were obtained from these figures are used as inputs to models. Additional figures for other reservoir intervals can be seen in Appendix B. To obtain fluid properties, fluid substitution was performed with Hampson Russell software using Gassmann's fluid substitution (FMI). Gassmann's fluid substitution was performed on

each reservoir interval modeled. The values from the fluid substitutions were used for the various fluid cases for the reservoir interval. Gassmann's. To perform fluid substitution, parameters such as pressure, temperature, oil gravity, gas gravity, gas oil ratio, and salinity are required for the fluid property calculator in the software. The FLAG software was used to calculate Oil gravity, gas gravity and GOR. Pressure temperature and salinity were assumed based on previous knowledge of the Gulf of Mexico conditions (Batzle, 2005) to the software. Table 3 below displays the input parameters used for fluid substitutions.

Pressure	**6000 psi**
Temperature	**.80 API/80 C**
Oil gravity	**43.34**
Gas gravity	**.8 API**
GOR	**1000 L/L**
Salinity	**50,000 ppm**

Table 3 Input parameters for fluid substitutions.

Reservoir intervals were originally saturated with fluids as interpreted by Hilterman (2001). These interpretations of the intervals were confirmed with log analysis of Ursa well number one. All reservoir intervals were back saturated to brine based on the initial interpreted fluid using Hampson Russell software. Then, each reservoir interval was re-saturated using Gassmann's relation. first with oil, then 10%, gas and finally 50% gas. Figures 64, 65 and 66 show an example of one sheet sand facies with various fluid saturations in an overpressured zone. (Additional plots for other reservoir facies can be found in Appendix C)

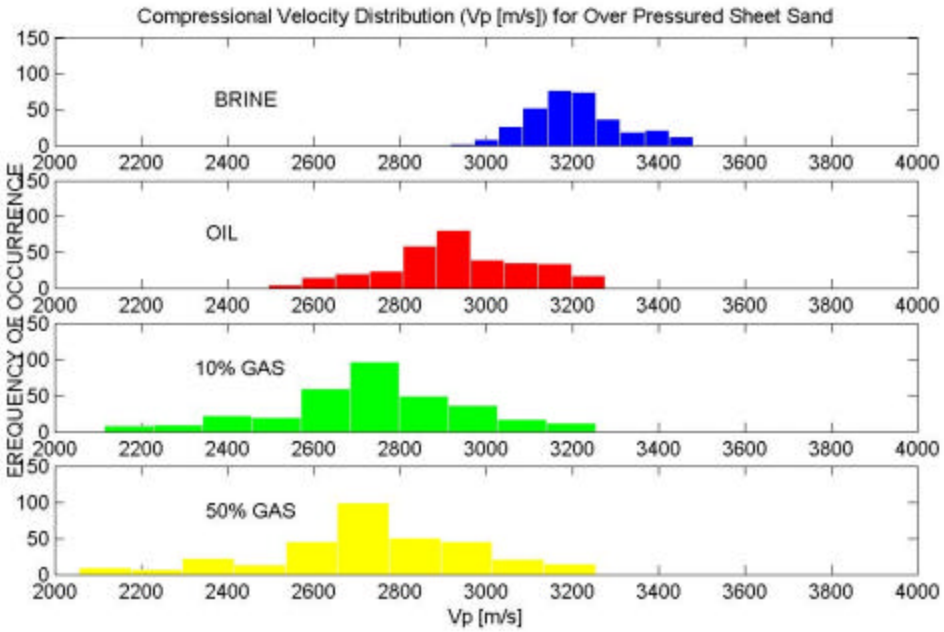

Figure 64. Histograms of frequency of occurrence of compressional velocities of overpressured sheet sands with varying fluid saturations of brine, oil, 10% gas and 50% gas. (Y-axes show frequency, x axes show compressional wave velocity).

Table 4 shows a summary of reservoir intervals observed, pressures, depths, facies interpretation and mean velocities for brine saturated zones. The change from dark yellow to light yellow colored rows on the table indicate a difference in pore pressure and seismic facies where upper and lower reservoir intervals are normal pressured and bypass (spill) facies, while the lower reservoir intervals are considered overpressured and severely overpressured ponded (fill) facies. The parameters in these figures are extremely valuable and are used extensively to calibrate the models to the subsurface data.

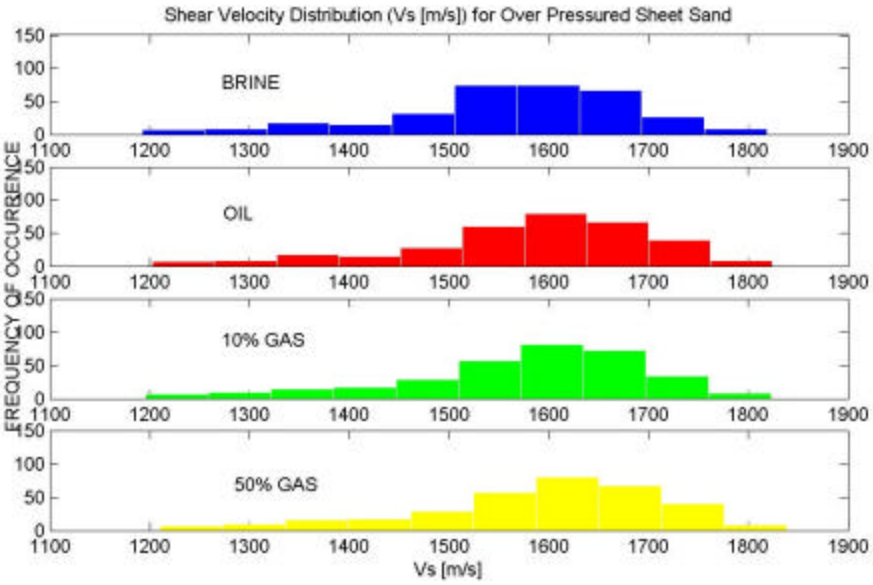

Figure 65. Histograms of frequency of occurrence of estimated shear velocities of overpressured sheet sands with varying fluid saturations of brine, oil, 10% gas and 50% gas. (Y-axes show frequency, x axes show shear wave velocity).

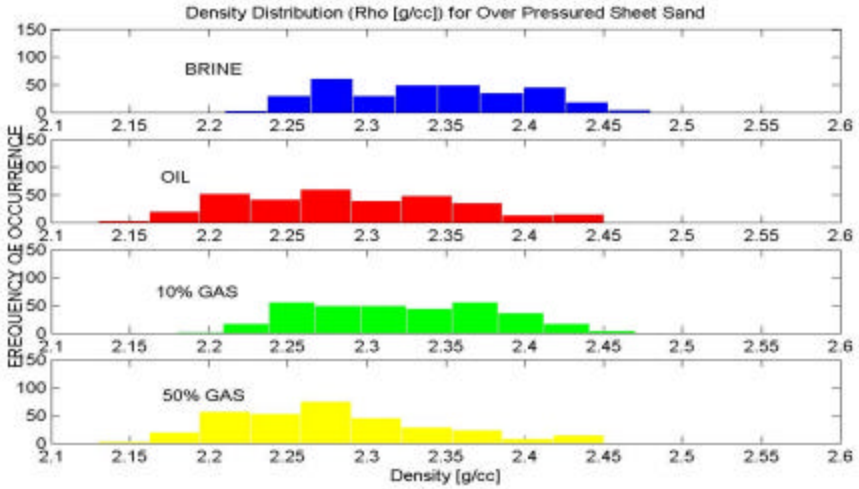

Figure 66. Histograms of frequency of occurrence of densities of overpressured sheet sands with varying fluid saturations of brine, oil, 10% gas and 50% gas. Y axes show frequency, x axes show shear wave velocity.

Mars-Ursa Intraslope Basin Shales in Ursa #1 Well								
RESERVOIR	FLUID THICKNESS [Ft] (Hilterman, 01)	Pressure [psi] (Meckel et al, 02)	STRATIGRAPHIC INTERP 4th order (Meckel et al, 02)	TOPS and Bottoms in Well#1 [MD-m]	Vp avg [m/s]	Vs avg [m/s]	Rho avg [g/cc]	Time [ms]
Upper (12000')	**GAS 37**	**N/A**	**Levee/overbank**	**3639-3652**	**2597.26**	**1151.55**	**2.26**	**4008-4018**
Lower (12460')	**OIL 19**	**N/A**	**Sheet Sand**	**3780-3786**	**2308.72**	**1348.53**	**2.23**	**4110-4131**
ABOVE MAGENTA	**OIL 55**	**2200**	**Amalgamated channel system**	**5108-5141**	**2840.06**	**1577.44**	**2.28**	**5231-5235**
MAGENTA	**BRINE**	**2200**	**Sheet Sand**	**5198-5214**	**3164.25**	**1684.86**	**2.38**	**5272-5282**
BELOW MAGENTA	**BRINE**	**2200**	**Sheet Sand**	**5233-5250**	**3197**	**1398**	**2.37**	**5294-5304**
LIME GREEN	**GAS 38**	**2200-3000**	**Non amalgamated channel**	**5258-5274**	**2664.8**	**1480.91**	**2.19**	**5309-5321**
UPPER YELLOW	**OIL 39**	**3900**	**Non amalgamated channel**	**5410-5432**	**3042.73**	**1622.24**	**2.30**	**5409-5423**
LOWER YELLOW	**OIL 167**	**3900**	**Sheet sand**	**5479-5542**	**2965.7**	**1595.35**	**2.26**	**5454-5496**

Table 4 Table shows some major reservoir intervals in Ursa well and data and interpretation associated with each one.

Relationship to outcrop analog

There are a variety of considerations to be taken into account when comparing the Brushy Canyon outcrops to the Ursa field data. The first main element is that the Brushy Canyon, is a sand rich depositional environment whereas the Gulf of Mexico sediments are mud rich. This causes extensive differences in lithology and cementation, which creates very different petrophysical parameters. Another key difference in the fact that the in the proximal basin setting, the Brushy Canyon sediments are confined in incised valleys and then sediments are carried into an unconfined basin setting. The build, cut, and fill, spill, models of the Brushy Canyon occur at small scales when channels fill and then are refilled. The Ursa basin is similar in that the salt sutures provide conduits that direct sediment flow into the basin, but once inside the basin the sediments enter another less confined setting provided by changes in topography due to presence of salt. The sediments are deflected off of topographic highs and fill-spill models are directed more towards these topographic highs and lows in the basin than in individual channels fill and spill. Nevertheless both systems allow channels to form in the basin or distal setting, which result in similar geometries. Likewise, the sheet sands and overbank elements also have similar geometries despite differences in setting. As mentioned before, there is never a perfect analog. However, Brushy Canyon geometries are still quite similar to what is found in the Ursa basin but with different modes of transport and varying lithologies associated with them.

This chapter summarized the information available for the Ursa field in the Mississippi Canyon, GOM. The location of the field and data available were discussed. Previous work done by Hilterman and Meckel were reviewed and integrated. In addition,

the pressure trends were analyzed, as were rock and fluid properties for brine and hydrocarbon saturated cases. Finally the Ursa field depositional setting was compared to the Brushy Canyon depositional setting to establish the commonalities between the two deepwater settings. These observations and reservoir properties are essential in developing geologically realistic models that will be discussed in the next chapter for forward modeling.

Forward modeling

Forward modeling was performed on six geologic models built to represent three different reservoir intervals. The first reservoir interval is the Lower yellow reservoir interval, which will have two geologic models; an amalgamated sheet sand and a basin floor channel system. The second reservoir to be modeled is the Above Magenta reservoir, which will be modeled with an amalgamated and non-amalgamated channel complex. Finally, the Upper reservoir interval will be modeled with proximal and distal levee overbank facies. These reservoir intervals were chosen because they can be associated with high amplitude events on seismic data and each one represents one of the three common reservoir facies mentioned above (sheet sand, channel fill and levee/overbank). Each of these six geologic models were saturated with brine, oil, 10% and 50% gas respectively. The models were calibrated with the Ursa reservoir fluid and rock properties. Forward modeling was performed using a simple convolution between the impedance volume and extracted wavelet was preformed on each model. Also, Amplitude Versus Offset (AVO) modeling using the Zoeppritz equation was preformed on one pseudo well for each model. A total of 24 separate 2D synthetic models and 24 AVO models were made, one for each reservoir facies and fluid case. For each reservoir interval that was modeled the two possible seismic facies interpretations were compared to determine if the lithology and fluids could be differentiated. This chapter will describe the method of developing the reservoir models and rock and fluid properties from the reservoir interval. This chapter will also give a general summary of the method used to develop each of the models and precedes the three chapters that will discuss each reservoir and its models and results in detail.

Example of forward modeling method

To generate the reservoir model, first the geologic model was created with an image file. This image was created as an 8-bit grayscale bitmap image which with a total of 256 possible colors associated with it where each color is represented by a number, black being 0 and white 255. The image is then scaled to the size of the reservoir by converting pixels to meters. This calibrated image is then output as a digital file using the United States National Institute of Health (NIH) imagej freeware (http://rsb.info.nih.gov/ij/). Each number/pixel represents a location in the reservoir model. Not every pixel was used to model the reservoir. Instead the model was sampled at 50 meter lateral spacing to match the Ursa seismic trace spacing. A matlab code (Appendix D) was written to sort the imajej output text file into columns that would eventually represent pseudo well logs spaced 50 m apart. Once these new 50-meter spaced bitmap pixel numbers were sorted, they were placed into an excel spreadsheet and converted to proper Vp, Vs, and density values associated with the reservoir interval being modeled. For all models, the horizontal scale was developed using the depositional history of the reservoir interval. The vertical scale was developed using the Ursa number

1 well log as a guide. The water column was assumed to have a Vp of 1500 m/s, Vs of 0 m/s and density of 1.03 g/cc. In populating the background overburden and underlying sediments, the depth and pressure trend were used as a guide as well as the original well log. Figures from Appendix E were used to calibrate the models to appropriate velocity and densities for brine, oil, 10% gas and 50% gas. This was done by comparing mean and mode values from calculated results of reservoir intervals and histograms. The histograms and cumulative distribution functions show the frequency of occurrence of a set of values and the probability that a certain velocity will occur. (Appendix E) Pseudo well logs were made for brine, oil, 10% and 50% Gas saturated reservoir intervals. The separate fluid cases of each model were sorted into pseudo well logs curves with a matlab code which can be found in Appendix F. For the Above Magenta and Lower Yellow reservoir models the actual well log was used for the background rock properties values. The pseudo well logs were then imported into Hampson Russell software for the forward modeling and AVO modeling. An example of one pseudo well log can be seen in figure 67. Each of the text files contains a Vp, Vs density and depth column.

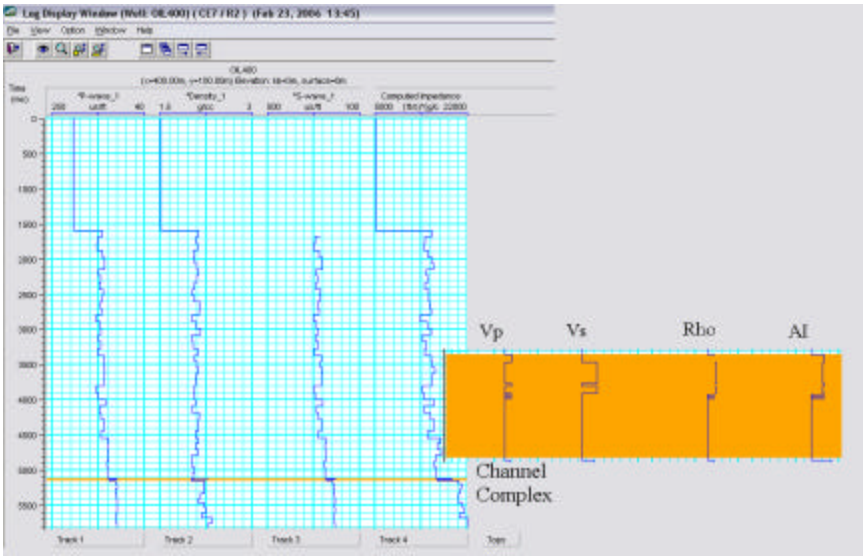

Figure 67. One pseudo well log displayed in Hampson Russell software used to create P-Impedance model. Vp, Vs, density and acoustic impedance are shown and an example of a channel complex model is highlighted in orange.

Once imported into Hampson-Russell the acoustic impedance of the pseudo logs can be calculated. This impedance is then convolved with a selected wavelet and results in a 2-D seismic section. Figure 68 shows the resulting P impedance model, which is the converted into a 2-D synthetic model using a simple convolution. For each reservoir, a wavelet was extracted statistically from the reservoir's time window and modified to reduce ringing and high frequency noise. These wavelets will be presented with their respective reservoir models. Figure 68 shows an impedance model that is convolved with a wavelet to result in a 2-D synthetic model and later compared with the seismic data.

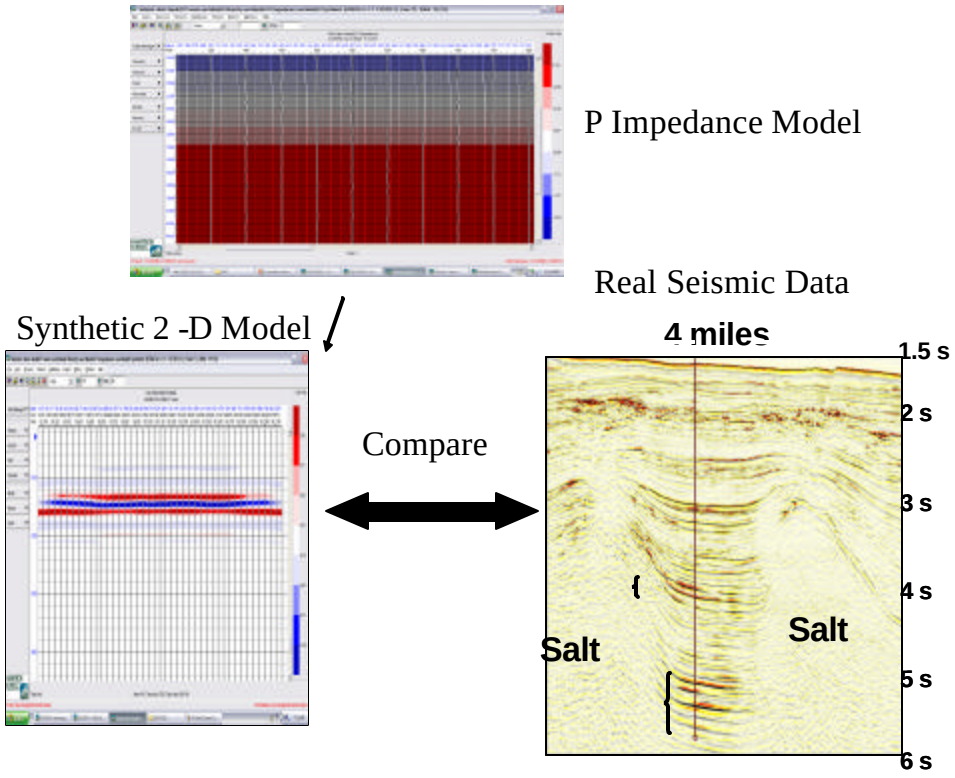

Figure 68. An example of the methodology used to perform forward modeling. Shows a P impedance section this is convolved with an extracted wavelet to get a 2-D synthetic model which, is then compared to the actual seismic data.

Test model

In order to understand the complex seismic response the first step was to model the simplest scenario of one reflector with changing the impedance and reservoir thickness. This gives information about the tuning point and also indicates which polarity will represent an increase or decrease in impedance. Figure 69 shows the results of decreased and increased impedance models. Here a 30 Hz ricker wavelet with a 50 ms wavelength was used. Wave interference due to tuning effects begins to occur at approximately 10 m thickness.

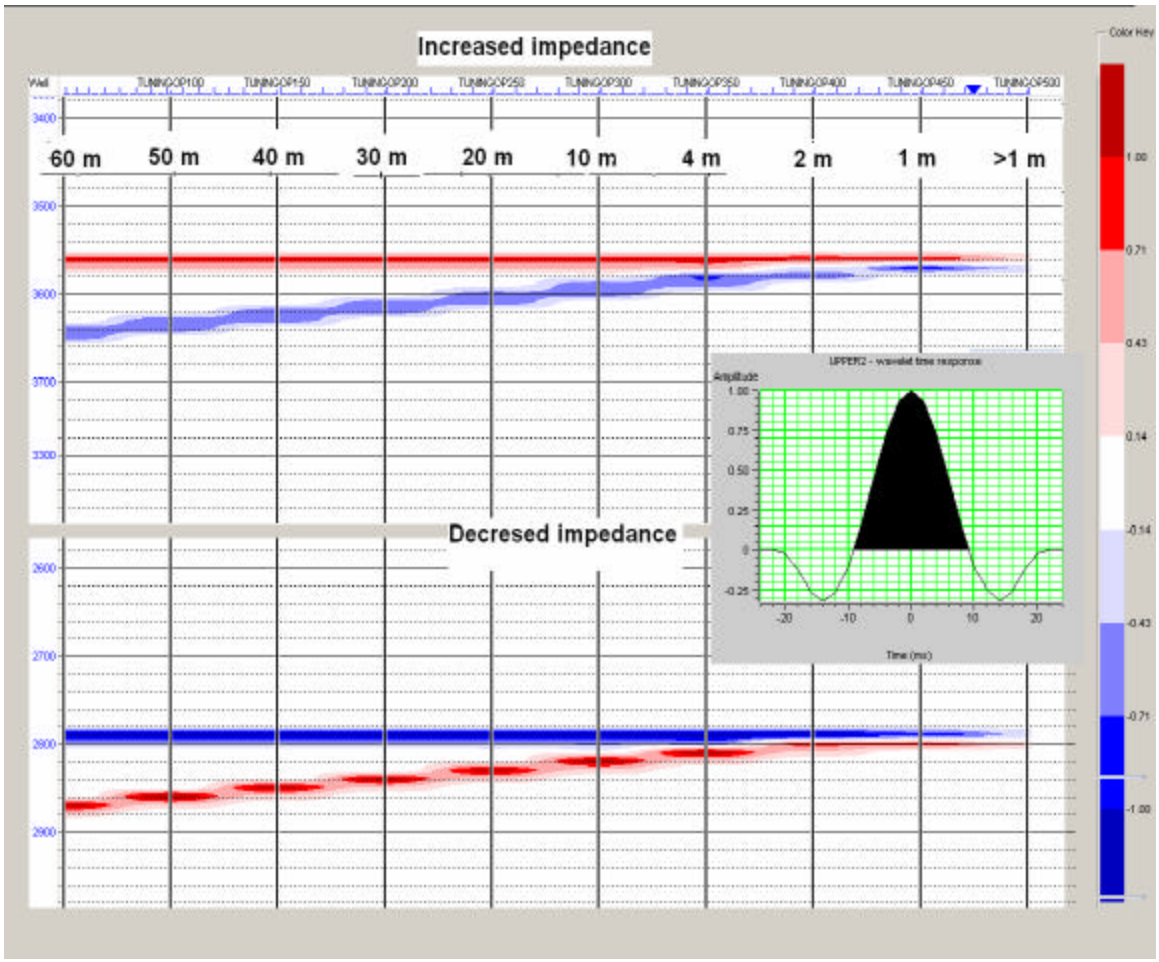

Figure 69. Increase in acoustic impedance results in a peak at the reservoir top. Decreased acoustic impedance results in a trough at the reservoir top. Tuning point occurs around 10 m thickness.

These results will help to interpret the results of the more complex models and verify if the model response is accurate. It is important to note that the tuning effects can be much more complex than simple tuning between the, top and base of the reservoir. Internal reservoir complexities can also cause complications with the tuning effect, which are beyond the scope of this study.

This chapter summarizes the method of building models and general forward modeling. The next three chapters will show three reservoirs representing three separate deepwater facies. Along with each reservoir will be two models that were developed with Brushy Canyon outcrop models, AVO models and the interpretation of the forward model results. Finally, these models will be compared to the actual Ursa seismic data.

Above Magenta reservoir model

The Above Magenta reservoir interval was interpreted to be an amalgamated channel (Hilterman, 2001, Meckel et al., 2001). Its log signature (Figure 70) shows a blocky fining upward gamma with flat base that changes over long distances. It has high resistivity indicating hydrocarbon presence and relatively high porosity. (Meckel, 2001)

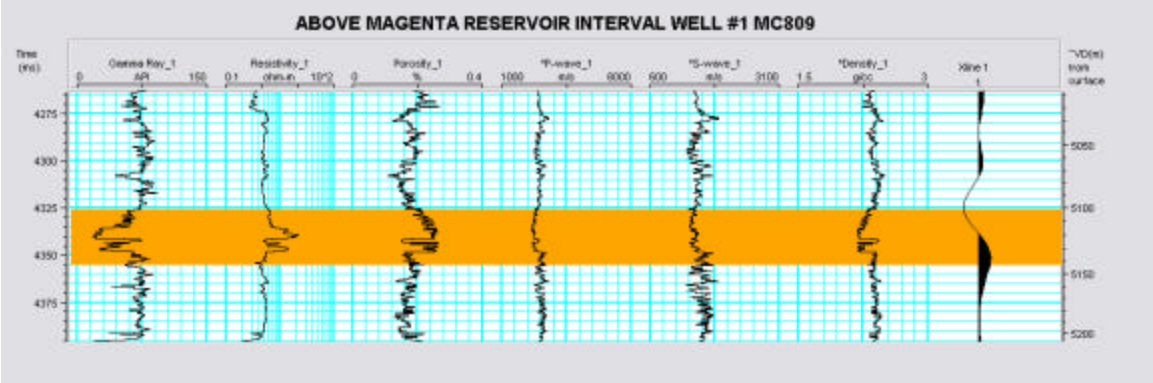

Figure 70. Wireline log of Ursa Above Magenta interval (orange) with gamma, resistivity, porosity, sonic, computed shear sonic, density and synthetic trace.

The seismic response of the Above Magenta reservoir interval can be seen in Figure 71 The reservoir top occurs as a strong trough. The reservoir is expressed as a shingled seismic geometry that converges along the 2-D seismic profile. According to Meckel (2001), the reservoir occurs as a sheet channel couplet in the continuous parallel facies. The prestack gathers in Figure 72 show a decrease in amplitude with offset.

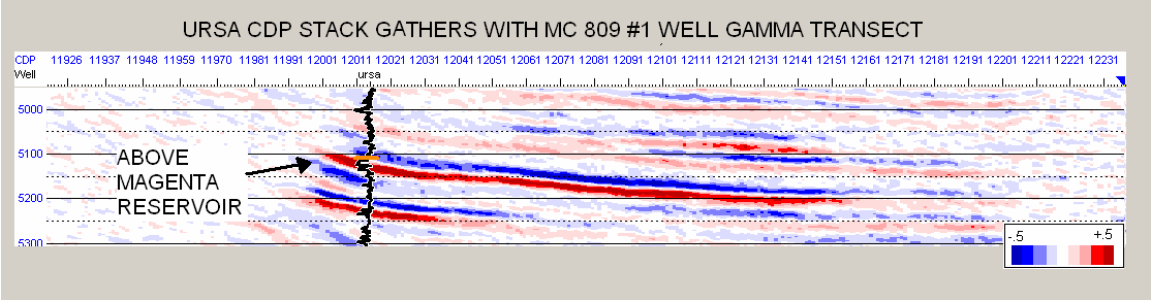

Figure 71. Above Magenta reservoir interval in seismic data.

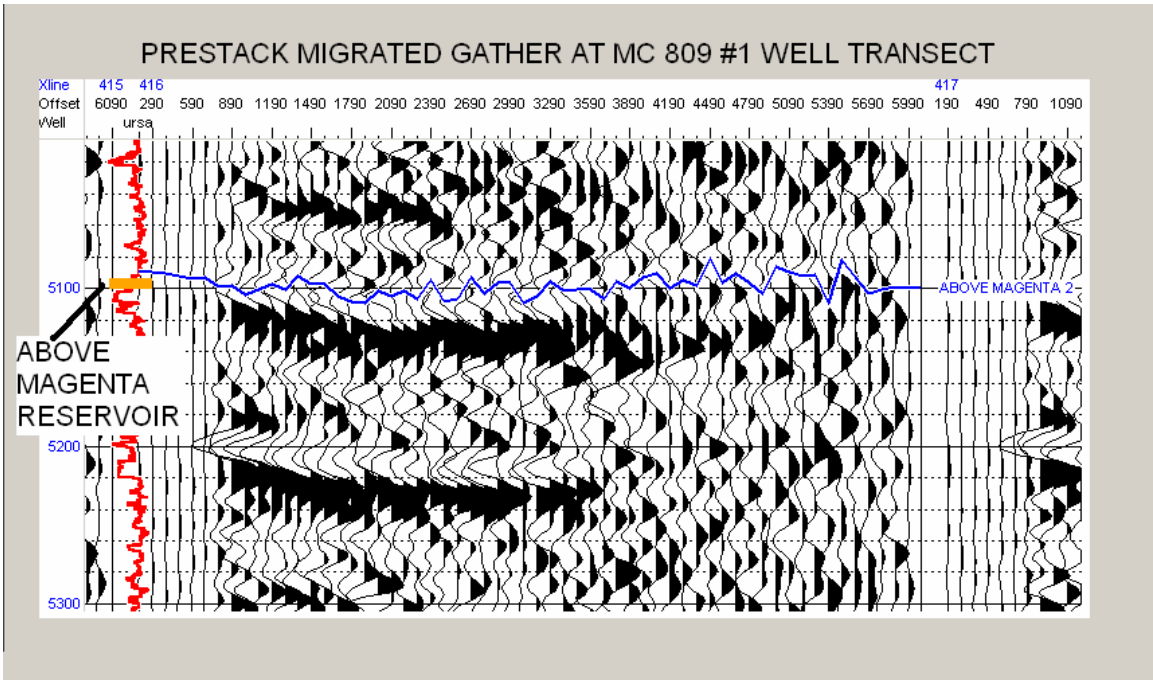

Figure 72. Prestack gathers for the Above Magenta reservoir interval. Here an amplitude decrease with offset occurs.

Figure 73 shows the extracted wavelet from the reservoir interval between the time window 5050-5200 ms. The new wavelet was designed to resemble the extracted wavelet and to remove the high frequency ringing that would cause wavelet interference and possibly unwanted artifacts in the forward modeling.

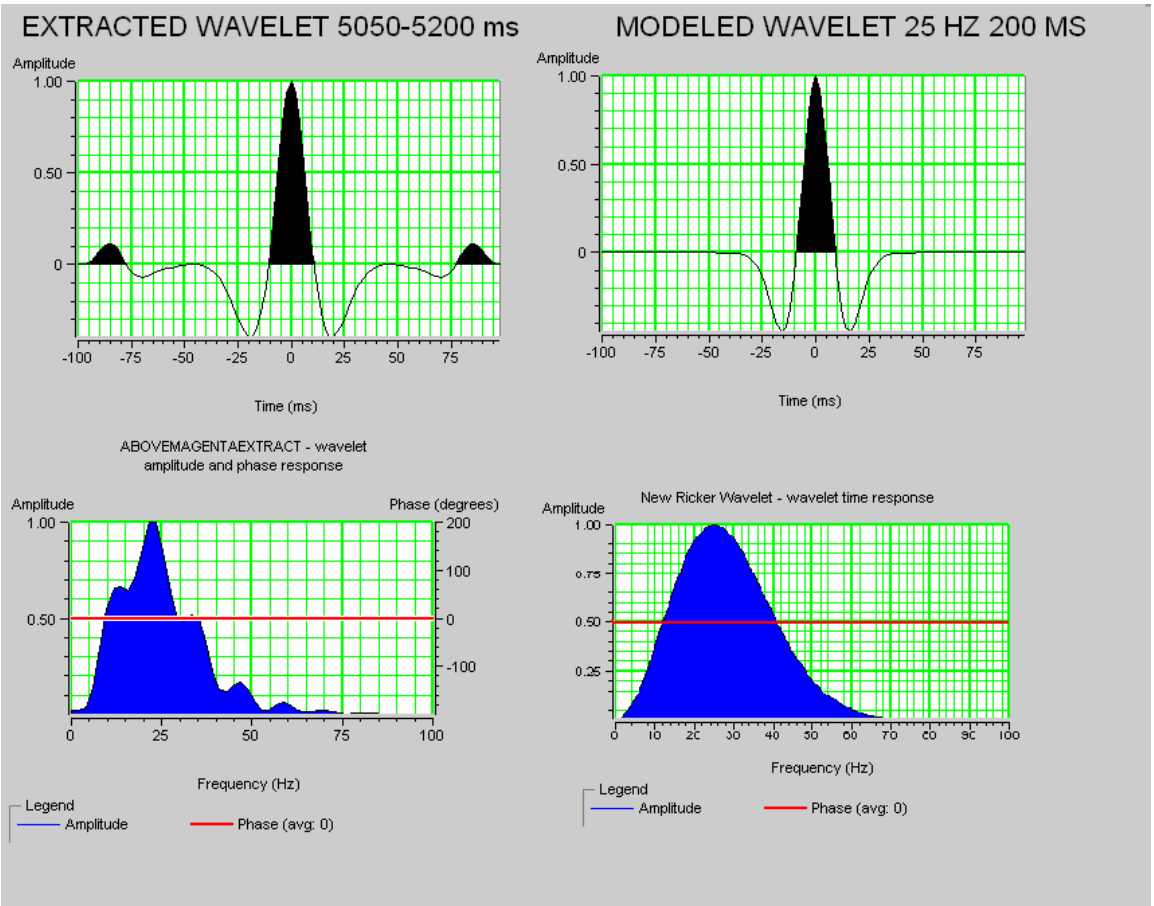

Figure 73. The extracted wavelet and the remodeled wavelet from the Above Magenta reservoir interval . The model wavelet is 25 Hz and 200 ms wavelength.

Figure 74 shows the results of fluid substitution on the interval and the synthetic repose of brine, oil, 10% gas and 50% gas. The oil and 50% gas cases result in the larger amplitude change with offset.

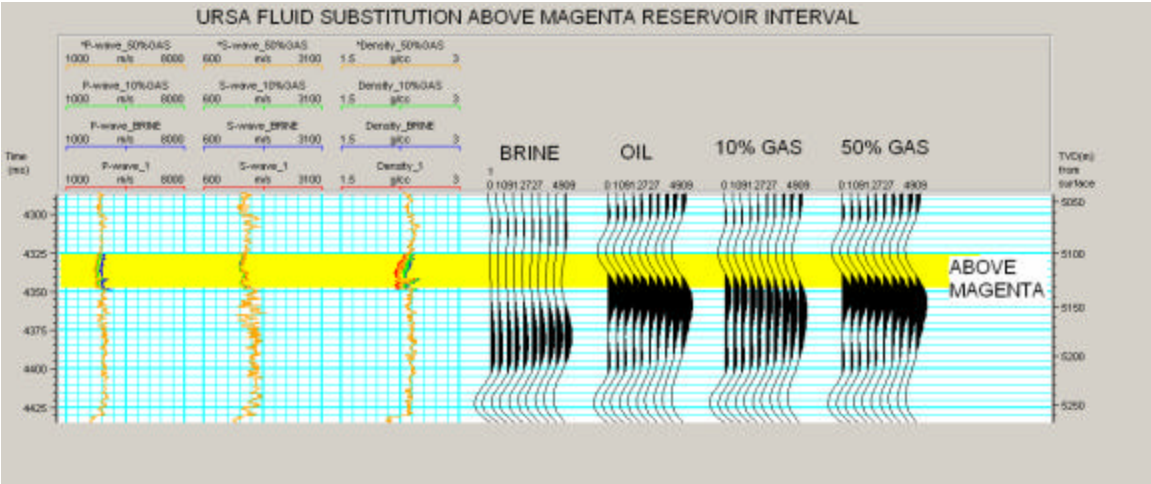

Figure 74. Figure 75 Fluid substitution on the Above Magenta interval Ursa #1 well showing brine, oil, 10% and 50% gas response and Zoeppritz modeled AVO with the extracted seismic wavelet and 6000 m offset.

Two-dimensional channel models

Channels can be problematic because they have fluid compartments that can be isolated or connected to each other laterally or connected downdip in the basin to sheet sands. Also vertical stacking patterns, channel lobe transition zones and terminations against levees can be features that impact fluid flow and compartmentalization. These features can be either beneficial or detrimental in reservoir production. The Above Magenta reservoir was originally interpreted as an amalgamated channel, but the gamma shows a shale break in the mid reservoir that may indicate a possible transition to sheet sand, or a misinterpreted interval that indicate a non-amalgamated channel system. Many times the hemipelagic sediments that cause compartmentalization can be sub-seismic in resolution. Two models used for this reservoir were developed to represent the differences in heterogeneities that occur in channel facies mainly associated with compartmentalization caused by hemipelagic sediments or drape.

Channel complex model 1

The channel complex model in Figure 75 shows a system of amalgamated channel sands with isolated channel sand compartments (gray) separated by drape or hemipelagic suspension fallout (dark gray). The black represents sheet sand; white is where the fluid substitutions were performed and the dark green is the background, which was created from the original wireline sonic and density logs. The actual reservoir model is scaled to be the same size as the Above Magenta reservoir, which has dimensions of 2000 m by 32 m at 5108 m depth.

The dimensions of the reservoir were modeled across the basin for 2000 m and the reservoir thickness was 32 m. Pseudo wells were spaced every 50 m starting at 0-2000 m. In this first model (Figure 76), the channels are non-amalgamated and some are stacked. The input values for the rock properties in the pseudo wells can be seen in Appendix E. Velocities were calibrated to Vp/Vs ratios to yield more accurate results. Figure 77 shows the forward models of the channel complex 1 from brine, oil, 10% gas

saturation and 50% gas saturation. The yellow line identifies the reservoir model top. In the brine-saturated model, subtle changes in the seismic response occur between wells 200-500, 900-1100 and 1350-1650. The reservoir top occurs at a peak when brine saturated and trough when saturated with oil, 10% and 50% gas. The fluid saturated compartment becomes brighter when hydrocarbons are present the brightest occurs with oil and 50% gas content. More information can be obtained from figure 78, which shows the synthetic AVO response for each case. The AVO models were run on the 500 m well that intersects the fluid saturated interval. As expected, the brine case has a very weak and almost no amplitude reflection but dims with offset, while the oil and gas zones show a strong trough with decreasing amplitude associated with the reservoir top. The fluid compartment is well imaged with respect to the other compartments.

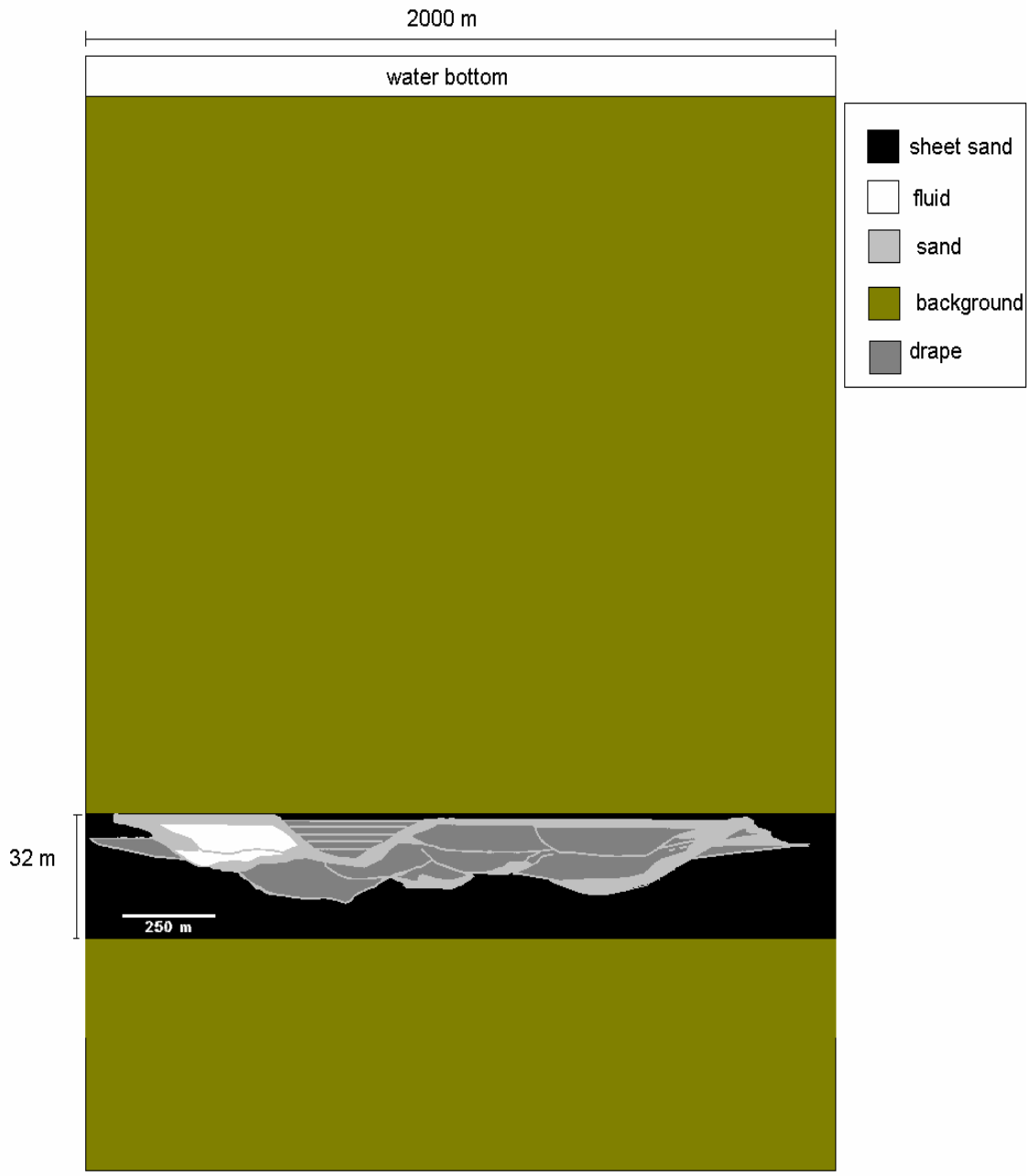

Figure 76. Channel complex model 1 shows the modeled reservoir interval with dimensions 2000 m by 32 m at 5108 m depth. The reservoir model is vertically exaggerated to display model detail.

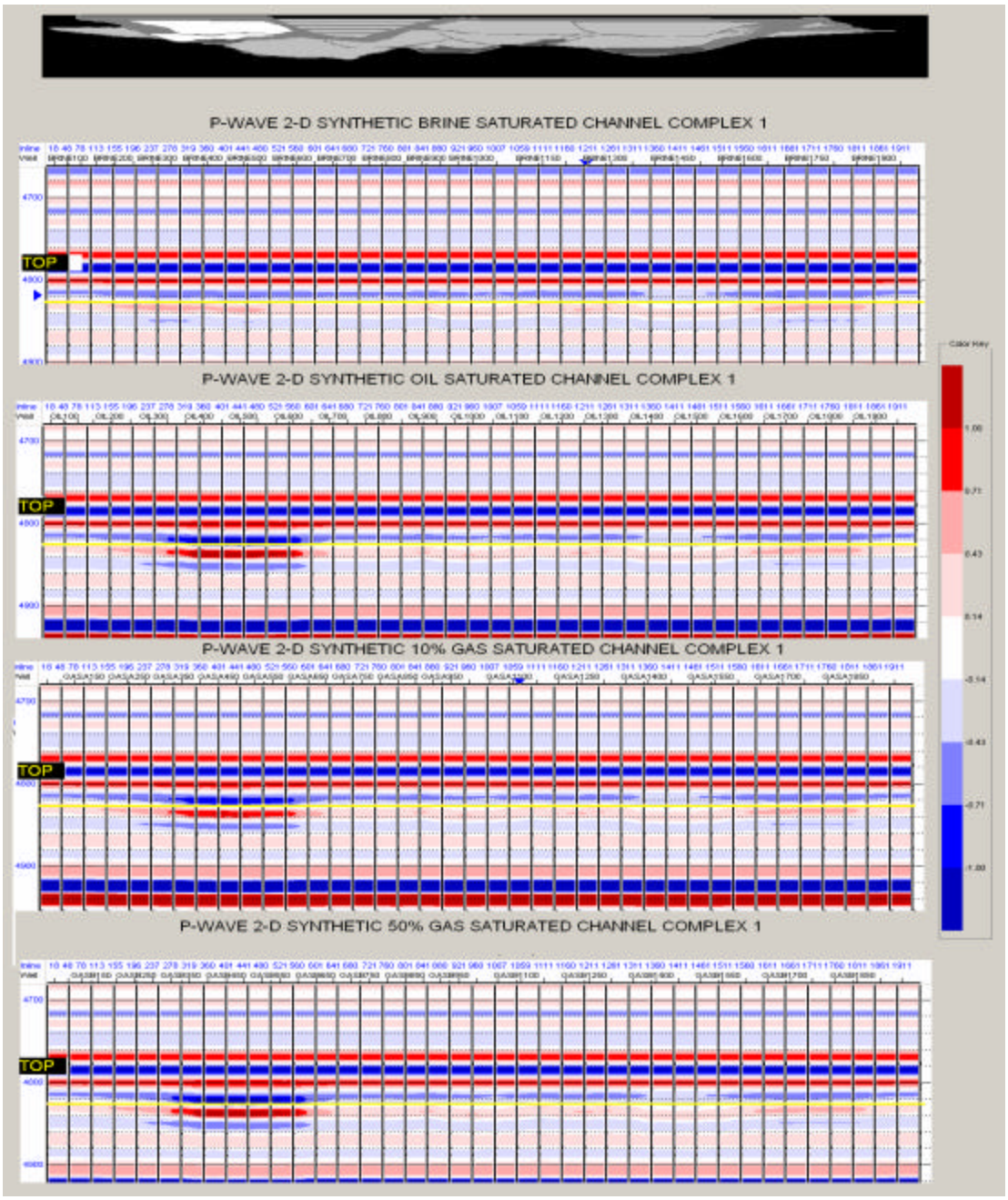

Figure 77. The amalgamated channel system fluid saturated model. Calibrated to the Above Magenta reservoir properties and populated with water column and background velocity and density data as well as fluid saturated data in red.

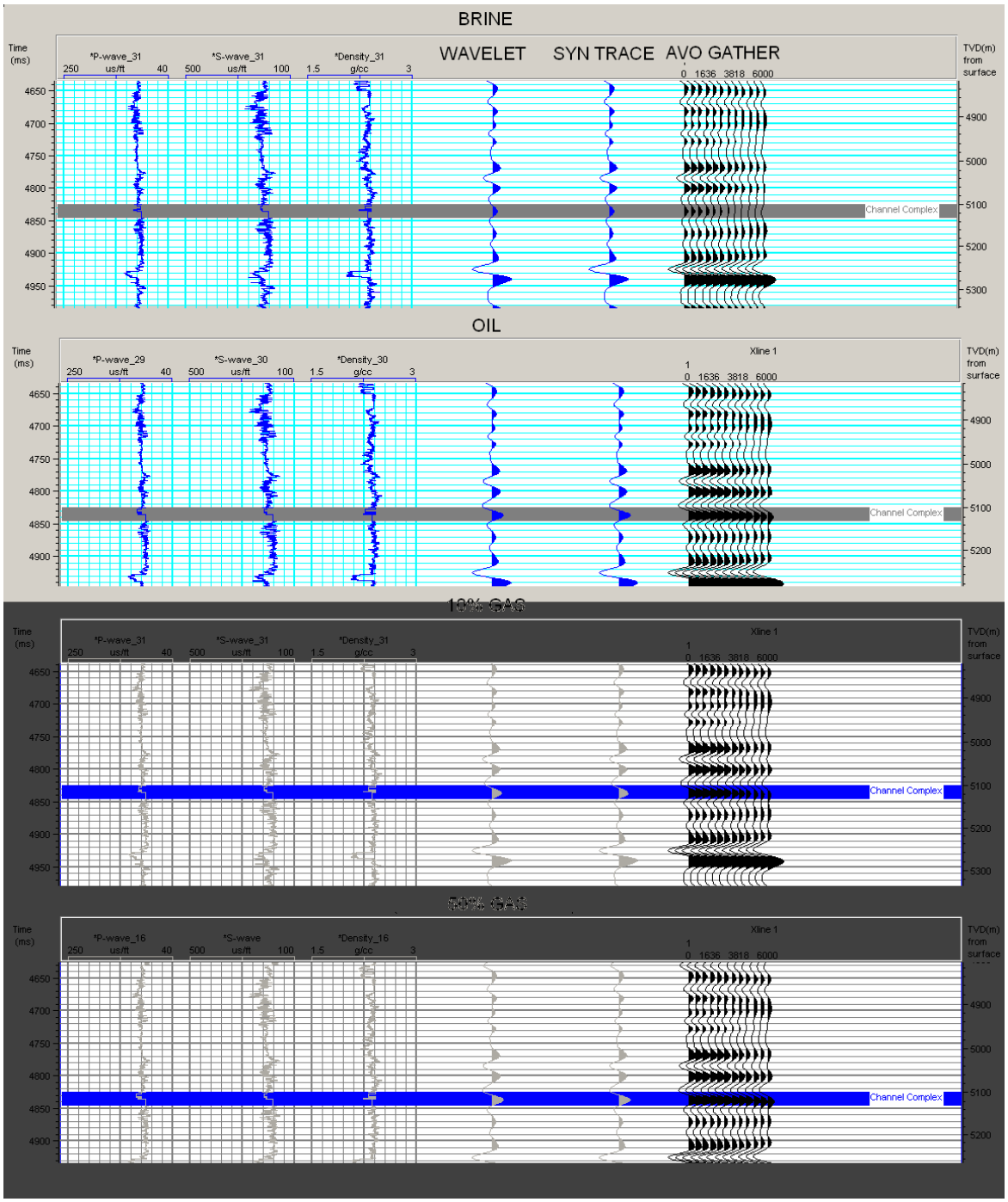

Figure 78. Stack and gather AVO response of well 500 for brine, oil 10% and 50% gas saturated reservoir models.

Channel complex 2

The channel complex 2 model is shown in Figure 79. This model is almost identical to the channel complex 1 model; except that some of the fine-grained hemipelagic sediment boundaries have been removed from the original fluid compartment.

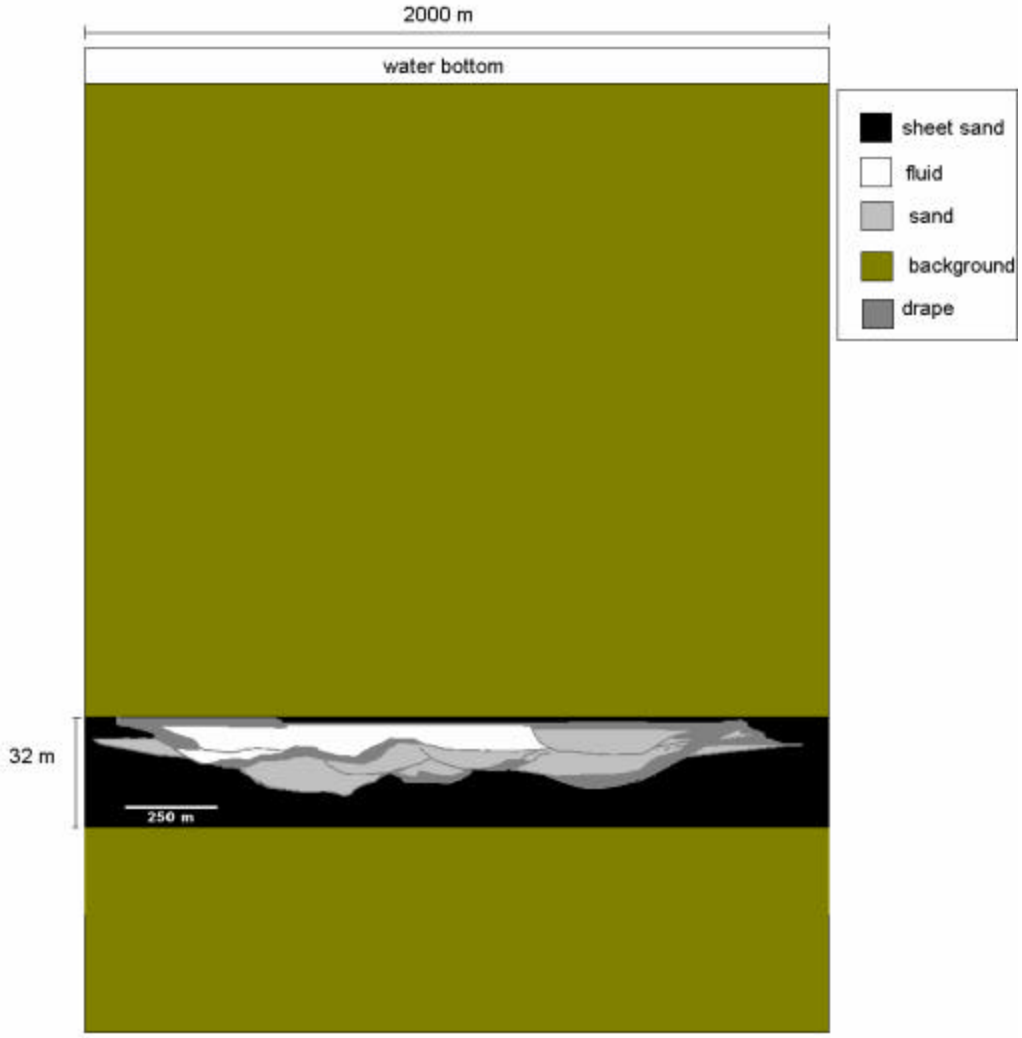

Figure 79. Channel complex model 2 shows the modeled reservoir interval with dimensions 2000 m by 32 m at 5102 m depth. The reservoir model is vertically exaggerated to display model detail.

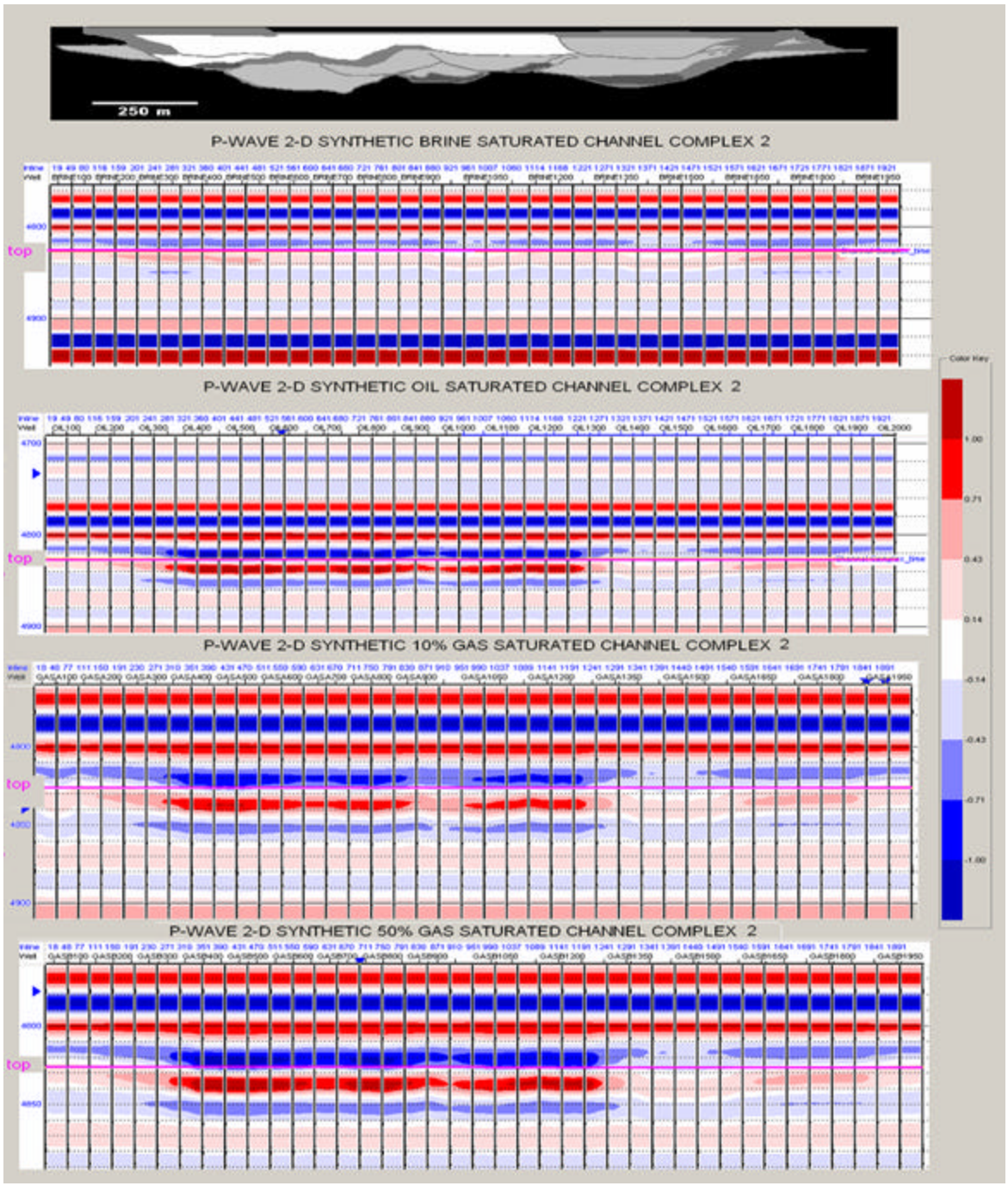

Figure 80. 2-D synthetic P-wave models for brine, oil, 10% and 50% gas. Tops are highlighted in magenta.

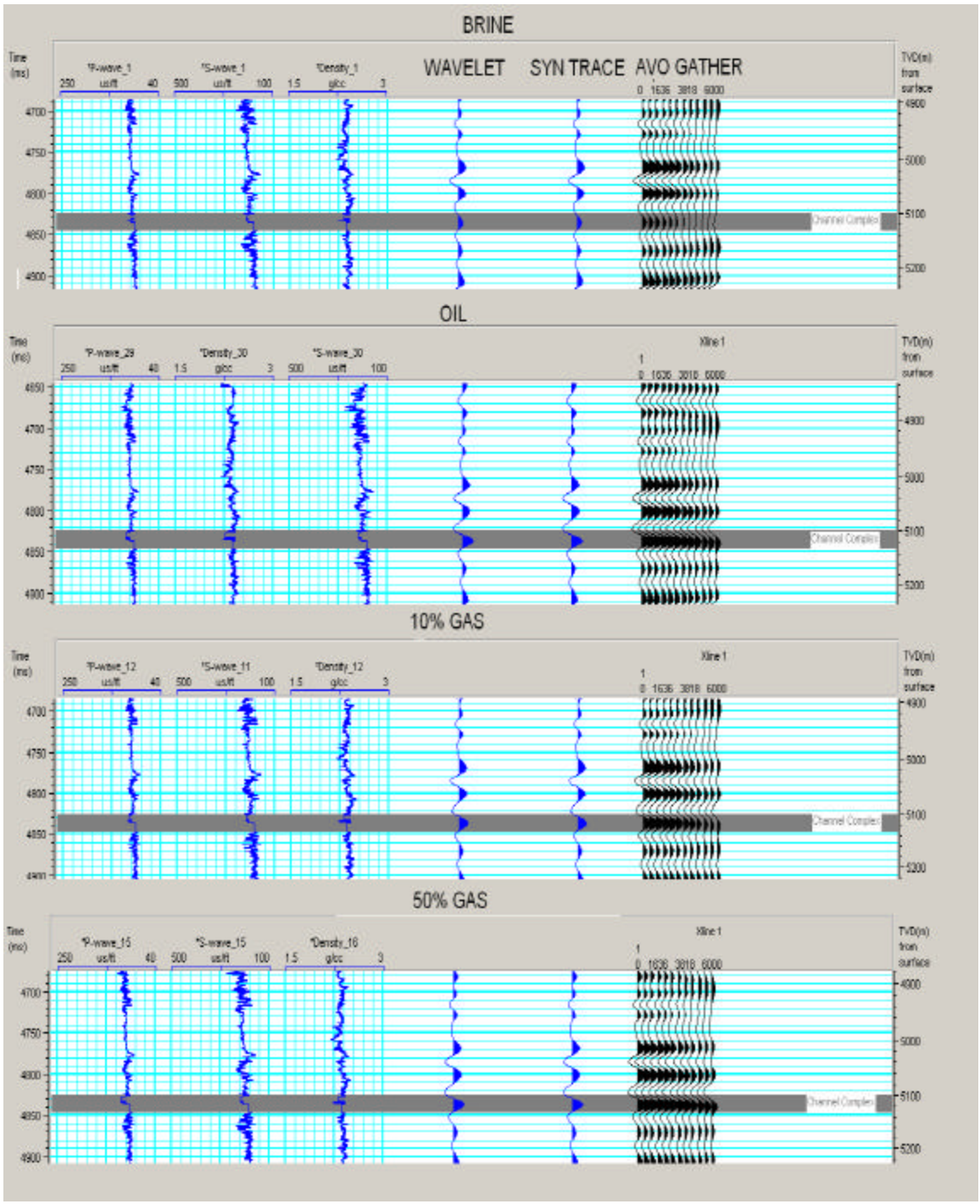

Figure 81. AVO stack and gathers for brine, oil, 10% gas and 50% gas saturated reservoir model.

The channel complex 2 has the same dimensions, rock properties and depth as channel complex 1. The 2-D synthetic brine model in Figure 80 appears to have little to no change, but some of the prominent channels in the model appear to impact the amplitude slightly. When the reservoir is saturated with hydrocarbons, the seismic signature

associated with the channel feature becomes pronounced. Figure 81 shows the pseudo well logs, wavelet and synthetic trace as well as Zoeppritz modeled AVO response for the fluid intervals. The AVO response for the brine case is a small trough, which decreases to no trough or peak. The hydrocarbon saturated reservoir cases show troughs associated with the reservoir top that decrease with offset. The oil and 50% gas fluid phases appear to have the strongest impact on the seismic amplitudes. Observations of these models show that the channel fill compartments can be imaged even if they are brine saturated. Connected amalgamated channel bodies produce a more continuous signature than that of a non-amalgamated channel body represented by an isolated channel model. But the details of where the fluid barriers occur cannot be accurately defined. Stratigraphic pinch-outs can be imaged but not clearly defined due to tuning effects (thickness < ¼ wavelength). These features may be resolved by using higher frequency wavelets.

Lower Yellow reservoir character

The Lower Yellow reservoir interval was originally interpreted to be sheet sand (Hilterman, 2001, Meckel et al., 2001). The Lower Yellow Sand is rectangular in shape and has dimensions of ~3.2-4.8 km (Weimer et al., 2004). The sand is 15-18 m thick with an estimated aspect ratio 250:1. It produced 62 BOPD and 62 MCFGPD from six wells in 2002 (Weimer et al., 2004). The Lower Yellow reservoir was interpreted to have a channel cutting through it connecting the two reservoirs. Sheet sands are deposited from decelerating flows at the termini of channels. Therefore, one major problem with the interpretation is that it is difficult to distinguish between sheet sands and channel deposits. They have good continuity and connectivity, high aspect ratios, and high permeability and porosity. One possible property to differentiate the two is aspect ratio because it is much higher for channel sands. The contact between sheets and channel sands is transitional, which puts sheets in connection with channels updip and has potential for fluid migration in the reservoir. (Weimer et. al, 2004) Another challenge associated with sheet sands is differentiating amalgamated (non-layered) from non-amalgamated (layered) sand. Moving downdip, a transition from amalgamated to non-amalgamated sheets often occurs. The log signature (Figure 81) has a sharp base and top and has a blocky to serrate pattern, which is consistent with the character of sheet sands in Weimer (2004). Generally the seismic signature of a sheet sand is expressed by one single seismic event. The seismic signature (Figure 82) shows good continuity with little change in the wavelet. Interplay of different stacking patterns can result in different seismic signatures. In the intraslope basin setting the reflections tend to thin out or lap out against another surface. The AVO response in figure 83 shows a decrease in amplitude with offset.

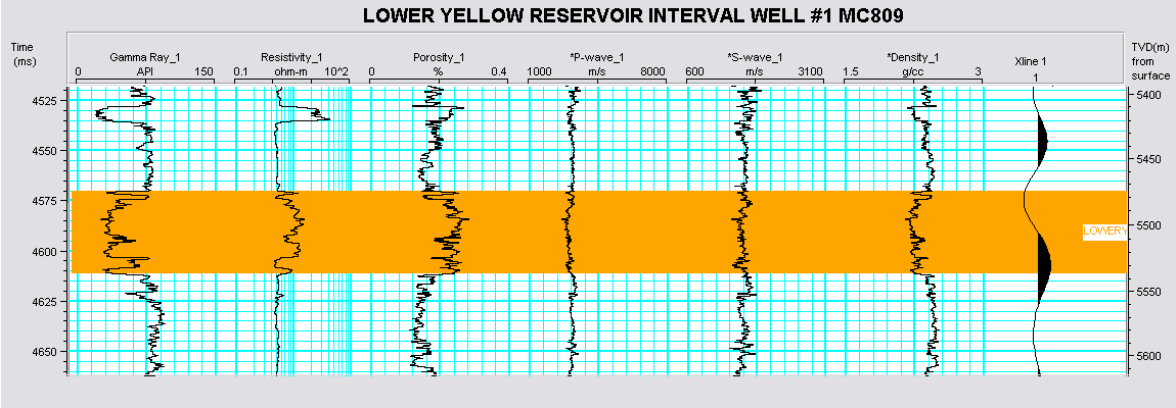

Figure 82. Log signature includes gamma, resistivity, porosity, P-wave, s-wave and density as well as synthetic seismic stacked AVO response using Zoeppritz modeling with a 6000 m offset. Gamma shows blocky serrated signature with sharp top and base contacts.

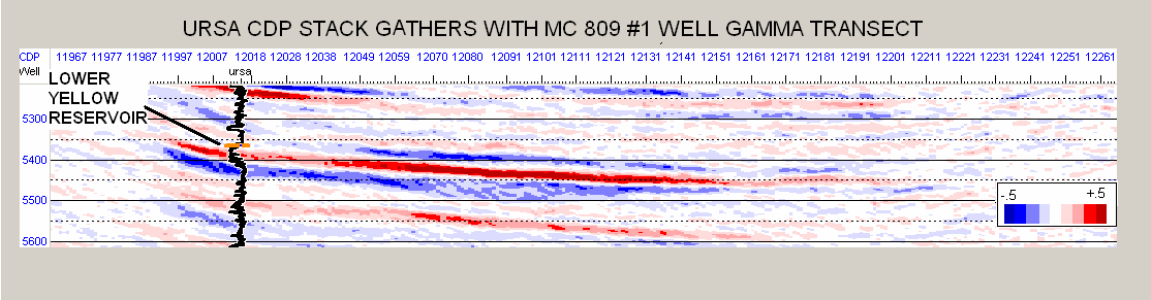

Figure 83. Seismic response of the Lower Yellow reservoir interval shows the reservoir top corresponding with the trough of the wavelet in post stack data.

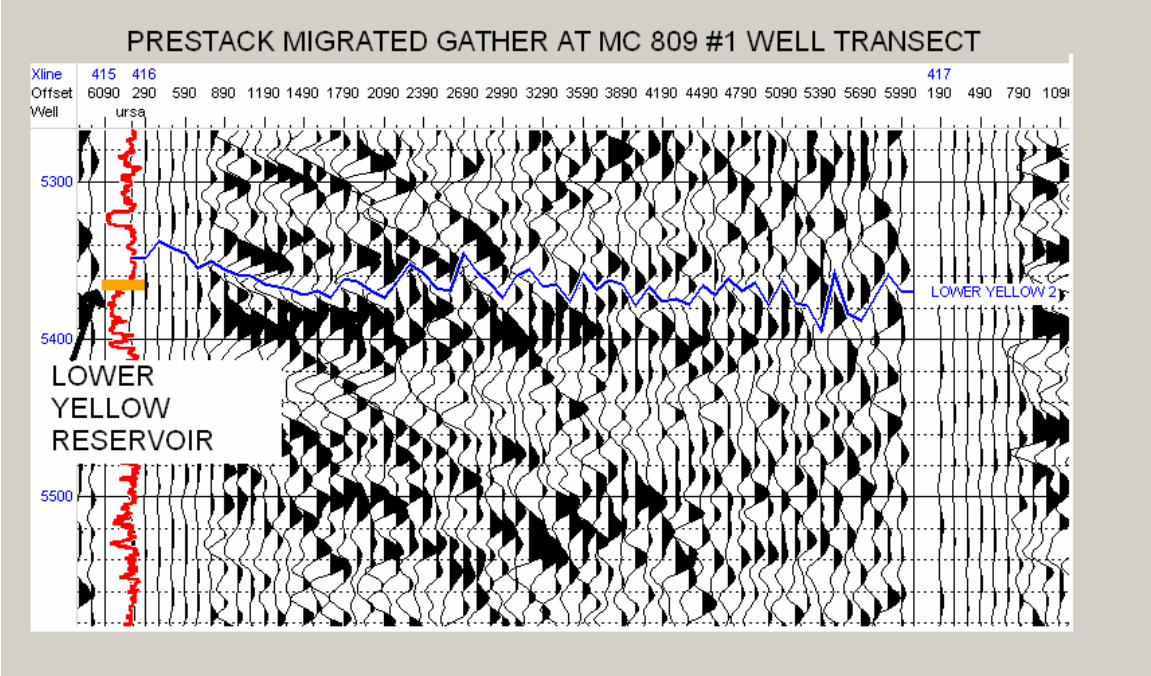

Figure 84. Although difficult to read, the amplitude response of the reservoir top appears to slightly decrease with offset at the well transect.

Figure 85 shows the extracted wavelet and modeled wavelet. The modeled wavelet was made after the extracted wavelet, which was statistically extracted from the 5000-6000 m depth. The new wavelet was a 13 Hz, zero phase wavelet that has a 150 ms wavelength. The fluid substitutions were performed with Hampson Russell software and the assumed initial oil saturated interval was then back saturated to brine. The brine interval was then re-saturated with 10% Gas and 50 % Gas; the remaining 90% and 50% was brine. The fluid AVO response shows a peak for the brine saturated case and trough for oil, 10% and 50% gas case. The modeled wavelet was a zero phase Ricker wavelet of 13 Hz in frequency and 150 ms wavelength. The results from the fluid substitution can be seen in Figure 86.

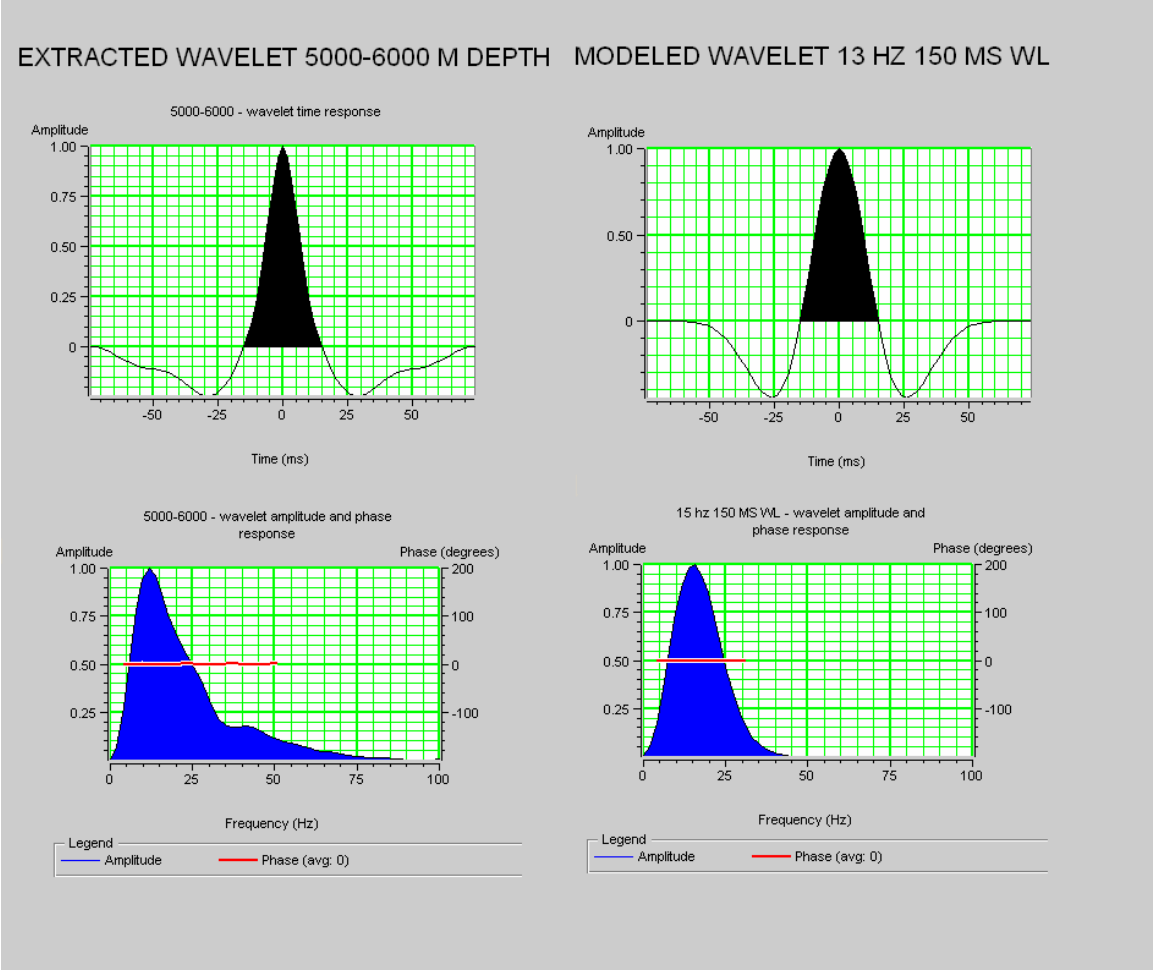

Figure 85. Extracted wavelet and modeled wavelet 15 Hz 150 ms wavelength.

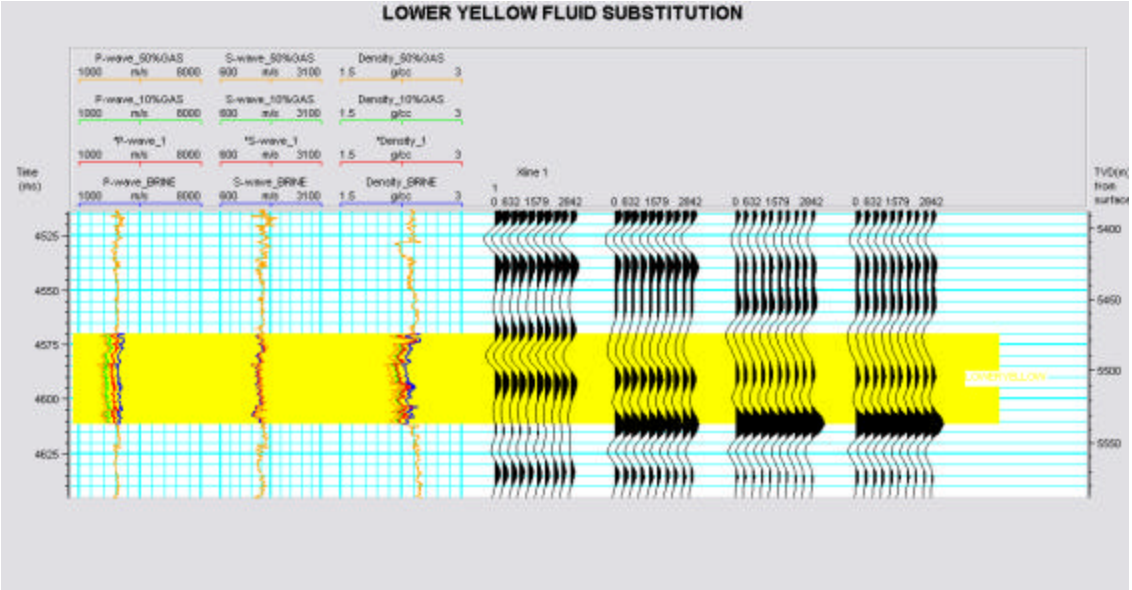

Figure 86. Zoeppritz modeled response for Brine, Oil 10% and 50% gas saturated reservoir intervals respectively.

Two-dimensional models

Two different models were used to compare two different interpretations of the Lower Yellow reservoir interval. The reservoir is in a distal position relative to the sediment source, therefore it is compared to the distal deposits in the unconfined basin setting in the Brushy where the transition of channel sands to sheets sands occur at channel termini. The problem with sheet sands and channel sands is that they can be hard to identify because channels transition into sheet sands as they move downdip into the basin. Therefore two possible interpretations could be made of the Lower Yellow reservoir interval. The other possible interpretation, which, is a channel sand, will be modeled after the Brushy Canyon distal channel seen in Figure 3.11. The next two sections will display the models used to interpret the Lower Yellow reservoir interval.

Amalgamated sheet sand model

The amalgamated sheet sand model can be seen in Figure 87. This model has a relatively continuous expression and is also fairly homogeneous internally. Figures 88 and 89 show the results of the forward modeling.

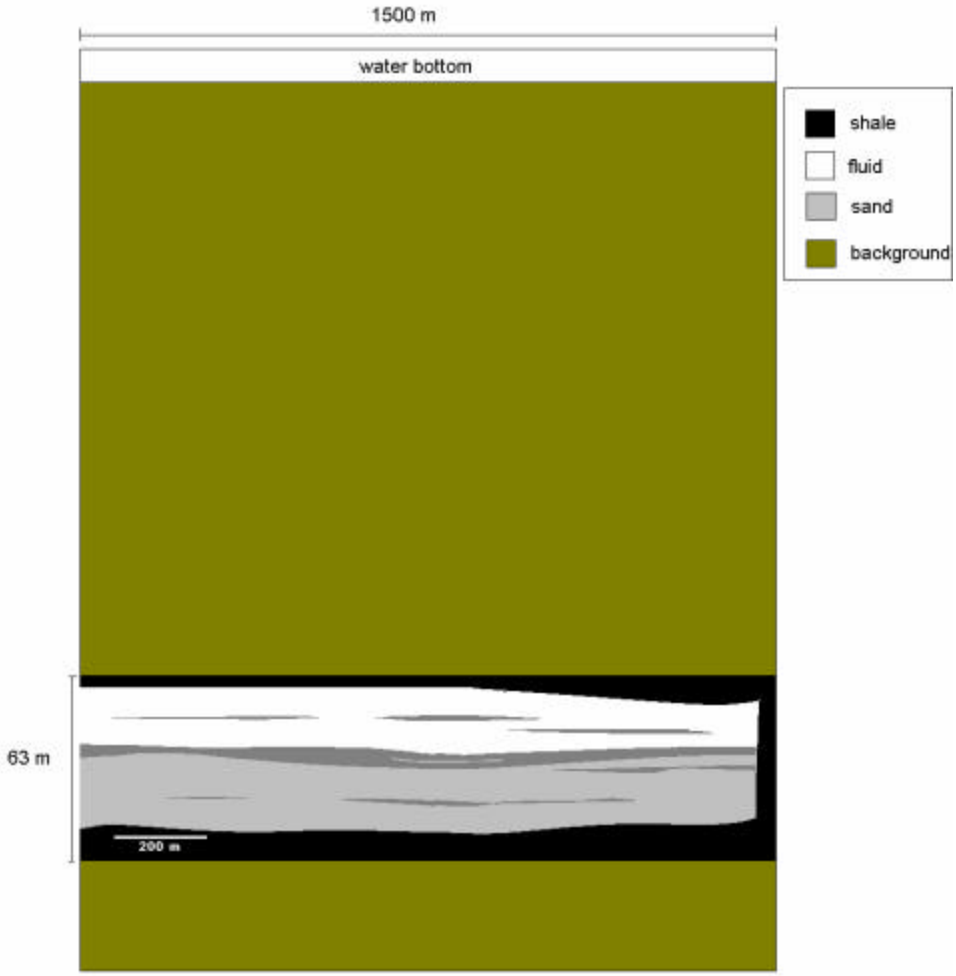

Figure 87. Amalgamated sheet sand model shows relatively continuous and homogeneous geology. The modeled reservoir interval has dimensions 1500 m by 63 m at 5479 m depth. The reservoir model is vertically exaggerated to display model detail.

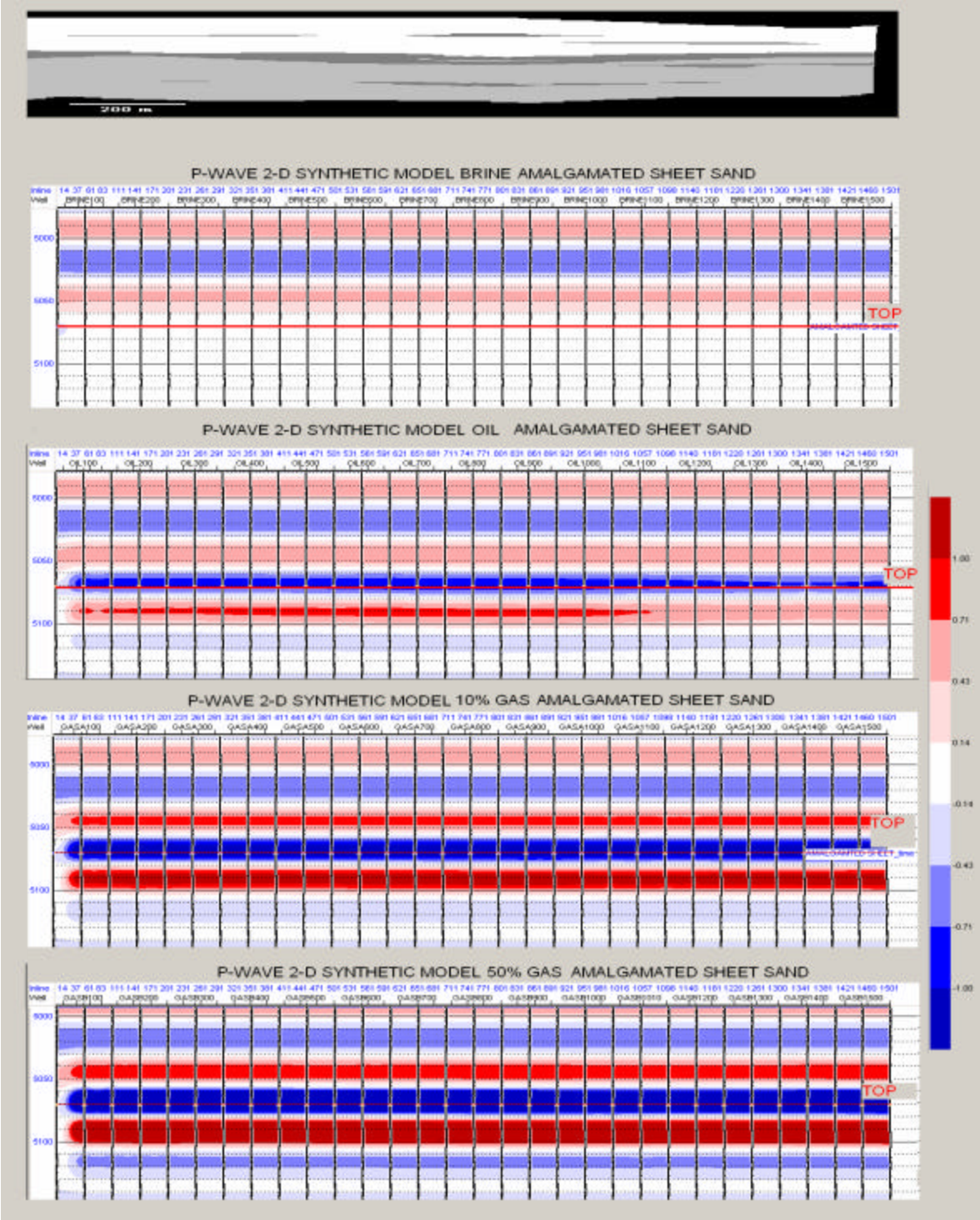

Figure 88. 2-D synthetic p-wave response for brine, oil, 10% gas and 50% gas.

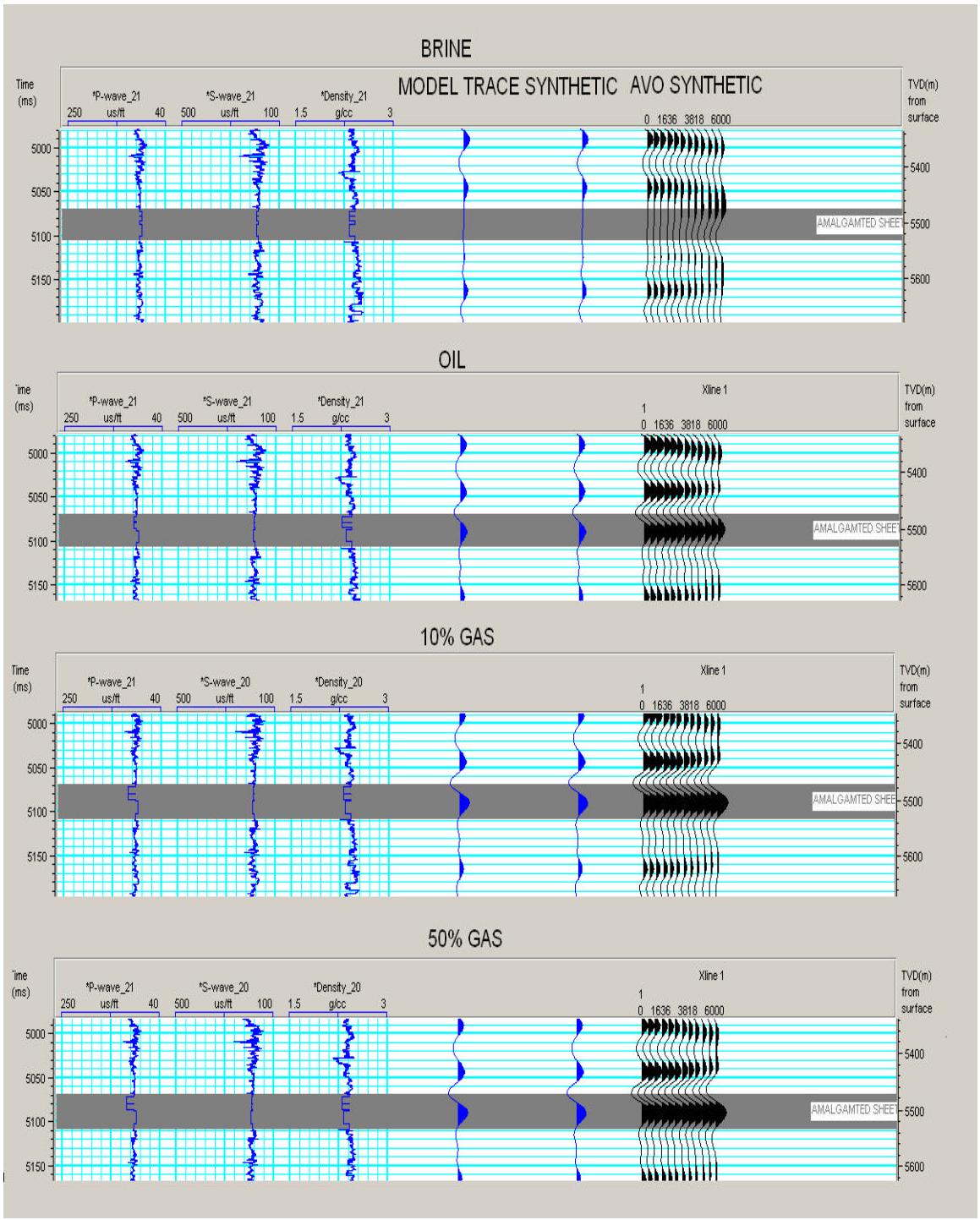

Figure 89. Pseudo logs, wavelet, synthetic trace and Zoeppritz modeled AVO.

The seismic models show a continuous and fairly homogeneous event until the sheet sand begins to thin to the right. The 50% gas appears to have the strongest amplitude response on the synthetic 2-D profile. The AVO response shows a relatively neutral response to the brine-saturated reservoir, while for the oil and gas cases there are significantly bright amplitude anomalies that decrease in amplitude with offset.

Basin floor channels

The channel sand model can be seen in Figure 90. This model has high net-to- gross channel sands. The channel sand forward models in Figures 91 and 92 show that there is little to no change in the seismic response when the channel sands are brine saturated; when saturated with fluids, subtle features change in the response but they don't seem to correlate to lithologic boundaries as much as the proximal channels. The AVO response is relatively neutral for the brine case. For the oil, 10% and 50% gas cases the reservoir top corresponds with a trough that in each case decreases with offset. The 50% gas case has the strongest amplitude anomaly associated with it.

Conclusions

The amalgamated sheet sands and channel sands are very hard to differentiate from each other in the seismic expression except, the channel sands seem to be slightly more undulating than the sheet sand expression. The best way to differentiate channel sands from sheet sands is to connect well log expressions of the reservoir interval. If they are continuous over long distances, they are most likely sheet sands.

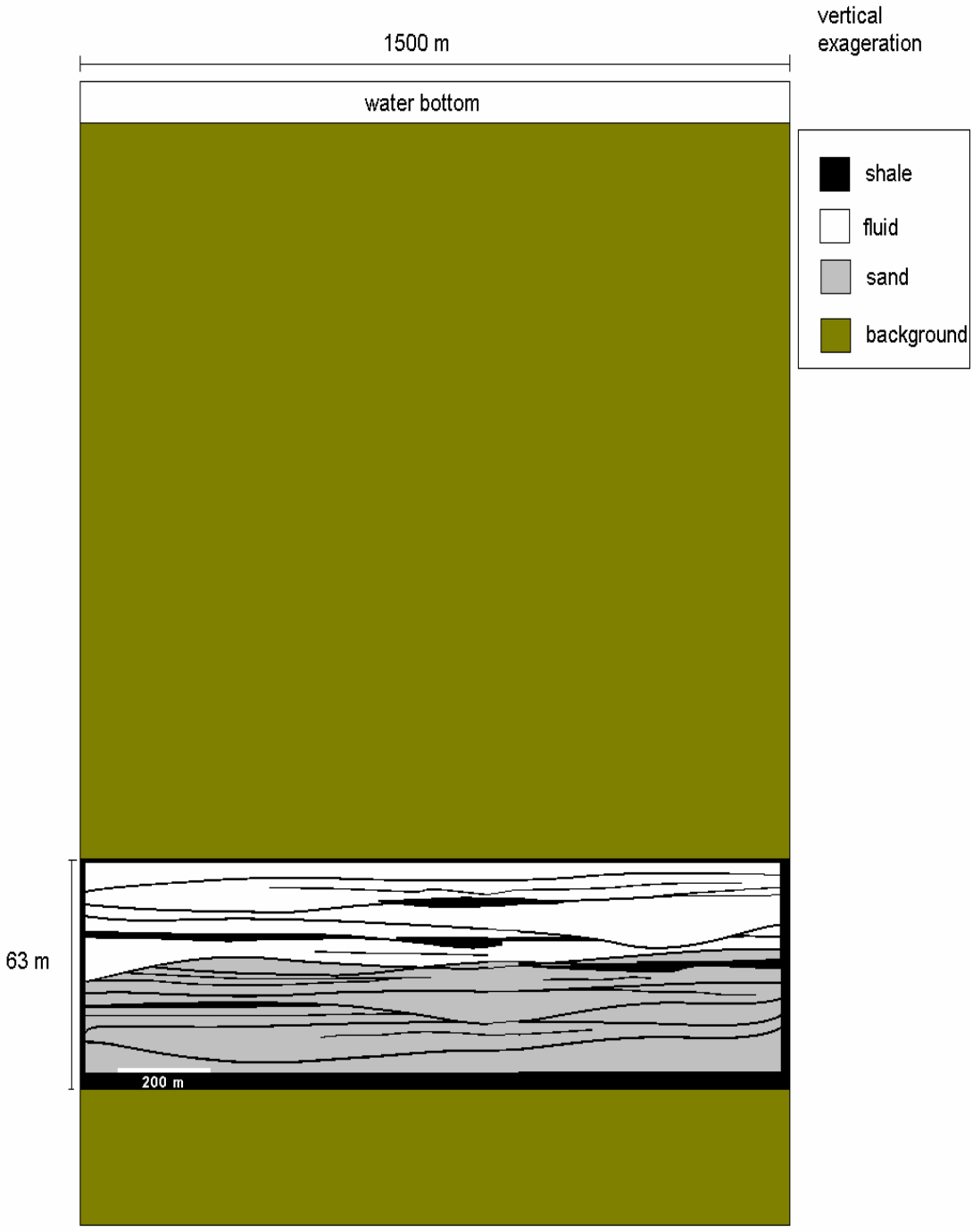

Figure 90. Medial basin floor channel sands.

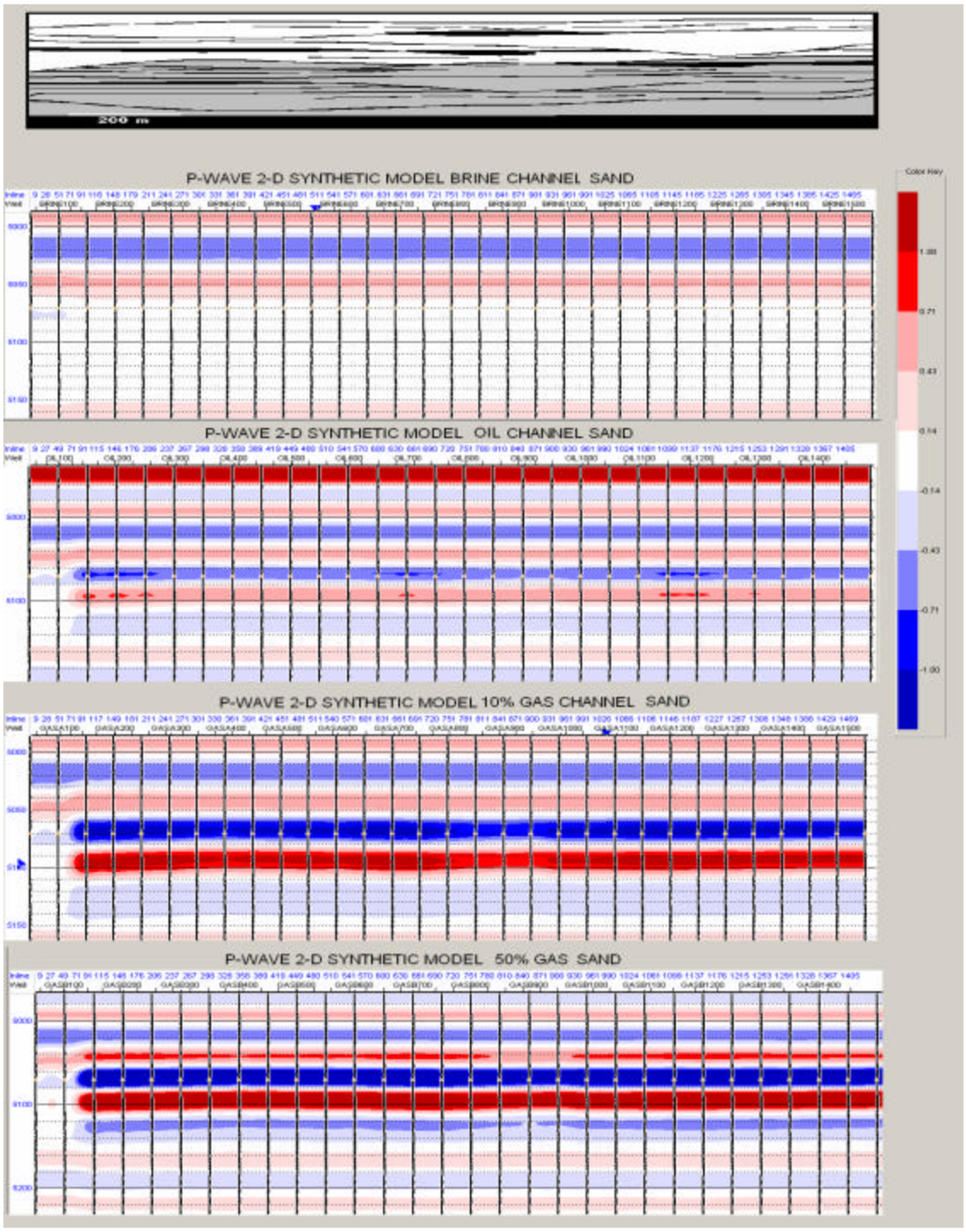

Figure 91. 2-D P-wave synthetic of the channel sand model.

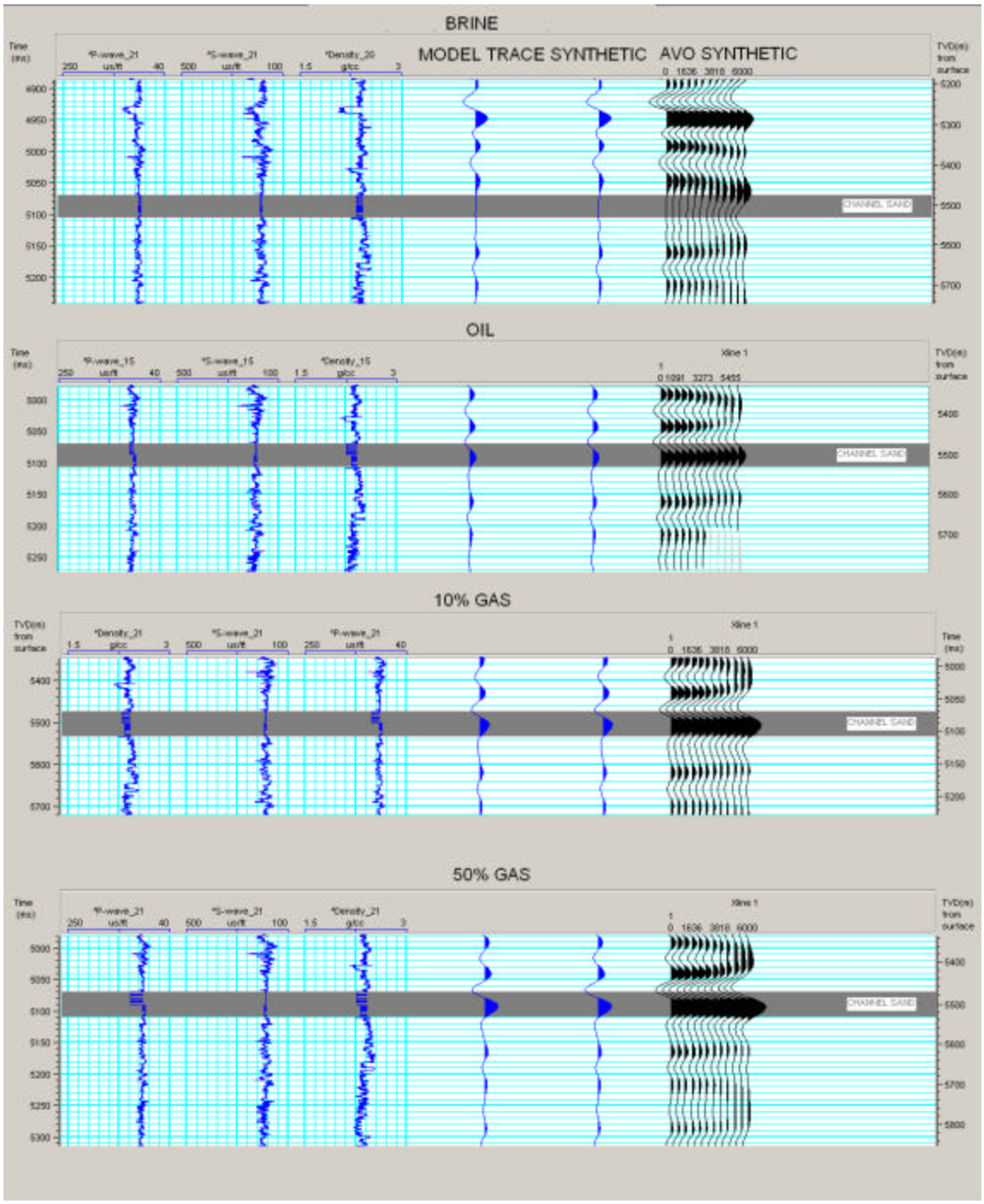

Figure 92. Pseudo logs, wavelet, synthetic trace and Zoeppritz modeled AVO response.

Upper reservoir character

The Upper reservoir interval associated with a bright spot on the seismic section was originally interpreted to be a fizz gas reservoir in a normal pressure zone by Hilterman (2001). The log signature of the reservoir interval can be seen in figure 93, the gamma signature shows a serrated curve and a low resistivity. Well log signatures indicate high porosity shaley sands with little to no indication of hydrocarbon presence. (Figure 93)

Although there is a relatively higher porosity, it does not appear to significantly impact the sonic log response.

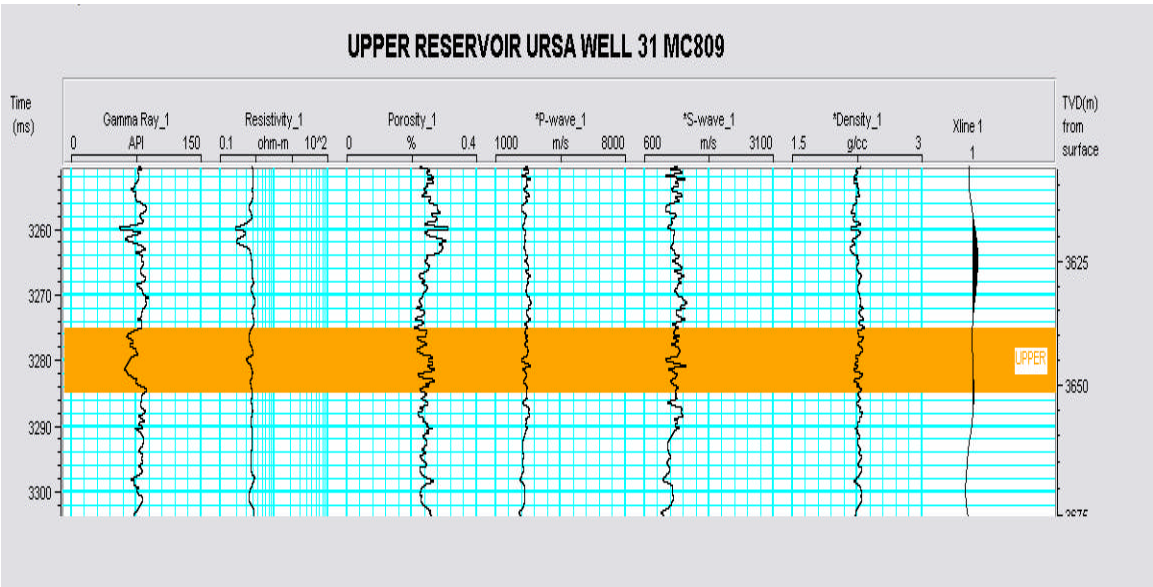

Figure 93. The log expression of the Upper reservoir highlighted with orange shows a serrate gamma, relatively moderate to low resistivity, slightly higher porosity as well as varying P-wave and density and increasing slowness.

The seismic horizon that corresponds with the Upper reservoir interval can be seen in Figure 93 and its pre-stack migrated gathers can be seen in Figure 94.

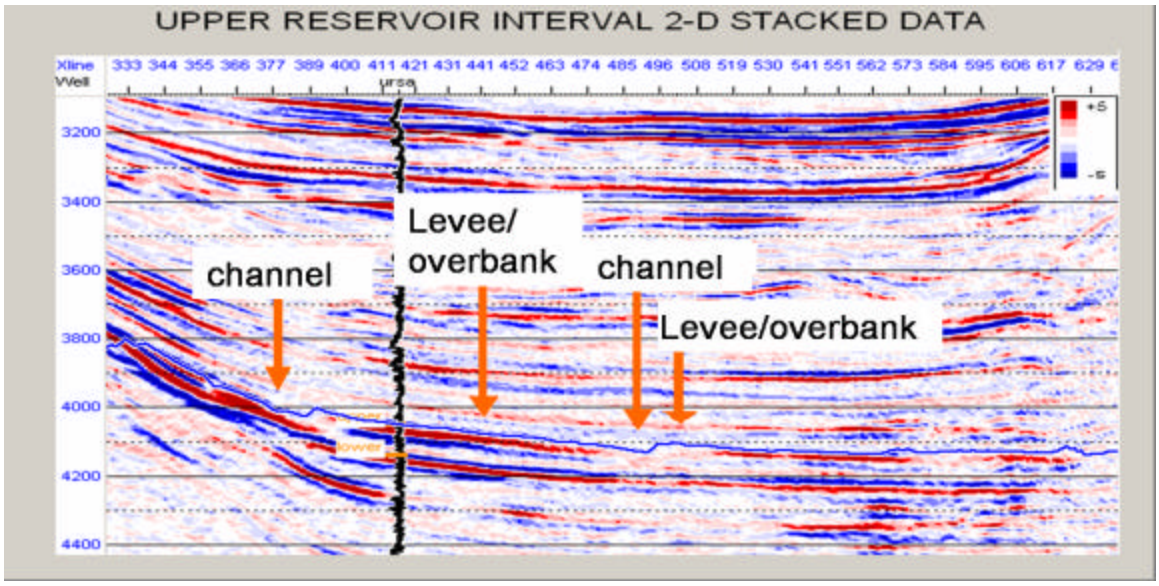

Figure 94. The post stack seismic expression of the Upper reservoir interval in the Ursa field is marked with orange on the gamma log. This reservoir zone appears as a bright spot at the well transect but dies out to the east of the basin (right of well).

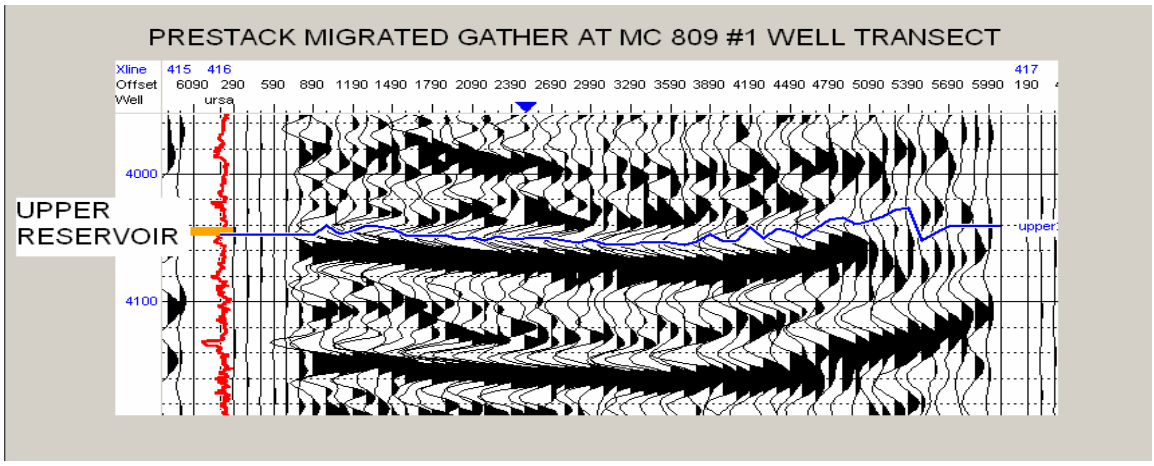

Figure 95. The prestack migrated gathers show decreasing amplitude with offset at the well. The Upper reservoir top is marked in blue.

The seismic signature contradicts the well log signature because the bright spot indicating a possible hydrocarbon presence is not associated with a large sand body in the well. The seismic expression of the Upper Reservoir shows a high reflectivity surface with a strong trough at the reservoir top. The surface converges and laps on or is truncated by what appears to be an erosional surface (Figure 95). The erosional feature at the center of the seismic profile and the adjacent sides are slightly elevated. This could be interpreted as a channel feature with adjacent levee overbank deposits. The prestack gathers in Figure 90 show a decrease in amplitude with offset. Far offset traces are contaminated with arrivals through salt and are therefore invalid.

One interpretation of this reservoir could be a levee overbank deposit. Levee overbank reservoirs are commonly referred to as low resistivity pay and, low contrast pay. One of the major issues with levee overbank deposits is that although they have the potential to be economical, they tend to be overlooked because on logs they have a high shale or mud content that reduces resistivity and increases the gamma signal. Near levee channel transitions, the levee overbank facies lap out against the erosional feature. In proximal levee facies, thin-bedded turbidites interbedded with fine-grained suspension fallout occur. In the distal levee overbank facies, an increase in fine-grained suspension fallout deposits (shale) can be observed. If thin beds that have pay are present, they will be disguised by the resolution limits of the logging tools. In seismic the levee overbank surfaces tend to converge away from the erosional feature or channel due to the increase in shale content. Generally, levee overbank deposits are elevated bathymetrically with respect to an adjacent channel. The facies usually has a gull wing shape and tapers away from the channel. In the intraslope basin setting the levee can extend across the basin (Weimer et. al, 2004) To perform modeling, extracted wavelets from near the well bore were taken from the zone of interest corresponding to the reservoir interval. The original statistically extracted wavelet and a new, modeled wavelet can be seen in figure 96. The model wavelet was created to mimic the extracted wavelet but to eliminate ringing due to noise. This modeled wavelet was used in forward modeling.

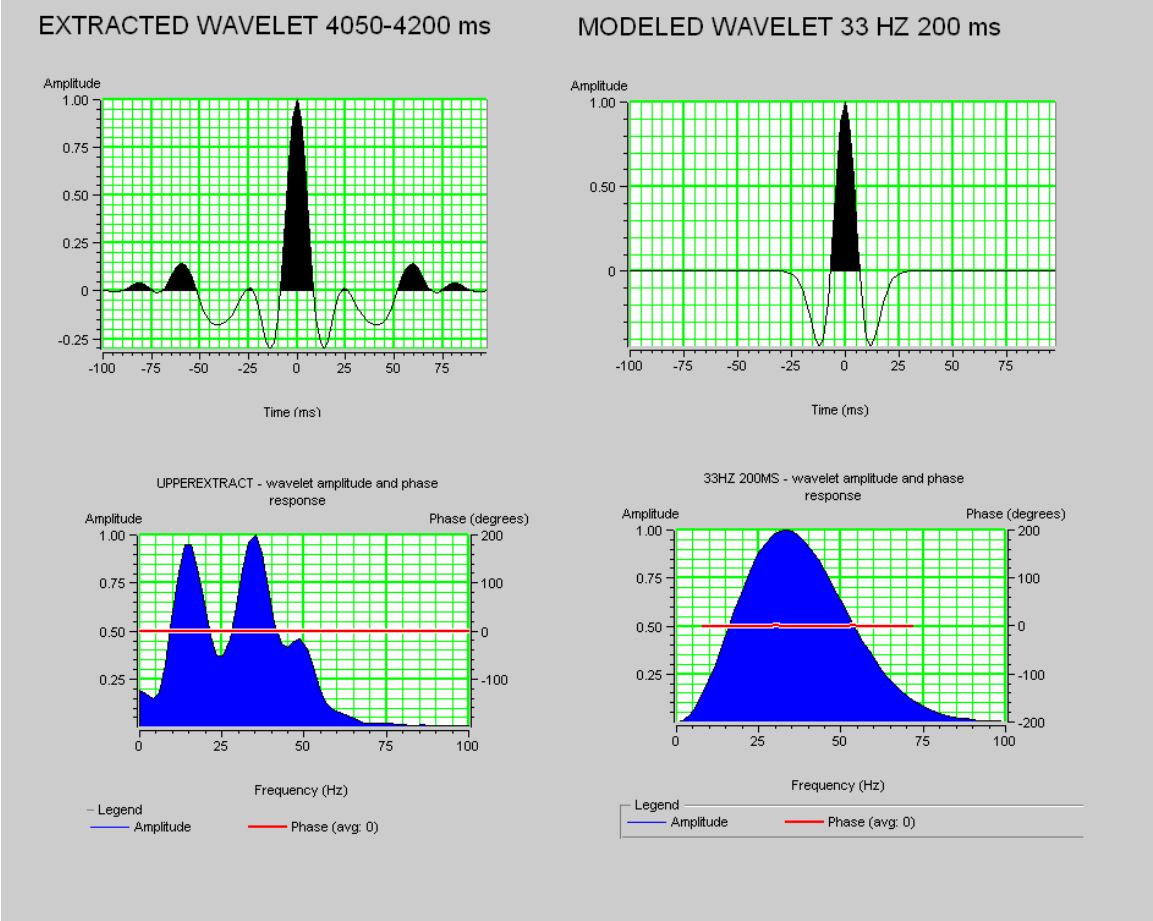

Figure 96. Statistically extracted wavelet from 4050-4200 ms time window and its frequency response. The model wavelet has 33 Hz frequency and 200 ms wavelength.

In order to ensure the proper values were placed into the model for various fluid properties, fluid substitution was preformed in Hampson Russell software. The fluid substitution was performed on the Upper reservoir interval using brine, oil, 10%, and 50% gas. The fluid substituted logs cans be seen in Figure 97 along with the Zoeppritz AVO offset synthetic model for each of the cases. The velocity and density model inputs can be seen in Appendix E.

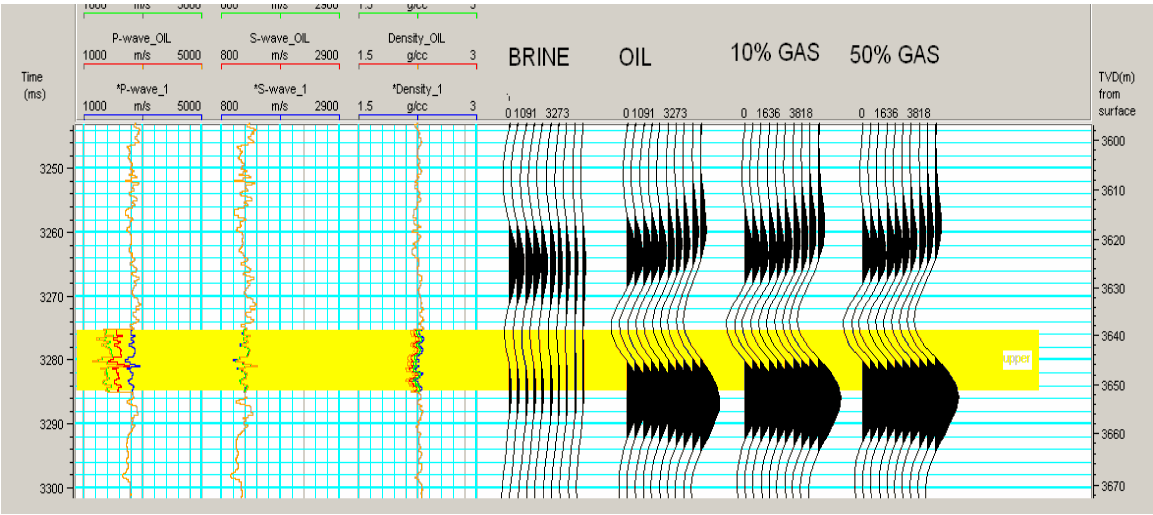

Figure 97. Fluid substitution using Gassmann's relations to predict velocity and density response to brine, oil, 10%, and 50% gas saturations. The synthetic AVO response can also be seen for each case.

The fluid response of the synthetic traces for each fluid case shows that it could be difficult to distinguish between oil versus 10% or 50% gas saturation in the reservoir interval.

Two-dimensional models

Two models were selected to represent the Upper reservoir interval interpreted to be a channel levee overbank system; A proximal levee which has relatively high net-to-gross, and a distal levee model which has relatively low net-to-gross. Due to the reservoir complexities, four total models were created to differentiate background noise from the reservoir response. The first models both have constant backgrounds and the second models have the well log sonic and density logs as background. The following subsections show the geologic models and their respective forward model results.

Proximal levee overbank model

The proximal levee overbank model can be seen in Figure 98. The model shows a channel fairway with adjacent levee overbank deposits. Proximal levee deposits have higher net to gross than distal levee deposits.

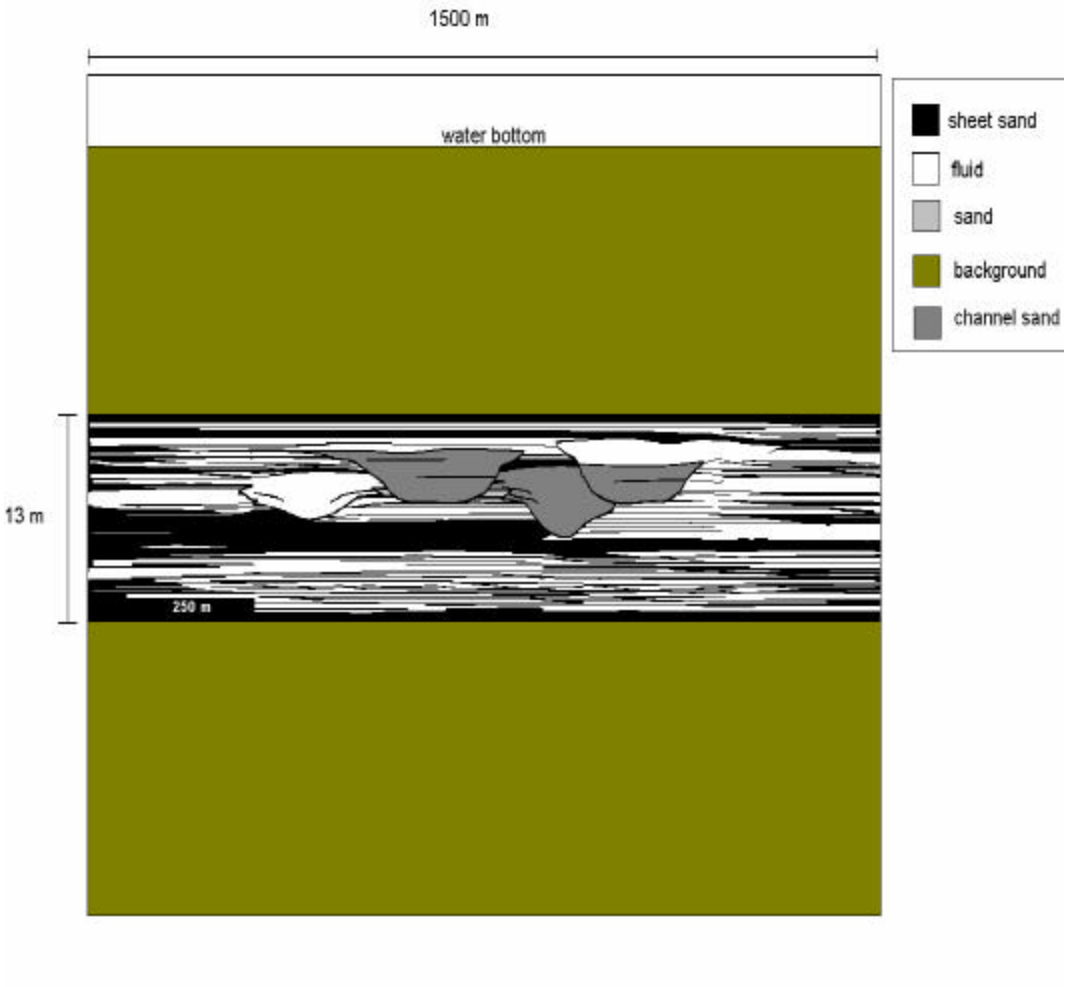

Figure 98. The proximal levee overbank model has relatively high net to gross.

The dimensions of the reservoir are scaled to the Ursa Upper reservoir to be 13 m in the vertical and 1500 m in the horizontal direction. The white color facies represents sands where fluid saturation is charged, the black deposits represent shales, light gray deposits represent inter-bedded sands and dark gray deposits are channel fill sands. The model input parameters such as velocity and density can be found in Appendix E. Velocities were calibrated to Vp/Vs ratios to yield more accurate results. The first forward model with constant background velocity can be seen in figure 99. This figure shows the four fluid cases for the model. The reservoir tops are marked in green. A well is marked on each profile at 300 m; that is the well that was used for AVO modeling. The results of this model show that the inter-beds of the levee overbank are invisible when brine saturated. A slight change in amplitude occurs in concurrence with the channel fill sands. When the inter-bedded sands are saturated with hydrocarbons, the seismic amplitude increase dramatically and there is a slight convergence or wedge shape that occurs as the model increases in shale sediments at distal levee overbank locations. Two separate amplitude anomalies occur that appear to be indirectly associated with channel fill but do not allow differentiation of channel compartments. A similar response can be seen in the

seismic synthetic signature that has a complex Ursa log background in Figure 100. The only difference occurs in the brine saturated model. There are two amplitude anaomalies that appear to be associated with channel compartments. The AVO response of each interval can be seen in Figure 101. In this figure, pseudo wells at 300 m for the respective fluid cases are shown, the wavelet convolved trace and the extracted synthetic trace are shown, and also the Zoeppritz modeled AVO gathers are shown. The brine and oil cases have slight increases in amplitude with offset. The 10% and 50% gas models show decrease in offset. These will later be compared to the original Ursa data AVO response.

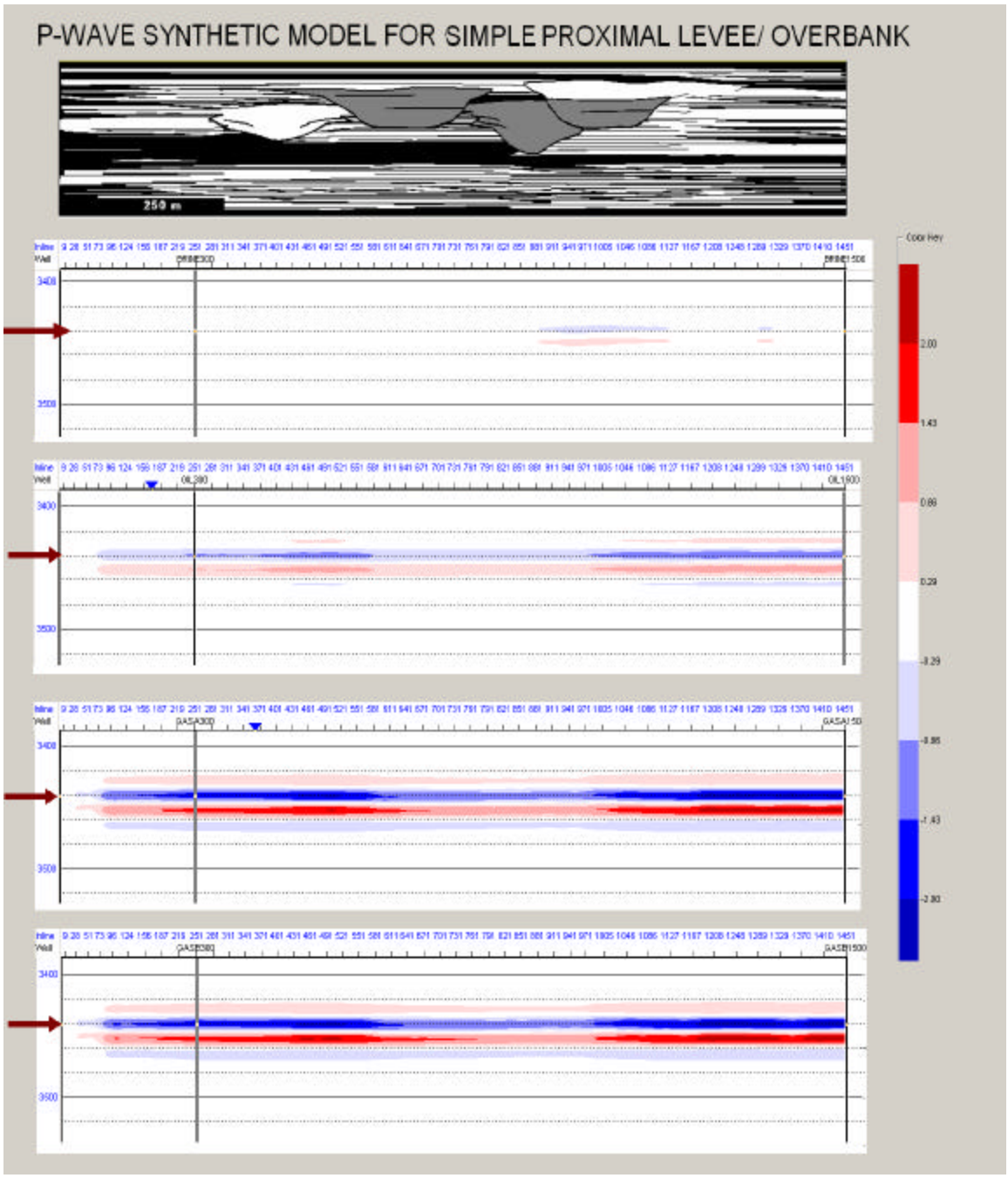

Figure 99. The response of the proximal levee overbank model shows reservoir top in green, pseudo well log 300 m. Shows brine, oil, 10% and 50% gas saturated reservoir respectively. Subtle response occurs at the channel features but the levee is essentially invisible until fluids are present.

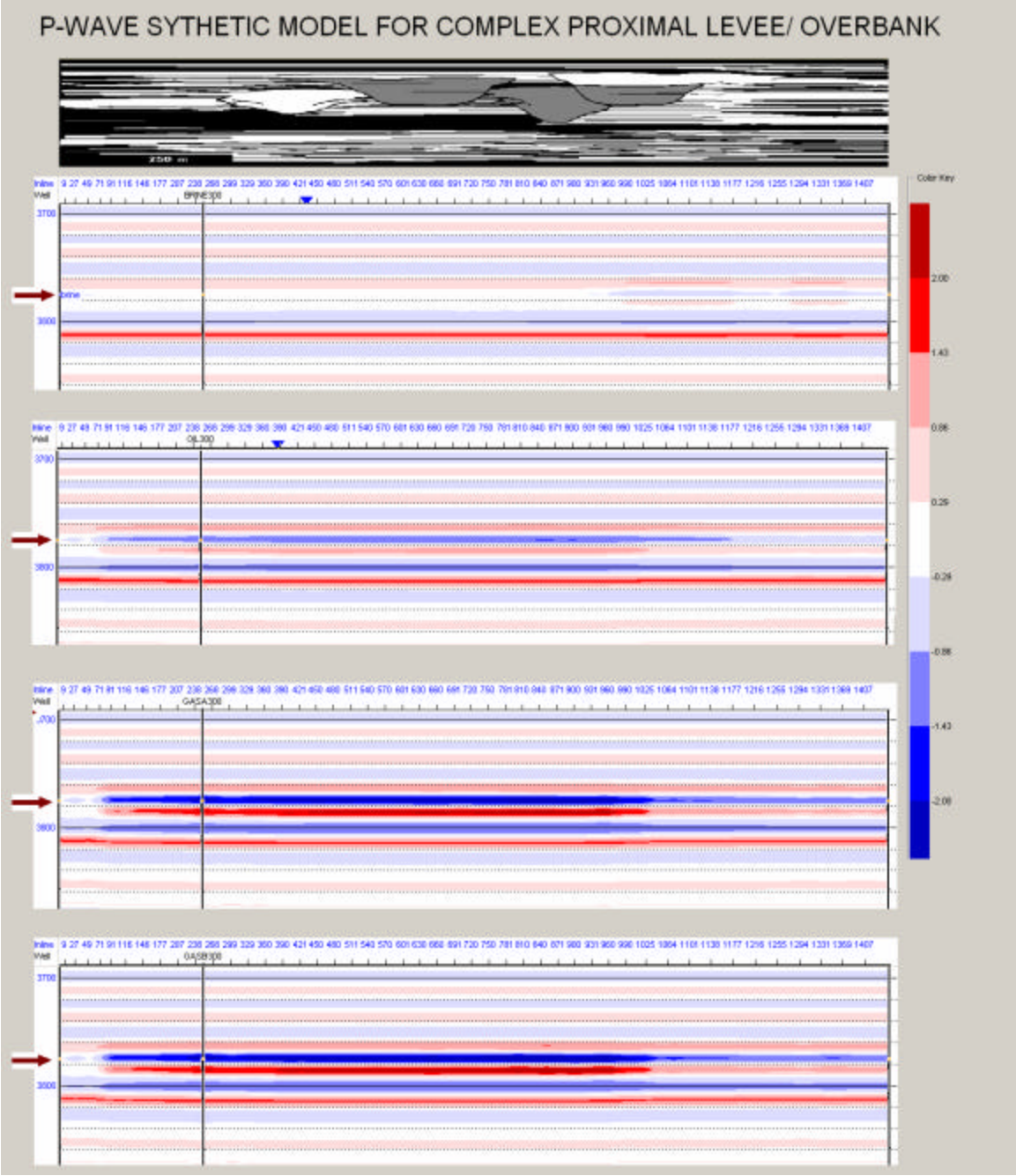

Figure 100. The synthetic 2-D P-wave response for brine, oil, 10% and 50% gas respectively with Ursa #1 log as background.

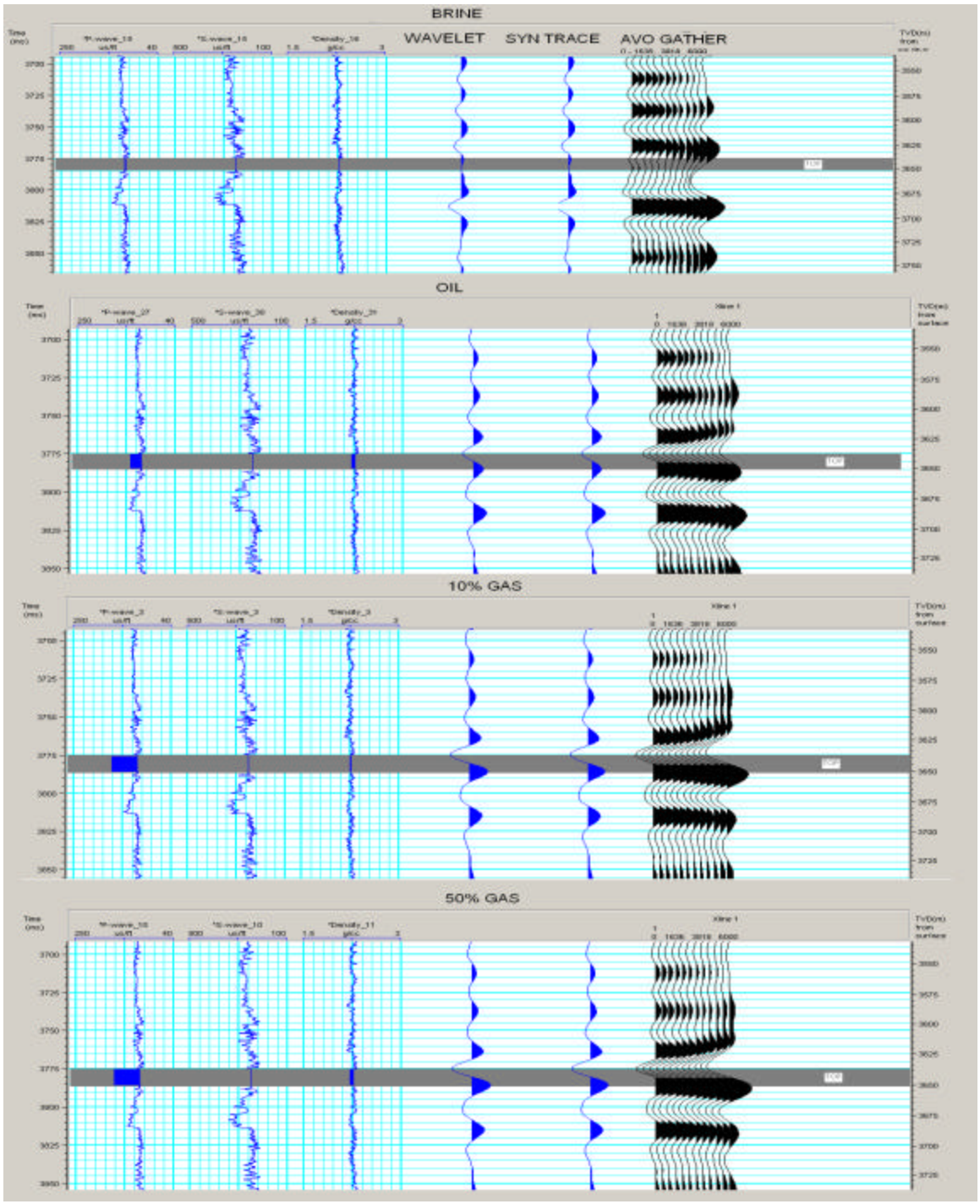

Figure 101. The pseudo log, wavelet, synthetic trace and Zoeppritz AVO response using 6000 m offset.

Distal levee overbank model with multiple channels

The distal levee overbank model can be seen in Figure 102. As with the previous model, the dimensions of the reservoir are scaled to the Ursa Upper reservoir to be 13 m in the

vertical and 1500 m in the horizontal direction. The white color facies represents sands in which different fluids were saturated. The black facies represent shales, light gray deposits represent inter-bedded sands and dark gray deposits are channel sands. The model input parameters, such as velocity and density, can be found in Appendix E. Velocities were calibrated to Vp/Vs ratios to yield more accurate results. The first forward model with constant background velocity can be seen in figure 103. This figure shows the four fluid cases for the model. The reservoir tops are marked in green. A well is marked on each profile at 300 m; that is the well that was used for AVO modeling. The results of this model are similar to the first and show that the distal inter-beds of the levee overbank are invisible when brine saturated, while there is a slight change in amplitude where channel fill sands occur. When the inter-bedded sands are saturated with hydrocarbons, the seismic amplitude changes significantly and there is a slight convergence or wedge shape that occurs as the model increases in shale sediments at distal levee overbank locations. With the complex Ursa log background in Figure 104. A similar response can be seen of the complex seismic synthetic signature, but the fluid response becomes more difficult to identify. The AVO response of each interval can be seen in Figure 105. In this figure, pseudo wells at 300 m for the respective fluids are shown, the wavelet convolved trace and the extracted synthetic trace are shown, and also the Zoeppritz modeled AVO gathers are shown. The synthetic response shows a neutral brine signature, while the 0% and 50% gas amplitude increases with offset are higher than for oil. These model responses were compared the actual Upper reservoir AVO response.

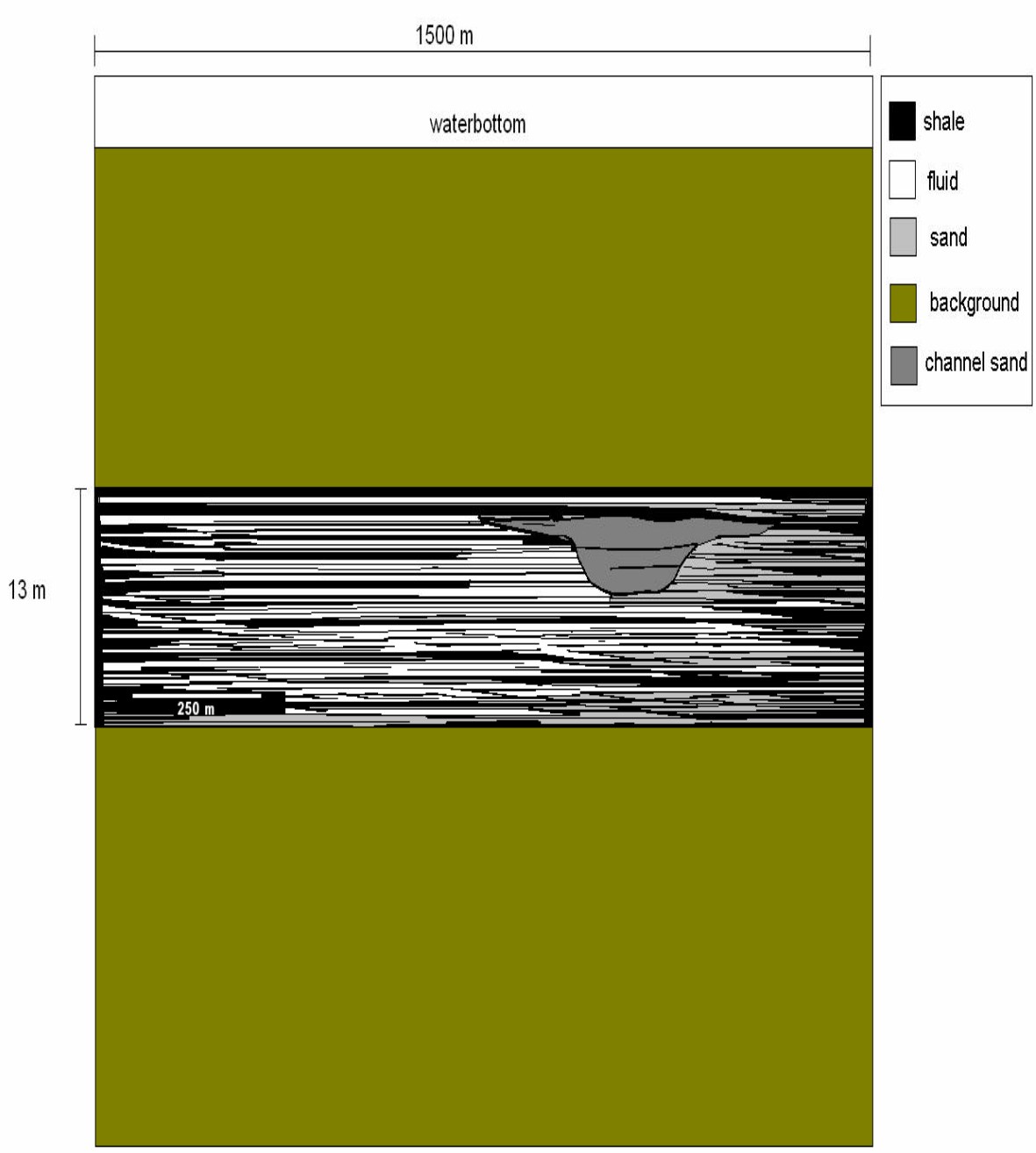

Figure 102. The distal levee overbank model shows decreased net to gross at distal levee locations.

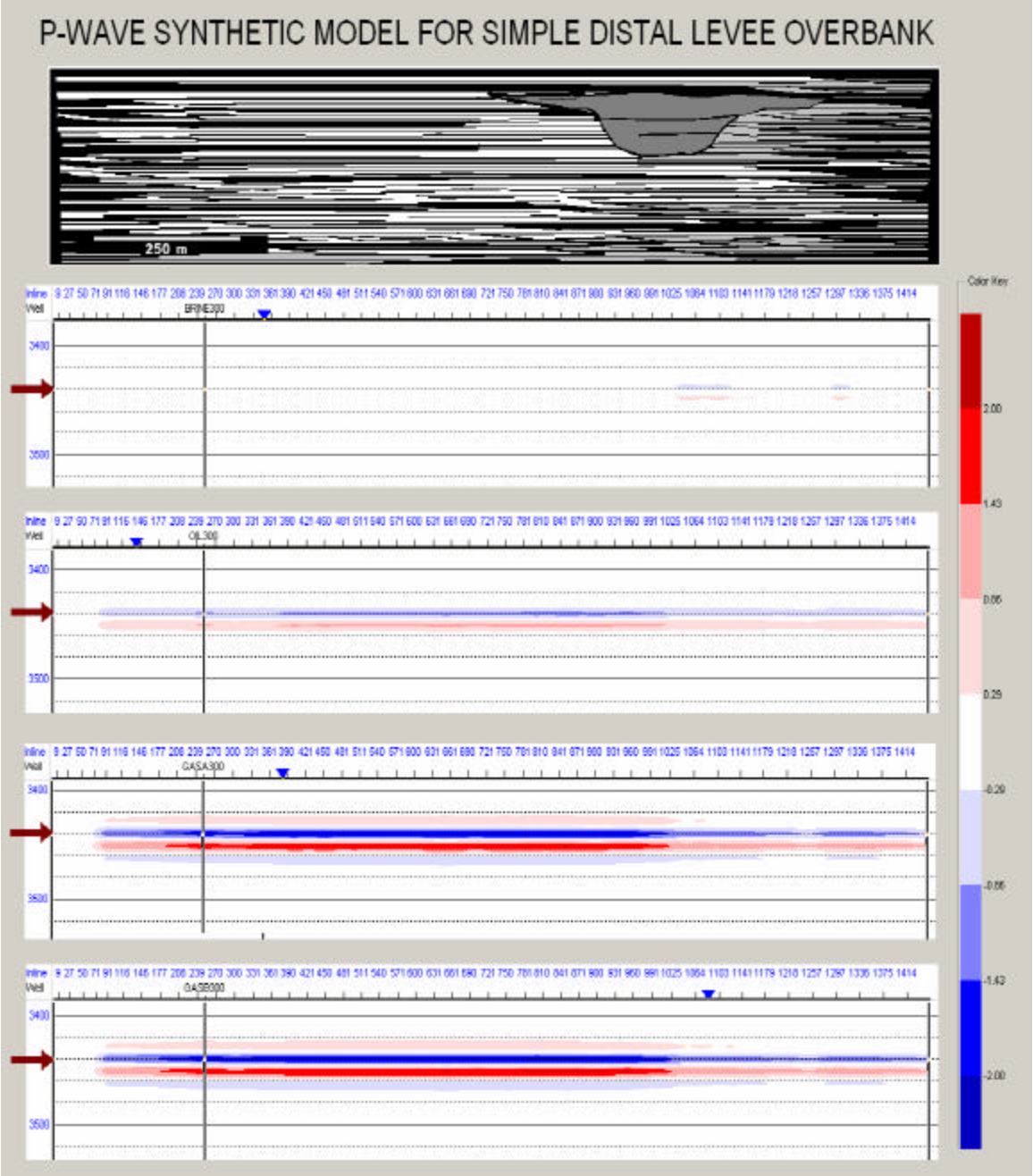

Figure 103. The distal levee overbank model shows a change in seismic amplitude in the brine case where the channel is but no amplitude response to thin beds until hydrocarbon saturated.

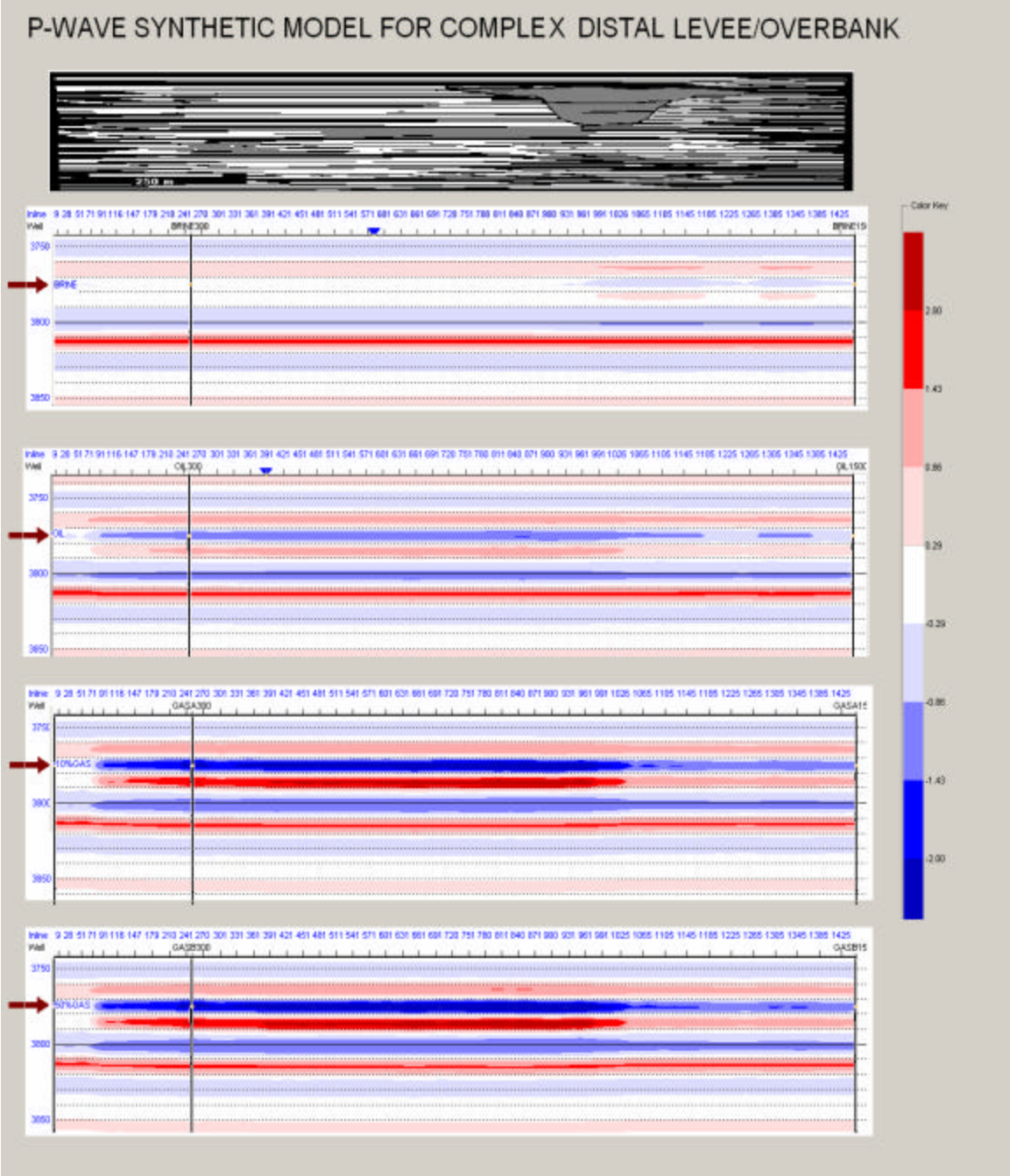

Figure 104. The complex well log background model with the distal levee reservoir model shows stronger change at reservoir interval. Green line indicates reservoir top, the well 300 m pseudo log transect is shown.

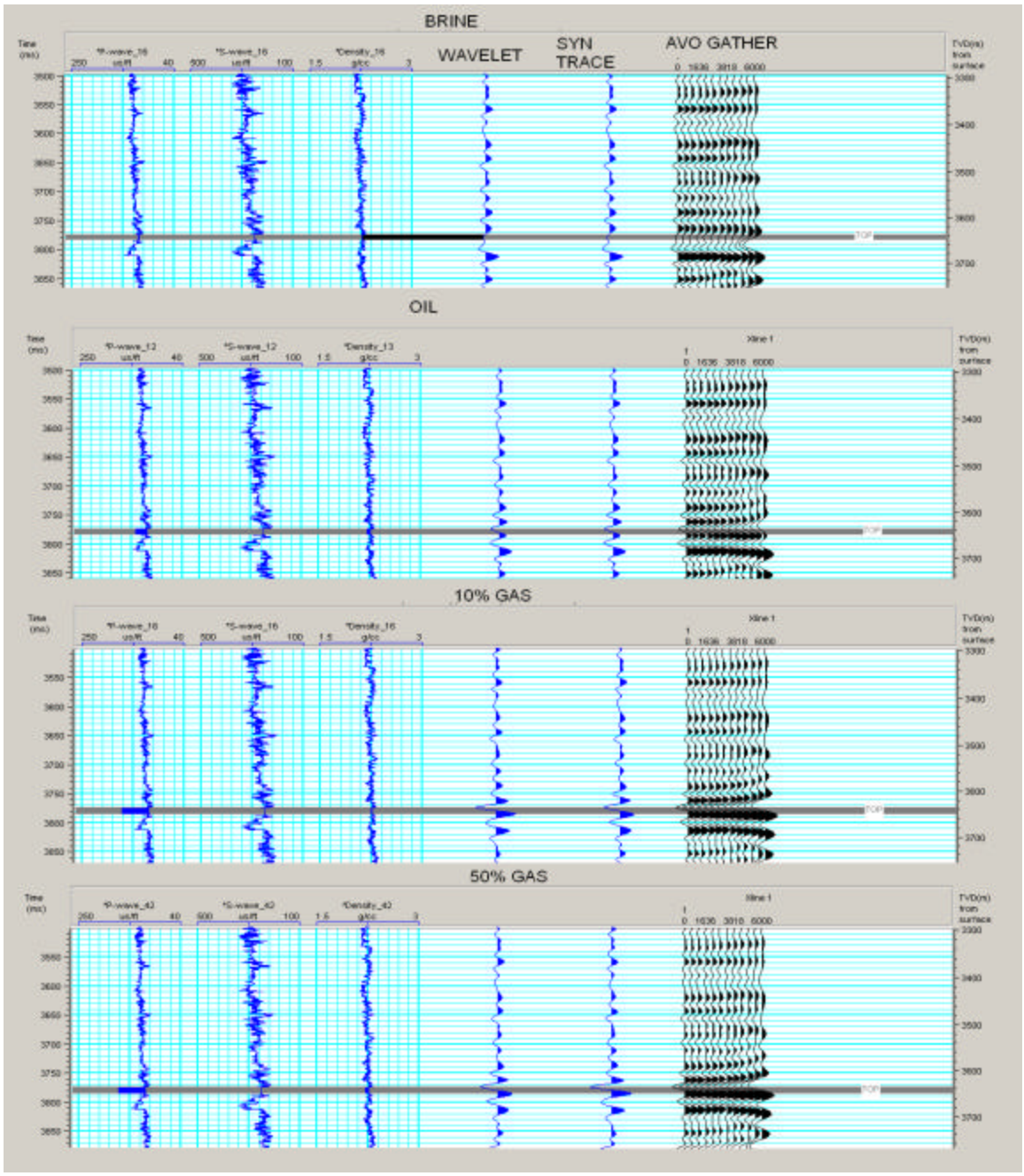

Figure 105. The pseudo log wavelet response, extracted 2-D trace and Zoeppritz model AVO response for distal levee overbank model show neutral brine response while 10 and 50% gas response are strongest.

The Upper reservoir amplitude traces for the pre stack gathers were extracted from for CDP gathers and the root mean squared values were calculated to determine the general magnitude of the values. The root mean square is the square root of the mean of the squared values or $(x_i^2+x_{i+1}^2+x_{i+n}^2/n)^{\wedge 1/2}$ and generally gives an idea of the magnitude of the numbers being dealt with. The RMS amplitude values of the Upper reservoir were

then scaled to the model data by multiplying it by a factor of $7.7*10^{-08,}$ which was determined from the comparing the original RMS amplitude values to the model amplitude values. Figure 106 shows a plot of the original Upper reservoir amplitudes to the eight models that were shown of the proximal and distal levee overbank facies models. The Figure shows the amplitude versus sine squared of the angle of offset for the brine, oil, 10% and 50% gas saturated proximal and distal levee overbank reservoirs respectively. In addition the Upper reservoir normalized amplitudes have been plotted on the same plot to compare the model results with the upper reservoir data. The Upper interval has a confidence interval of 95% (+/- .01163). It is important to note that the near angle gathers are muted and the far offset gathers are contaminated by the presence of salt diapers. Therefore the more reliable data is located at the mid angle gathers. The near offset traces of the upper reservoir data partially overlap with the oil models and then amplitudes increase in magnitude to and overlap with proximal and distal 10% and 50% gas models on the mid-stack section. The far offset angles show lower magnitude amplitude values. Overlap occurs for 10% and 50% gas saturated models for both facies. The figure shows that the Upper reservoir interval overlaps more with the distal 10% and 50% gas saturated reservoirs. From the results the fluid type could not be distinguished but the overlap between 10% and 50% gas saturated reservoir models with the data implies that the bright spot occurring in the seismic data could actually be a commercially saturated hydrocarbon zone instead of the original fizz gas interpretation. This is important because it indicates possibilities for secondary reservoir potential in these levee/overbank reservoirs that may have previously been overlooked in highly explored nd exploited deepwater fields.

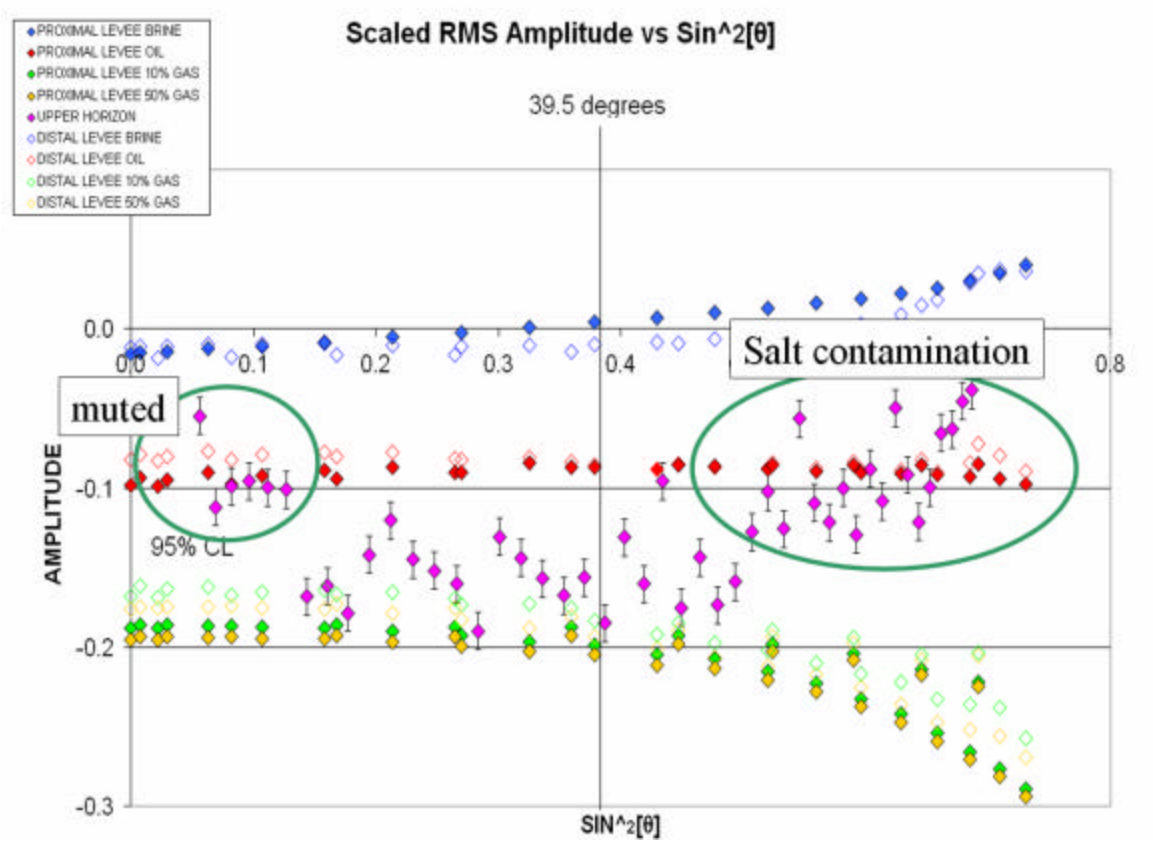

Figure 106. The synthetic model response and reservoir response compared. Upper reservoir amplitude values were normalized to the model amplitudes. Confidence Level of 95% (+/- .01163) for the Upper reservoir interval.

AVO modeling of levee overbank deposits

Additional modeling was performed by Rick Gibson (Baker et al., 2005) on the Upper reservoir and similar zones to estimate the seismic lithologic response of the thin beds that are the result of the levee overbank deposits seen in Figure 8.15. Synthetic seismic traces were generated for the lower interval 3.75-3.78 km depth on the logs. To generate the traces a 30 Hz Ricker wavelet with a 100 ms wavelength and a 4 ms sample rate were used. The Zoeppritz equation was then used to perform the model using offsets from 0-45 degrees. The results can be seen in Figure 107.

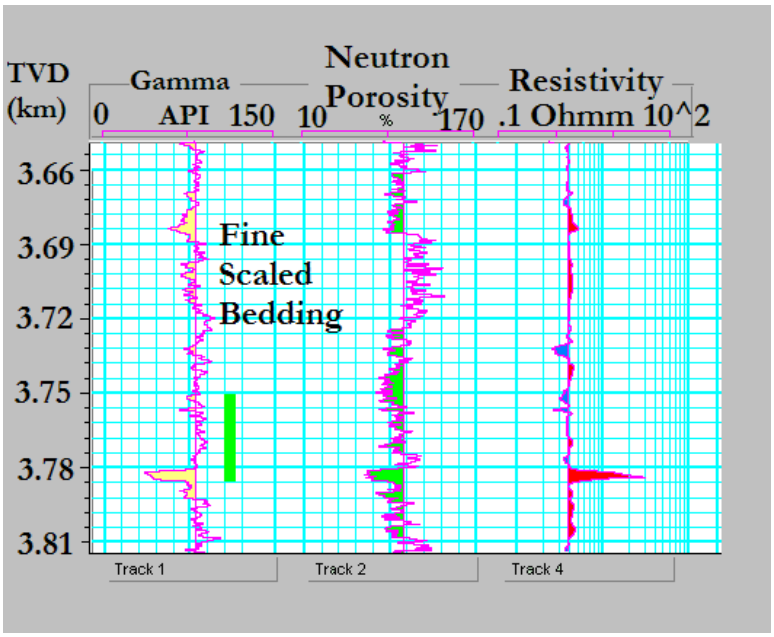

Figure 107. The Ursa log displays gamma, porosity, resistivity.The green bar shows amodeled turbidite interval, which were modeled to compare the reflectivity coefficient.

From the synthetic seismic model, we can see that there is indication of strong trough/peak pair event in the zone of interest. By changing the frequency and wavelength of the source wavelet, the thin bed interval may be resolvable. To further investigate, one dimensional models of the turbidite intervals were run for Vp, Vs, and density values and a composite reflection coefficient was generated for the deepest interval (3.75 to 3.78 km) for three frequencies (15 Hz, 30 Hz and 60 Hz) in red, blue and black respectively. The results can be seen in figure 108. The interpretation of finely bedded turbidite sequences may be more complicated, since seismic waves will be scattered by rapid fluctuations in velocity and density throughout the section. The observed response will then be a superposition of waves reflected by the various sand and shale intervals, not an individual wave reflected by a single boundary between two welded half spaces, the model assumed by conventional AVO equations (Baker et al., 2005).

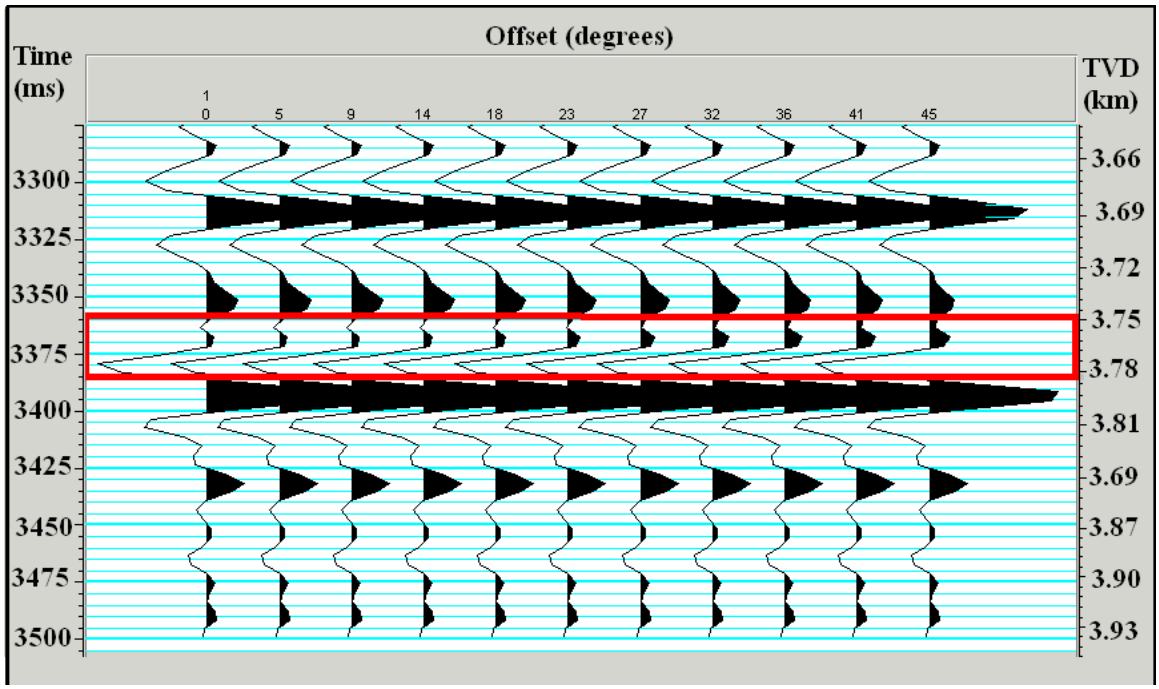

Figure 108. Synthetic seismic response generated with Zoeppritz approximation, and a 30Hz Ricker wavelet and a 45 degree offset was used in Hampson-Russell software. The equation assumes brine saturation and the red box corresponds to the lowest depth interval on the well log (3.75 to 3.78 km). (Adapted from Baker et al., 2005)

However, the complete response can be modeled using propagator matrix methods (Aki & Richards, 2002). Because this approach enforces all of the required boundary conditions at each interface between the numerous layers, the solution includes all wave propagation phenomena and is not restricted by any assumptions of weak contrasts in material properties or near vertical propagation. This composite reflection coefficient includes the superposition, or "tuning", of all waves reverberating in the model layer (Gibson, 2004). As an example, we show the results of computing the P-wave composite reflection coefficient for the 3.75 to 3.78 km interval in figure 104. The total unit thickness, 0.03 km, is relatively thin compared to a wavelength for frequencies typical of surface seismic data, so reflections from it will be comprised of a single tuned event and it is reasonable to characterize it using the single value of the composite reflection coefficient. Because the reflecting zone has a finite thickness, this coefficient is frequency dependent (Figure 109). As frequency increases from 15 to 60 Hz, the magnitude of the reflected signal increases, and the rate of decrease with an increasing angle of incidence also changes. This suggests that conventional AVO parameters, such as the gradient of the amplitude as a function of the squared sine of incident angle, will be sensitive to frequency.

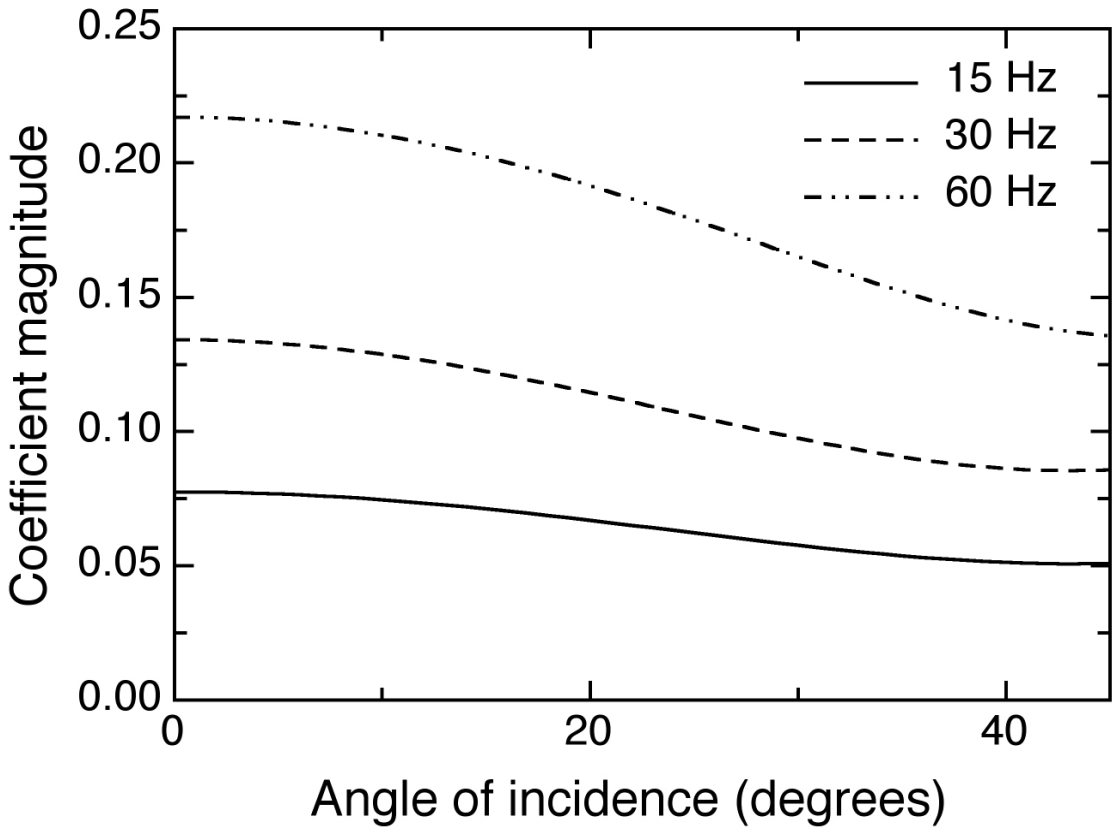

Figure 109. Composite reflection coefficient generated for interval (3.75 to 3.78 km) for three frequencies. (Adapted from Baker et. al, 2005)

Modeling of seismic composite reflection coefficients provides important insights into the use of seismic amplitudes for hydrocarbon detection in at least two ways. First, comparisons of results for different spatial correlations shows that the "smoother" the velocity profile (e.g., the Gaussian correlation), the smaller the amount of scatter in reflection amplitudes, especially at near offsets. Geologic environments such as turbidite flows are often important for the exploration and production of hydrocarbons in deep water sites, and these settings often will vary laterally because of different patterns of flow of sands and shales. Therefore, seismic measurements will be affected by different vertical velocity structures at different positions within the reservoir, even for reflections from the "same" reservoir. Our results show that this will introduce scatter, or uncertainty, into AVO results that might be associated with the type of geologic heterogeneity, which may be useful information. Secondly, that comparison of composite coefficients for different fluid contents helps to show how such uncertainty associate purely with lithologic variations might hinder hydrocarbon detection. Model calculations can help to determine whether scatter in AVO measurements will be large compared to the anomalies associated with hydrocarbons, in which case an AVO hydrocarbon indicator might not be effective.

The seismic turbidite models (STMs) that we developed based on well measurements can be used to apply the same ideas to a more geologically based model. In our approach,

cumulative distribution functions for seismic velocity, density and thickness of the sand and shale units appearing in observed turbidite sequences are used construct models that display trends similar to those in field settings. The models are more realistic than so-called binary models where the all sands have identical velocity and density (similarly for shale layers).

Our seismic processing developments emphasized the development of methods for robust analysis of frequency-dependent AVO, which has strong potential for improved and more sophisticated hydrocarbon detection in challenging areas. In some cases, existing data sets may be have been processed with normal moveout corrections applied that distort frequency content, and our approach will eliminate these distortions and allow reliable detection of frequency dependent anomalies that could be associated with hydrocarbons or other sources. Applications to data from Teal South showed that apparent frequency anomalies were suppressed by the correction procedure, which produce a frequency-independent result that matched model predictions. Additional processing refinements were developed for other cases, such as local averaging procedures that improve AVO analysis for noisy data.

Here we have seen that, although the individual thin bed deposits of levee overbank reservoir systems are irresolvable in the forward models there are several ways to identify the possible presence of this facies. The first way is by identifying a channel or erosional feature in the seismic and an adjacent gull wing structure. A corresponding seismic bright spot with a low resistivity pay response in the log signature may be an indication of a commercial pay zone composed of levee overbank deposits. Also, the use of higher frequency waveforms may help to resolve the thin beds. Another feature of the seismic response of the thin bed levee deposits is that the net to gross decreases as we move from proximal to distal levee overbank deposits. The convergent seismic signature produced from this type of lithology change may be an additional way to identify levee overbank deposits in seismic. The other interesting observation for these models is that hydrocarbon saturation helps to better differentiate fluid compartments but is still non-unique. Due to all of these inconsistencies the original interpretation of a fizz gas zone (Hilterman, 2001) could actually be a commercial hydrocarbon zone.

Conclusions

One of the main conclusions from this quarter was a new method to invert reservoir properties (water saturation and porosity) directly from seismic AVO attributes appears to yield consistent results with well data. The key step of the method is to establish the relationship between reservoir properties and seismic AVO attributes. The new method is tested on an area with two wells (post drill): a commercial gas well, A, and a low saturated gas well, B. Information from well A was used to build up the necessary relationships for the inversion. The inversion at the targeted horizons provides detailed porosity and water and gas distributions. The inverted saturations for the two patches show the extent of the gas distribution in the vicinity of well A, and the possibility of low saturated gas at well B, which is consistent with the drilling results. Computed density from the inverted Sw and porosity are also consistent with the well data.

Another advancement in our work has been to identify deep-water reservoir sands with unique sedimentary processes. These show progressive effect of compaction and cementation on porosity and frame velocities, which also incorporates the grain texture and fluid migration. It was discovered that compaction is a major driving force. Poor sorting will provide room for low initial packing porosity and more potential for continued compaction. Some of the main conclusions from the study are:

1. For deep-water sands, over pressure and early charge of hydrocarbon often block pore fluid flow to minimize the cementation effect.
2. With increasing depth and age, porosity reduces and dry velocity increase. Fluid saturation effect for deep-water sands can be described by the constant gain function of 2.5 and fluid modulus.
3. Velocity dispersion of deep-water sands is relatively small.
4. Compaction and weak cementation increases shear rigidity more than bulk modulus.
5. P and S-wave velocities of water sands tend to follow the Reuss trend and shows less dependence on porosity.
6. Pressure effect on velocity of VHP sands is relatively small. With weak cementation, pressure effect on velocity increases, which may be caused by core damage.
7. Dry shear modulus at high pressure is proportional to p-wave modulus.

In addition, we continue to incorporate the use of deep-water outcrop analogues help better predict frequency and occurrence of turbidite sequences when combined with well log and seismic and DHI's. These also assist in imposing constraints on seismic modeling. The combination of the geological study, which helps to identify depth intervals of interest, with the computed composite reflection coefficient provides some potentially important insights into seismic characterization of turbidite sequences. These

predictions can help to improve the interpretation of Direct Hydrocarbon Indicators. Presence of turbidite features might be an alternative explanation for the occurrence of high amplitude seismic events, which may be misidentified as hydrocarbon indicators. The combination of the geological study, which helps to identify depth intervals of interest, with the computed composite reflection coefficient provides some potentially important insights into seismic characterization of turbidite sequences.

Also, we found the use of outcrop observations could enhance interpretation of deepwater sediments and add to understanding of the lithology, geometry and rock properties that exist in these settings. It was recognized early that the Brushy Canyon deepwater outcrops are not a perfect analog to the deepwater intraslope basin setting of Ursa field. The Brushy is a sand rich system that is now highly cemented and was deposited in mainly unconfined conditions, whereas the Ursa field is a mud rich system that formed in a confined intraslope basin setting controlled by salt tectonics, sediment loading and eustacy. However, many of the deepwater elements of the Brushy such as sheet sands, thin bed levee overbank deposits and channel systems, could be found in both types of settings and both have similar stratigraphic patterns in common. By performing forward modeling on some of these main deepwater features, we can better understand the Ursa seismic data. To summarize, outcrop modeling of geobodies combined with Ursa data have enhanced interpretation by:

- Helping to identify patterns in deepwater seismic facies
- Helping to differentiate causes of a substantial DHI's (fluid vs lithology)
- Investigation of sub-seismic features that control fluid flow and compartmentalization
- Identification of a possible misinterpreted DHI
- Recommendations on future applications

A general summary of these observations can be seen in Table 5.

	Lithology	Fluid	Detectability (thickness and tuning)	Amplitude
Non amalgamated sheet sands	Easy to detect on logs Cannot differentiate internal shale breaks	No expression for brine Layers show when fluids added High amp for oil 10% & 50% gas	Internal layers complicate tuning but still high net to gross	Waveform Single seismic event but less continuous than amalgamated Waveforms vary with fluids
Amalgamated Sheet sands	Easy to detect on logs Somewhat detectable on seismic	No expression for brine Oil, 10% & 50% gas high amp; 10% vs 50% indistinguishable	Usually above tuning thickness simple to identify	Single seismic continuous event
Channels	Easy to detect on logs and seismic Cannot distinguish compartments unless large vertical and lateral scale	identify presence of channel with all fluids With HC the channel becomes more apparant	Identify channel complex presence but not individual compartments; If fluid saturated channel compartments may be distinguishable	High amplitudes at HC saturated channel compartments
Levee overbank	May be difficult to detect on logs and seismic; Low resistivity pay	Brine saturated facies appear to be background, oil., 10% and 50% gas associated with bright spots	Internal complexities cause problems with tuning and detectability	Single reflector bright spot with fluids No amplitude event with brine

Table 5 Summary of the model facies and the detection of lithology fluids, thickness, tuning and amplitude response.

Figure 110 shows a table and graph comparing detectability, lithology and amplitudes. This figure provides a qualitative visual comparison of the attributes and parameters associated with each reservoir facies modeled. The sheet sands are the easiest to identify lithology and fluids, the thicknesses are relatively large and less problems with tuning result. For channel sands the lithology is relatively easy to distinguish, amplitudes are moderately indicators of channel presence and the detectability depends on the channel size and amalgamation. The levee overbank facies are least detectable, lithology is difficult to identify and amplitudes can be variable depending on the fluid presence.

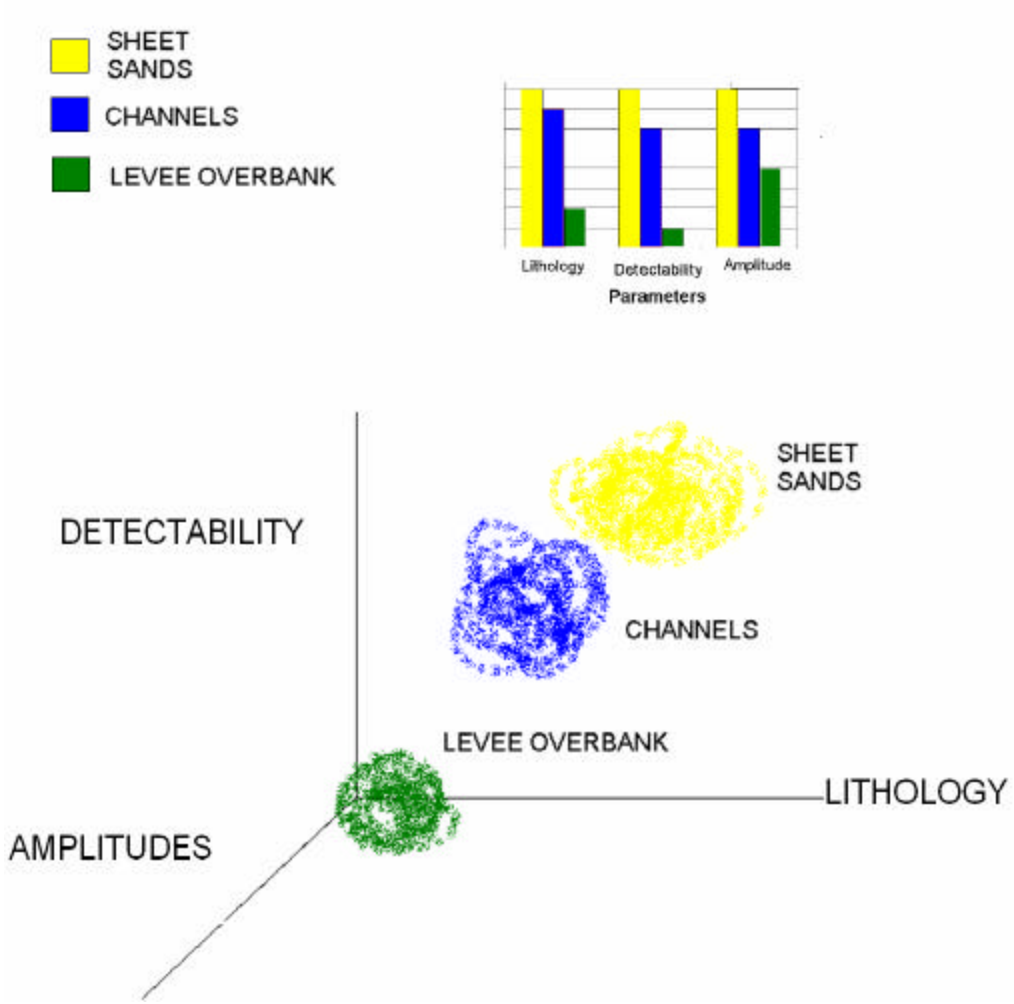

Figure 110. Graph summarizing the seismic expression of levee overbank, channels and sheet sands.

In conclusion, deep-water outcrop analogues help better predict frequency and occurrence of turbidite sequences and fluids when combined with well log and seismic data and DHI's. The combination of the geological study, which helps to identify depth intervals of interest, with the computed composite reflection coefficient, provides some potentially important insights into seismic characterization of turbidite sequences. These predictions can help to improve the interpretation of Direct Hydrocarbon Indicators. This combined understanding can help to identify commercial hydrocarbon zones that may otherwise be overlooked, help to better quantify reservoir compartments, and predict new drilling targets.

Further study

Some potential studies that could be improve interpretation of these deepwater facies could be the use of higher frequency seismic imaging. Also multicomponent seismic can be used to identify anisotropic media as well as help differentiate fluid saturation.

REFERENCES

Alford, R. M., Kelly, K. R., Boore, D. M., 1974, Accuracy of finite difference modeling of acoustic wave equation: Geophysics, 39, p.834-842.

Aki, K. and Richards, P., 2002. Quantitative Seismology, 2nd Ed., University Science Books, Sausolito, California.

Alford, R. M., Kelly, K. R., Boore, D. M., 1974, Accuracy of finite difference modeling of acoustic wave equation: Geophysics, 39, p.834-842.

Anderson, D., 2004, personal communication.

Avseth, P., Flesche, H., Van Wijngaarden, A. J., 2003, AVO classification of lithology and pore fluids constrained by rock physics depth trends, in The Leading Edge, October, p.1004-1011.

Baker, K. L., Batzle, M.L., Gibson, R.., 2005, Use of outcrop analogues to predict lithology influence on the seismic signature, SEG Abstract, Tulsa OK.

Backus, G.E., 1962. Long-wave elastic anisotropy produced by horizontal layering, J. Geophys. Res., 67, 4427-4440.

Bates, R.K., Jackson, J.A., 1984, Dictionary of geological terms, 3rd Ed., American Geological Institute, Random house Inc., N.Y., NewYork.

Batzle, M, Wang, Z., 1992, Seismic Properties of petroleum fluids: Geophysics, 57, 1396-1408.

Batzle, M., Gardner, M. H., 2000, Lithology and fluids: Seismic model of Brushy Canyon Formation, west Texas, in A. H. Bouma and C. G. Stone, eds., Fine-grained turbidite systems, AAPG memoir 72/SEPM Special Publication No 68, p.127-142.

Batzle, M., Han, D., and Hoffman, R., 2001, Optimal hydrocarbon indicators: Presented at the 71 Ann. Internat. Mtg., Soc. Expl. Geophys., Expended Abstracts,

Baud, R.D., and others, 2002, Deepwater Gulf of Mexico: America's expanding frontier: Mineral Management Service OCS report MMS 2002-021.

Beaubouef, R. T., C. Rossen, F. B. Zelt, M. D. Sullivan, D. C. Mohrig, and D. C. Jennette, 1999, Field guide for AAPG Hedberg Field Research Conference: deep-water sandstones, Brushy Canyon Formation, West Texas, April 15-20, 1999, Tulsa, Ok, AAPG, p. 99.

Borer, J., 2004, personal communication.

Borer, J., 2005, CSM PHd Thesis, Outcrop Analysis and geologic modeling of Submarine channels and related Strata, Permian Middle brushy Canyon Formation, West Texas, USA.

Bouma, A.H., Normark, W.R., Barnes, N.E., 1985, Submarine fans and related turbidite systems: New York, Springer-Verlag, p.7-12.

Bowers, G. L., and T. Katsube, J., 2002, The role of shale pore structure on the sensitivity of wire-line logs to overpressure, in A. R. Huffman and G. L. Bowers, eds., Pressure regimes in sedimentary basins and their prediction, AAPG Memoir 76, p. 43–60.

Carr, M., Gardner, M.H., 2000, Portrait of a basin floor fan for sandy deepwater system, Permian lower Brushy Canyon formation, west Texas, in A. H. Bouma and C. G. Stone, eds., Fine-grained turbidite systems, AAPG memoir 72/SEPM Special Publication No. 68, p. 215-232

Castagna, J. P., 1993, AVO analysis-tutorial and review, in J. P., Castagna and M. Backus, eds., Offset dependent reflectivity-theory and practice of AVO analysis, Society of Exploration Geophysicists, Tulsa, Oklahoma.

Chapin, M. A., Davies, J.L., Gibson, Pettingill, H.S., 1994, Reservoir architecture of turbidite sheet sandstones in laterally extensive outcrops, Ross formation western Ireland, in P. Weimer and B.F. Perkins Eds., Submarine fans and turbidite Systems, Gulf Coast Section-SEPM Foundation 15th annual research Conference, p.53-68.

Dalrymple, M., 2001, Fluvial reservoir architecture in the Statfjor formation North Sea augmented by outcrop analog statistics, in Petroleum Geoscience, vol. 7, p. 115-122.

Dunkin, J. W. and Levin, F. K., 1973, Effect of normal moveout on a seismic pulse: GEOPHYSICS, Soc. of Expl. Geophys., 38, 635-642.

Eschard, R., Doligez, B., 1992, Subsurface reservoir characterization from outcrop observations, Proceedings of the 7th IFP exploration and Production research conference, Scarborough, eds., Teqnip, Paris.

Frykman, P., Deutsch, C.V., 2002, Practical application of geostatistical scaling laws for data integration, Petrophysics, Vol. 43, No. 3, p.153-171.

Galloway, W.E., 1989, Genetic stratigraphic sequences in basin analysis I: Architecture and genesis of flooding-surface bounded depositional units, AAPG Bulletin, vol.73, p.125-142.

Gardner, M. H., and Borer, J. M., 2000, Submarine channel architecture along a slope to basin profile, Brushy Canyon formation, west Texas, in A. H. Bouma and C. G. Stone, eds., Fine-grained turbidite systems, AAPG memoir 72/SEPM Special Publication No. 68, p.195-214.

Gardner, M. H., Anderson, D. A., Borer, J. B., Carr, M., Batzle, M. L., Atan, S., Dechesne, M., Mavilla, N., Mellick, J. J., 2001, Building a three dimensional understanding of deepwater depositional systems, Colorado School of Mines, seventh annual field conference guide book to selected outcrops of the Permian Basin Brushy Canyon Formation, west Texas, unpublished Colorado School of Mines report for Slope and Basin Consortium, Golden, Colorado.

Gardner, M. H., Borer, J. B., Dechesne, M., Batzle, M. L., Carr, M., Atan, S., Umain, M. S., 2002, Colorado School of Mines Slope and Basin Consortium, seventh annual field conference to the Permian Brushy Canyon Formation, unpublished Colorado School of Mines report for Slope and Basin Consortium, Golden, Colorado.

Gardner, M.H., Borer, J. B., Dechesne, M., Carr, M., Atan, S., Umain, M. S., 2003, Stratigraphic process response model for submarine channels and related features from studies of Permian Brushy Canyon outcrops, west Texas, Marine and Petroleum Geology, 20, p. 757-787.

Gardner, M.H., 2004. Slope and Basin Consortium Website Colorado School of Mines: Resource optimization of slope and basin reservoirs through enhanced imaging of reservoir architecture,. www.mines.edu/Academic/geology/sbc/index.shtml

Gassmann, F., 1951, Elastic wave through packing of spheres, Geophysics, no.16, p. 673 –685.
Gassmann, F., 1951, Uber die Elastizitat poroser medien. Veri der nature Gesellshaft Zurich, 96, 1-23.

Grammer, M.G., Harris, P.M., Eberli, G.P., 2004, Integration of outcrop and modern analogues in reservoir modeling. AAPG memoir 80, AAPG Tulsa, OK.

Graul, M., 2003, Course notes: Seismic amplitude interpretation and AVO analysis, Society of Exploration Geophysics 74th annual conference, Denver, CO.

Han, D.H., Batzle, M. L., 2002, Gassmann equation and fluid saturation effects on seismic velocities, Geophysics, 67.

Han, D. H., Nur, A. M., Morgan, D., 1986, Effect of porosity and clay content on wave velocities in sandstones, Geophysics, 51, p. 2093-2107.

Hardage, B. A., Remington R. L., 1999, 3-D seismic strata-surface concepts applied to the interpretation of a fluvial channel system deposited in a high-accommodation environment: Geophysics, 64, p. 609-620.

Hart, B., Chen, M., 2004, Understanding seismic attributes through forward modeling, in The Leading Edge, October, SEG, Tulsa, OK.

Hill, S., 2002, Seismic Data Concepts of Transformations, ConocoPhillips Short course Notes, CSM Fall 2004, Golden, CO.

Hilterman, F., 2001, Seismic Amplitude Interpretation: Distinguished Instructor Short Course Series no. 4, SEG/EAGE, Tulsa, OK.

Hirsche, K., Boerner, S., Kalkomey, C., Gastaldi, C., 1998, Avoiding pitfalls in geostatistical reservoir characterization: A survival guide, in The Leading Edge, Tulsa, OK, April, p. 493-504.

Hiscott, R. N., Colella, A., Pezard, P., Lovell, A. M., and Malinverno, A., 1992, Sedimentology of deep-water volcaniclastics, Oligocene Izu-Bonin forearc basin, based on formation microscanner images.: Proceedings of the Ocean Drilling Program, Scientific Results, 126, 75–96.

Huffman, A.R., 2002, The future of pressure prediction using geophysical methods, in A. R. Huffman and G. L. Bowers, eds., Pressure regimes in sedimentary basins and their prediction, AAPG Memoir 76, p. 217–233.

Kelly, K., R., Ward, R. W., Treitle, S., and Alford, R. M., 1976, Synthetic seismogram: a finite-difference approach: Geophysics, 41, p. 2-27.

Kelly, K. R., and Marfurt, K. J., 1990, Numerical modeling of seismic wave propagation, Reprint Series, 13, Society of Exploration Geophysicists, Tulsa, Oklahoma.

Kendall, C. G. St., 2003, University of south Carolina, Geology Department, http://strata.geol.sc.edu/index.html, December 20, 2005.

Marfurt, K. J., 1983, Accuracy of finite-difference and finite-element modeling of the scalar and elastic wave equations: Geophysics, 49, 553-549.

Mavko, G., Mukeji, T., and Dvorkin, J., 1998, The rock physics handbook-Tools for seismic analysis in porous media: Cambridge University Press,Cambridge, UK.

Meckel, L.D., 2002, Genetic stratigraphy architecture and reservoir stacking patterns for upper Miocene-lower Pliocene greater Mars-Ursa intraslope basin Mississippi Canyon, Gulf of Mexico, 22nd Annual gulf Coast Section SEPM Foundation Bob F Perkins research Conference, p.113-146.

Larue, D.K., 2004, Outcrop waterflood simulation modeling of the 100 foot channel complex, Texas, and the Ainsa II channel complex, Spain: Analogs to multistory and multilateral channelized slope reservoirs, in Integration of outcrop and modern analogs in reservoir modeling: AAPG Memoir 80, p. 337-364.

Lomas, Joseph, 2004, Confined turbidite Systems, Geological Society of London Special Publications, 222, Geological Society of London, p.1-7.

Mahaffie, M.J., 1994, Reservoir classification for turbidite intervals at the Mars discovery, Mississippi canyon 807, Gulf of Mexico, in P. Weimer, A.H. Bouma, and B.F. Perkins, eds., Submarine fans and turbidite systems: Gulf Coast Section –SEPM Foundation 15th Annual research Conference, p. 233-244.

Marfurt, K. J., 1983, Accuracy of finite-difference and finite-element modeling of the scalar and elastic wave equations: Geophysics, 49, 553-549.

Mavko, G., Mukeji, T., and Dvorkin, J., 1998, The rock physics handbook-Tools for seismic analysis in porous media: Cambridge University Press, Cambridge, UK.

McPeek, L. A., 1981, Eastern Green River basin: A developing giant gas supply from deep, overpressured Upper Cretaceous sandstone: AAPG Bulletin, v. 65, p. 1078-1098.

Meckel, L.D., et al., 2002, Genetic Stratigraphy Architecture and Reservoir Stacking Patterns for Upper Miocene-Lower Pliocene Greater mars-Ursa Intraslope Basin Mississippi Canyon, Gulf of Mexico. 22nd Annual gulf Coast Section SEPM Foundation Bob F Perkins research Conference-2002. p. 113-146.

Mitchum, R.M. Jr., 1984, Seismic stratigraphic recognition criteria for submarine fans: GCS-SEPM Foundation Fifth Annual Research Conference, p. 63-85.

Mitchum, R.M. Jr., 1985, Seismic Stratigraphic recognition criteria for submarine fans, in O.R. Berg and D.G. Woolverton, eds., Seismic Stratigraphy II AAPG Memoir 39, p. 117-136.

Mutti, E., 1985, Turbidite Systems and their relation to depositional sequences, in G.G. Zuffa, ed., provenance of Arenites: NATO-ASI series: Dordrecht, Netherlands Reidel, p. 65-93.

Mutti, E., Normark W. R., 1987, Comparing examples of modern and ancient turbidite systems: problems and concepts, in J.K. Leggett and GG Zuffa, eds., Marine Clastic Sedimentology: London Grahm and Trotman, p. 1-38.

Mutti, E and Normark W. R, 1991, An integrated approach to the study of turbidite systems, in P. Weimer and M.H. Link, eds., Seismic facies and sedimentary processes of submarine fans and turbidite systems: New York, Springer-Verlag, p. 75-106.

Orange, D.L., Saffer, D., Jeanjean, P., Al-Khafaji, Z., Humphrey, G., and Riley, G., 2003, Measurements and modeling of the shallow pore pressure regime at the Sigsbee Escarpment: Successful prediction of overpressure and ground-truthing with borehole measurements. The Leading Edge 22, p. 906-913.

Payton, C.E., 1977, Seismic Stratigraphy-Applications to hydrocarbon exploration, AAPG memoir 26, Tulsa, OK..

Pettingill, H. S., Weimer, P., 2002, Global Deep Water Exploration: Past, Present and Future Frontiers: The Leading Edge, 4, p.371-377.

Pirmez, C., Hiscott, R. N., and Kronen, J. D. J., 1997, Sandy turbidite successions at the base of channel-levee systems of the Amazon fan revealed by FMS logs and cores; unraveling the facies architecture of large submarine fans: Proceedings of the Ocean Drilling Program, Scientific Results, 155, 7–33.

Posamentier, H.W., Jervey, M.T., Vail, P.R., 1988, Eustatic controls on clastic deposition I. Conceptual framework, in Wilgus, C.K., Hastings, B.S., Kendall, Posamentier, H.W., Ross, C.A., Van Wagoner, J.C., Eds., Sea Level Changes—An Integrated Approach, vol. 42. SEPM Special Publication, p.110– 124.

Posamentier, H.W., Jervey, M.T., Vail, P.R., 1988, Eustatic controls on clastic deposition. II. Sequence and Systems tract models: SEPM Special Publication 42, p. 124-154.

Poston, S.R., Berg, B.R.. 2002. Overpressured Gas Reservoirs, SPE Inc. Richardson, TX., p. 5-21.

Prather, B.E., Booth, J.R., Steffens, G. S., Craig, P.A., 1998, Classification, lithologic calibration, and stratigraphic succession of seismic facies of intraslope basins, Deep-Water Gulf of Mexico, AAPG Bulletin Volume 82., p.701 – 728.

Pratson, L., Gouveia, W., 2002, Seismic simulation of experimental strata: AAPG Bulletin, 86, p.129-144.

Pringle, J.K., Westerham, A.R., Clark, J.D., Drinkwater, N.J., Gardiner, A.R., 2004, 3-D high resolution digital models of outcrop analogue study sites to constrain reservoir model uncertainty: an example from Alport Castles, Derbyshire, UK, in Petroleum Geoscience, Vol. 10, 2004, p.1-11.

Pyrcz, M.J., Catuneanu, O., Deutsch, C.V., 2005, Stochastic surface based modeling of turbidite lobes, in AAPG Bulletin, Vol. 89, No. 2, (Feb, 2005). P. 177-191.

Reynolds, M. W., 1976, Influence of recurrent Laramide structural growth on sedimentation and petroleum accumulation, Lost Soldier area, Wyoming: AAPG Bulletin, v. 60, p. 12-33.

Rothman, D.H., Grotzinger, J.P., Flemings, P., 1994, Scaling in turbidite deposition, Journal of sedimentary research, Vol. A64, No. 1, January 1994, p.59-67.

Resnik, J.R., 1993, Seismic Data processing for AVO and AVA analysis in AVO analysis-tutorial and review, in: Offset dependent reflectivity-theory and practice of AVO analysis by J. P., Castagna and M. M. Backus, eds., Society of Exploration Geophysicists, Tulsa Oklahoma, p. 175-188.

Rothman, D.H., Grotzinger, J.P., Flemings, P., 1994, Scaling in turbidite deposition, Journal of sedimentary Research, Vol. A64, No. 1, January 1994, p. 59-67.

Satterfield, W. M., Behrens, E. W., 1990, A Late Quaternary canyon/channel system, northwest Gulf of Mexico continental slope, Marine Geology, v.92, Issues 1-2, p. 51-67.

Scales, J.A., Martin, S.L., Treitel, S., 1997, Introductory geophysical Inverse theory, Samizdat Press, Golden, CO.

Schlumberger, 2005, Schlumberger Oilfield Glossary,www.glossary.oilfield.slb.com. March 26, 2005.

Sheriff, R.E., 1975, Factors affecting seismic amplitudes: Geophysical Prospecting, 23, p.159-186.

Shew, R.D., Rollins, D.R., Tiller, G.M, Hackbarth, C.J., White, C.D., 1994, Characterization and modeling of thin bedded turbidite deposits from Gulf of Mexico using detailed surface and analogue data, in P. Weimer, A.H. Bouma, and B.F. Perkins, eds., Submarine fans and turbidite systems, Gulf Coast Section-SEPM foundation 15th annual research conference, p. 327-334.

Shucy, R. T., 1985, A simplification of the Zoeppritz equations: Geophysics, 50, p. 609-614.

Shuey, R. T., 1985, A simplification of the Zoeppritz's equations: Geophysics, 50, 609–614.

Slatt, R.M., Browne, G.H., 1997, Thin-bedded slope Fan (Channel-Levee) Deposits from New Zealand: An Outcrop Analog for reservoirs in the gulf of Mexico, in Gulf Coast Association of Geological Societies transactions, Vol. XLVII.

Slatt, R.M., 2005, AAPG/SEG Spring Student Expo: Petroleum geology of Deepwater Turbidite Depositional Systems Short Course Notes, Hosted by School of geology and Geophysics university of Oklahoma. March 10-12, 2005.

Sloss, L.L., 1963, Sequences of the cratonic interior of North America: Geological Society of America Bulletin, v. 74, p. 93-114.

Smith, Michael A., 2002, Geological Controls and Variability in Pore Pressure in the Deep-Water Gulf of Mexico, in A. R. Huffman and G. L. Bowers, eds., Pressure regimes in sedimentary basins and their prediction: AAPG Memoir 76, p. 107–113.

Spencer, C. W., 1994, Abnormal formation pressures caused by hydrocarbon generation-examples from the Rocky Mountain region: in W. H., Fertl, R. E., Chapman, and R. F.,

Stelting, C. E., A. H. Bouma, and C. G. Stone, 2000, Fine-grained turbidite systems: overview, in A. H. Bouma and C. G. Stone, eds., Fine-grained turbidite systems, AAPG memoir 72/SEPM Special Publication No 68, p. 1-8.

Stephen, K.D., Clark, J.D, Gardiner, A.R., 2001, Outcrop based stochastic modeling of turbidite amalgamation and its effects on hydrocarbon recovery, Vol. 7, 2001, p. 163-172.

Stovas, A., Landro, M., and Avseth, P., 2004, Estimation of net-to-gross and fluid saturation in a fine-layered sand-shale sequence — tested on offshore Brazil data: SEG Technical Program Expanded Abstracts, 23, no. 1, 228–231.

Sullivan, M.D., Foreman, J.L., Jennette, D.C., Stern, D., Jensen, D.N., Goulding, F.J., 2004, An integrated approach to characterization and modeling of deep-water reservoirs, Diana field, Western gulf of Mexico, in Integration of outcrop and modern analogs in reservoir modeling: AAPG Memoir 80, p. 215-234.

Suryanto, Doddy, 2003, 3-D geologic model of the Lewis Shale in the Great Divide and Washakie Basins, Wyoming, CSM Thesis (January 2003) Chapter 4: Overpressure, p.101-132.

Surdam, R. C., Z. S. Jiao, and J. Liu, 1995, Pressure regime in the Upper Cretaceous shales and sandstones in the Washakie basin, Wyoming: in R. W.

Surdam, R. C., 1997, A new paradigm for gas exploration in anomalously pressure “tight gas sands” in the Rocky Mountain Laramide Basins: in R. C.,

Surdam, ed., Seals, traps, and the petroleum system: AAPG Memoir 67, p. 283-298.

Surdam, R. C., Z. S. Jiao, H. P. Heasler, 1997, Anomalously pressured gas compartments in Cretaceous rocks of the Laramide basins of Wyoming: a new class of hydrocarbon accumulation: in R. C. Surdam, ed., Seals, traps, and the petroleum systems: AAPG Memoir 67, p. 199-222.

Swarbrick, R. E., 1999, GeoPOP, University of Durham, UK, A Research Project Documenting the Pressure History of an Overpressured Basin - Application to Deep Water Pressure. AAPG Bulletin, V. 83, No. 8, p.1296-1346.

Takahashi, I., Mukerji, T., and Mavko, G., 1999, Effect of thin-layering on seismic reflectivity: Estimation of sand/shale ratio using stochastic simulation and Bayes’ inversion: SEG Technical Program Expanded Abstracts, 18, no. 1, 1787–1790.

Taner, M. T., E. E. Cook, and N. S. Neidell, 1970, Limitations of the reflection seismic method: lesson from computer simulations, Geophysics, 35, p. 551-573.

Umam, M. S., 2002, Seismic modeling of deepwater outcrop analogs, CSM Masters Thesis, CSM, Golden, CO. CSM Thesis (2002) .

Vail, P., 1977, Seismic Stratigraphy-Applications to hydrocarbon exploration in Payton, C.E., AAPG memoir 26, Tulsa, OK.

Vail, P.R., 1987, Seismic stratigraphy interpretation using sequence stratigraphy: Part 1: Seismic Stratigraphy Interpretation Procedure, AAPG Studies in Geology #27, volume 1: Atlas of Seismic Stratigraphy, AAPG Special Volumes, AAPG, Tulsa, OK, p. 1 – 10.

Van Wagoner, J.C., Mitchum, R.M., Campion, K.M., Rahmanian, V.D., 1990, Siliciclastic Sequence Stratigraphy in Well Logs, cores, and Outcrops: Concepts for high resolution Correlation of Time and Facies, AAPG Methods in exploration Series, No. 7, AAPG, Tulsa, OK..

Weimer, P., and T. L. Davis, 1996, Applications of 3-D Seismic Data to exploration and Production, eds., in AAPG Studies in Geology 42/ SEG Geophysical Development Series 5, AAPG/SEG Tulsa, Oklahoma, p. 123-132.

Weimer, P., Slatt, R.M., 2004, Petroleum Systems of Deepwater Settings, 2004 Distinguished Instructor Short Course, distinguished Instructor Series No. 7, Society of Exploration Geophysicists and European Association of Geoscientists and Engineers, Tulsa Oklahoma.

Wescot, W. A., Boucher, P. J., 2000, Imaging submarine channels in the western Nile Delta and interpreting their paleohydraulic characteristics from 3-D seismic, The Leading Edge, Vol. 19, No. 6, 5, p. 80-5 90.

Wheeler, H.E., 1958, Time Stratigraphy: AAPG Bulletin, v. 42, p.1047-1063.
Winker, C.D., 1996, High resolution seismic Stratigraphy of late Pliocene submarine fan ponded by salt-withdrawl mini-basins on the Gulf of Mexico continental slope: Offshore Technology Conference Proceedings, OTC 8024, p. 619-628.

Winker, C.D., Booth, J.R., 2000, Sedimentary Dynamics of the salt dominated continental slope, Gulf of Mexico: Integration of observations from the seafloor, near-surface, and deep subsurface, eds., in Weimer, P., Slatt, R.M., Coleman, J.L., Rosen, N. Nelson, C.H., Bouma, A.H., Styzen, M. Lawrence, D.T., Global deepwater reservoirs: gulf coast section-SEPM Foundation 20th Annual Bob F. Perkins Research conference, p.1016.

Yilmaz, O., 2001, Seismic data analysis: processing, inversion, and interpretation of seismic data, Society of Exploration Geophysicists, Tulsa, Oklahoma.

APPENDIX A: GLOSSARY

accommodation (Jervey, 1998): the space available for potential sediment accumulation. This space can be viewed as the combined product of eustacy, tectonics and rates of sediment accumulation.

Amalgamated: a single body

avulsion (Webster's, 2006): The sudden movement of soil from one property to another as a result of a flood or a shift in the course of a boundary stream.

Amplitude or Angle Variation with Offset (AVO) (Schlumberger, 2006): Variation in seismic reflection amplitude with change in distance between shot point and receiver that indicates differences in lithology and fluid content in rocks above and below the reflector. A gas-filled sandstone might show increasing amplitude with offset, whereas a coal might show decreasing amplitude with offset. A limitation of AVO analysis using only P-energy is its failure to yield a unique solution, so AVO results are prone to misinterpretation. One common misinterpretation is the failure to distinguish a gas-filled reservoir from a reservoir having only partial gas saturation ("fizz water"). However, AVO analysis using source-generated or mode-converted shear wave energy allows differentiation of degrees of gas saturation.

baselap (Mitchum, 1977):A term describing terminations of strata along the lower boundary of a depositional sequence, used only where discrimination between onlap and downlap is difficult or impossible.

Bouma Sequence (Schlumberger, 2006): A sequence of sedimentary structures occurring in sedimentary rocks deposited in areas of deep water sedimentation by turbidity currents, which form deposits called turbidites. In theory, a complete Bouma sequence comprises sediments that fine upwards, consisting of a lowermost layer of coarse, chaotic clastic sediments deposited under conditions of high depositional energy overlain by successively finer grained and better stratified sediments like sands and muds deposited under calmer conditions. In practice, however, the chaotic, high-energy nature of turbidite deposition can alter or remove underlying sediments so that incomplete sequences of sediments typically remain preserved.

channel (Mutti and Normark, 1991, Anderson, 2005): Elongate negative relief features produced &/or maintained by turbidity current flow. They represent long-term pathways of sediment transport. The shape and position of the channel within a system are controlled by depositional processes or erosional downcutting. Channels can be amalgamated or clustered together or they can be non-amalgamated or totally isolated.

condensed section (Weimer, 2004): Thin marine stratigraphic units that consist of pelagic to hemipelagic sediments characterized by very slow sedimentation rates. They are areally extensive at the time of maximum regional transgression of the shoreline.

deepwater sediments (Weimer, 2004): Sediments that have been deposited in water beyond 500 m water depth.

depositional Lobes (Mutti and Normark, 1987, 1991): Areas of sand deposition that are located downslope from the main channel. They can be characterized to have tabular geometry, have thicknesses generally 3-15 m and they are usually made up of coarse sandstone beds that are parallel sided.

downlap (Mtchum, 1977): A base-discordant relation in which initially inclined strata terminate downdip against an initially horizontal or inclined surface.
eustacy (Kendall, 2005): Global sea level, which refers only to the position of the sea surface with reference to a fixed datum, such as the center of the earth, and is therefore independent of local factors.
first order cycle (Mitchum, 1977, AAPG Memoir 26): A cycle of relative or eustatic change of sea-level that has duration in the order of 100 to 200 million years.
fifth order cycle (Kendall, 2006): Global sea-level changes at the scale of a few tens years.
fizz gas (Batzle, 2001): non-commercial low gas saturation.
fourth order cycle (Kendall, 2006): Global sea-level changes at the scale of a few hundred thousand years, which are thought to be caused by changes in global ice volume.
geobody: A package or body of sediments that represents a depositional event.
hemipelagic (Kendall, 2006): Deep sea "half" pelagic muddy sediment with more than 5% biogenic grains and a terriginous component that may be more than 40% silt. Others believe that at least 25% of the sediment coarser than 5 microns is composed of terrigenous, volcanogenic, and/or neritic material. Usually accumulates near continental margins.
HST-Highstand Systems Tract (Kendall, 2006): The regressive deposits that form when sediment accumulation rates exceed the rate of relative sea-level rise and increase in accommodation constitutes the upper systems tract in either a type 1 or type 2 sequence. The base of this systems tract is formed by the maximum flooding surface (mfs) over which the Highstand Systems Tract sediments prograde and agrade. The top of this systems tract is formed by the eroded unconformity surface that develops when a sea level fall initiates erosion of the now subaerial Highstand system sediment surface and the start of the Falling Stage Systems Tract.
lapout (Mitchum, 1977) : Lateral termination of strata at their depositional pinchout. Lapout may occur at the upper boundary of a sequence, where it is called toplap, or at the lower boundary, where it is called onlap or downlap.
levee/overbank (Mutti and Normark, 1991): fine grained to thin bedded turbidite sediments, that can be laterally extensive and are adjacent to main channels in a turbidite system and can consist of two parts 1) those with levee relief and 2) those without relief.
LST-Lowstand Systems Tract (Kendall, 2006, Plint and Nummedal, 2000; Coe et al, 2002): Sediments deposited during a relative fall in sea level. These Lowstand Systems Tract sediments form a lowstand wedge and often fill incised valleys that cut down into the Highstand Systems Tract.
mass transport complex (Weimer, 2004): generally a seismic facies description, they are hummocky and mounded reflections with poor to fair continuity; sediments that occur at the base of sequences and are overlain and or onlapped by channel and levee sediments. They commonly overlie an erosional base upfan, becoming mounded downfan and are externally mounded in shape and pinch out laterally.
maximum flooding surface (Kendall, 2006, Posamentier, et al., 1999, Mitchum, AAPG Memoir 26): A surface of deposition at the time the shoreline is at its maximum landward position (i.e. the time of maximum transgression). The surface marks the time of maximum flooding or transgression of the shelf. It separates the Transgressive and Highstand Systems Tract. Seismically, it is often expressed as a downlap surface. Marine

shelf and basinal sediments associated with this surface are the result of slow rates of deposition by pelagic-hemipelagic sediments and they are usually thin and fine grained. These fine sediments make up the condensed section. An mfs is often characterized by the presence of radioactive and often organic rich shales, glauconite, and hardgrounds.

Non amalgamated: layered body

onlap (Mitchum, 1977): A base-discordant relation in which initially horizontal strata terminate progressively against an initial inclined surface, or in which initially inclined strata terminate progressively updip against a surface of greater initial inclination.

overbank (Bates and Jackson, 1984): Silt and clay deposited from suspension on a flood plain by flood waters that cannot be contained within the stream channel.

pelagic (Kendall, 2006): Fine grained deep sea sediment composed of largely of biogenic ooze that is often rich in foraminifera with 60% pelagic and neritic grains. It can also be a red clay, with less than 40% siliciclastic and volcaniclastic grains or silica ooze (often rich in radiolaria)

progradation (Kendall, 2006, Posamantier, 1999): Lateral outbuilding, or progradation, of strata in a sea-ward direction. Progradation can occur as a result of a sea-level rise accompanied by a high sediment flux (causing a regression). The latter usually occurs during the late stages of the development of a Highstand Systems Tract and/or a Falling Stage Systems Tract. A Progradational stacking pattern of parasequences refers to the pattern in which facies at the top of each parasequence becomes progressively more proximal.

second order cycle (Mitchum, 1977, AAPG Memoir 26): A cycle of relative or eustatic change of sea level that has duration in the order of 10 to 80 million years. Supercycles are second-order cycles.

sequence (Kendall, 2006, Posamentier, et al., 1988, Vail, et al., 1977): A relatively conformable succession of genetically related strata bounded at its top and base by unconformities and their correlative conformities. It is composed of a succession of genetically linked deposition systems (systems tracts) and is interpreted to be deposited between eustatic-fall inflection points.

sheet (Mahaffie, 1994): fan lobe deposits that are laterally continuous, tabular geometry. They can be amalgamated or non-amalgamated (layered) where amalgamated sheets are high net/gross, stacked assemblages, of top absent Bouma sequences and layered sheets are lower net/gross with complete Bouma sequences. These range from thick to thin bedded sheets.

slides (Weimer, 2004): a mass movement or descent from failure of earth.

third order sequence (Kendall, 2006):A sequence deposition in about 1-10 million years. This sequence has no internal unconformities and consists of Systems Tracts and their constituent parasequences. There are no high-frequency sequences within a third-order sequence. However, composite sequences deposited in 1-10 million years are common in the rock record.

thin beds (Shew et al., 1994): thin beds are interpreted to include levee, interchannel and outer fan fringe deposits and are composed of fine grained sands or silt and graded beds.

TST-Transgressive Systems Tract (Kendall, 2006): The Transgressive Systems Tract follows the Lowstand Systems Tract and comprises the deposits accumulated from the onset of coastal transgression until the time of maximum transgression of the coast, just prior to renewed regression. Parasequences onlap the sequence boundary in a landward

direction and downlap onto the transgressive surface in a basinward direction. The lower boundary of this systems tract is marked by the development of the transgressive surface that steps up onto the shelf margin. This surface may be marked by erosion and cementation, and often Glossifungites are burrowed into this during or just after the inital transgressive phase that immediately follow sea level lowstands. The top of this systems tract is formed by the maximum flooding surface (mfs) over which the Highstand Systems Tract sediments prograde and agrade.

turbidite (Schlumberger, 2006): Sedimentary deposits formed by turbidity currents in deep water at the base of the continental slope and on the abyssal plain. Turbidites commonly show predictable changes in bedding from coarse layers at the bottom to finer laminations at the top, known as Bouma sequences that result from different settling velocities of the particle sizes present. The high energy associated with turbidite deposition can result in destruction of earlier deposited layers by subsequent turbidity currents.

turbidity current (Schlumberger, 2006): An influx of rapidly moving, sediment-laden water down a slope into a larger body of water; also called a density current because the suspended sediment results in the current having a higher density than the clearer water into which it flows. Such currents can occur in lakes and oceans, in some cases as by-products of earthquakes or mass movements such as slumps. The sedimentary deposits that form as the current loses energy are called turbidites and can be preserved as Bouma sequences. Turbidity currents are characteristic of trench slopes of convergent plate margins and continental slopes of passive margins.

APPENDIX B: RESERVOIR INTERVAL AND SHALE STATISTICS

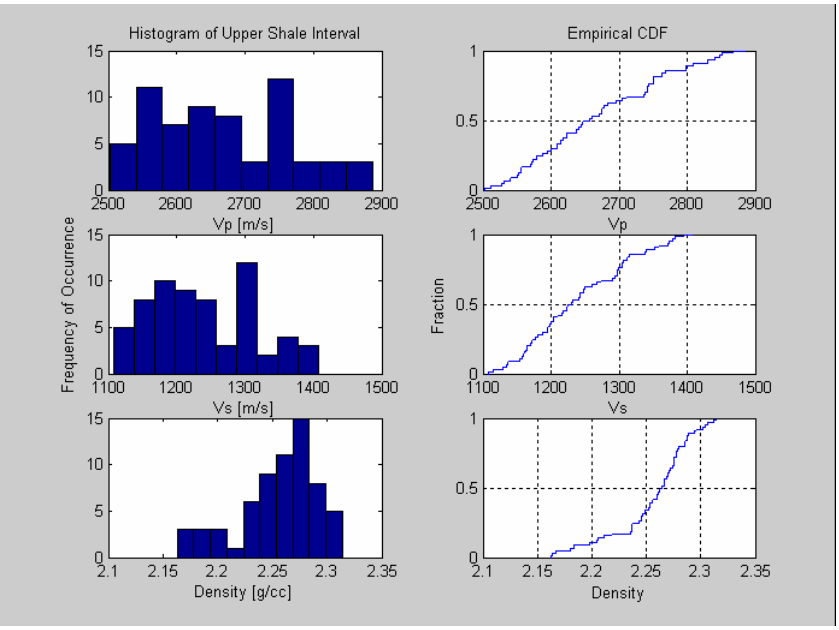

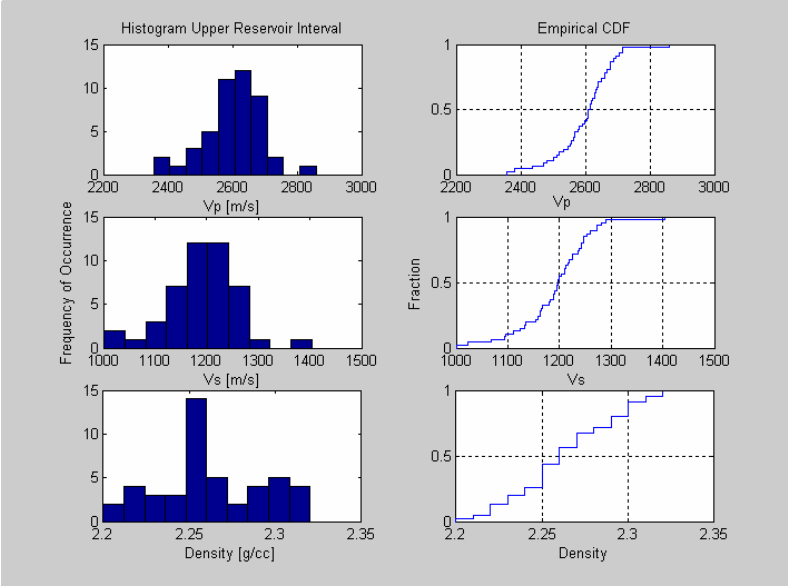

UPPER SHALE				
	Vp [m/s]	Vs [m/s]	density [g/cc]	Vp/Vs
Mean	2667.49	1239.73	2.26	2.16
Variance	9634.09	5727.37	0.00	0.00
Standard Deviation	98.15	75.68	0.04	0.05
Q1	2585.25	1175.50	2.24	2.11
Q2	2652.75	1227.77	2.26	2.16
Q3	3060.86	1569.24	2.37	2.10
Q4	2886.36	1408.12	2.31	2.26
Median	2652.75	1227.77	2.26	2.16

UPPER				
	Vp [m/s]	Vs [m/s]	density [g/cc]	Vp/Vs
Mean	2601.03	1192.74	2.26	2.18
Variance	8207.89	5016.14	0.00	0.00
Standard Deviation	90.60	70.82	0.03	0.06
Q1	2743.47	1310.42	2.27	1.95
Q2	2611.83	1197.36	2.26	2.18
Q3	2659.12	1237.85	2.29	2.20
Q4	2859.29	1403.31	2.32	2.35
Median	2611.83	1197.36	2.26	2.18

UPPER BRINE SAND				
	Vp [m/s]	Vs [m/s]	density [g/cc]	Vp/Vs
Mean	2464.52	1091.98	2.20	2.26
Variance	3272.59	1940.92	0.00	0.00
Standard Deviation	57.21	44.06	0.04	0.04
Q1	2464.64	1080.90	2.19	2.18
Q2	2905.62	1441.69	2.32	2.02
Q3	2490.52	1113.94	2.24	2.29
Q4	2540.00	1149.53	2.24	2.29
Median	2455.24	1083.99	2.21	2.27

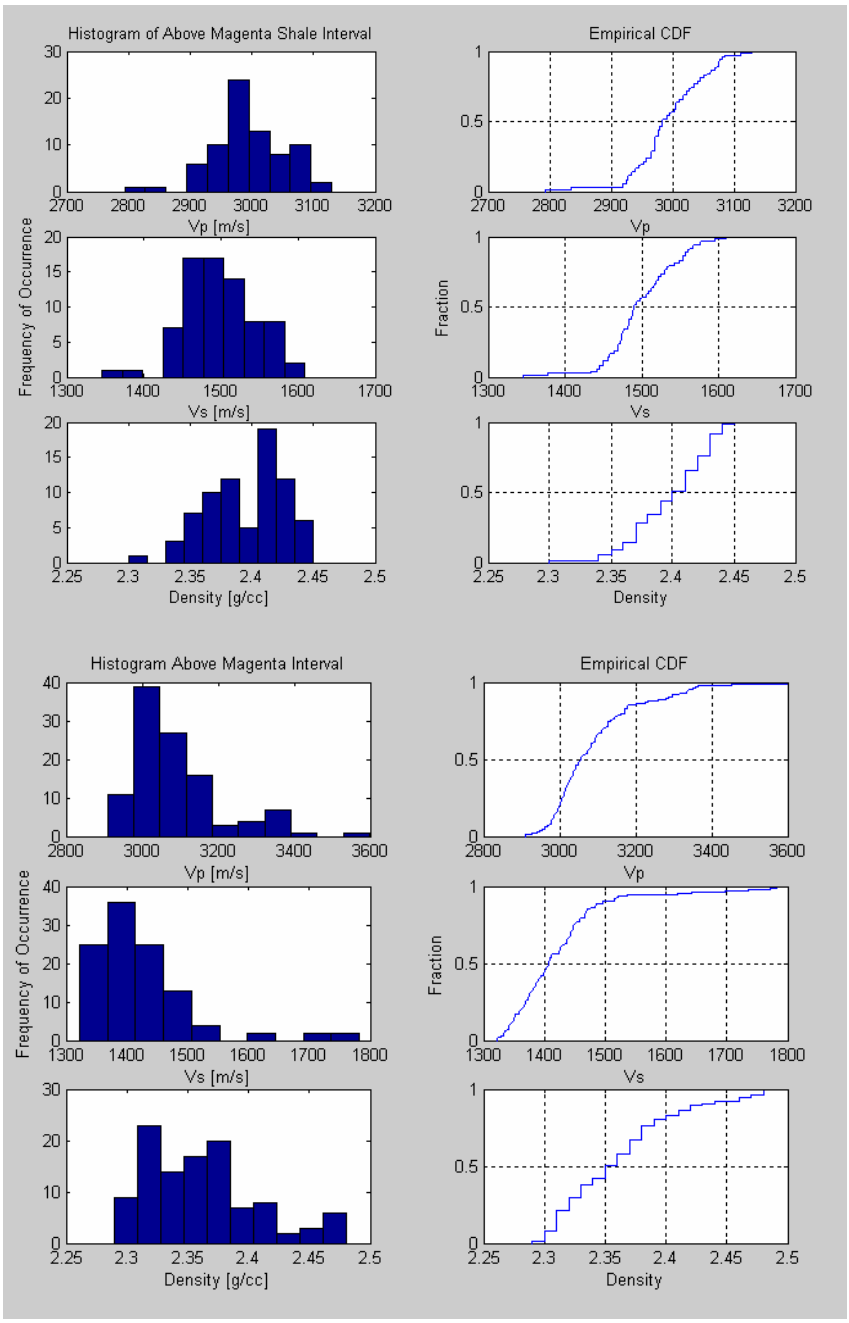
Histogram of Above Magenta Shale Interval
Empirical CDF
Vp [m/s]
Vp
Vs [m/s]
Vs
Frequency of Occurrence
Fraction
Density [g/cc]
Density
Histogram Above Magenta Interval
Empirical CDF
Vp [m/s]
Vp
Vs [m/s]
Vs
Frequency of Occurrence
Fraction
Density [g/cc]
Density

ABOVE MAGENTA SHALE				
	Vp [m/s]	Vs [m/s]	density [g/cc]	Vp/Vs
Mean	2992.76	1498.39	2.40	2.00
Variance	3638.17	2261.79	0.00	0.00
Standard Deviation	60.32	47.56	0.03	0.02
Q1	2964.98	1472.05	2.37	1.98
Q2	2982.39	1489.90	2.40	2.00
Q3	3034.35	1529.50	2.42	2.01
Q4	3129.68	1609.14	2.45	2.08
Median	2982.39	1489.90	2.40	2.00

ABOVE MAGENTA				
	Vp [m/s]	Vs [m/s]	density [g/cc]	Vp/Vs
Mean	2776.75	1448.12	2.26	1.92
Variance	17220.26	5184.48	0.00	0.00
Standard Deviation	131.23	72.00	0.07	0.06
Q1	2704.53	1400.57	2.21	1.86
Q2	2741.01	1437.09	2.25	1.94
Q3	2796.33	1481.61	2.29	1.96
Q4	3358.31	1795.81	2.42	2.04
Median	2741.01	1437.09	2.25	1.94

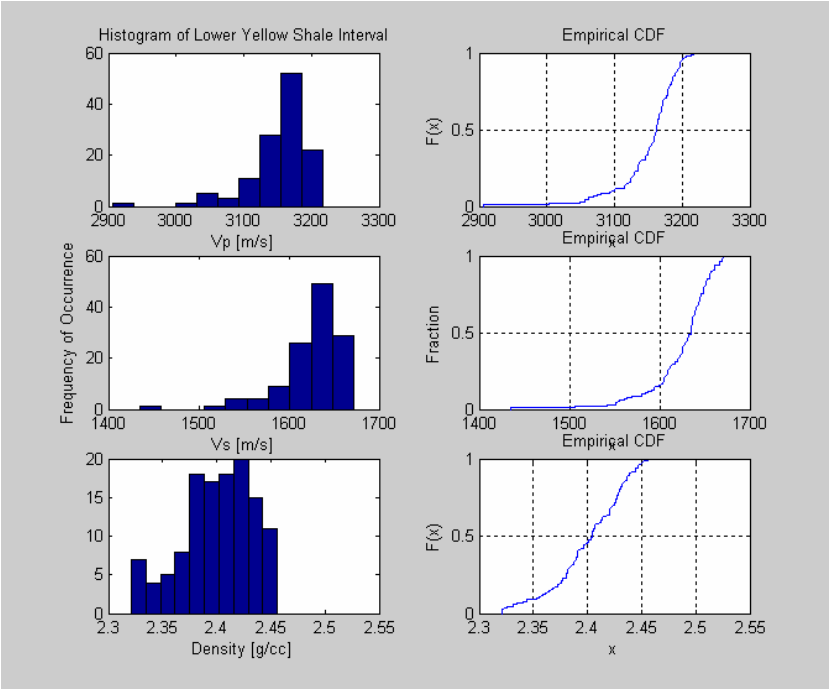

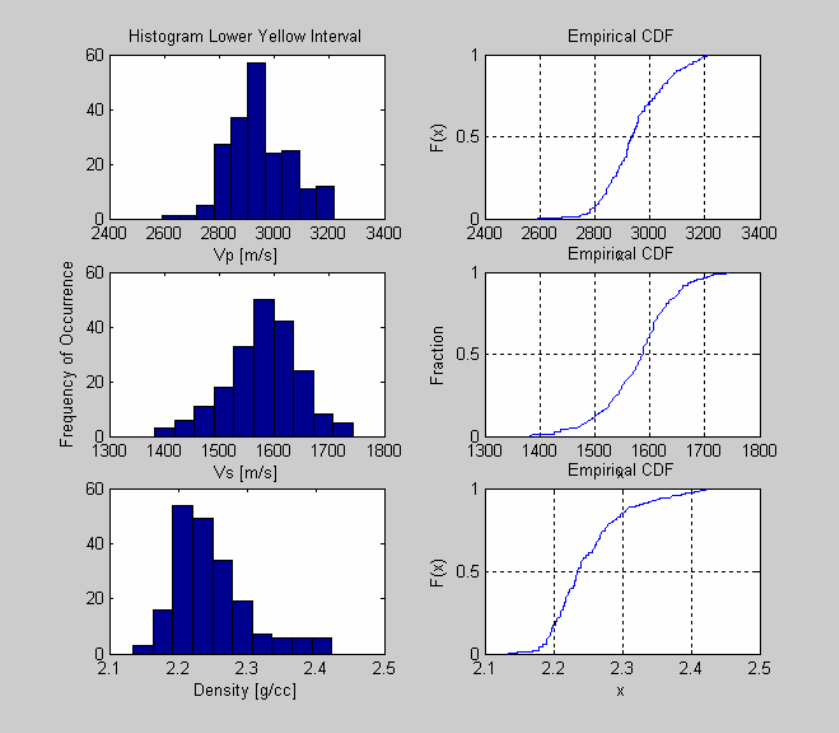

LOWER YELLOW SHALE				
	Vp [m/s]	Vs [m/s]	density [g/cc]	Vp/Vs
Mean	3151.61	1624.83	2.40	1.94
Variance	1929.28	1203.42	0.00	0.00
Standard Deviation	43.92	34.69	0.03	0.02
Q1	3135.64	1609.42	2.38	1.93
Q2	3161.83	1634.81	2.40	1.94
Q3	3178.31	1645.95	2.43	1.95
Q4	3216.55	1672.35	2.46	2.02
Median	3161.83	1634.81	2.40	1.94

LOWER YELLOW				
	Vp [m/s]	Vs [m/s]	density [g/cc]	Vp/Vs
Mean	2947.06	1579.38	2.25	1.87
Variance	12475.72	4448.06	0.00	0.00
Standard Deviation	111.69	66.69	0.06	0.05
Q1	2873.44	1542.43	2.21	1.84
Q2	2936.42	1586.88	2.24	1.85
Q3	3018.57	1618.55	2.28	1.88
Q4	3215.19	1743.02	2.42	2.02
Median	2936.42	1586.88	2.24	1.85

APPENDIX C: FLUID SATURATED RESERVOIR FACIES STATISTICS

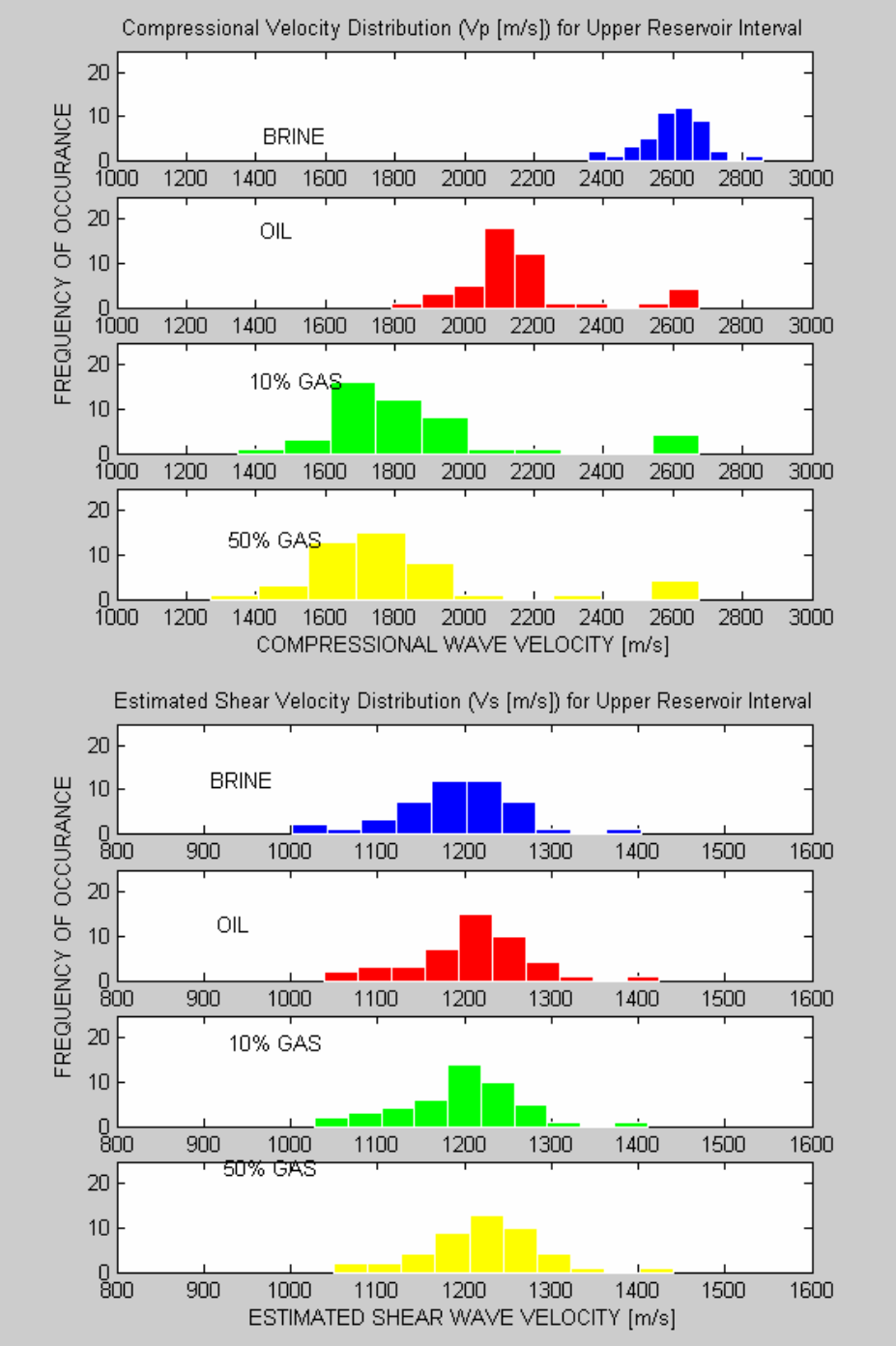
Compressional Velocity Distribution (Vp [m/s]) for Upper Reservoir Interval
FREQUENCY OF OCCURANCE
BRINE
OIL
10% GAS
50% GAS
COMPRESSIONAL WAVE VELOCITY [m/s]
Estimated Shear Velocity Distribution (Vs [m/s]) for Upper Reservoir Interval
FREQUENCY OF OCCURANCE
BRINE
OIL
10% GAS
50% GAS
ESTIMATED SHEAR WAVE VELOCITY [m/s]

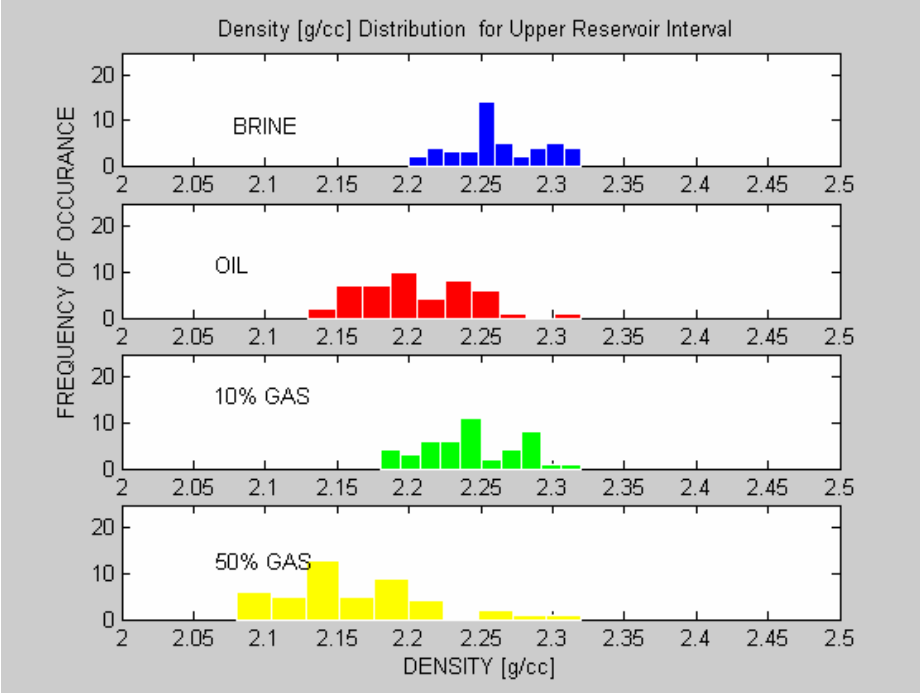
Density [g/cc] Distribution for Upper Reservoir Interval
FREQUENCY OF OCCURANCE
BRINE
OIL
10% GAS
50% GAS
DENSITY [g/cc]

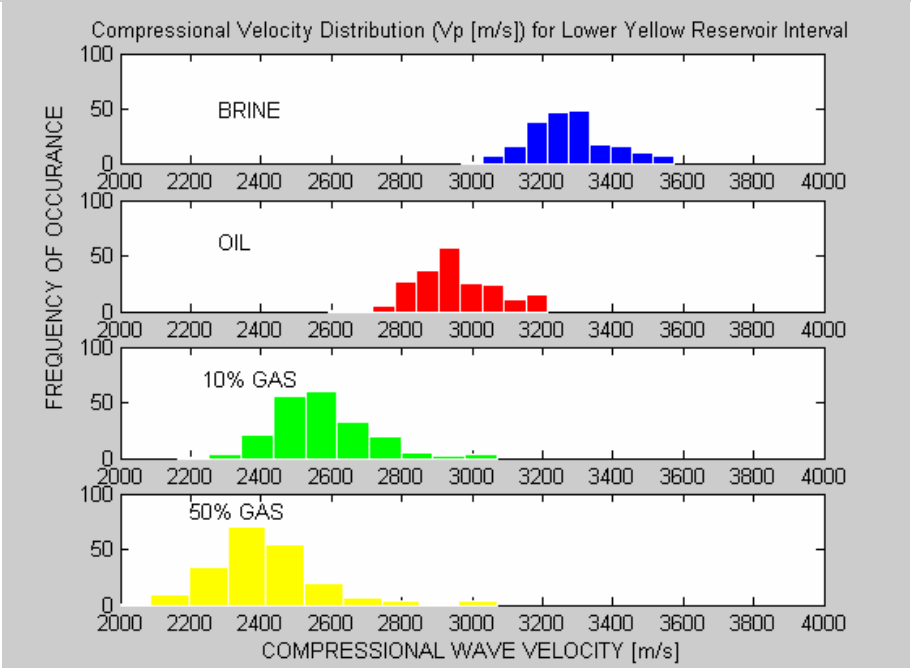
Compressional Velocity Distribution (Vp [m/s]) for Lower Yellow Reservoir Interval
FREQUENCY OF OCCURANCE
BRINE
OIL
10% GAS
50% GAS
COMPRESSIONAL WAVE VELOCITY [m/s]

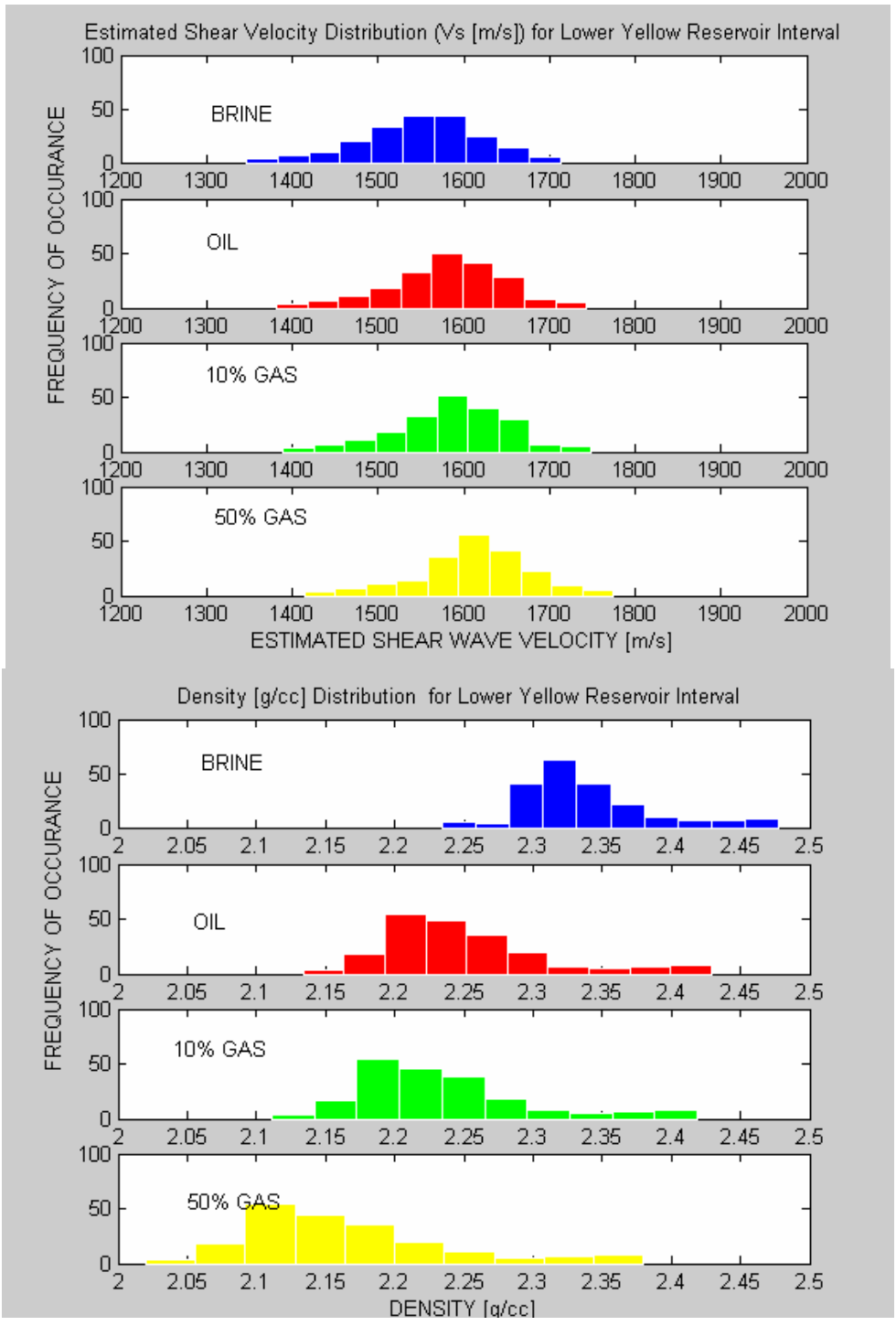
Estimated Shear Velocity Distribution (Vs [m/s]) for Lower Yellow Reservoir Interval
FREQUENCY OF OCCURANCE
BRINE
OIL
10% GAS
50% GAS
ESTIMATED SHEAR WAVE VELOCITY [m/s]
Density [g/cc] Distribution for Lower Yellow Reservoir Interval
FREQUENCY OF OCCURANCE
BRINE
OIL
10% GAS
50% GAS
DENSITY [g/cc]

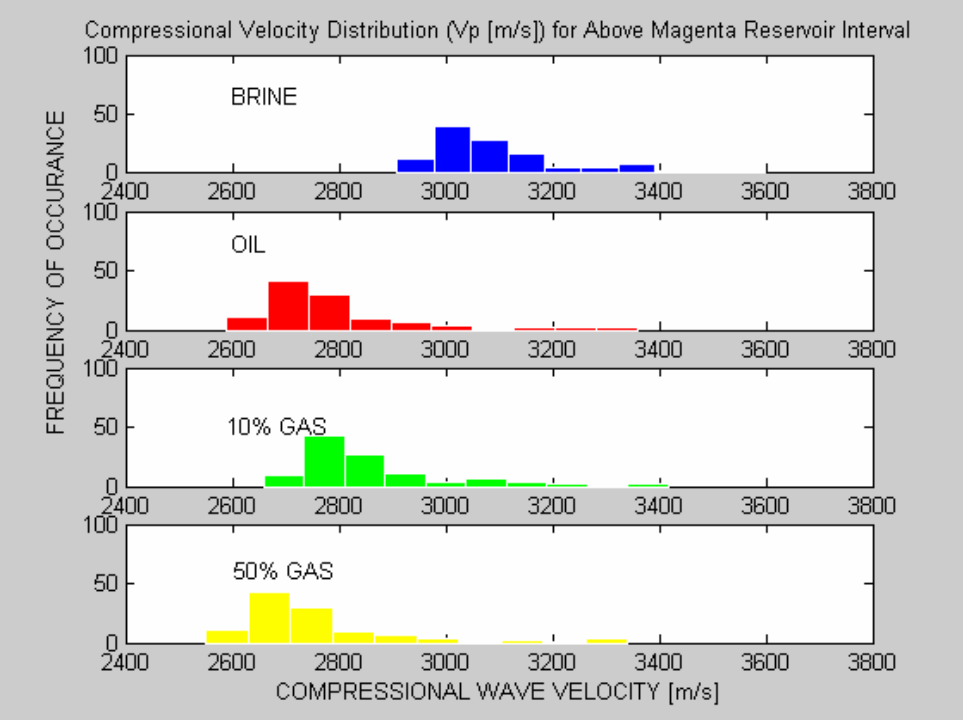
Compressional Velocity Distribution (Vp [m/s]) for Above Magenta Reservoir Interval
FREQUENCY OF OCCURANCE
BRINE
OIL
10% GAS
50% GAS
100
50
0
2400
2600
2800
3000
3200
3400
3600
3800
COMPRESSIONAL WAVE VELOCITY [m/s]

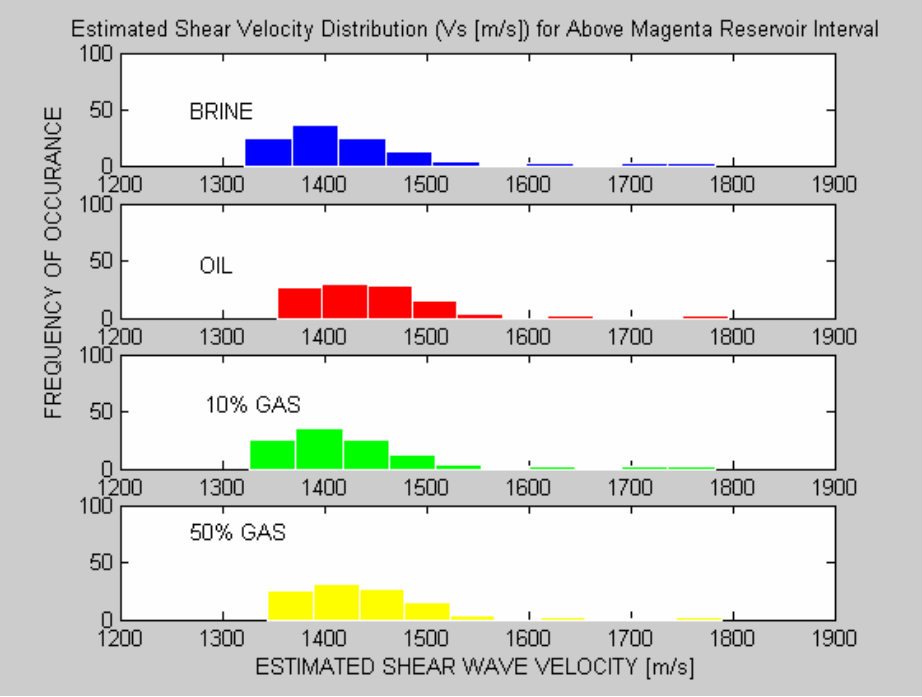
Estimated Shear Velocity Distribution (Vs [m/s]) for Above Magenta Reservoir Interval
FREQUENCY OF OCCURANCE
BRINE
OIL
10% GAS
50% GAS
100
50
0
1200
1300
1400
1500
1600
1700
1800
1900
ESTIMATED SHEAR WAVE VELOCITY [m/s]

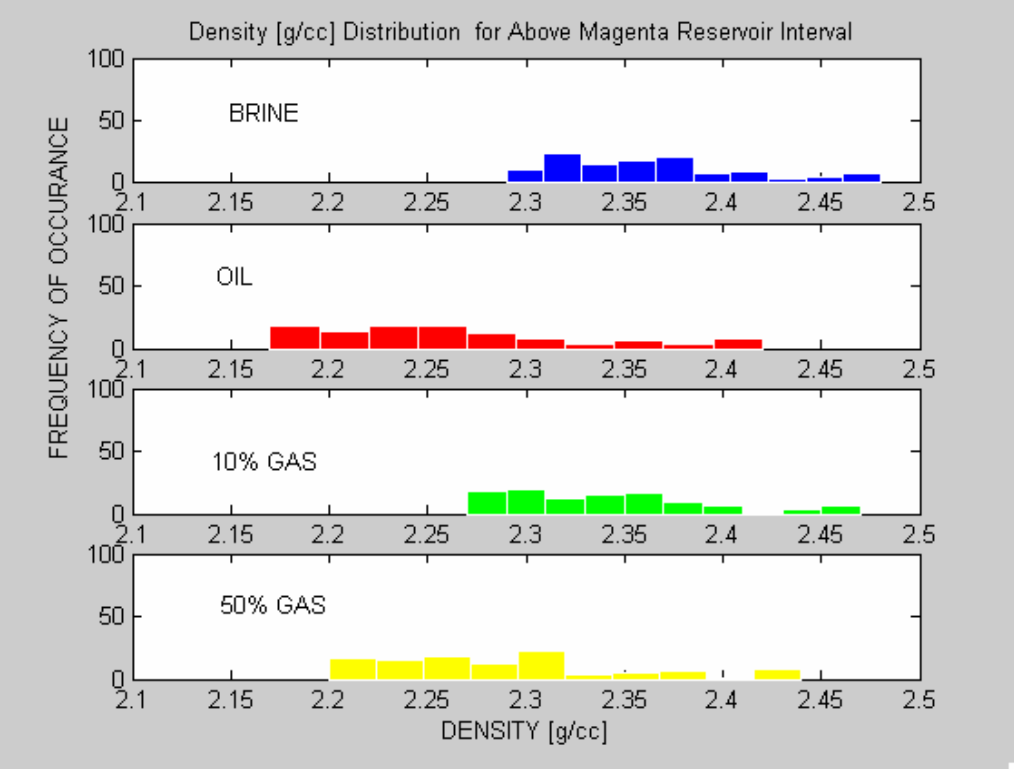
Density [g/cc] Distribution for Above Magenta Reservoir Interval
FREQUENCY OF OCCURANCE
BRINE
OIL
10% GAS
50% GAS
100
50
0
2.1
2.15
2.2
2.25
2.3
2.35
2.4
2.45
2.5
DENSITY [g/cc]

APPENDIX D: CODE FOR SORTING IMAJE J OUTPUT FILES

```
clear all;
close all;
 % code to take the data column every 50 m and put it into a new matrix and
 % output it as a text file.
% read in numbers
x=dlmread('AboveMagentaFluid.txt')
% define array
hs=16;  %this is the spacing between well log traces default 50 m
d = size(x); % get size of matrix
[m,n] = size(x); %seperates and identifies x and y components of matrix size

l=1
       for k = 1:hs:n; %length in horizontal direction
          l=l+1;
            for i = 1:m;  %ok   length in vertical direction

          a(i,l)= (x(i,k));
```

APPENDIX E: VALUES USED FOR RESERVOIR MODELS

ABOVE MAGENTA MODEL

ABOVE MAGENTA RESERVOIR MODEL							
	RANGE VP	RANGE VS	RANGE RHO	VP	VS	RHO	MEAN VP/VS
BACKGROUND	2800-3150	1350-1600	2.3-2.45	2900	1450	2.4	2.00
SHALE/CAPROCK	2800-3151	1350-1601	2.3-2.45	2900	1450	2.4	2.00
CHANNEL SAND							
BRINE	2900-3990	1350-1550	2.29-2.43	3100	1410	2.32	2.20
OIL	2600-3050	1351-1550	2.17-2.43	2700	1400	2.25	1.93
10% GAS	2700-3200	1350-1550	2.26-2.4	2790	1400	2.3	1.99
50% GAS	2850-3000	1350-1550	2.2-2.39	2650	1400	2.3	1.89

Normal incidence Acoustic Impedance of Brine, oil, 10% Gas and 50% gas respectively: 0.02, -0.07, -0.04, -0.07.

LOWER YELLOW MODEL

LOWER YELLOW RESERVOIR MODEL							
	RANGE VP	RANGE VS	RANGE RHO	VP	VS	RHO	MEAN VP/VS
BACKGROUND	2079-3499	772-1884	2.12-2.49	2400	1200	2.1	2.00
SHALE/CAPROCK	3000-3230	1510-1680	2.33-2.45	3151	1624	2.4	1.94
SHEET SAND							
BRINE	3020-3590	1390-1700	2.24-2.47	3330	1551	2.32	2.15
OIL	2600-3200	1390-1750	2.14-2.43	2950	1580	2.25	1.87
10% GAS	2210-3000	1390-1710	2.12-2.42	2700	1590	2.29	1.70
50% GAS	2050-2810	1410-1780	2.05-2.37	2500	1600	2.25	1.56

Normal incidence Acoustic Impedance of Brine, oil, 10% Gas and 50% gas respectively: 0.01, -0.065, -0.1003, -0.14.

UPPER FIZZ ZONE MODEL

NORMAL PRESSURED LEVEE OVERBANK								
		RANGE VP	RANGE VS	RANGE RHO	VP	VS	RHO	MEAN VP/VS
BRINE								
BACKGROUND	=	2375-2886	945-1408	2.16-2.27	2540.00	1140.00	2.24	2.26
SHALES	=	2400-2480	925-1100	2.25-2.30	2650.00	1200.00	2.26	2.30
BRINE SAND	NOT IN RESERVOIR				2464.00	1091.00	2.20	
BRINE		2800-3000	1025-1310	2.26-2.36	2680.00	1200.00	2.25	2.23
OIL		2400-2800	1050-1350	2.16-2.34	2200.00	1200.00	2.20	1.83
10% GAS		2100-2550	1050-1350	2.23-2.34	1800.00	1200.00	2.24	1.50
50% GAS		2000-2600	1060-1380	2.16-2.34	1800.00	1200.00	2.20	1.50

APPENDIX F: CODE FOR SORTING IMAJE J OUTPUT FILES

%CODE TO READ IN FILES AND OUTPUT INTO PSEUDO WELL LOG FILES.

```
% read in numbers
x=dlmread('BRINEVP.txt'); %VPBRINE
y=dlmread('BRINEVS.txt'); %VsBRINE
z=dlmread('BRINERHO.txt'); %RHOBRINE

BRINE50   = [x(:,1),x(:,2),y(:,2),z(:,2)];
BRINE100  = [x(:,1),x(:,3),y(:,3),z(:,3)];
BRINE150  = [x(:,1),x(:,4),y(:,4),z(:,4)];
```

```
BRINE200  = [x(:,1),x(:,5),y(:,5),z(:,5)];
BRINE250  = [x(:,1),x(:,6),y(:,6),z(:,6)];
BRINE300  = [x(:,1),x(:,7),y(:,7),z(:,7)];
BRINE350  = [x(:,1),x(:,8),y(:,8),z(:,8)];
BRINE400  = [x(:,1),x(:,9),y(:,9),z(:,9)];

dlmwrite('BRINE50.txt',BRINE50,'\t')
dlmwrite('BRINE100.txt',BRINE100,'\t')
dlmwrite('BRINE150.txt',BRINE150,'\t')
dlmwrite('BRINE200.txt',BRINE200,'\t')
dlmwrite('BRINE250.txt',BRINE250,'\t')
dlmwrite('BRINE300.txt',BRINE300,'\t')
dlmwrite('BRINE350.txt',BRINE350,'\t')
dlmwrite('BRINE400.txt',BRINE400,'\t')
```